Lithospheric field modeling based on equivalent point sources

- an alternative method for directional wellbore surveying

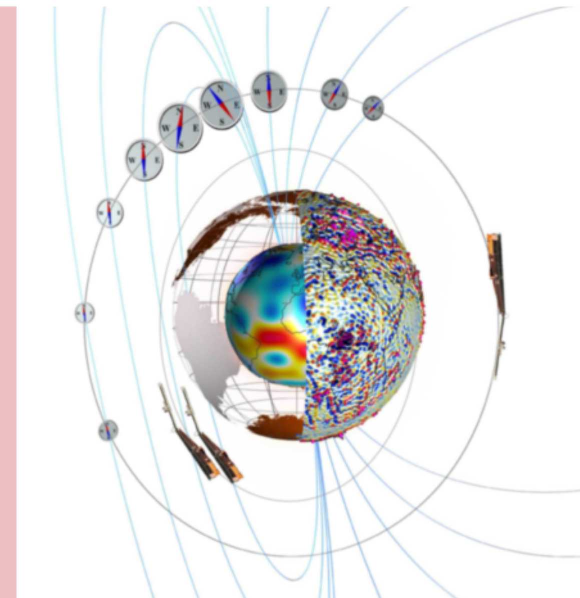

Livia Kother
PhD Thesis
May 2017

Livia Kother
Lithospheric field modeling based on equivalent point sources

DTU Space - National
Space Institute
Elektrovej, building 371
DK-2800 Kgs. Lyngby

+45 / 4525 9500
www.space.dtu.dk

Preface

The content of this thesis was derived during a three-year PhD program at the Division of Geomagnetism, Technical University of Denmark. Due to a one-year maternity leave and a three-month part-time period working on geomagnetic observatory data, the PhD period lasted from March 2013 to June 2017.
The project has been funded by the Technical University of Denmark, ConocoPhillips, Lundin Norway, and the Research Council of Norway through the Petromaks programme. Additional grants for the participation at different conferences and a research stay in Nantes were kindly provided by: Oticon fonden, COWI fonden, Otto Mønsted fonden and Petromaks.

Supervisors:

Prof. Dr. Nils Olsen
Technical University of Denmark
DTU Space, Devision of Geomagnetism
Denmark

Dr. Christopher C. Finlay
Technical University of Denmark
DTU Space, Devision of Geomagnetism
Denmark

Dr. Jürgen Matzka
Helmholtz Centre Potsdam
GFZ German Research Centre for Geosciences
Section 2.3: Earth's Magnetic Field
Germany

Time and place of Ph.D. defence:

Friday, the 15th of September 2017
Technical University of Denmark
Building 308, Auditorium 12
DK-2800 Kongens Lyngby

Examiners:

Dr. Ciaran Beggan
British Geological Survey
Scotland

Dr. Erwan Thébault
University of Nantes
France

Prof. Dr. Per Knudsen
Technical University of Denmark - DTU Space
Denmark

Abstract

Studying the Earth's lithosphere has been an important field within solid Earth geophysics for many decades. The respective signals originate from induced and remanent magnetic minerals in the crust and upper part of the mantle. The lithospheric magnetic field is often denoted as a magnetic anomaly field, as the respective signals are derived after removing the core field and external field contributions from the Earth's magnetic field observations. Apart from observations by satellites, the magnetic anomalies can be studied using marine and aeromagnetic surveys. Such measurements have contributed to our current knowledge of sea-floor spreading and plate tectonics. They are also crucial for prospecting geologic structures, natural resource exploration, determining the depth to magnetic basements, and subsurface navigation.

Global models of the Earth's magnetic field are commonly based on spherical harmonics. This mathematical representation has some limitations when dealing with regional near-surface data or when data are not distributed equally at the Earth's surface. As an alternative, in this study schemes are developed that use equivalent potential field sources for modeling the global and regional lithospheric magnetic field at the Earth's surface. The equivalent sources are arranged in equal-area grids below the Earth's surface. The source amplitudes are estimated using an iteratively re-weighted least-squares algorithm that includes model regularization and Huber weighting.

An application of the proposed method to global field modeling is demonstrated using three-component satellite measurements from CHAMP during its final operational period 2009–2010. Stable model predictions at the Earth's surface are derived using either quadratic, L_1-norm or maximum entropy regularization. The final models are chosen based on the model misfits and assessment of the derived lithospheric field structures on surface maps. The derived model predictions show a degree correlation greater than 0.7 out to spherical harmonic degree 100 with respect to other state-of-the-art global lithospheric field models. Compared to the quadratic and L_1-norm regularization approach, the preferred entropy regularized model possesses notably lower power above degree 70 and a lower number of degrees of freedom despite globally fitting the observations to a very similar level.

A demonstration of the regional application of the equivalent point source routine is carried out based on aeromagnetic scalar data from off-shore Norway. The chosen source grid size, source depth and regularization parameter are important factors determining the level of misfit to the data and the model stability on downward continuation. The regional application is also tested against real well data from the Ekofisk field in the North Sea. For this test, small-scale signals of the lithospheric field are estimated using an equivalent potential field source model based on aeromagnetic data, combined with the CHAOS-6 model (Finlay et al., 2016a) for main field and large-scale lithospheric field predictions. Differences between the final model predictions and actual measurements are found to be within the acceptance limits of the industry. The model is also compared to the industry-standard model BGGM2016, with differences mainly seen in the small-scale lithospheric field predictions.

Finally, an attempt to combine satellite and near-surface measurements is made by producing an equivalent point source model based on both radial CHAMP data and regional geomagnetic intensity data from North America. Both the resulting intensity field map at the Earth's surface and the regional power spectrum compare well with alternative high-resolution global lithospheric field models derived from satellite and near-surface measurements.

Overall, this study demonstrates that equivalent point sources are a powerful tool for modeling the lithospheric field on both global and regional scales. The scheme has no restrictions on the data density, altitude or area shape. Additionally, the model predictions can easily be projected to any surface and transferred into spherical harmonics. The methodology is thereby a suitable candidate for future advanced applications in directional surveying.

Dansk resumé

I mange årtier har undersøgelsen af litosfæren været et aktuelt emne indenfor geofysik. Litosfæren er den yderste og faste del af jorden og inkluderer både skorpen og den øverste del af kappen. Magnetiserede mineraler i disse lag er årsagen til litosfærens bidrag til jordens magnetfelt. Til trods for dens lille andel i det samlede geomagnetiske signal ved jordoverfladen har litosfærens magnetfelt en stor betydning for undersøgelser af råstoffer, tykkelsen af det magnetiske lag og underjordisk navigation. Udover det skyldes en stor del af vores nutidige viden om havbundsspredningen og pladetektonik studier af litosfærens magnetfelt.

Globale modeller af jordens magnetfelt er ofte baseret på kuglefunktioner. Den tilsvarende matematiske beskrivelse er ikke optimal når man har regionale data eller data med inhomogen fordeling. Som et alternativ bliver der i denne afhandling produceret en metode baseret på ækvivalente punktkilder (monopoler) for at modellere litosfærens globale og regionale magnetfelt på jordens overflade. Monopolerne er fordelt i et gitter med lige store arealer under jordens overflade. De tilsvarende monopol amplituder estimeres ved brug af en iterativ genvægtet mindste kvadraters metode som inkluderer model regularisering og Huber vægtning. De resulterende modeller skal beskrive målingerne så godt som muligt, og derfor skal de tilsvarende forskelle være lille.

Den globale anvendelse af metoden undersøges ved hjælp af de sidste års magnetfeltmålinger af satellitten CHAMP. Modellernes stabile opførelse i feltstrukturen opnås ved brug af regularisering. Der undersøges tre forskellige versioner heraf: kvadratisk, L1-norm og entropi regularisering. For hver af disse bliver der bestemt en endelig model på baggrund af mindst mulig diskrepans til målingerne, samt de modellerede feltstrukturer på jordens overflade. Vores resultater indikerer god overensstemmelse med eksisterende globale litosfæriske modeller. Sammenlignet med den endelige kvadratisk og L1-norm regulariserede model har den foretrukne entropi regulariserede model mindre energi for bølgelængder mindre end 570 km og færre frihedsgrader selv om alle tre modeller repræsenterer målingerne med lignende præcision.

Den regionale anvendelse af metoden testes ved brug af aeromagnetiske feltstyrke målinger fra Norge. I forhold til den globale metode bruges der kun monopoler omkring data området. Den tilsvarende mængde af monopoler, deres dybde og metodens regulariseringsparametre er vigtige faktorer for modellernes forskelle til målingerne og evne til at estimere feltværdier under jordens overflade. Sidstnævnte er altafgørende for at kunne bruge metoden for underjordisk navigation. For at undersøge om den regionale metode kan anvendes i sådan en sammenhæng, bliver en monopol-baseret model sammenlignet med målinger fra en brønd i Nordsøen. For denne test bliver de små bølgelængder af litosfærens magnetfelt repræsenteret af en monopol model fra aeromagnetiske data, mens de store bølgelængder og kernefeltet er estimeret ved brug af CHAOS-6 (Finlay et al., 2016a). Forskelle mellem model og brøndmålinger er indenfor de accepterede grænseværdier af industrien. Modellen er også sammenlignet med industriens standardmodel BGGM2016 og de tilsvarende forskelle viser sig at være størst for de korte bølgelænger.

I afhandlingens sidste del bruges metoden til at modellere litosfærens magnetfelt ved at invertere både radiale CHAMP målinger og feltstyrke data fra Nord Amerika. Den resulterende model og dens regionale power spektrum er i god overensstemmelse med andre globale modeller som er baseret på satellit og overflade målinger.

Afhandlingen viser at ækvivalente punkt kilder kan med fordel bruges for at modellere litosfærens globale og regionale magnetfelt. Metoden har ingen restriktioner på målingernes fordeling, højde eller areal. I tillæg kan kilderne bruges til at estimere lithosfærens vektorfelt i forskellige dybdelag, hvilket er en vigtig forudsætning for at kunne anvende metoden til underjordisk navigering. De resulterende modelværdier kan nemt omformes til kuglefunktioner.

Acknowledgements

The production of this PhD thesis has been a long journey which could not have been accomplished without the help and support of many great people.

My first thoughts are devoted to my supervisors Nils Olsen, Christopher C. Finlay and Jürgen Matzka who have shared their great knowledge of geomagnetism already years before I started to work as a PhD student. I am fully indebted to Christopher C. Finlay. His combination of scientific expertise and encouraging enthusiasm has been a great source for this work. Warm thanks go also to Jürgen Matzka. The collaboration between the oil industry, Norwegian Geological Survey (NGU) and DTU Space would not have been as fruitful without his great effort at the initial stages of this project.

Also the rest of the geomagnetism group at DTU Space deserves my genuine gratitude, as they have contributed to a perpetual warm and friendly work atmosphere during my time at DTU.

I would also like to thank the geomagnetic group and all PhD students at the "Laboratoire de Planétologie et Géodynamique de Nantes" in France for making my four month research stay a memorably experience. In particular, I would like to thank Erwan Thébault for his time and explanations of different aeromagnetic topics, as well as his support and useful suggestions during the revision work of my first paper.

The work with aeromagnetic data from the NGU would not have been possible without the help of Odleiv Olesen and Aziz Nasuti. I am grateful for their patience, data support and explanations of the different data processing routines.

To Inge Edvarsen at Baker Hughes, I would like to express my deep gratitude. He allowed me to gain insight into the world of directional drilling and spent much time explaining the different routines of the industry. I appreciate his support throughout the years and that he never got tired of my questions.

I thank Fotini Vervelidou for the generation of regional power spectra of my models.

I would also like to thank Mike Herbert from ConocoPhillips Norway for his help regarding wellbore data request, Kim Eilief Madsen for his friendly and efficient technical support at DTU, and Georges Maynet for providing me with an office whenever I came to the astrophysical observatory in Geneva.

Many thanks also to the diligent proof readers of this thesis: Christopher C. Finlay, Nils Olsen, Anna Naemi Willer, Magnus Danel Hammer, Inge Edvardsen, Diana Saturnino, Dhananjay Ravat, Ida A. Nissen and Mads Sørensen. Your comments and suggestions have improved the manuscript tremendously. Special thanks go to Truls Hansen, who reviewed most of the manuscript.

To all my friends and family for supporting me through the ups and downs of the project. I feel lucky to have you all by my side.

Last, but by no means least, I owe my deepest gratitude to my partner Mads and son Leopold. Your love and patience have been invaluable precious to me.

List of Tables

List of Figures

List of acronyms and abbreviations

BGGM	British Geological Survey Global Geomagnetic Model
BHA	Bottom Hole Assembly
CHAMP	Challenging Minisatellite Payload
CM	Comprehensive Modeling approach
DTU	Danish Technical University
ER	Maximum Entropy Regularization
FAC	Field-Aligned Currents
HDGM	High Definition Geomagnetic Model
HS	Harmonic Splines
IFR	In-Field Referencing
IGRF	International Geomagnetic Reference Field
IMF	Interplanetary Magnetic Field
IRLS	Iteratively Re-weighted Least Squares
ISCWSA	Industry Steering Committee on Wellbore Survey Accuracy
L1	L_1-norm Regularization
MF	Lithospheric field model estimated by sequential analysis
MSA	Multi Station Analysis
MWD	Measurement While Drilling
NGU	Norwegian Geological Survey
ODE	Ordinary Differential Equations
POGO	Polar Orbiting Geophysical Observatory
QD	Quasi Dipole
QR	Quadratic Regularization
RMS	Root Mean Square
R-SCHA	Revised Spherical Cap Harmonic Analysis
RSS	Rotary Steerable System
SCHA	Spherical Cap Harmonic Analysis
SH	Spherical Harmonics
TVD	True Vertical Depth
WDMAM	World Digital Magnetic Anomaly Map

Contents

1 Introduction

The Earth has possessed a magnetic field for at least 3.2 Ga. It originates in the Earth's core and reaches out to several Earth's radii where it meets the solar wind and its accompanying interplanetary magnetic field. In that sense, the geomagnetic field defines a boundary between the Earth's domain and outer space. It was the historical work of William Gilbert (1544-1603) *De Magnete* which placed geomagnetism on the scientific agenda in 1600. He was the first to enunciate that the shape of the geomagnetic field outwardly is similar to that of a bar magnet: "Magnum magnes ipse est globus terrestris". In the previous 400 years geomagnetism has been studied for mainly two reasons: its source was unknown and marine navigation. Concerning the latter, compasses have been used extensively for navigation at sea since the 13th century. The corresponding maps of declination have been crucial for the sailing nations of that time. Today, compasses have been replaced by radio- and satellite navigation systems. However, the need of magnetic field as a navigational tool continues to live in the drilling industry. But also our current knowledge of the Earth's tectonic history and deep interior structure as well as present societal issues like the security of satellites and electric power systems, and mineral exploration campaigns benefit from the science of geomagnetism.

The geomagnetic field can be measured both at or near the Earth's surface using base stations, observatories, aeromagnetic or marinemagnetic surveys, or from space using satellites. In both cases the measurements comprise a superposition of different geomagnetic sources of internal and external origin. The internal sources (originating below the Earth's surface) are dominated by the main field which is generated from current motions in the outer liquid core. Additional contributions are given by the magnetized rocks in the lithosphere as well as fields generated by the movements of conducting seawater. Field signals from external sources are based on the interaction between the Earth's internal magnetic field and the solar wind. The corresponding current systems are initiated in the outermost part of the geomagnetic field, the magnetosphere, which shields the planet against charged particles from the solar wind and cosmic radiation. Both internal and external sources have overlapping spatial and temporal signatures, which makes it challenging to model the individual source contributions. Improving knowledge of the geomagnetic sources, their mechanisms and temporal-spatial behavior, as well as high quality satellite, near-surface and ground based measurements are therefore crucial for the generation of realistic field models.

Below the subsurface, GPS (or other satellite/radio based navigation systems) cannot be used for navigation. Instead, navigation can be based on three other references for orientation: the gravity field, the geomagnetic field or the Earth's rotation (using a gyro compass). For technical and economical reasons, the present-day drilling industry uses a combination of the former two for directional wellbore surveying. Highly accurate geomagnetic field models are thus important to minimize both the positional error ellipsis, economic consequences, and the risk to hit existing pipeline systems and miss the original target. The accuracy of geomagnetic models used for directional wellbore surveying improves distinctively with the implementation of regional lithospheric field data from either marine or airborne surveys. This background initiated two PhD projects which are co-financed by the Technical University of Denmark, ConocoPhillips, Lundin and the Norwegian research council. The first project investigates a new modeling approach for estimating high temporal fluctuations in the external field at polar regions (Aakjær et al., 2016). These geomagnetic signals are a major error source for directional drilling at high latitudes. The second project, this thesis, focuses on an alternative modeling scheme for global and regional lithospheric field models which is easy to implement in the industry and may be used to improve navigational wellbore accuracy.

Based on the potential properties of the geomagnetic field and assuming a current-free region at the Earth's surface, the geomagnetic field can be expressed by the gradient of a scalar potential consisting of linear combinations of spherical harmonics (SH). This mathematical representation was introduced by Carl Gauss (1777–1855) in the 19th century and enables the geomagnetic source separation of internal and external origin. SH are still widely used for global geomagnetic field models. However, the method has distinct disadvantages for regional models of the magnetic field, especially the lithospheric field, which can be circumvented using alternative mathematical approaches. The models derived for this thesis are for instance based on magnetic monopoles as equivalent sources. The respective mathematical representation is convenient and simple to implement into an inversion scheme. Chapter 2 gives the corresponding mathematical background and model inversion routine. Based on this routine, both global and local lithospheric field models are generated from satellite and aeromagentic data, respectively. The corresponding results are presented in chapter 3 for the global models, and chapter 4 for the local models. The latter also comprises a case study, comparing the industry standard BGGM2016 model with an equivalent source based model for actual directional survey measurements from a specific well within the Ekofisk field in the North Sea.

The final part of the thesis uses the equivalent source routine and combines satellite measurements and a compiled aeromagnetic map for generating a high resolution lithospheric field model of North America. The corresponding method and results can be found in chapter 5.

The thesis terminates with chapter 6, which summarizes and discusses the derived results.

1.1 Geomagnetic field sources

The geomagnetic field $\mathbf{B}(\mathbf{r}, t)$ measured at and near the Earth's surface at time t and location $\mathbf{r} = (r, \theta, \phi)$ is a superposition of several field contributions with a variety of spatial and temporal scales, as illustrated in Fig. 1. These different field sources are commonly divided into internal sources, originating inside the Earth, and external sources $\mathbf{B}^{ext}(\mathbf{r}, t)$ that are generated from current systems in the ionosphere and magnetosphere. All sources are dynamic and thus vary with time, but an estimate of the external part of the observed geomagnetic field is approximately 3%. The internal sources are dominated by convective motions in the outer liquid core $\mathbf{B}^{core}(\mathbf{r}, t)$, representing about 95% of the observed geomagnetic field during quiet conditions (i.e periods with low external activity). The remaining part is generated from magnetized rocks in the lithosphere and motion-induced oceanic currents (by e.g. lunar tidal forces), as well as secondary lithospheric and oceanic fields due to temporal changes of the external fields $\mathbf{B}^{lit}(\mathbf{r}, t)$ (Olsen et al., 2010a; Thébault et al., 2010). The latter are sometimes classified as part of the external sources. Additionally accounting for measurement errors $\epsilon(t)$, the observed geomagnetic field is given by

$$\mathbf{B}(\mathbf{r}, t) = \mathbf{B}^{core}(\mathbf{r}, t) + \mathbf{B}^{ext}(\mathbf{r}, t) + \mathbf{B}^{lit}(\mathbf{r}, t) + \epsilon(t). \tag{1}$$

Knowledge of the different geomagnetic source contributions and their separation is crucial for our understanding of the geomagnetic field. This is in particular the case for the lithospheric part, as the respective source signal is highly localized and overshadowed by other field contributions at satellite altitude. Insufficient removal of these contributions will mask the resulting lithospheric field models and reduce the corresponding accuracy.

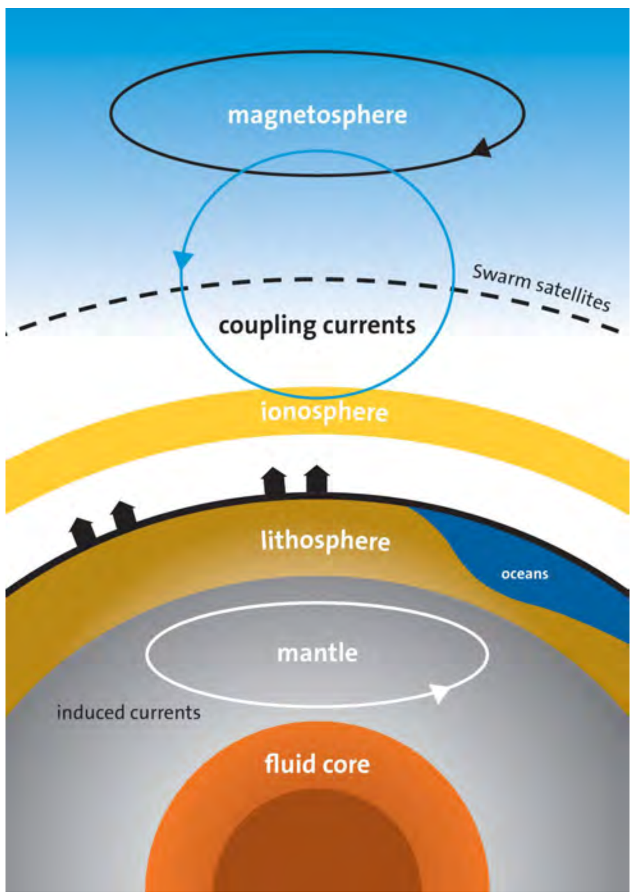

Figure 1 Different sources contributing to the near-Earth geomagnetic field. Credit: ESA/DTU Space

1.1.1 Internal sources

Core field

The main part of the geomagnetic field originates in the outer core at a depth between 2900 and 5200 km (Thébault et al., 2010). This part of the Earth consists mainly of iron and up to 10% nickel, liquified due to the intense pressure and heat produced by long lived radioactive elements (Lowrie, 2007). It is believed that the cooling of the outer core solidifies the inner core, leaving behind a less-dense fluid which causes convective motions with typical velocities of a few tens of kilometers per year. The motion of the electrically conductive matter in the geomagnetic field, together with the different rotation speeds of the outer and inner core, generate electrical currents which maintain the geomagnetic field (Olsen et al., 2010a). This self-sustaining dynamo produces a magnetic field which can be approximated by a geocentric dipole aligned along the spin axis (Merrill and McFadden, 1999). Corresponding near-surface intensities range from 25,000 nT near the equator to 65,000 nT near the poles (Olsen and Stolle, 2012).

Since the spatial small-scale features of the core field are masked by the lithospheric field, see Fig. 4, and the temporal high frequency features are to some extent shielded by the conducting mantle (Olsen, 2002), only part of the dynamo-generated field is observable at and above the Earth's surface.

Variations in the outer core motions introduce temporal changes of the geomagnetic core field on timescales of years to centuries. These slow changes are known as *secular variation* and have typical values of 40 nT/yr (Thébault et al., 2010). But also sudden changes in the secular variation (so-called *jerks*) and geologically long time variations which change the polarity of the core-field (reversals) have been observed in both sedimentary, marine and volcanic magnetic rock material throughout the globe. The magnetic memory ability of these rocks enables the lithosphere to record the historical changes of the core field. The investigation of these paleomagnetic samples reveals that the Earth's magnetic field and its dynamo have existed for at least 3.5 Ga (Olson and Amit, 2006) and that the dipole part of the magnetic field has reversed its sign several hundred times in the Earth's history (Glatzmaier et al., 1999). The study of these polarity transitions is important for understanding the mechanisms of the dynamo as well as the processes connecting the physics of the core and mantle. Additionally, several studies have indicated a possible connection between the Earth's reversal pattern and changes in the biodiversity, the eccentricity of the Earth's orbit, the ice ages, tectonic conditions, sea surface temperatures as well as changes in the solar activity and cosmic radiations (Cox, 1969; Jacobs, 1994; Wendler, 2004).

Lithospheric field

The magnetic field of the Earth's lithosphere, also denoted as an *anomaly field*, is masked by core field and external field contributions, which have to be removed from the raw magnetic measurements prior to lithospheric investigations. Since the magnetic signal below spherical harmonic (SH) degree 15 cannot be separated from the core-field (see section 1.2), only lithospheric length scales smaller than 2500 km are resolvable (Thébault and Mandea-Alexandrescu, 2007).

The lithospheric field is characterized by a complex mixture of spatial diverse features with amplitudes ranging from 0 to ± 1000 nT (Thébault and Mandea-Alexandrescu, 2007). The diffuse field pattern is caused by the lithospheric magnetic materials, mostly ferromagnetic minerals like magnetite, which become magnetized when exposed to a magnetic field. Because magnetization is lost beyond mineral specific Curie temperatures, the magnetic material responsible for the lithospheric signal is located above the Curie-isotherm (ca 580°C) which is commonly found in the upper part of the mantle at approximately 30 km depth below continents and 6 km in the oceanic regions. Rocks responsible for the lithospheric signal carry two different types of magnetization: induced and remanent. The former is only valid in the presence of an ambient field and generates magnetic signatures which are proportional to the corresponding strength and direction. Induced magnetization is most prominent in continental regions and contributes mainly to large-scale structures of the lithospheric field. Remanent magnetization, on the other hand, is more pronounced on a local scale and within oceanic basin rocks. This type of magnetization is acquired during rock formation and continues to produce permanent magnetism in the absence of an inducing field. Since only rarely intense pressure forces, temporal or chemical processes can alter remanent magnetization, important knowledge of the ancient main field orientation is locked inside remanent magnetic samples.

The ratio between induced and remanent magnetization is rock dependent, making both the mineral com-

position, their magnetic susceptibility, grain size, pressure forces and temperature important factors for the amount of magnetization measured.
Since the lithosphere is about five times thicker below continents than oceans, magnetic field amplitudes are typically lowest above oceanic regions.
The large-scale structures of the lithospheric field can be estimated using global measurements from satellites which are corrected for external- and core field contributions by geomagnetic models. These structures reveal information of the rock type variations in the lower crust (Thébault and Mandea-Alexandrescu, 2007). More detailed and high-resolution models of the local anomaly field and information on the upper crust variations cannot be revealed from satellite data as signals with short wavelengths attenuate more rapidly with altitude than signals with long wavelengths (see equations (18) and (20)) (Thébault et al., 2010). This type of information is based on regional magnetic measurements using either marine or aeromagnetic surveys. The present study uses satellite and aeromagnetic data for the generation of global and regional lithospheric field models, respectively. The reader is referred to Appendix A for an introduction to aeromagnetic data processing routines.

Oceanic contributions

The movement of electrically conducting seawater relative to the Earth's main field induces oceanic currents and hence secondary magnetic fields (Tyler et al., 2003; Kuvshinov and Olsen, 2005). The poloidal part of these fields (in the direction of the main field) is detectable at satellite altitude with typical field amplitudes of a few nT, whereas the toroidal part (perpendicular to the main field direction) contributes up to 100 nT at the Earth's surface (Tyler et al., 2003). Despite the small geomagnetic contribution from oceanic tides, separating the corresponding signals from the other internal sources will increase the accuracy of lithospheric field models.

1.1.2 External sources

Geomagnetic external sources, with a time spectrum ranging between seconds and decades, are generated by large-scale current systems in the magnetosphere and ionosphere as the result of a complex interaction between the Earth's internal magnetic field, the solar wind plasma, and the interplanetary magnetic field (IMF) (Thébault et al., 2010). This interaction disturbs the general structure of the Earth's magnetic field, compressing the field lines at day-side and extending their length to several Earth radii at night-side. The resulting outermost layer of the Earth's magnetic field which sets the boundary to outer space is denoted as magnetosphere, incorporating the magnetopause and magnetotail. Some of the charged particles from the solar wind and cosmic radiation, which are generally shielded from the Earth's magnetic field, are able to enter the magnetosphere, especially when dayside magnetic reconnection is facilitated by a southward directed IMF, and generate various current systems which result in geomagnetic signals between 1 nT during quiet conditions and up to a few thousands of nT during magnetic active periods (Olsen and Stolle, 2012).
The most prominent magnetospheric current system is the geomagnetic ring current circulating along the Earth's magnetic equatorial plane. This large-scale current system contributes with a few tens of nT to the surface Earth magnetic field during quiet conditions and several hundreds of nT during geomagnetic storms (Thébault et al., 2010). Other noticeable currents within the magnetosphere are the cross-tail currents and magnetopause currents.
Both reconnection on the dayside, enhanced magnetospheric convection and reconnection in the magnetotail generate instabilities which can propagate through the magnetosphere in the form of waves. An important wave mode that can carry such disturbances from the magnetosphere to the ionosphere is the shear Alfvén wave, a transverse wave that travels along the magnetic field lines (Cramer, 2001). The field-aligned currents (FAC), which link ionospheric and magnetospheric fields during magnetically disturbed times at high latitudes, are set up by this type of waves (Lysak, 1990; Kan et al., 1991). FACs are associated with rapid temporal and spatial fluctuations. The difficulty in predicting and modeling the corresponding field contributions is a major error source for directional surveying in high latitude regions.
Another major constituent to magnetic disturbance fields at polar latitudes is represented by polar electrojets. The corresponding horizontal current sheets flow at approximately 110 km altitude along a closed oval curve. The area of that curve is defined by the auroral oval during magnetically quiet periods, and expands to lower latitudes during magnetically active periods.

The ionosphere encompasses the uppermost layer of the atmosphere which is ionized by the short-wavelength part of the solar radiation. At middle and low latitudes the ionospheric field contributions are dominated by plasma motions originating from atmospheric heating at the day-side and cooling at the night-side for altitudes between 90 and 150 km (E-region). The resulting currents are local time dependent and generate solar quiet (Sq) signals at middle latitudes on the day-side. This diurnal system comprises of two vortices in each sun-lit hemisphere, connected by the eastward equatorial electrojet (EEJ). EEJ is characterized by intense electric currents flowing along the day-side magnetic equator. The electric currents located in the higher altitude F-region (above 120 km) generate magnetic signals of generally lower amplitudes than within the E-region. However, the corresponding signals are also detectable during local night-times (Olsen et al., 2010a).
In order to reduce the effect of external field sources when modeling the internal fields, satellite data are commonly selected for geomagnetic quiet periods as indicated from global activity indices like *Dst* or *Kp*, as well as local night-times.

1.1.3 Source separation

In order to generate global lithospheric field models, all source contributions from non-lithospheric origin have to be identified and removed from the measurements. Since both internal and external sources have overlapping spatial and temporal signatures, separation is challenging and can only be achieved approximately using either a sequential or comprehensive modeling approach. Both methods are based upon the spherical harmonic representation (Thébault et al., 2010).
The sequential technique models the individual sources separately using specific data selection, correction and processing routines (Maus et al., 2008). The external field contributions are removed using along-track filtering, a technique which may introduce artificial north-south directed features and east-west oscillations in the resulting models (Thébault et al., 2010, 2017). MF7 (Maus, 2010) represents the latest CHAMP lithospheric field model estimated by sequential analysis. The model has a spatial resolution of approximately 300 km, resolving the lithospheric field up to spherical harmonic (SH) degree 133.
The overlapping spatial and temporal signatures of the geomagnetic sources generate erroneous signatures in lithospheric field models based on the sequential technique. The comprehensive modeling approach (CM) aims to circumvent these problems by modelling the core field, lithospheric field and prominent quiet-time external fields simultaneously using both satellite (POGO, Magsat, Ørsted and CHAMP) and hourly observatory data (Sabaka et al., 2004, 2015; Sabaka and Olsen, 2006). Unlike the CM models, comprehensive-like models like CHAOS (Olsen et al., 2006, 2009, 2010b, 2014; Finlay et al., 2015, 2016a) are based on potential theory. The main focus of these models is the Earth's core field, which results in more robust but lower resolution lithospheric field models than the sequential counterpart (Thébault et al., 2010).
Both sequential and comprehensive methods are based on spherical harmonics and satellite measurements. The corresponding distance between measurements and the lithospheric sources as well as the spatial data resolution of approximately 350 km limit the lithospheric model resolution to about SH degree 130 (Thébault et al., 2010). Higher resolution models demand both near-surface and high resolution measurements as provided by aeromagnetic or marine magnetic surveys. However, this cannot be achieved on a global basis without varying data density and the introduction of synthetic data. The world digital magnetic anomaly map (WDMAM) is an international attempt to produce high-resolution global lithospheric field maps based on different regional magnetic surveys around the world (Dyment et al., 2015). As more surveys are produced with time and provided for scientific usage, the model is continuously updated. Typical challenges of merging different types of regional surveys are the different survey times, altitudes, source corrections, filtering routines, and missing documentation of performed data processing. The long wavelength signal is usually filtered out and replaced by model values based on satellite measurements, while regions of missing survey data are replaced with lithospheric magnetization predictions (Lesur et al., 2016). Figure 2 illustrates the latest WDMAM generation with the corresponding grid altitude of 5 km above mean sea level.

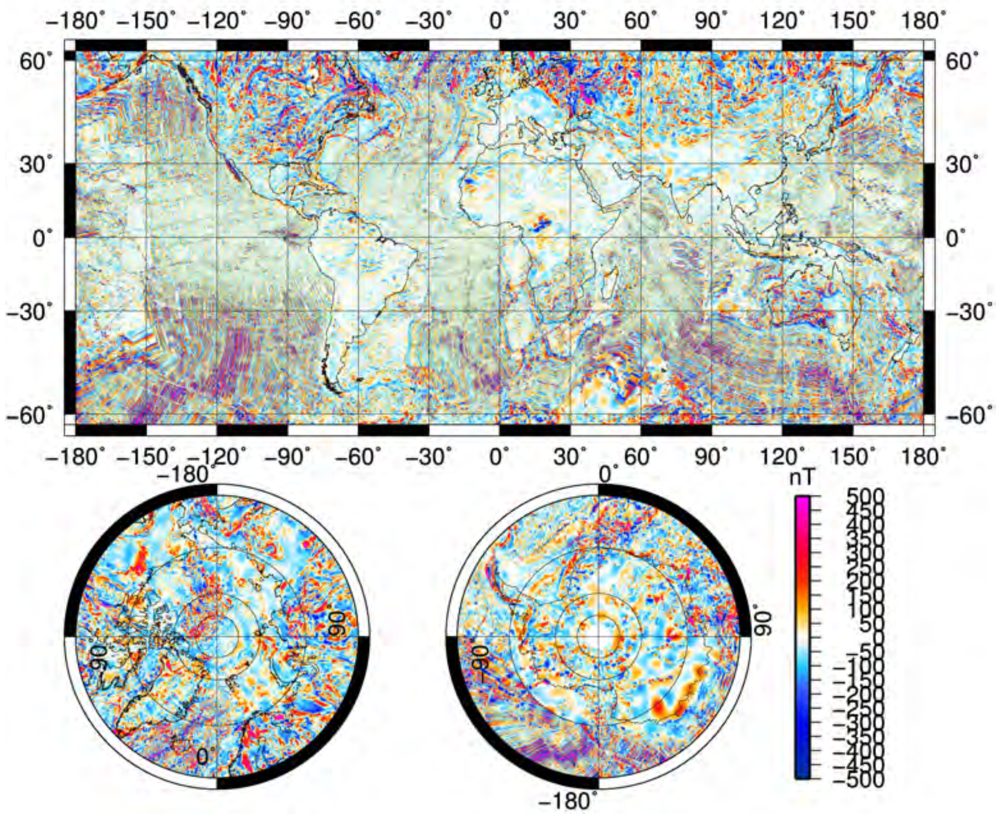

Figure 2 The latest version of the WDMAM is generated by compiling anomaly intensities seen by satellites, ships and airplanes. Credit: http://www.wdmam.org/

1.2 Geomagnetic field representation with spherical harmonics

Since the introduction of spherical harmonics (SH) by Carl Friedrich Gauss (1777-1855) in 1840, it has been a classical mathematical procedure for the processing of potential vector and scalar field data. Within geomagnetism, the method is typically used for global field models.

Spherical harmonics are functions defined on a sphere which can be approximated by a weighted sum over orthogonal functions. For the two-dimensional case, the latter is often represented by Legendre functions (or Legendre polynomials) P_n which are only dependent on co-latitude θ. They are a subset of the three-dimensional associated Legendre functions $P_{n,m}$, also called "spherical functions" or surface harmonics, of degree n and order m. Associated Legendre functions are defined on the sphere and thus dependent on both co-latitude and longitude. The corresponding Schmidt semi-normalized version is denoted as P_n^m and ensures that the magnitude of each coefficient reflects the relative importance with respect to the corresponding term in the expansion (Blakely, 1996). Thus, the mean square value of $2n+1$ Schmidt semi-normalized associated Legendre functions of degree n is not unity but $\frac{1}{2n+1}$ (Backus et al., 1996; Winch et al., 2005). Using $\nu = \cos\theta$ it yields

$$
\begin{aligned}
P_n(\nu) &= \frac{1}{2^n n!}\left(\frac{d}{d\nu}\right)^n (\nu-1)^n \\
P_{n,m}(\nu) &= \sin^m\theta \cdot \left(\frac{d}{d\nu}\right)^m P_n(\nu) \\
&= (1-\nu^2)^{m/2}\left(\frac{d}{d\nu}\right)^m P_n(\nu) \\
P_n^m(\nu) &= \begin{cases} P_{n,m}(\nu) = P_n(\nu) & \text{for } m=0 \\ P_{n,m}(\nu)\left[2\frac{(n-m)!}{(n+m)!}\right]^{\frac{1}{2}} & \text{for } m>0 \end{cases}
\end{aligned}
\tag{2}
$$

For $m = 0$ the semi-normalized surface harmonics are only dependent on co-latitude (zonal harmonics), whereas a pure longitudinal dependence is given for $n - m = 0$ (sectoral harmonics). If both of these terms are larger than zero, the normalized surface harmonics are denoted as tesseral harmonics.

Other fundamental equations within geomagnetic potential field theory are the Maxwell's equations (Backus et al., 1996)

$$\nabla \times \mathbf{E} = -\frac{\partial \mathbf{B}}{\partial t} \tag{3a}$$

$$\nabla \cdot \mathbf{D} = \rho^F \tag{3b}$$

$$\nabla \times \mathbf{H} = \mathbf{J}^F + \frac{\partial \mathbf{D}}{\partial t} \tag{3c}$$

$$\nabla \cdot \mathbf{B} = 0 \tag{3d}$$

for $\mathbf{D} = \epsilon_0\mathbf{E} + \mathbf{P}$ and $\mathbf{H} = \mathbf{B}/\mu_0 - \mathbf{M}$. Here, $\epsilon_0 = \frac{1}{c^2\mu_0} \approx 8.854 \cdot 10^{-12}$ As/Vm is the permittivity of free space (with $c \approx 300\ 000$ km/s being the speed of light in vacuum), $\mu_0 = 4\pi 10^{-7}$ Vs/Am is the magnetic permeability of free space, $\mathbf{H}$ is the magnetic displacement vector [A/m], $\mathbf{B}$ the magnetic induction [gauss or tesla (T), $1nT = 10^{-9}T$ with $1T = 1Vs^{-1}m^{-2}$], $\mathbf{D}$ is the electric displacement vector [C/m^2], $\mathbf{J}^F$ is the electric current density due to free charges [A/m^2], $\mathbf{E}$ is the electric field [V/m], $\mathbf{M}$ is the magnetization per unit volume [A/m], $\mathbf{P}$ is the electric polarization per unit volume [C/m^2], and ρ^F is the charge density due to free charges.

The representation of the geomagnetic field near the Earth's surface builds on the assumption that the source region is limited to a sphere of radius a (representing the mean Earth's radius of 6371.2 km) whereas the measurements are performed within a source-free region of radial boundaries a and b, see Fig. 3.

The atmosphere contains no magnetized particles and it can be assumed that no electric currents flow at lower altitudes, which leads to both $\mathbf{J}^F$ and $\mathbf{M}$ being zero for near-Earth regions. Additionally assuming $\mathbf{P} = 0$ transforms Ampére's law of equation (3c) into $\nabla \times \mathbf{B} = \mu_0\epsilon_0\frac{\partial \mathbf{E}}{\partial t}$. Further, the quasi-stationary assumption $\mu_0\epsilon_0\frac{\partial \mathbf{E}}{\partial t} \ll \nabla \times \mathbf{B}$, meaning that the considered period is longer than the time it takes for light to travel the distance of interest (Olsen and Finlay, 2012), leads to the approximation $\nabla \times \mathbf{B} = 0$. Combined with the Helmholtz' theorem, the magnetic induction $\mathbf{B}$ can thus be represented as the negative gradient of a scalar potential V,

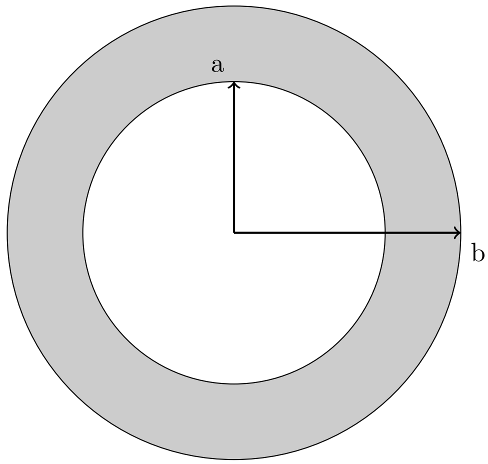

Figure 3 Assumptions for the geomagnetic field representation. The source region is defined within a sphere of radius a, whereas the geomagnetic field representation is valid for the spherical source-free region (gray area) between radius a and b.

$$\begin{aligned}\mathbf{B}(r,\theta,\phi) &= -\Big(\frac{\partial V}{\partial r}, \frac{\partial V}{\partial \theta}, \frac{\partial V}{\partial \phi}\Big) \\ &= -\nabla V\end{aligned} \tag{4}$$

where θ and ϕ represent the geocentric co-latitude and eastern longitude, respectively.
The magnetic potential V is defined to solve the second-order partial differential equation $\nabla^2 V(r,\theta,\phi) = 0$, which is also known as "Laplace's equation". The corresponding solution is given by a harmonic function if the respective first derivatives are continuous and the second derivatives exist (Blakely, 1996). In spherical coordinates, the Laplacian operator is defined as

$$\nabla^2 \equiv \frac{1}{r^2}\frac{\partial}{\partial r}\Big(r^2 \frac{\partial}{\partial r}\Big) + \frac{1}{r^2 \sin^2\theta}\frac{\partial^2}{\partial \phi^2} + \frac{1}{r^2 \sin\theta}\frac{\partial}{\partial \theta}\Big(\sin\theta \frac{\partial}{\partial \theta}\Big). \tag{5}$$

Applying spherical coordinates, the Laplace's equation is conventionally solved via separation of variables $V = R(r)\Theta(\theta)\Phi(\phi)$. The resulting ordinary differential equations (ODE) are given as follows:

$$\frac{d}{dr}\Big(r^2 \frac{dR(r)}{dr}\Big) - \lambda R(r) = 0 \tag{6a}$$

$$\frac{1}{\sin\theta}\frac{d}{d\theta}\Big(\sin\theta \frac{d\Theta(\theta)}{d\theta}\Big) - \frac{m^2}{\sin^2\theta}\Theta(\theta) + \lambda\Theta(\theta) = 0 \tag{6b}$$

$$\frac{d^2\Phi(\phi)}{d\phi^2} + m^2\Phi(\phi) = 0. \tag{6c}$$

Equation (6a) corresponds to the Euler class of ODE. Using the chain rule and performing a variable exchange $r = a \cdot e^t$ the equation can be linearized into

$$\frac{d^2 R(t)}{dt^2} + \frac{dR(t)}{dt} - \lambda R(t) = 0 \tag{7}$$

with the respective roots being

$$r_1 = \frac{-1+\sqrt{1+4\lambda}}{2}, \quad r_2 = \frac{-1-\sqrt{1+4\lambda}}{2}. \tag{8}$$

If $1 + 4\lambda = 0$ the solution $R(t)$ consists of the single roots $r_1 = r_2 = -1/2$ and the eigenvalue $\lambda = -1/4$. Transforming the result back into radial dependence yields

$$R(r) = A\sqrt{\frac{a}{r}} + B\ln\Big(\frac{r}{a}\Big)\sqrt{\frac{a}{r}}. \tag{9}$$

For eigenvalues $\lambda \neq -1/4$ and $\lambda = n(n+1)$ the radial solution is given as

$$R(r) = A\Big(\frac{r}{a}\Big)^{n} + B\Big(\frac{a}{r}\Big)^{n+1}. \tag{10}$$

The classical solution of equation (6b) is given by the Schmidt semi-normalized associated Legendre functions of real degrees n and order of the polynomial m, $\Theta(\theta) = P_n^m(\cos\theta)$.
The solution of the differential equation (6c) comprises of two complex roots and is thus expressed as

$$\Phi(\phi) = A\cos(m\phi) + B\sin(m\phi). \tag{11}$$

Combining all three variables, the potential V expands in terms of two infinite series, $V = V^i + V^e$, which are based on internal source contributions (i, decreasing with increasing r) and external source contributions (e, decreasing with decreasing r), respectively.

$$\begin{aligned} V(r,\theta,\phi,t) = &\sum_{n=1}^{\infty}\sum_{m=0}^{n}\Big(\frac{a}{r}\Big)^{n+1}\Big[R_n^m(\theta,\phi) + S_n^m(\theta,\phi)\Big] \\ &+ \sum_{n=1}^{\infty}\sum_{m=0}^{n}\Big(\frac{r}{a}\Big)^{n}\Big[R_n^m(\theta,\phi) + S_n^m(\theta,\phi)\Big], \end{aligned} \tag{12}$$

where R_n^m and S_n^m represent the Schmidt semi-normalized surface spherical harmonics

$$R_n^m(\theta,\phi) = \begin{cases} R_n^0(\theta,\phi) = R_{n0}(\theta,\phi) & \text{for } m = 0 \\ P_n^m(\cos\theta)\cos(m\phi) = \sqrt{2\frac{(n-m)!}{(n+m)!}}R_{nm}(\theta,\phi) & \text{for } m > 0 \end{cases} \tag{13}$$

$$S_n^m(\theta,\phi) = \begin{cases} 0 & \text{for } m = 0 \\ P_n^m(\cos\theta)\sin(m\phi) = \sqrt{2\frac{(n-m)!}{(n+m)!}}S_{nm}(\theta,\phi) & \text{for } m > 0 \end{cases} \tag{14}$$

and R_{nm} and S_{nm} the corresponding un-normalized versions

$$R_{nm}(\theta,\phi) = P_{n,m}(\cos\theta) \tag{15}$$

$$S_{nm}(\theta,\phi) = P_{n,m}(\cos\theta). \tag{16}$$

Note that the equation (12) is only valid for $\lambda \neq -1/4$.
Equation (12) is often given relative to a reference sphere of radius $a = 6371.2\,\text{km}$ (mean Earth radius) and by means of the Schmidt semi-normalized associated Legendre functions,

$$\begin{aligned} V(r,\theta,\phi,t) = a&\sum_{n=1}^{\infty}\sum_{m=0}^{n}\Big(\frac{a}{r}\Big)^{n+1}\Big[g_n^{m,i}(t)\cos(m\phi) + h_n^{m,i}(t)\sin(m\phi)\Big]P_n^m(\cos\theta) \\ + a&\sum_{n=1}^{\infty}\sum_{m=0}^{n}\Big(\frac{r}{a}\Big)^{n}\Big[g_n^{m,e}(t)\cos(m\phi) + h_n^{m,e}(t)\sin(m\phi)\Big]P_n^m(\cos\theta) \end{aligned} \tag{17}$$

with $[g_n^{m,i}, h_n^{m,i}]$ and $[g_n^{m,e}, h_n^{m,e}]$ being the time dependent Gauss coefficients for the internal and external sources, respectively. The additional scaling factor a in equation (17) ensures that the Gauss coefficients have the same dimensions as the magnetic induction (tesla, gauss or nT).
Depending on the given data quality and model capabilities, the infinite sum of the magnetic scalar potential has in practice a limit of n_{max}, resulting in $n_{max}(n_{max}+2)$ Gauss coefficients. Increasing n_{max} enables the spherical harmonics to capture smaller frequencies (more small-scale structures) of the potential field.

Geomagnetic power spectrum

Modeling the geomagnetic field by means of spherical harmonics allows the separation into internal and external field contributions with respect to a given radius r (equation 17), upward- and downward continuation, spatial and temporal model resolution as well as spectral analysis (Thébault et al., 2010). The latter is given by the spatial power spectrum R_n [given in nT^2], also denoted as Mauersberger–Lowes spherical harmonic power spectrum (Mauersberger, 1956; Lowes, 1974), which estimates the contribution to the squared magnetic internal field amplitude for a given SH degree n (Thébault et al., 2010),

$$R_n = \left(\frac{a}{r}\right)^{2n+4} (n+1) \sum_{m=0}^{n} \left[(g_n^m)^2 + (h_n^m)^2 \right]. \tag{18}$$

Thus, summing over the spectrum for all SH degrees gives the mean-squared internal magnetic field intensity averaged over a sphere of radius r (Backus et al., 1996, p. 147),

$$\langle |\mathbf{B}|^2 \rangle = \sum_{n=1}^{\infty} R_n. \tag{19}$$

The horizontal wavelength λ_n for a given SH degree n is given by (Backus et al., 1996, p. 103)

$$\lambda_n = \frac{2\pi r}{\sqrt{n(n+1)}}. \tag{20}$$

Figure 4 shows the spectrum at the Earth's surface ($r = a$ in equation (18)) based on the Gauss coefficients of CHAOS-6. The prominent break in the spectrum around SH degree 15 (black dashed line) is commonly explained by the assumption that the long wavelength field contributions for $1 \leq n \leq 12$ originate mainly in the core, while the short wavelength features for $16 \leq n$ are dominated by lithospheric signals. The exact transition between these two contributions is unknown, and it is very likely that core- and lithospheric field signals overlap each other in an intermediate range of approximately $13 \leq n \leq 15$ (Backus et al., 1996; Langel and Hinze, 1998). Within this shared spectral domain it is impossible to distinguish the two sources from each other. The transition degree used for the generation of synthetic data in this thesis is 15.

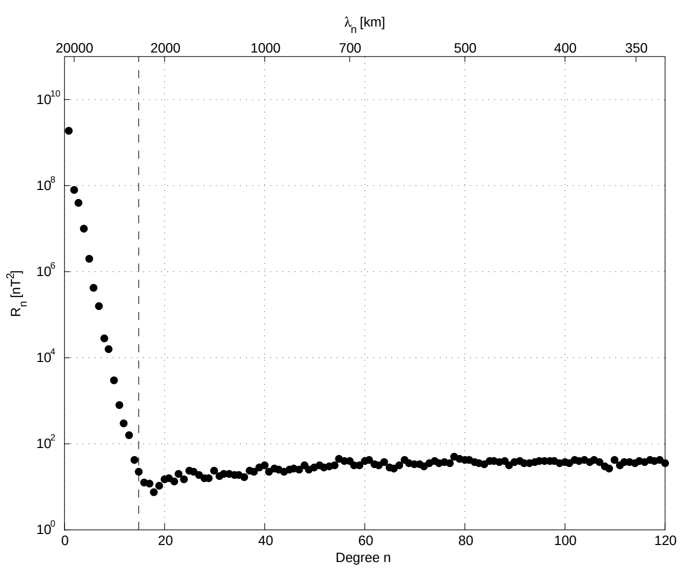

Figure 4 Mauersberger–Lowes spherical harmonic power spectrum of the (static) internal geomagnetic field at the Earth's surface as given by the global geomagnetic field model CHAOS-6 (Finlay et al., 2016a). The corresponding values are dependent on the spherical harmonic degree n (bottom axis) and the horizontal wavelength λ_n (top axis).

1.3 Alternatives to spherical harmonics

The method of spherical harmonics is characterized by global basis functions and hence dependent on global distributed data. As a consequence, the smallest spatial wavelength in the data set dictates the maximum degree for spherical harmonic series (Purucker and Whaler, 2007). Satellites provide globally distributed data at an expense of low resolution compared to near-surface measurements. However, lithospheric field models are in need of data both close to the sources and with a high degree of spatial density. Regional airborne or marine magnetic measurements fulfill these criteria. Since SH cannot account for data sets of varying spatial density or data sets covering only a regional portion of the Earth, a different mathematical approach is needed for the processing of regional potential field measurements. Alternatively, data interpolation and the introduction of synthetic data are necessary to accommodate the SH requirement of global and evenly distributed data coverage (Schott and Thébault, 2011).
Another disadvantage of SH, concerning both global and regional lithospheric field models, is the truncation of SH expansions. Due to computational limits, spherical harmonic series are not infinite but extended up to a certain degree. This introduces power leakage from higher into lower SH degrees, also known as Gibbs phenomenon, and affects all SH coefficients, causing undesirable oscillations over the entire sphere. Thus, regions of high observational density cannot be represented by truncated spherical harmonics without the introduction of artificial features in regions of sparse observations (Hodder, 1982).
Based on the SH drawbacks for lithospheric field modeling and the analysis of high resolution regional magnetic measurements at different altitudes, alternative techniques have been developed during the past decades (Purucker and Whaler, 2007).
Examples for methods which, similar to SH, are based on a global support on the sphere are localized spherical functions like spherical harmonic splines (HS) and wavelets (Chambodut et al., 2005; Holschneider et al., 2003). The former consist of polynomial functions defined on intervals, thus circumventing SH expansion truncation. The method was introduced by Shure et al. (1982) for global main field models at the core surface (Purucker and Whaler, 2007). A main disadvantage of the harmonic spline expansion is that it is based on one spline function for each observation location, demanding an enormous computational effort to solve the resultant systems of linear equations. Parker and Shure (1982) presented the depleted basis harmonic splines, an alternate version which only uses a data subset (Purucker and Whaler, 2007).
Another widely used approach for the representation of regional lithospheric field data using global base functions are wavelets (Schott and Thébault, 2011). The method has a history within different scientific genres, e.g. medical signal processing, geophysics and finance (Chambodut et al., 2005), and is characterized by representing the magnetic field only within the area corresponding to the used data set (Schott and Thébault, 2011).

SH alternatives can either be based on functions with global support, like HS and wavelets, or on functions with local support. The latter is especially useful when data is only given on a regional scale. Spherical Cap Harmonic Analysis (SCHA) introduced by Haines (1985), its revised version R-SCHA and equivalent potential field sources are examples for regional methods with local support. A major difference between these methods and SH lies in the fact that the functions corresponding to the former only have non-zero values for regions where data exist.
The revised spherical cap harmonic analysis (R-SCHA) is a modeling technique for potential fields at regional scale (Thébault et al., 2004, 2006b,a; Thébault, 2006). The method is based on multilevel measurements of e.g. repeat stations, observatories, airborne data or satellite data. The related approach R-SCHA2D is valid when data is available at one surface only (Thébault, 2008).

Building on the work of Hammer (2011), this thesis uses a series of magnetic equivalent potential field sources (monopoles) at a certain depth below the Earth's surface for the generation of both regional, global and combined regional-global lithospheric field models. The method is able to utilize all three components of the vector field data and/or measured scalar data. The procedure is to relate satellite and/or airborne magnetic measurements to a set of monopoles by least squares matrix inversion, with the source distribution being dependent on both the density and altitude of the used data. Similar to SCHA and R-SCHA, the monopole procedure is applicable for both regional data and data with different altitudes while satisfying the constraints of potential field theory (Schott and Thébault, 2011). But unlike the former two methods,

the study region for equivalent potential field sources can have any shape.
The history of the use of monopoles to model features of the geomagnetic field reaches back at least 60 years. The first application was possibly provided by Serson and Hannaford (1957) who used a random arrangement of magnetic monopoles as a tool for determining the source depth of magnetic anomalies observed with a three-component airborne magnetometer over Western Canada and the Atlantic Ocean east of Bermuda.
Later McLeod and Coleman (1980) generated statistical models of randomly distributed magnetic monopoles in order to predict the great circle power spectrum for both the core and the lithospheric field in agreement with observations made by the POGO spacecraft.
Another monopole-based lithospheric field model from POGO satellite data was derived by Von Frese et al. (1981). Building on this work, von Frese et al. (1988) made another effort seeking to better exploit computer resources for geomagnetic field modeling. They used the monopole representation together with damped least-squares in combination with bootstrap inversion for processing Magsat magnetic anomaly data over India.
Models of the geomagnetic secular variation are based on the global network of observatory data which is known to be more dense in the Northern Hemisphere than in the Southern Hemisphere. Since SH are not capable of easily handling spatial differences in data density, Hodder (1982) used a mesh of monopoles for geomagnetic secular variation field modeling. Each of the 80 sources was located below a given observatory below the core-mantle-boundary and, similar to the approach of this thesis, the author ensured a zero net flux and transformed the derived source values into spherical harmonics. The model results were in good agreement with the observations, demonstrating that the monopole approach is a useful alternative to spherical harmonics.
Another important contribution for the validation of using equivalent potential field sources for geomagnetic field modeling was provided by O'Brien and Parker (1994). Based on a regularized inversion of monopoles, the authors generated both global radial core field models and regional lithospheric field models which were in good agreement with previous results based on harmonic splines and SCHA.
Finlay et al. (2016b) presented a recent new application of monopole modeling. Using two global monopole grids at different altitudes and minimizing the L_1-norm of the radial field separately on the core-mantle-boundary and the Earth's surface, the authors proposed a possible method for separating the magnetic signals from the core and the lithosphere. It is also interesting to mention that the equivalent potential field sources method can be used to investigate the magnetic fields of other members of our solar system than the Earth, for instance the Moon (Toyoshima et al., 2008). Like many mathematical tools in geomagnetism, equivalent sources are also widely used for the processing of geodetic data (Dampney, 1969).

Before giving a detailed description of the used mathematical routine in chapter 2, the following section gives a short introduction to how geomagnetic field models are used for subsurface navigation of wellbores.

1.4 Directional wellbore surveying using the geomagnetic field

This section investigates directional wellbore surveying and focuses mainly on its application of the magnetic field for navigation. The presented magnetic surveying technique is one of several methods for orientation of subsurface devices. Alternatives, which will not be discussed in this thesis, are given by gyro surveying and ultrasound surveying.

Directional drilling is a major discipline within the oil industry and refers to the drilling of wells containing both vertical and curved sections. Thanks to the flexibility of the drill-string, the drill-bit can be forced to change direction, which enables drilling in any direction, including horizontal. The advantage is obvious, a single fixed drill site can be used to reach targets with horizontal distances more than 10 km from the drill site. Wellbores with multiple branches are another valuable feature made possible by directional drilling.

A well documented geometrical description of a wellbore is critical for several reasons. When drilling a well with known positional uncertainty, it is easier to hit predefined geological targets and avoid faults and offset wells.

Directional drilling requires a means for navigation in order to ensure that a wellbore follows a predefined well-path. In addition to the distance along the well, we need references to determine the direction at any point. The direction of gravity serves as the vertical reference, while the geomagnetic field or a north seeking gyro are the options for the horizontal reference. Both are in use, but for technical and economical reasons the magnetic field is presently the one preferred by the industry.

There are two main drilling technologies in use today: downhole drilling motors (mud motors) and rotary steerable system (RSS). The former is driven by drilling fluid circulated from the rig down to the drillstring. While most of the drillpipe is held stationary when using a conventional mud motor, the pipe is continuously rotating with a RSS. It is also possible to combine the two systems. Concerning mud motors, the drillstring is typically built up of three section: bottom hole assembly (BHA that includes a motor), transition pipe and drillpipe. The former contains tools for both orientation, steering and drilling, see Fig. 5.

The geomagnetic and gravity fields are measured by a directional instrument within the BHA and compared to model predictions. Regarding the predictions of the geomagnetic field these models are typically valid for the large-scale structures of the Earth's magnetic field during quiet conditions. Further model enhancement on a local basis requires In-Field Referencing (IFR) and Interpolation In-Field Referencing (IIFR), which account for the short-wavelength lithospheric field and rapid temporal variations of the external field, respectively. Section 1.4.1 presents the most common magnetic field models applied in wellbore surveying and section 1.4.3 gives an overview of some of the most common error sources to magnetic directional surveying. Methods for determining the magnetic field at the wellbore vicinity are presented in section 1.4.2. A path correction requires an accurate determination of the wellbore orientation in space. Examples for corresponding techniques are also given in section 1.4.2. An actual case study, comparing the industry standard BGGM2016 model (including IFR) with an equivalent source based model for actual directional survey measurements from a specific well within the Ekofisk field in the North Sea is given in chapter 4.5.

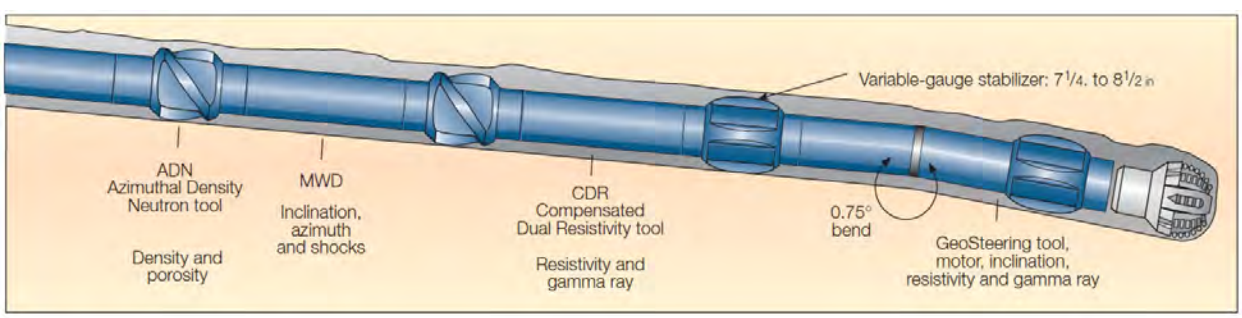

Figure 5 Typical components in a mud motor BHA applied for the orientation and steering of wellbores (Allen et al., 1997).

Note that this section only provides a brief introduction to the complex topic of directional surveying. There exist a vast amount of literature on the subject and the interested reader is referred to e.g. Inglis (2013);

Halliburton (2001); Jamieson et al. (2016); Beggan et al. (2014) for extensive descriptions.

1.4.1 Magnetic field models used in directional drilling

Due to several error sources in the viscinity of a well (see section 1.4.3), the BHA measurements of the magnetic field used for subsurface navigation need to be quality controlled and verified. The downhole observations are compared to model predictions to ensure that the wellbore is on the right track for the predefined target. These models are generated for the individual well, giving predictions of the total field intensity and magnetic inclination (also denoted as "dip angle") for the different well sections. The differences between BHA measurements and model predictions have to be within certain limits which are defined by the individual drilling companies or operators.
The oil industry uses typically the International Geomagnetic Reference Field (IGRF) models, the British Geological Survey Global Geomagnetic Model (BGGM) or the High Definition Geomagnetic Model (HDGM). All models are based on spherical harmonics and provide estimations of the long wavelength effects of the Earth's magnetic field and to some extend the contributions from external field variations and localized lithospheric field signals.

IGRF and DGRF

The IGRF provides a model estimation of the large-scale internal geomagnetic field near and above the Earth's surface (Macmillan and Finlay, 2011). Rapid temporal variations in the external field as well as small-scale lithospheric field contributions are thereby not represented. Due to secular variation, the model has been updated regularly since 1969 with each generation comprising of three parts: a) the non-definitive IGRF which represents the main field on a 5-year interval, assuming a linear time dependence of the Gauss coefficients for each interval; b) a predictive model for the temporal changes of the main field, extending the time-span of the IGRF with further five years; c) The definitive version of the previous IGRF, except for the last 5-year predictions based on secular variation models, (DGRF) which will not be altered further in future revisions. Thus, each DGRF model is definitive for five more years than the previous DGRF generation (Thébault et al., 2015).
Each IGRF generation is a combination of certain candidate models provided by different institutions around the globe. Both the individual candidate models as well as the evaluation of the final IGRF version, derived from an international team of scientists, are well documented and freely accessible to the user.
The IGRF can be represented by a set of spherical harmonics similar to equation (17), however with a finite sum extending up to degree n_{max}:

$$V(r,\theta,\phi) = a \sum_{n=1}^{n_{max}} \sum_{m=0}^{n} \left(\frac{a}{r}\right)^{n+1} \Big[g_n^m \cos(m\phi) + h_n^m \sin(m\phi)\Big] P_n^m(\theta). \tag{21}$$

The Gauss coefficients of the latest IGRF version, IGRF-12, are derived for $n_{max} = 10$ for the period 1900 - 2000 and hereafter up to SH degree 13 (Thébault et al., 2015). The secular variation predictions are valid for the period 2015-2020 and the corresponding temporal variations of the Gauss coefficients are given up to SH degree and order 8.
Unlike BGGM and HDGM, IGRF models are named after the corresponding generation and not the year of release.

BGGM

Similar to IGRF models, BGGM are global geomagnetic models which contain a retrospective part and a predictive part. The former is based on measurements from satellites, observatories and repeat stations, while the future field predictions are given by models of the secular variation and secular acceleration (BGS, 2016; Beggan et al., 2014; Hamilton et al., 2015). Also the large-scale external field contributions are incorporated to some extent in the model predictions. BGS models are updated every year. The latest version BGGM-2016 represents the internal fields up to SH degree 133, corresponding to a spatial half wavelength of approx. 150 km, and the parametrization of both external fields and induced fields are given up to SH degree 1 (Macmillan and Grindrod, 2010; Hamilton et al., 2015).

HDGM

The High Definition Geomagnetic Model (HDGM) has been generated by a joint project from the drilling industry and the U.S. National Geophysical Data Center (NGDC) (NOAA, 2016). Like the models from the British Geological Service, HDGMs are updated on an annual basis and account for the latest measurements from both satellite and near-surface (marine magnetic and aeromagnetic) surveys (Maus et al., 2012). The latter enables models of much higher SH degrees than provided by IGRF or BGGM, resulting in high-resolution predictions for the internal geomagnetic field. Additional real-time magnetospheric field predictions are given in the extended model version HDGM-RT.
The most recent model HDGM-2016 resolves the internal field up to degree and order 720, corresponding to a spatial half wavelength of approx. 30 km, and the secular variation up to degree and order 15. Similar to BGGM-2016, the external fields and corresponding time variations are given to degree and order 1 (Maus et al., 2012).

1.4.2 Measurement while drilling

Positional estimates of a wellbore during drilling are based on local gravity (**G**) and magnetic field (**B**) measurements from the "measurement while drilling" (MWD) directional tool, see Fig. 5. The directional sensors are built into a non-magnetic drill collar with three orthogonal oriented accelerometers and magnetometers, as well as a data recovery device (Jamieson et al., 2016). The accelerometers are applied for the derivation of local wellbore inclination, whereas both gravity and magnetic measurement are needed for wellbore azimuth and toolface calculations.
The wellbore inclination Υ represents the angle between the local vertical and the tangent to the wellbore axis. A horizontal well is thus represented by an inclination of 90°, while drilling straight down gives an inclination of 0°.
The wellbore azimuth Λ is given by the angle between the horizontal component of the wellbore direction and a reference (magnetic north, true north or grid north). Applying magnetic north as reference, the wellbore azimuth is 0° and 90° when drilling towards magnetic north and east, respectively.
Considering the z-axis of both accelerometers and magnetometers pointing down hole, wellbore inclination and azimuth are defined as follows,

$$\begin{aligned} \Upsilon &= \cos^{-1} \frac{G_z}{\sqrt{G_x^2 + G_y^2 + G_z^2}} \\ \Lambda &= \tan^{-1} \frac{\sqrt{G_x^2 + G_y^2 + G_z^2}(G_x B_y - G_y B_x)}{B_z(G_x^2 + G_y^2) - G_z(G_x B_x - G_y B_y)}. \end{aligned} \tag{22}$$

The most dominant magnetic MWD errors for wellbore azimuth are due to drillstring interference (see section 1.4.3) and errors in magnetic declination (Edvardsen et al., 2014).
Except from error sources in the gravity and magnetic measurements, the three orthogonal accelerometers ensure the definition of vertical down and the three orthogonal magnetometers together with the accelerometers give the orientation of magnetic north.
The MWD tools perform gravity and magnetic field measurements at several along-hole depth locations, usually at every "stand" which is about 30 m or 40 m, dependent on the drilling rig. The respective magnetic field declination, inclination and intensity values are compared with magnetic field predictions as described in section 1.4.1. Note that the magnetic inclination Υ_{mag} used for model comparisons is different from the wellbore inclination,

$$\Upsilon_{mag} = \sin^{-1} \frac{G_x B_x + G_y B_y + G_z B_z}{\sqrt{G_x^2 + G_y^2 + G_z^2}\sqrt{B_x^2 + B_y^2 + B_z^2}}. \tag{23}$$

Determining survey positions

In order to compare the measured magnetic inclination and field intensity values with model predictions, it is crucial to know the location of the measurements. The drilling industry makes use of different techniques for estimating the well-bore position in space. An interesting overview over existing methods is given by Jamieson et al. (2016).
It is important to determine the wellbore location as accurate as possible, as systematic prediction errors accumulate along the well path which can lead to the final well location being far away from the originally planned target.
The tangential method is the easiest and least accurate technique to estimate the wellbore orientation. It simply assumes that the wellbore follows a straight line between two adjacent measurement points, neglecting any change in wellbore inclination and direction. The minimum curvature method, on the other hand, takes also a curved well-path into account and allows for changes within both inclination and azimuth. The method provides the most accurate predictions of the wellbore position and corresponds to the industry standard today.
The wellbore inclination and azimuth are measured continuously during drilling. The corresponding values for two adjacent measurement points are denoted Υ_1, Υ_2, Λ_1 and Λ_2, respectively. The minimum curvature method uses these values to fit a spherical arc between the measurement points by determining the so-called "dog-leg" angle β,

$$\beta = \cos^{-1}[\cos(\Upsilon_2 - \Upsilon_1) - \sin(\Upsilon_1)\sin(\Upsilon_2)(1 - \cos(\Lambda_2 - \Lambda_1))]. \tag{24}$$

Using $\Psi = \frac{2}{\beta}\tan(\frac{\beta}{2})$, the change in true vertical depth (TVD) as well as the horizontal location with respect to grid North and East between the two points can now be determined to

$$\begin{aligned}\Delta\mathrm{TVD} &= \frac{\Psi\delta}{2}\cdot(\cos(\Upsilon_1) + \cos(\Upsilon_2))\\ \Delta\mathrm{N} &= \frac{\Psi\delta}{2}\cdot(\sin(\Upsilon_1)\cos(\Lambda_1) + \sin(\Upsilon_2)\cos(\Lambda_2))\\ \Delta\mathrm{E} &= \frac{\Psi\delta}{2}\cdot(\sin(\Upsilon_1)\sin(\Lambda_1) + \sin(\Upsilon_2)\sin(\Lambda_2))\end{aligned} \tag{25}$$

where δ represents the measured depth difference between the two points, see Fig. 6.

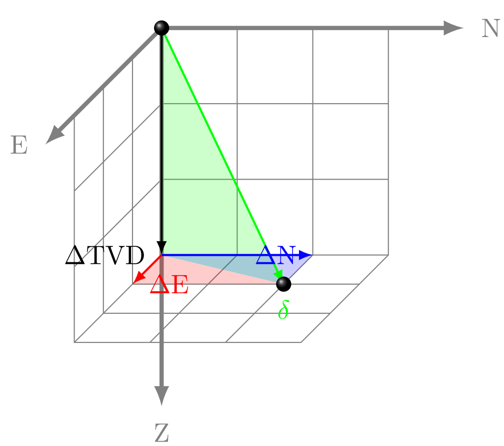

Figure 6 Two adjacent measurement points in a north-east-vertical down coordinate system. The minimum curvature method uses the corresponding inclination and azimuth measurements for determining the horizonal and vertical differences between the two points.

1.4.3 Improving MWD positioning

Magnetic MWD measurements have two main error sources: the highly localized structure of the lithospheric field (which is accounted for using IFR) and drillstring interferences. However, other error sources exist and require different techniques for reducing the corresponding impact on wellbore positioning. A brief introduction to some of these errors and techniques is given in the following.

In-field referencing

The geomagnetic parameters used in wellbore directional surveying are often obtained from global geomagnetic field models (Edvardsen et al., 2013). Uncertainties in these models give rise to navigational errors, which can be reduced by further implementation of local geomagnetic field models of the drilling area. This technique is referred to as "in-field referencing" (IFR), and based on aeromagnetic, marine magnetic and/or on-shore magnetic measurements. Interpolated in-field referencing (IIFR) takes additionally the diurnal magnetic field variations into account. Due to the increase of magnetic field disturbances towards polar regions, high accuracy MWD is crucial for directional drilling applications at especially high latitudes (Jamieson et al., 2016).
IFR results in crustal corrections of the reference field inclination, declination and intensity. For instance, the uncertainty in magnetic declination can be reduced with approximately 40% at 1σ when applying IFR to a MWD survey (Jamieson et al., 2016).

Multi-station analysis

Multi-station analysis (MSA) is a technique to validate and improve MWD wellbore directional survey quality and accuracy. The method estimates the consistency between theoretical data and actual magnetic data by using directional sensor measurements several survey stations along the wellbore. A collection of respective formulae is given in chapter 14 in Jamieson et al. (2016).
MSA can be used for magnetic interference and misalignment corrections to magnetic directional surveys.

Magnetic interference

Even if the BHA magnetometers are housed within a non-magnetic drill collar, accumulated disturbances from several surrounding magnetic interference sources (e.g. drillstring, adjacent wells, casing and magnetic formations) may affect the magnetometer measurements (Cheatham et al., 1992). Since the wellbore inclination is independent of the local magnetic field measurements, only the wellbore azimuth is affected by magnetic interference. Magnetic interference from drillstring may sometimes be corrected for using a correction algorithm, or accepted as an error source to the azimuth reading. If correction is applied the azimuth is often called "corrected azimuth" and if not "uncorrected azimuth". When correcting for drillstring interference, the corresponding calculations are dependent on both magnetic field intensity and inclination. Errors in these values will automatically lead to uncertainties in the corrected wellbore azimuth. This is one reason to why the uncorrected azimuth is preferred in some situations (Edvardsen et al., 2014).
The dominant error source to uncorrected azimuth is drill string interference and can be reduced by increasing the amount of non-magnetic steel in the BHA and/or placing the magnetic measurement devices at certain distances from magnetic BHA material (Edvardsen et al., 2014). For instance, Statoil demands that 20 m behind and 8 m in front of the magnetic measurement device need to consist of non-magnetic material when using uncorrected azimuth (Inge Edvardsen, pers.comm., March 2017).

Magnetic drilling fluid

While drilling, the drill bit is cooled by drilling fluid, which is continuously pumped into and out of the bore hole. This drilling fluid (or mud) has magnetic properties which may affect the MWD sensor readings by reducing the amplitude of cross-axial (transverse to the wellbore direction) magnetometer measurement. Resulting distortions in wellbore azimuth and positioning can reach up to 5° and 50 m, respectively (Torkildsen et al., 2004). The negative effects of magnetic drilling fluid can be circumvented by either using a gyroscope for determining the wellbore azimuth or applying MSA to analyze and make corrections of the magnetic survey data (Torkildsen et al., 2004).

Misalignment

A significant error source in wellbore directional surveying is misalignment. The part of the drill collar where the directional sensors are placed can be misaligned with respect to the actual drilled hole or there can be a misalignment between the drill collar and the directional sensors. The corresponding uncertainties are important for the determination of the hole axis direction and wellbore direction.

Sag

The flexible design of the BHAs has the consequence that the MWD drill collar can be deflected under gravity and borehole curvature. This leads to BHA sag, which is a misalignment of the drill collar and its directional sensors with the borehole direction. This effect is handled by sag correcting the inclinations using special designed softwares. Corresponding values are mainly dependent on the sine of the wellbore inclination, the BHA type and geometry, sensor spacing, build-up rate and hole size (Jamieson et al., 2016).

Error ellipse

In MWD positioning there are both random and systematic error sources. Along the well path, the former type of errors will cancel out if the directional surveys are taken at different toolfaces. Systematic errors, on the other hand, propagate along the computed wellbore trajectory and are quantified and collected in a three-dimensional uncertainty ellipse with the long axis perpendicular to the wellbore direction.
The shape of the error ellipse represents the assumption that azimuth errors are larger than inclination errors, since the ellipse's lateral, high side and wellbore axis dimensions are proportional to the wellbore azimuth error, the wellbore inclination error, and the depth error, respectively (Jamieson et al., 2016), see Fig. 7.

In order to keep track on the constant development of subsurface navigational improvements, the Industry Steering Committee on Wellbore Survey Accuracy (ISCWSA) produces and maintains industry standards related to wellbore-survey accuracy since 1995. The corresponding standards for the different error sources are used to decrease the uncertainty of well positions which is crucial for collision risk with existing wellbores, target sizing, and log positional accuracy (Jamieson et al., 2016; Macmillan and Grindrod, 2010; Williamson et al., 2000).

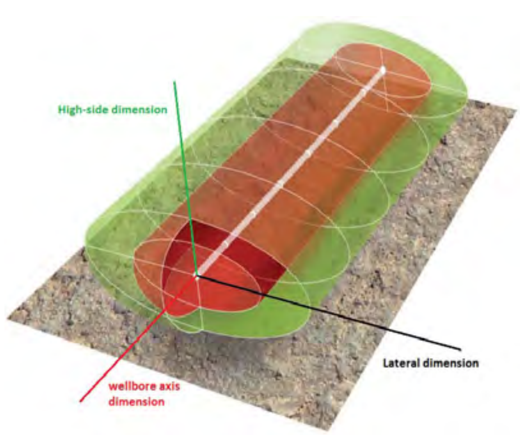

Figure 7 3D error ellipse with corresponding dimensions being defined by the wellbore azimuth error (lateral dimension), wellbore inclination error (high-side dimension) and vertical error (wellbore axis dimension). Source: https://www.spe.org/en/jpt/jpt-article-detail/?art=968

2 Methodology of equivalent point sources

The equivalent point source technique is based on a discrete amount of sources placed at an arbitrary depth below the observations. It is required that the corresponding potential field both reproduces the observations to an adequate level of misfit, is harmonic in the area of interest, and vanishes when upward continuing to large distances from the observations (Blakely, 1996). In this thesis equivalent point sources will also be denoted as *monopoles*, *equivalent potential field sources* and *sources*.

The remaining part of this chapter outlines the mathematical background for the equivalent point source method of this thesis. Sections 2.3 to 2.9 explain the inversion scheme used to derive the global and regional lithospheric field models which are presented in chapter 3 and 4, respectively.

2.1 Equivalent point source formulation

Neglecting currents in the ionosphere and adopting the quasi-stationary approximation, the magnetic vector field $\mathbf{A}(\mathbf{r}_i)$ at locations $\mathbf{r}_i = [r_i, \theta_i, \phi_i]$ (for $i = 1, ..., N$) above the Earth's surface can be described by the scalar potential $\Phi(\mathbf{r}_i)$,

$$\mathbf{A}(\mathbf{r}_i) = -\nabla\Phi(\mathbf{r}_i). \tag{26}$$

This potential can be modeled as a linear combination of K globally distributed equivalent potential field sources (monopoles) located at $\mathbf{s}_k = [r_k, \theta_k, \phi_k]$ and with source strength q_k (for $k = 1, ..., K$) (O'Brien and Parker, 1994)

$$\Phi(\mathbf{r}_i) = \sum_{k=1}^{K} q_k \frac{r_k^2}{r_{ik}} \tag{27}$$

where r_{ik} and μ_{ik} are the distance and angle between the position vectors of the location of interest i and source k, respectively (see Fig. 8):

$$\begin{aligned} r_{ik} &= |\mathbf{r}_i - \mathbf{s}_k| \\ &= \sqrt{r_i^2 + r_k^2 - 2r_i r_k \cos(\mu_{ik})} \\ \cos(\mu_{ik}) &= \cos(\theta_i)\cos(\theta_k) + \sin(\theta_i)\sin(\theta_k)\cos(\phi_i - \phi_k). \end{aligned} \tag{28}$$

The squared source radius in equation (27) ensures that the source strength is given in nT.
It is noteworthy that the potential due to equivalent point sources decreases with $\frac{1}{r_{ik}}$ rather than $\frac{1}{r_{ik}^2}$ for equivalent dipole sources.
Combining equations (26) and (27) gives

$$\begin{aligned} \mathbf{A}(\mathbf{r}_i) &= -\sum_{k=1}^{K} q_k \hat{\mathbf{e}}_i \cdot \nabla \frac{r_k^2}{r_{ik}} \\ &= \sum_{k=1}^{K} q_k g_{ik} \\ &= \underline{\underline{\mathbf{G}}}\mathbf{q} \end{aligned} \tag{29}$$

where $\hat{\mathbf{e}}_i$ represents the unit vector, $\mathbf{q}$ is a vector of source amplitudes and $\underline{\underline{\mathbf{G}}}$ is an $N \times K$ Green's matrix with elements g_{ik} that are directional derivatives of source k evaluated at the location and measurement direction i,

$$g_{ik} = -\hat{\mathbf{e}}_i \cdot \nabla \frac{r_k^2}{r_{ik}}. \tag{30}$$

The corresponding formulae for the directions r, θ, ϕ are

$$\begin{aligned}
g_{ik}^{r} &= -\frac{\partial}{\partial r_i}\Big(\frac{r_k^2}{r_{ik}}\Big) \\
&= \frac{r_k^2}{r_{ik}^3}[r_i - r_k\cos(\mu_{ik})] \\
g_{ik}^{\theta} &= -\frac{1}{r_i}\frac{\partial}{\partial \theta_i}\Big(\frac{r_k^2}{r_{ik}}\Big) \\
&= \frac{r_k^3}{r_{ik}^3}[\sin(\theta_i)\cos(\theta_k) - \cos(\theta_i)\sin(\theta_k)\cos(\phi_i - \phi_k)] \\
g_{ik}^{\phi} &= -\frac{1}{r_i\sin(\theta_i)}\frac{\partial}{\partial \phi_i}\Big(\frac{r_k^2}{r_{ik}}\Big) \\
&= \frac{r_k^3}{r_{ik}^3}[\sin(\theta_k)\sin(\phi_i - \phi_k)].
\end{aligned} \tag{31}$$

The respective derivations are given in Appendix B.

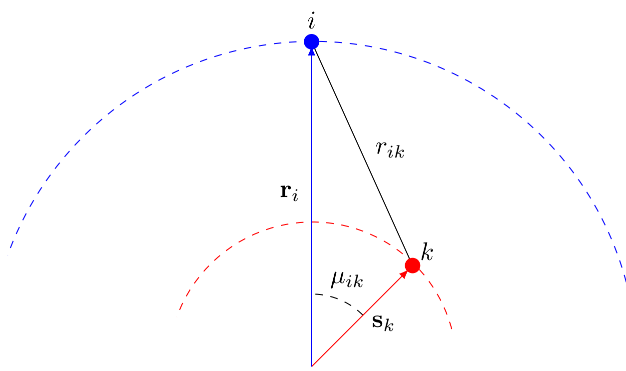

Figure 8 2D illustration of the equivalent point source potential field formulation. The origo represents the center of the Earth.

2.2 Transformation from equivalent point source values to Gauss coefficients

One advantage of the equivalent point source method is that the source values can be transformed into spherical harmonic Gauss coefficients, which facilitates straight-forward comparisons between equivalent source models and SH based models like CM5, MF7 and CHAOS-6.
Following Blakely (1996, p. 119), the spatial distance between source and data for $r_k < r_i$ can be written as

$$\begin{aligned}
\frac{1}{r_{ik}} &= [r_i^2 + r_k^2 - 2r_ir_k\cos(\mu_{ik})]^{-1/2} \\
&= \frac{1}{r_i}[1 + \big(\frac{r_k}{r_i}\big)^2 - 2\frac{r_k}{r_i}\cos(\mu_{ik})]^{-1/2}
\end{aligned} \tag{32}$$

and expanded in a binominal series

$$\begin{aligned}
\frac{1}{r_{ik}} = \frac{1}{r_i}\Big[1 - \frac{1}{2}\Big(\frac{r_k^2}{r_i^2} - 2\frac{r_k}{r_i}\cos(\mu_{ik})\Big) \\
+ \frac{(-\frac{1}{2})(-\frac{3}{2})}{2!}\Big(\frac{r_k^2}{r_i^2} - 2\frac{r_k}{r_i}\cos(\mu_{ik})\Big)^2 \\
+ \frac{(-\frac{1}{2})(-\frac{3}{2})(-\frac{5}{2})}{3!}\Big(\frac{r_k^2}{r_i^2} - 2\frac{r_k}{r_i}\cos(\mu_{ik})\Big)^3 + ...\Big].
\end{aligned} \tag{33}$$

Rearranging the above equation into terms of $\frac{r_k}{r_i}$ leads to a function of Legendre polynomials $P_n(\cos(\mu_{ik}))$ of degree n,

$$\begin{aligned}\frac{1}{r_{ik}} &= \frac{1}{r_i}\Big[1 + \Big(\frac{r_k}{r_i}\Big)\cos(\mu_{ik}) + \Big(\frac{r_k}{r_i}\Big)^2\Big(-\frac{1}{2} + \frac{3}{2}\cos(\mu_{ik})^2\Big) + ... \\ &\quad \Big(\frac{r_k}{r_i}\Big)^3\Big(-\frac{3}{2}\cos(\mu_{ik}) + \frac{5}{2}\cos(\mu_{ik})^3\Big) + ...\Big] \\ &= \frac{1}{r_i}\sum_{n=0}^{\infty}\Big(\frac{r_k}{r_i}\Big)^n P_n(\cos(\mu_{ik}))\end{aligned} \tag{34}$$

for

$$P_n(\cos(\mu_{ik})) = \frac{1}{n!2^n}\frac{d^n}{d(\cos(\mu_{ik}))^n}\big(\cos(\mu_{ik})^2 - 1\big)^n. \tag{35}$$

Using the decomposition formula from Torge (2001),

$$\begin{aligned}P_n(\cos\mu_{ik}) =& P_n(\cos\theta_i)P_n(\cos\theta_k) + ... \\ & 2\sum_{m=1}^{n}\frac{(n-m)!}{(n+m)!}\Big[R_{nm}(\theta_i,\phi_i)R_{nm}(\theta_k,\phi_k) + S_{nm}(\theta_i,\phi_i)S_{nm}(\theta_k,\phi_k)\Big],\end{aligned} \tag{36}$$

and employing Schmidt-semi-normalization of the surface spherical harmonics R_{nm} and S_{nm} (see equations (13) and (14)) gives the Schmidt-normalized version of equation (36) (Blakely, 1996),

$$\begin{aligned}P_n(\cos\mu_{ik}) &= P_n(\cos\theta_i)P_n(\cos\theta_k) + ... \\ &\quad 2\sum_{m=1}^{n}\frac{(n-m)!}{(n+m)!}\frac{1}{2\frac{(n-m)!}{(n+m)!}}\Big[R_n^m(\theta_i,\phi_i)R_n^m(\theta_k,\phi_k) + S_n^m(\theta_i,\phi_i)S_n^m(\theta_k,\phi_k)\Big] \\ &= P_n(\cos\theta_i)P_n(\cos\theta_k) + \sum_{m=1}^{n}\Big[R_n^m(\theta_i,\phi_i)R_n^m(\theta_k,\phi_k) + S_n^m(\theta_i,\phi_i)S_n^m(\theta_k,\phi_k)\Big] \\ &= \sum_{m=0}^{n}\Big[R_n^m(\theta_i,\phi_i)R_n^m(\theta_k,\phi_k) + S_n^m(\theta_i,\phi_i)S_n^m(\theta_k,\phi_k)\Big] \\ &= \sum_{m=0}^{n}P_n^m(\cos\theta_i)P_n^m(\cos\theta_k)\cos(m\phi_i - m\phi_k).\end{aligned} \tag{37}$$

Note that the last two lines include $m = 0$ on the basis of

$$P_n(\cos\theta) = P_n^0(\cos\theta) = R_n^0(\theta,\phi). \tag{38}$$

Using equations (34) and (37), the Schmidt-normalized potential due to equivalent point sources can now be written as

$$\Phi(\mathbf{r}_i) = \sum_{k=1}^{K} r_k q_k \sum_{n=0}^{\infty}\left(\frac{r_k}{r_i}\right)^{n+1}\sum_{m=0}^{n}P_n^m(\cos\theta_i)P_n^m(\cos\theta_k)\cos(m\phi_i - m\phi_k). \tag{39}$$

Comparing the spherical harmonic- and source potential expansion (equation (17) for internal sources and equation (39), respectively) enables the conventional spherical harmonic Gauss coefficients to be synthesized directly from the equivalent point source coefficients $\mathbf{q}$ (Hodder, 1982),

$$g_n^m = \sum_{k=1}^{K}\left(\frac{r_k}{a}\right)^{n+2} q_k P_n^m(\cos\theta_k)\cos(m\phi_k) \tag{40}$$

$$h_n^m = \sum_{k=1}^{K}\left(\frac{r_k}{a}\right)^{n+2} q_k P_n^m(\cos\theta_k)\sin(m\phi_k). \tag{41}$$

This transformation is used when comparing the power spectra between the derived equivalent source models and the models CM5, MF7 and CHAOS-6 in chapter 3.

2.3 The inverse problem

Estimating the lithospheric field at the Earth's surface from a finite set of imperfect satellite measurements is an ill-posed and non-unique inverse problem, i.e. there exist several solutions for $\mathbf{q}$ which are able to represent the field measurements $\mathbf{d}$ within their respective estimated errors. Different mathematical techniques exist for dealing with this problem (e.g. Menke, 2012; Aster et al., 2013). In order to derive robust model solutions which account for a non-Gaussian data error distribution, an iteratively re-weighted least squares algorithm (Walker and Jackson, 2000) is often applied that includes model regularization and Huber weighting (Constable, 1988). The corresponding model solution minimizes both the differences between model predictions and measurements (misfit norm) and a measure of the model complexity $\mathbf{R}$ (regularization norm).
From equation (29) the forward problem of the magnetic field due to equivalent sources may be written

$$\mathbf{A} = \underline{\underline{\mathbf{G}}}\mathbf{q}, \tag{42}$$

where $\mathbf{A} = [\mathbf{A}^r, \mathbf{A}^\theta, \mathbf{A}^\phi]$ is a column vector containing model predictions for $3N$ vector components at the N locations of magnetic field measurements, $\underline{\underline{\mathbf{G}}} = [\underline{\underline{\mathbf{G}}}^r, \underline{\underline{\mathbf{G}}}^\theta, \underline{\underline{\mathbf{G}}}^\phi]$ represents the corresponding $3N \times K$ Green's matrix, and $\mathbf{q}$ is the model vector of all K source strengths.
Here, we are interested in the inverse problem where $\mathbf{q}$ is to be determined from imperfect observations $\mathbf{d} = [\mathbf{d}^r, \mathbf{d}^\theta, \mathbf{d}^\phi]$. Finding a suitable estimation of the model vector $\mathbf{q}$ involves the minimization of the residual vector $\mathbf{e}$, which represents observation errors and data contamination from unmodelled sources,

$$\mathbf{e} = \mathbf{d} - \mathbf{A} = \mathbf{d} - \underline{\underline{\mathbf{G}}}\mathbf{q}. \tag{43}$$

2.4 The least squares solution

The model which minimizes the squared L_2-norm of the residuals, equivalent to the squared Euclidean length of the vector $\mathbf{e}$, $\|\mathbf{d} - \underline{\underline{\mathbf{G}}}\mathbf{q}\|_2^2 = \mathbf{e}^T\mathbf{e}$, is commonly known as the least squares solution $\mathbf{q}^{LS}$,

$$\begin{aligned} min &= \|\mathbf{d} - \underline{\underline{\mathbf{G}}}\mathbf{q}\|_2^2 \\ &= (\mathbf{d} - \underline{\underline{\mathbf{G}}}\mathbf{q})^T(\mathbf{d} - \underline{\underline{\mathbf{G}}}\mathbf{q}) \\ &= \sum_\psi \sum_{i=1}^{N} (d_i^\psi - (\underline{\underline{\mathbf{G}}}^\psi \mathbf{q})_i)^2 = \sum_\psi \sum_{i=1}^{N} (d_i^\psi - \sum_{k=1}^{K} g_{ik}^\psi q_k)^2 \end{aligned} \tag{44}$$

$$\mathbf{q}^{LS} = (\underline{\underline{\mathbf{G}}}^T \underline{\underline{\mathbf{G}}})^{-1} \underline{\underline{\mathbf{G}}}^T \mathbf{d} \tag{45}$$

where ψ represents one of the three vector field components r, θ or ϕ.
It is important to note that $\underline{\underline{\mathbf{G}}}^T\underline{\underline{\mathbf{G}}}$ has to be non-singular in order to solve the above least-squares solution. A singular matrix contains columns (or rows) with only zero values, or columns (or rows) which are linearly dependent on each other (Aster et al., 2013).

2.5 Maximum likelihood and robust estimation

Maximum likelihood estimation can be applied when the data observations contain independent random errors with known statistical properties (Aster et al., 2013).
Assuming independent observations with identically distributed errors, the probability density function $p(\mathbf{d}|\mathbf{q})$, or likelihood, for obtaining a given data vector component $\mathbf{d} = \{d_1, d_2, ..., d_N\}$ given the model parameters $\mathbf{q} = \{q_1, q_2, ..., q_K\}$, is

$$\begin{aligned} p(\mathbf{d}|\mathbf{q}) &= p(d_1|\mathbf{q}) \cdot p(d_2|\mathbf{q}) \cdot ... \cdot p(d_N|\mathbf{q}) \\ &= \Pi_i^{i=N} p(d_i|\mathbf{q}). \end{aligned} \tag{46}$$

The corresponding formula for Gaussian (normal) and Laplacian (double-sided exponential) distributions are

$$\begin{aligned} \text{Gaussian}: p(d_i|\mathbf{q}) &= \frac{1}{\sigma_i\sqrt{2\pi}} \exp^{-\frac{1}{2}\frac{(d_i-(\underline{\underline{\mathbf{G}}}\mathbf{q})_i)^2}{\sigma_i^2}} \\ \text{Laplacian}: p(d_i|\mathbf{q}) &= \frac{1}{\sigma_i\sqrt{2}} \exp^{-\sqrt{2}\frac{|d_i-(\underline{\underline{\mathbf{G}}}\mathbf{q})_i|}{\sigma_i}} \end{aligned} \tag{47}$$

with σ_i being the standard deviation of the errors corresponding to the ith datum, and $(\underline{\underline{\mathbf{G}}}\mathbf{q})_i$ represents the prediction of the model $\mathbf{q}$ for the ith datum.

Applying the maximum likelihood principle, the desired model vector results in the maximization of the likelihood probability function, which is equivalent to minimizing the corresponding negative natural logarithm,

$$p(\mathbf{d}|\mathbf{q}) = max \rightarrow -\ln p(\mathbf{d}|\mathbf{q}) = min. \tag{48}$$

The latter, also known as the loss function $\rho(\mathbf{d}|\mathbf{q}) = \rho(\mathbf{e})$, is a function of residuals $\mathbf{e} = \sum_{i=1}^{N}(d_i - (\underline{\underline{\mathbf{G}}}\mathbf{q})_i)$ and thus dependent on the data error distribution,

$$\begin{aligned} \rho(\mathbf{d}|\mathbf{q}) &= -\ln p(\mathbf{d}|\mathbf{q}) \\ &= -\ln \Pi_{i=1}^{N} p(d_i|\mathbf{q}) \\ &= -\sum_{i=1}^{N} \ln p(d_i|\mathbf{q}) \\ &= \sum_{i=1}^{N} \rho(d_i|\mathbf{q}) \\ &= \sum_{i=1}^{N} \rho(e_i). \end{aligned} \tag{49}$$

The loss functions corresponding to errors following the Gaussian and Laplacian probability functions of equation (47) are thus given by

$$\begin{aligned} \text{Gaussian}: \rho(d_i,\mathbf{q}) &= \ln(\sigma_i\sqrt{2\pi}) + \frac{1}{2}\frac{(d_i-(\underline{\underline{\mathbf{G}}}\mathbf{q})_i)^2}{\sigma_i^2} \rightarrow \sum_{i=1}^{N}\frac{(d_i-(\underline{\underline{\mathbf{G}}}\mathbf{q})_i)^2}{\sigma_i^2} = min \\ \text{Laplacian}: \rho(d_i,\mathbf{q}) &= \ln(\sigma_i\sqrt{2\pi}) + \sqrt{2}\frac{|d_i-(\underline{\underline{\mathbf{G}}}\mathbf{q})_i|}{\sigma_i} \rightarrow \sum_{i=1}^{N}\frac{|d_i-(\underline{\underline{\mathbf{G}}}\mathbf{q})_i|}{\sigma_i} = min \end{aligned}$$

Assuming a Gaussian error distribution, the loss function to be minimized is thus $\sum_{i=1}^{N}\frac{(d_i-(\underline{\underline{\mathbf{G}}}\mathbf{q})_i)^2}{\sigma_i^2}$. Introducing a diagonal inverse data error covariance matrix $\underline{\underline{\mathbf{C}}}^{-1} = \text{diag}(1/\sigma_1^2, 1/\sigma_2^2, ..., 1/\sigma_N^2)$, the Gaussian loss function is equivalent to equation (44): $\|\mathbf{d}_V - \underline{\underline{\mathbf{G}}}_V\mathbf{q}\|_2^2$, for $\mathbf{d}_V = \underline{\underline{\mathbf{C}}}^{-1/2}\mathbf{d}$ and $\underline{\underline{\mathbf{G}}}_V = \underline{\underline{\mathbf{C}}}^{-1/2}\underline{\underline{\mathbf{G}}}$ (Aster et al., 2013). The respective compact notation in terms of the vector of residuals is $\mathbf{e}^T\underline{\underline{\mathbf{C}}}^{-1}\mathbf{e}$. Thus, taking the individual data error variances into account, the model or least-squares solution which minimizes the squared residual L_2-norm is statistically the most likely solution when the data errors follow a Gaussian distribution. This means also that least-squares model solutions are not the maximum likelihood solution when the corresponding data error distribution is not Gaussian (Fox and Weisberg, 2002).

The method of minimizing functions that give smaller weight to large values of the residuals is an attempt to reduce the effect of possible data outliers, allowing more robust model solutions to be achieved. This approach substitutes the removal of noisy data and leads to model results which are less sensitive to data outliers.

Minimizing $\rho(e_i)$ is equivalent to setting $\Psi(e_i) = \frac{\partial\rho(e_i)}{\partial e_i} = 0$, where $\Psi(e_i)$ is known as the influence function. The weight function for generating robust model solutions is defined to be $w_i = \frac{\Psi(e_i)}{e_i}$, which leads to $\sum_{i=1}^{N} w_i e_i = 0$. Table 1 lists possible influence functions and weight functions corresponding to typically

assumed loss functions: Gaussian, Laplacian, Huber, Tukey and Ekblom.
For Gaussian loss functions this approach yields $\Psi(e_i) = e_i$, which results in a unity weight function. However, non-Gaussian error distributions result in non-unity weight functions, and require to minimize $\mathbf{e}^T \underline{\underline{\mathbf{C}}}^{-1/2} \underline{\underline{\mathbf{H}}} \underline{\underline{\mathbf{C}}}^{-1/2} \mathbf{e}$, with $\underline{\underline{\mathbf{H}}} = \mathrm{diag}(w_1, w_2, ..., w_N)$ being a diagonal matrix containing the individual weight functions for the given error distribution. Since the weight functions are dependent on the residuals and thereby also on the model values $\mathbf{q}$, robust model solutions for data with non-Gaussian error distributions can only be derived iteratively, updating the weights for every iteration until model convergence is reached. The corresponding approach is known as the *iteratively re-weighted least squares* (IRLS) method.
While Gaussian error distributions are characterized by unity weights, the weights decline for the *Huber* ρ-functions when $|e_i| > \vartheta$. ϑ symbolizes a tuning constant which decreases for increasing resistance towards data outliers (Fox and Weisberg, 2002). The weights corresponding to the Tukey bisquare ρ-function are zero for $|e_i| > \vartheta$ and decline for $0 < |e_i| \leq \vartheta$ (Fox and Weisberg, 2002).

Data error distribution	**Loss function** $\rho(e) \propto$	**Influence function** $\Psi(e) = \frac{\delta\rho(e)}{\delta e}$	**Weight function** $w(e) = \frac{\Psi(e)}{e}$
Gaussian (normal)	$\frac{1}{2}e^2$	e	1
Laplacian	$\|e\|$	$sgn(e)$	$\frac{sgn(e)}{e}$
Huber	$\begin{cases} \frac{1}{2}e^2 & \text{if } \|e\| \leq \vartheta \\ \vartheta\|e\| - \frac{1}{2}\vartheta^2 & \text{if } \|e\| > \vartheta \end{cases}$	$\begin{cases} e & \text{if } \|e\| \leq \vartheta \\ \vartheta & \text{if } \|e\| > \vartheta \end{cases}$	$\begin{cases} 1 & \text{if } \|e\| \leq \vartheta \\ \frac{\vartheta}{\|e\|} & \text{if } \|e\| > \vartheta \end{cases}$
Tukey (bisquare)	$\begin{cases} \frac{\vartheta^2}{6}[1 - [1 - (\frac{e}{\vartheta})^2]^3] & \text{if } \|e\| \leq \vartheta \\ \frac{\vartheta^2}{6} & \text{if } \|e\| > \vartheta \end{cases}$	$\begin{cases} e(1 - \frac{e^2}{\vartheta^2})^2 & \text{if } \|e\| \leq \vartheta \\ 0 & \text{if } \|e\| > \vartheta \end{cases}$	$\begin{cases} [1 - (\frac{e}{\vartheta})^2]^2 & \text{if } \|e\| \leq \vartheta \\ 0 & \text{if } \|e\| > \vartheta \end{cases}$
Ekblom	$(e^2 + \vartheta^2)^{p/2}$	$pe(e^2 + \vartheta^2)^{p/2-1}$	$p(e^2 + \vartheta^2)^{p/2-1}$

Table 1 Comparison of the loss-functions corresponding to different data error distributions. The respective influence (Ψ) and weight functions (w) are given in the last two columns. ϑ and *sgn* represent a positive constant and the signum function, respectively. p indicates the type of norm (L_1-norm $\rightarrow p = 1$, L_2-norm $\rightarrow p = 2$, etc.)

2.6 Data discrepancy functional

Assuming a general least-squares problem and a non-Gaussian data error distribution, the least-squares solution is fit to the data by minimizing a data discrepancy functional, which can be expressed as the sum over loss functions ρ of the residuals (as described in section 2.5). The data discrepancy functional of the current study uses a squared L_2-norm of the residuals which accounts for the expected data error variances and provides equal area weighting. The latter is ensured by the implementation of the sine function of the data latitudes into the diagonal inverse data error covariance matrix $\underline{\underline{\mathbf{C}}}^{-1} = \mathrm{diag}(\frac{\sin\theta_1}{(\sigma_1^r)^2}, \frac{\sin\theta_2}{(\sigma_2^r)^2}, ..., \frac{\sin\theta_N}{(\sigma_N^r)^2}, \frac{\sin\theta_1}{(\sigma_1^\theta)^2}, \frac{\sin\theta_2}{(\sigma_2^\theta)^2}, ..., \frac{\sin\theta_N}{(\sigma_N^\theta)^2}, \frac{\sin\theta_1}{(\sigma_1^\phi)^2}, \frac{\sin\theta_2}{(\sigma_2^\phi)^2}, ..., \frac{\sin\theta_N}{(\sigma_N^\phi)^2})$. In order to account for non-Gaussian data errors, Huber weights are implemented and, similar to Olsen (2002), with the corresponding tuning constant chosen as $\vartheta = 1.5$. For a given iteration $j+1$ the discrepancy functional is given by

$$(\mathbf{d} - \underline{\underline{\mathbf{G}}}\mathbf{q}_{j+1})^T \underline{\underline{\mathbf{W}}}_j (\mathbf{d} - \underline{\underline{\mathbf{G}}}\mathbf{q}_{j+1}) = \sum_{\psi} \sum_{i=1}^{N} \frac{\sin(\theta_i) \cdot h_{i,j}^{\psi} \cdot [d_i^{\psi} - (\underline{\underline{\mathbf{G}}}^{\psi}\mathbf{q})_i]^2}{(\sigma_i^{\psi})^2}. \tag{50}$$

with

$$\underline{\underline{\mathbf{W}}}_j = \underline{\underline{\mathbf{C}}}^{-1/2} \underline{\underline{\mathbf{H}}}_j \underline{\underline{\mathbf{C}}}^{-1/2}. \tag{51}$$

and ψ representing a given vector component (r, θ or ϕ).
Note that the diagonal *Huber* weighting matrix $\underline{\underline{\mathbf{H}}}_j = [\mathbf{h}_j^r, \mathbf{h}_j^\theta, \mathbf{h}_j^\phi]$ is determined by the model solution of the previous iteration. According to Table 1, the respective components are given by

$$h_{i,j}^{\psi} = \begin{cases} 1 & \text{if } \epsilon_{i,j}^{\psi} \leq 1.5, \\ 1.5/\epsilon_{i,j}^{\psi} & \text{if } \epsilon_{i,j}^{\psi} > 1.5 \end{cases} \tag{52}$$

with $\boldsymbol{\epsilon}_j^{\psi}$ representing the normalized residuals with respect to the expected latitude-dependent data error standard deviation values $\boldsymbol{\sigma}^{\psi}$,

$$\boldsymbol{\epsilon}_j^{\psi} = |\mathbf{e}_j^{\psi}/\boldsymbol{\sigma}^{\psi}|. \tag{53}$$

The *Huber* distribution consists of a Gaussian distribution in the center, and a Laplace distribution in the tails. Whenever the values of $\boldsymbol{\epsilon}_j^{\psi}$ are smaller than 1.5, the model derivation is performed under the L_2-norm measure of misfit, which assumes that small residuals follow a Gaussian distribution. Huber weight values below unity, on the other hand, mimic a L_1 misfit norm, accounting for unmodeled fluctuations in the measurements and assuming that the corresponding data errors originate from a double exponential (or Laplace) distribution (Walker and Jackson, 2000).

2.7 Model regularization

The general least-squares problem, $(\mathbf{d} - \underline{\underline{\mathbf{G}}}\mathbf{q}_{j+1})^T \underline{\underline{\mathbf{W}}}_j (\mathbf{d} - \underline{\underline{\mathbf{G}}}\mathbf{q}_{j+1})$, has infinitely many least square solutions which, in the presence of data noise, are unstable and highly susceptible to outliers (Aster et al., 2013). A common approach for stabilizing the model solution and solving ill-posed discrete inverse problems is to introduce model regularization, as pioneered by Tikhonov and Arsenin (1977). The respective model minimizes an objective function $\boldsymbol{\Theta}$ which combines the data discrepancy functional, quantifying the misfit between the measurements $\mathbf{d}$ and the model predictions $\underline{\underline{\mathbf{G}}}\mathbf{q}$, and a penalty functional $\mathbf{R}$, inducing stability and information regarding the final model complexity. The objective function for the corresponding damped least squares problem is

$$\boldsymbol{\Theta}(\mathbf{q}_{j+1}) = (\mathbf{d} - \underline{\underline{\mathbf{G}}}\mathbf{q}_{j+1})^T \underline{\underline{\mathbf{W}}}_j (\mathbf{d} - \underline{\underline{\mathbf{G}}}\mathbf{q}_{j+1}) + \alpha \mathbf{R}(\mathbf{q}_{j+1}). \tag{54}$$

where $\alpha \geqslant 0$ is a regularization parameter, representing the trade-off between the two functionals (Menke, 2012). For $\alpha = 0$, the resulting model solution solely minimizes the data misfit, while the data influence is almost zero in favour of the minimization of the specified property of the model for $\alpha = 1$ (dependent on the setup of $\mathbf{R}$). Note that the units of α are dependent on the type of regularization.Ionospheric magnetic signals or data noise which have not been removed from the original measurements can be mapped into lithospheric field estimates, resulting in erroneous small-scale spatial field structures. Regularization can be used to control these short wavelength signals and reduces their tendency of blowing up in amplitude on downward continuation (e.g. O'Brien and Parker (1994); Maus et al. (2006)).

2.8 A regularized IRLS approach

If a forward problem is non-linear, iterative approaches (e.g. the gradient and related Newton methods) can be used to minimize the objective function $\boldsymbol{\Theta}$ by linearizing the forward problem about an estimate of the model solution $\mathbf{q}_j$ for a given iteration j (Luenberger, 1969).
Some of the regularization norms we investigate (L_1-norm and maximum entropy) result in non-linear objective functions. Thus, an iterative approach is necessary. Applying the Newton method, the predicted model parameters at the $j+1$ iteration are given by (eq. 3.84 in Tarantola (2005))

$$\mathbf{q}_{j+1} = \mathbf{q}_j - \kappa_j [\nabla\nabla \boldsymbol{\Theta}(\mathbf{q}_j)]^{-1} [\nabla \boldsymbol{\Theta}(\mathbf{q}_j)], \tag{55}$$

where $\nabla\nabla$ represents the Hessian matrix of second order partial derivatives, and κ_j is a real constant small enough for preventing the algorithm to diverge and large enough for allowing the algorithm to advance (Tarantola, 2005). Since the Hessian matrix accounts for the local geometry of the objective function, κ_j is unity for most applications. For $\boldsymbol{\Theta}(\mathbf{q}_{j+1}) = (\mathbf{d} - \underline{\underline{\mathbf{G}}}\mathbf{q}_{j+1})^T \underline{\underline{\mathbf{W}}}_j (\mathbf{d} - \underline{\underline{\mathbf{G}}}\mathbf{q}_{j+1}) + \alpha \mathbf{R}(\mathbf{q}_{j+1})$ the gradient and Hessian operators with respect to $\mathbf{q}$ are

$$\nabla \boldsymbol{\Theta}(\mathbf{q}_{j+1}) = -2 \underline{\underline{\mathbf{G}}}^T \underline{\underline{\mathbf{W}}}_j (\mathbf{d} - \underline{\underline{\mathbf{G}}}\mathbf{q}_{j+1}) + \alpha \nabla \mathbf{R}(\mathbf{q}_{j+1}) \tag{56a}$$

$$\nabla\nabla \boldsymbol{\Theta}(\mathbf{q}_{j+1}) = 2 \underline{\underline{\mathbf{G}}}^T \underline{\underline{\mathbf{W}}}_j \underline{\underline{\mathbf{G}}} + \alpha \nabla\nabla \mathbf{R}(\mathbf{q}_{j+1}). \tag{56b}$$

Using the above notations and taking $\kappa_j = 1$, equation (55) can be written as a perturbation $\delta\mathbf{q}$ to $\mathbf{q}_j$,

$$\begin{aligned} \mathbf{q}_{j+1} &= \mathbf{q}_j + \delta\mathbf{q} \\ \rightarrow \delta\mathbf{q} &= \mathbf{q}_{j+1} - \mathbf{q}_j \\ &= [2\underline{\underline{\mathbf{G}}}^T \underline{\underline{\mathbf{W}}}_j \underline{\underline{\mathbf{G}}} + \alpha\nabla\nabla\mathbf{R}(\mathbf{q}_j)]^{-1}[2\underline{\underline{\mathbf{G}}}^T \underline{\underline{\mathbf{W}}}_j(\mathbf{d} - \underline{\underline{\mathbf{G}}}\mathbf{q}_j) - \alpha\nabla\mathbf{R}(\mathbf{q}_j)]. \end{aligned} \tag{57}$$

We apply a variant of the Newton method which solves for the vector $\mathbf{q}_{j+1}$, rather than $\delta\mathbf{q}$ (Stockmann et al., 2009). Using equations (56a) and (56b), equation (55) transforms into

$$\mathbf{q}_{j+1} = (2\underline{\underline{\mathbf{G}}}^T \underline{\underline{\mathbf{W}}}_j \underline{\underline{\mathbf{G}}} + \alpha\nabla\nabla\mathbf{R}(\mathbf{q}_j))^{-1}(2\underline{\underline{\mathbf{G}}}^T \underline{\underline{\mathbf{W}}}_j \mathbf{d} + \alpha\nabla\nabla\mathbf{R}(\mathbf{q}_j)\mathbf{q}_j - \alpha\nabla\mathbf{R}(\mathbf{q}_j)). \tag{58}$$

Equation (58) can be applied to both quadratic and non-quadratic regularization norms. Iteration is performed until the norm of the model change is less than 1% of the model norm (Aster et al., 2013; Stockmann et al., 2009),

$$\frac{\sum(\mathbf{q}_j - \mathbf{q}_{j+1})^2}{\sum \mathbf{q}_{j+1}^2} = \frac{\|\mathbf{q}_j - \mathbf{q}_{j+1}\|_2^2}{\|\mathbf{q}_{j+1}\|_2^2} < 0.01\ . \tag{59}$$

2.8.1 Quadratic regularization

Choosing the regularization norm to be the quadratic (or L_2) norm of the model parameters, also sometimes known zeroth-order Tikhonov regularization, results in a model solution which satisfactorily fits the data and simultaneously minimizes $\mathbf{R}^{QR}(\mathbf{q}) = \mathbf{q}^T\mathbf{q}$. This leads to the following objective function:

$$\begin{aligned} \mathbf{\Theta}(\mathbf{q}) &= \|\mathbf{d} - \underline{\underline{\mathbf{G}}}\mathbf{q}\|_2^2 + \alpha\|\mathbf{q}\|_2^2 \\ &= (\mathbf{d} - \underline{\underline{\mathbf{G}}}\mathbf{q})^T \underline{\underline{\mathbf{W}}}(\mathbf{d} - \underline{\underline{\mathbf{G}}}\mathbf{q}) + \alpha\mathbf{q}^T\mathbf{q}. \end{aligned} \tag{60}$$

Applying $\mathbf{R}(\mathbf{q}) = \mathbf{R}^{QR}(\mathbf{q})$, equation (58) transforms into the well known damped least squares solution

$$\mathbf{q}_{j+1}^{QR} = (\underline{\underline{\mathbf{G}}}^T \underline{\underline{\mathbf{W}}}_j \underline{\underline{\mathbf{G}}} + \alpha\mathbf{I})^{-1} \underline{\underline{\mathbf{G}}}^T \underline{\underline{\mathbf{W}}}_j \mathbf{d} \tag{61}$$

where a factor $\frac{1}{2}$ has been included into the constant α.
The applied quadratic regularization norm leads to model solutions with smallest possible amplitudes of the monopole values. However, this constraint may not always be geologically relevant because there are several large amplitude local magnetic field anomalies, e.g. the West African Craton anomaly and the Bangui anomaly. Allowing a model to create such locally high amplitude anomalies is possible by regularizing the model entropy or an L_1-norm of the model rather than the squared amplitude of the model parameters, see sections 2.8.3 and 2.8.2.
The investigated quadratic regularization models, with their different α values, share the same starting point, a well-converged, but un-regularized ($\alpha = 0$), model solution. The initial *Huber* weights $\underline{\underline{\mathbf{H}}}_0$ are defined to be unity.
The above routine has been investigated for different values of α. The preferred quadratic regularization models of this thesis are found based on the corresponding L-curve (Aster et al., 2013; Menke, 2012), model statistics, predicted magnetic field maps at the Earth's surface and power spectra. Respective figures and discussions of the choice of α are given in section 3.5. All presented models fulfill the convergence criterion of equation (59).
In the current study the quadratic regularization norm is equivalent to the squared amplitude of the model parameters. However, other functions of the model parameters could have been used instead if other model characteristics are to be minimized. For instance, other models of the lithospheric field have applied quadratic regularization to the modelled radial magnetic field values at the Earth's surface (e.g. Stockmann et al. (2009)).

2.8.2 Maximum entropy regularization

The maximum entropy regularization approach was originally introduced by Gull and Daniell (1978) as a mathematical tool to improve astronomical image resolution. However, the method's ability to recognize patterns by the enhancement of local signals has been valuable in many scientific fields (Gull and Skilling, 1989, 1999; Smith and Grandy, 2013), e.g. tomography (Hanson and Silver, 2012) and natural language processing (Berger et al., 1996). Within geomagnetism, the technique has successfully been applied for model predictions of the core field (Jackson et al., 2007; Gillet et al., 2007) and lithospheric field (Stockmann et al., 2009; Kother et al., 2015). Especially lithospheric magnetic field models benefit from the preservation of high amplitude local field structures.
Gull and Skilling (1999) define the entropy S of a model $\mathbf{q}$, which can consist of both negative and positive values, as

$$S(\mathbf{q},\omega) = \sum_{k=1}^{K} \Big[\upsilon_k - 2\omega - q_k \ln\Big(\frac{\upsilon_k + q_k}{2\omega}\Big)\Big]. \tag{62}$$

with ω being a default parameter, with the units as $\mathbf{q}$, which defines the scale of the entropy function (Maisinger et al., 2004) and $\upsilon_k = \sqrt{q_k^2 + 4\omega^2}$.
The maximum entropy function is non-quadratic and results in a non-linear objective function $\mathbf{\Theta}$, requesting the iterative scheme of equation (58) to determine a model with minimal complexity for a given level of misfit. Similar to Stockmann et al. (2009), we apply the negative entropy (negentropy) as regularization norm (Gillet et al., 2007),

$$\mathbf{R}^{ER}(\mathbf{q},\omega) = -4\omega S(\mathbf{q},\omega) \tag{63}$$

The negentropy $\mathbf{R}^{ER}$ becomes identical to the quadratic norm for large values of ω, thus making comparisons between the two regularization methods possible.
Keeping in mind the following first order derivatives,

$$\frac{\delta}{\delta q}\sqrt{q^2+4\omega^2} = \frac{q}{\sqrt{q^2+4\omega^2}} \tag{64}$$

$$\begin{aligned} \frac{\delta}{\delta q}\Big[q \ln\Big(\frac{\sqrt{q^2+4\omega^2}+q}{2\omega}\Big)\Big] &= \ln\Big(\frac{\sqrt{q^2+4\omega^2}+q}{2\omega}\Big) + \frac{q\Big(\frac{q}{\sqrt{q^2+4\omega^2}}+1\Big)}{\sqrt{q^2+4\omega^2}+q} \\ &= \frac{\sqrt{q^2+4\omega^2}\ln\Big(\frac{\sqrt{q^2+4\omega^2}+q}{2\omega}\Big)+q}{\sqrt{q^2+4\omega^2}} \end{aligned} \tag{65}$$

the gradient and Hessian operators of $\mathbf{R}^{ER}$ for a given source q_k are

$$\begin{aligned} (\nabla \mathbf{R}^{ER})_k &= -4\omega\Big[\frac{q_k}{\sqrt{q_k^2+4\omega^2}} - \frac{\sqrt{q_k^2+4\omega^2}\ln\Big(\frac{\sqrt{q_k^2+4\omega^2}+q_k}{2\omega}\Big)+q_k}{\sqrt{q_k^2+4\omega^2}}\Big] \\ &= 4\omega \ln\Big(\frac{\sqrt{q_k^2+4\omega^2}+q_k}{2\omega}\Big) \\ &= 4\omega \ln\Big(\frac{\upsilon_k+q_k}{2\omega}\Big) \end{aligned} \tag{66}$$

$$\begin{aligned} (\nabla\nabla \mathbf{R}^{ER})_k &= \frac{4\omega}{\sqrt{q_k^2+4\omega^2}}\delta_{kk} \\ &= \frac{4\omega}{\upsilon_k}\delta_{kk} \end{aligned} \tag{67}$$

with δ_{kk} representing the Kronecker delta.
Using $\mathbf{R}^{ER}(\mathbf{q},\omega)$ as the regularization norm and applying the respective gradient and Hessian operators in equation (58), the Newton-type iterative scheme becomes

$$\begin{aligned} \mathbf{q}_{j+1}^{ER} &= (2\underline{\underline{\mathbf{G}}}^T \underline{\underline{\mathbf{W}}}_j \underline{\underline{\mathbf{G}}} + \alpha\nabla\nabla\mathbf{R}^{ER}(\mathbf{q},\omega))^{-1}(2\underline{\underline{\mathbf{G}}}^T\underline{\underline{\mathbf{W}}}_j\mathbf{d} + \alpha\nabla\nabla\mathbf{R}^{ER}(\mathbf{q},\omega)\mathbf{q}_j^{ER} - \alpha\nabla\mathbf{R}^{ER}(\mathbf{q},\omega)) \\ &= (2\underline{\underline{\mathbf{G}}}^T \underline{\underline{\mathbf{W}}}_j \underline{\underline{\mathbf{G}}} + \alpha\boldsymbol{\gamma}_j)^{-1}(2\underline{\underline{\mathbf{G}}}^T\underline{\underline{\mathbf{W}}}_j\mathbf{d} + \alpha\boldsymbol{\gamma}_j\mathbf{q}_j^{ER} - 4\alpha\omega\boldsymbol{\beta}_j) \end{aligned} \tag{68}$$

with

$$\boldsymbol{\gamma}_j = \text{diag}\left(\frac{4\omega}{\upsilon_{1,j}}, \frac{4\omega}{\upsilon_{2,j}}, ..., \frac{4\omega}{\upsilon_{K,j}}\right)$$
$$\boldsymbol{\beta}_j = \left(ln(\frac{\upsilon_{1,j}+q_{1,j}}{2\omega}), ln(\frac{\upsilon_{2,j}+q_{2,j}}{2\omega}), ..., ln(\frac{\upsilon_{K,j}+q_{K,j}}{2\omega})\right). \tag{69}$$

The iterative scheme requires a starting condition for the model $\mathbf{q}_0^{ER}$, which is defined to be the converged quadratic regularization model with the same α: $\mathbf{q}_0^{ER}(\alpha) = \mathbf{q}_{final}^{L2}(\alpha)$. As before, the initial values for the *Huber* weights are unity and the convergence criterion of equation (59) is used to determine the final model solution.
Different values for ω are investigated by means of the corresponding model statistics, predicted magnetic field maps at the Earth's surface and power spectra. Respective figures and discussions are given in section 3.6.

2.8.3 L_1-norm regularization

The derivation of sparse models with as many as possible model parameters pushed towards zero, can be achieved by means of the L_0 or L_1 norm regularization of the model parameters. The former is numerically difficult to implement, thus the current study applies the L_1 norm to ensure model sparsity (Schmidt, 2005).
L_1-norm regularization involves a regularization norm $\mathbf{R}(\mathbf{q}) = \|\underline{\underline{\mathbf{L}}}\mathbf{q}\|_1$, where $\underline{\underline{\mathbf{L}}}$ is a matrix representing any linear function of the model parameters $\mathbf{q}$. The current study investigates the L_1 norm of the model parameters, which leads to $\underline{\underline{\mathbf{L}}}$ being the identity matrix - neglectable from further equations. The objective function to be minimized with respect to the model parameters is thus given by

$$\boldsymbol{\Theta}(\mathbf{q}) = \|\mathbf{d} - \underline{\underline{\mathbf{G}}}\mathbf{q}\|_2^2 + \alpha\|\mathbf{q}\|_1 \ . \tag{70}$$

Note that the units of α are now $[nT^{-1}]$.
Using the L_1-norm for model regularization implies that the equivalent point source amplitudes are assumed to follow a Laplacian distribution. The resulting field predictions will possess localized anomalies with large amplitudes, which is a characteristic feature of the lithospheric magnetic field.
The gradient and Hessian operators corresponding to the L_1 regularization norm are dependent on the signum function

$$\text{sgn}(q_k) = \begin{cases} 1 & \text{for } q_k > 0 \\ 0 & \text{for } q_k = 0 \\ -1 & \text{for } q_k < 0 \end{cases} \tag{71}$$

and given by

$$\nabla\mathbf{R} = \sum_{k=1}^{K} \text{sgn}(q_k) = \sum_{k=1}^{K} \frac{q_k}{|q_k|} = \underline{\underline{\mathbf{T}}}\mathbf{q} \tag{72a}$$
$$\nabla\nabla\mathbf{R} = \underline{\underline{\mathbf{T}}} \tag{72b}$$

with $\underline{\underline{\mathbf{T}}}$ being a $K \times K$ diagonal weighting matrix of elements $T_{k,k} = \frac{1}{|q_k|}$ (Aster et al., 2013).
The formulae of equations (72a) and (72b) give the following solution for equation (58) (Olsen and Finlay, 2016)

$$\mathbf{q}_{j+1}^{L_1} = [\underline{\underline{\mathbf{G}}}^T\underline{\underline{\mathbf{W}}}_j\underline{\underline{\mathbf{G}}} + \alpha\underline{\underline{\mathbf{T}}}_j]^{-1}\underline{\underline{\mathbf{G}}}^T\underline{\underline{\mathbf{W}}}_j\mathbf{d} \tag{73}$$

where a factor $\frac{1}{2}$ has again been included into the constant α.
Since both $\underline{\underline{\mathbf{W}}}$ and $\underline{\underline{\mathbf{T}}}$ are dependent on the model parameters, equation (73) needs an iterative scheme to be solved. The corresponding elements are updated for each iteration depending on the residuals and model parameters, respectively. The necessary starting model and initial *Huber* weights are defined to be the converged quadratic regularization model with $\alpha = 500\,\text{nT}^{-2}$ and the corresponding weights, respectively.
The L_1 regularization norm transforms the objective function $\boldsymbol{\Theta}$ into a convex optimization problem in terms

of $\mathbf{q}$, as the function is non-differentiable for $q_k = 0$ ($T_{k,k}$ is undefined for $q_k = 0$) (Schmidt, 2005). Different techniques exist for preventing this singularity of $\underline{\underline{\mathbf{T}}}$. One approach suggested by Aster et al. (2013) involves approximating the L_1 norm minimizing solution by means of a constant tolerance value ϑ, which is much smaller than the value of q_k:

$$T_{k,k} = \begin{cases} \frac{1}{|q_k|} & \text{if } |q_k| \geq \vartheta \\ \frac{1}{\vartheta} & \text{if } |q_k| < \vartheta \end{cases} \tag{74}$$

However, the routine applied in this thesis is based on the study of Farquharson and Oldenburg (1998). Letting $\underline{\underline{\mathbf{T}}}$ be a function of the Ekblom weight (see Table 1, for the L_1 norm $\rightarrow p = 1$) rather than the model parameters, the respective diagonal matrix elements are instead

$$T_{k,k} = \frac{1}{(q_k^2 + \vartheta^2)^{1/2}} \tag{75}$$

with $\vartheta > 0$. Small tolerance values let the measure tend to the L_1 norm, while large values let the regularization matrix behave like a scaled sum of squares measure (Farquharson and Oldenburg, 1998). The performed calculations use $\vartheta = 1 \cdot 10^{-4}$nT. The derived global lithospheric field models based on equivalent monopoles and using L_1-norm regularization are presented in section 3.6. All models fulfill the convergence criterion of equation (59).

2.9 Imposing the divergence-free constraint

Isolated magnetic monopoles are only a practical tool and do not exist in reality ($\nabla \cdot \mathbf{B} = 0$), so the derived model solutions must ensure a zero magnetic net flux (O'Brien and Parker, 1994) as

$$\sum_{k=1}^{K} q_k = 0. \tag{76}$$

This requirement is equivalent to a zero mean value of $\mathbf{q}$.
The enforcement of the divergence-free condition for the quadratic regularization scheme can be acquired by means of Lagrange multipliers (T. J. Sabaka, private communication with N. Olsen and M.D. Hammer, 2011):

$$\begin{aligned} &\min\ (\mathbf{d} - \underline{\underline{\mathbf{G}}}\mathbf{q})^T \underline{\underline{\mathbf{W}}}(\mathbf{d} - \underline{\underline{\mathbf{G}}}\mathbf{q}) + \alpha \mathbf{R}(\mathbf{q}) \\ &\text{subjected to } \mathbf{L}\mathbf{q} = 0 \end{aligned} \tag{77}$$

where $\mathbf{L}$ represents a linear function of $\mathbf{q}$, which in this case is a row vector containing ones, and $\mathbf{R}$ is the chosen regularization function, for illustration here set to $\mathbf{R}^{QR} = \|\mathbf{q}\|_2^2$.
Utilizing Lagrange multipliers $\mathbf{u}$, equation (77) is expressed as

$$J(\mathbf{q}, \mathbf{u}) = (\mathbf{d} - \underline{\underline{\mathbf{G}}}\mathbf{q})^T \underline{\underline{\mathbf{W}}}(\mathbf{d} - \underline{\underline{\mathbf{G}}}\mathbf{q}) + \alpha \mathbf{R}(\mathbf{q}) + \mathbf{u}\mathbf{L}^T \mathbf{q} \tag{78}$$

The stationary condition requires $\frac{\partial J(\mathbf{q},\mathbf{u})}{\partial \mathbf{q}} = \frac{\partial J(\mathbf{q},\mathbf{u})}{\partial \mathbf{u}} = 0$. Thus,

$$\begin{aligned} \frac{\partial J(\mathbf{q}, \mathbf{u})}{\partial \mathbf{q}} &= 0 = -2\underline{\underline{\mathbf{G}}}^T \underline{\underline{\mathbf{W}}}(\mathbf{d} - \underline{\underline{\mathbf{G}}}\mathbf{q}) + \alpha \nabla \mathbf{R}(\mathbf{q}) + \mathbf{u}\mathbf{L}^T \\ &\rightarrow \mathbf{q} = (\underline{\underline{\mathbf{G}}}^T \underline{\underline{\mathbf{W}}}\underline{\underline{\mathbf{G}}} + \alpha \underline{\underline{\mathbf{I}}})^{-1}(\underline{\underline{\mathbf{G}}}^T \underline{\underline{\mathbf{W}}}\mathbf{d} - \frac{1}{2}\mathbf{u}\mathbf{L}^T) \end{aligned} \tag{79}$$

$$\begin{aligned} \frac{\partial J(\mathbf{q}, \mathbf{u})}{\partial \mathbf{u}} &= 0 = \mathbf{L}^T \mathbf{q} \\ &= \mathbf{L}^T \mathbf{Y}(\underline{\underline{\mathbf{G}}}^T \underline{\underline{\mathbf{W}}}\mathbf{d} - \frac{1}{2}\mathbf{u}\mathbf{L}^T) \\ &= \mathbf{L}^T \mathbf{Y}\underline{\underline{\mathbf{G}}}^T \underline{\underline{\mathbf{W}}}\mathbf{d} - \mathbf{L}^T \mathbf{Y}\frac{1}{2}\mathbf{u}\mathbf{L}^T \\ &\rightarrow \mathbf{u} = 2\mathbf{L}^T \mathbf{Y}\underline{\underline{\mathbf{G}}}^T \underline{\underline{\mathbf{W}}}\mathbf{d}(\mathbf{L}^T \mathbf{Y}\mathbf{L})^{-1} \end{aligned} \tag{80}$$

Using the equation of $\mathbf{u}$ for solving equation (79) with respect to $\mathbf{q}$, the constrained quadratic regularized model solution with zero mean is given by

$$\begin{aligned}\mathbf{q} &= \mathbf{Y}\underline{\underline{\mathbf{G}}}^T\underline{\underline{\mathbf{W}}}\mathbf{d} - \mathbf{Y}\mathbf{L}^T \cdot \mathbf{Y}\underline{\underline{\mathbf{G}}}^T\underline{\underline{\mathbf{W}}}\mathbf{d}(\mathbf{L}^T\mathbf{Y}\mathbf{L})^{-1}\mathbf{L}^T \\ &= \mathbf{q}_* - \mathbf{Y}\mathbf{L}^T\mathbf{q}_*(\mathbf{L}^T\mathbf{Y}\mathbf{L})^{-1}\mathbf{L}^T\end{aligned} \tag{81}$$

with $\mathbf{Y} = \mathbf{Y}^{L_2} = (\underline{\underline{\mathbf{G}}}^T\underline{\underline{\mathbf{W}\mathbf{G}}} + \alpha\underline{\underline{\mathbf{I}}})^{-1}$, $\mathbf{q}_* = \mathbf{Y}\underline{\underline{\mathbf{G}}}^T\underline{\underline{\mathbf{W}}}\mathbf{d}$ being the converged un-constrained model solution of equation (61), and $\underline{\underline{\mathbf{W}}}$ containing the respective *Huber* weights.

The above method is also applicable for the L_1-norm regularization scheme. In this case the regularization function of equation (77) is given by $\mathbf{R}^{L_1} = \|\mathbf{q}\|_1$, which leads to a similar version of equation (81). The only difference is seen in the definition of $\mathbf{Y}$, which is a function of both $\mathbf{q}_*$, the converged un-constrained model solution of equation (73), and the corresponding IRLS weights:
$\mathbf{Y} = \mathbf{Y}^{L_1} = (\underline{\underline{\mathbf{G}}}^T\underline{\underline{\mathbf{W}\mathbf{G}}} + \alpha\underline{\underline{\mathbf{T}}})^{-1}$.

The constrained model solution for the maximum entropy regularization scheme is dependent on the converged and un-constrained model predictions of equation (68) ($\mathbf{q}_*$) as well as the corresponding values for $\boldsymbol{\gamma}$, $\boldsymbol{\beta}$ and the weighting matrix $\underline{\underline{\mathbf{W}}}$. Assuming $2\underline{\underline{\mathbf{G}}}^T\underline{\underline{\mathbf{W}}}\mathbf{d} >> \alpha\boldsymbol{\gamma}\mathbf{q}_* - 4\alpha\omega\boldsymbol{\beta}$, which is a good approximation for small values of α, the constrained maximum entropy regularized model solution with zero mean can be approximated by equation (81) with $\mathbf{Y} = \mathbf{Y}^{ER} = (\underline{\underline{\mathbf{G}}}^T\underline{\underline{\mathbf{W}\mathbf{G}}} + \frac{\alpha}{2}\boldsymbol{\gamma})^{-1}$.

2.10 Geomagnetic assumptions when using scalar data

When the observed data is given by scalar (intensity) values rather than vector measurements of the geomagnetic field, some modifications have to be made in order to use the above described mathematical routine. Scalar values are defined by the square root of the sum of the squared vector components: $A = |\mathbf{A}| = \sqrt{A_r^2 + A_\theta^2 + A_\phi^2}$ (for $\mathbf{A} = [A_r, A_\theta, A_\phi]$), which leads to a non-linear version of equation (42), $A = \mathcal{G}(\mathbf{q})$. This relation is typically linearized by projecting the lithospheric field onto the main field direction (Blakely, 1996, p. 179),

$$A = |\widetilde{\mathbf{B}}^{core} + \mathbf{A}| - |\widetilde{\mathbf{B}}^{core}| \tag{82a}$$

$$= \sqrt{(\widetilde{\mathbf{B}}^{core} + \mathbf{A})(\widetilde{\mathbf{B}}^{core} + \mathbf{A})} - |\widetilde{\mathbf{B}}^{core}| \tag{82b}$$

$$= \sqrt{\widetilde{\mathbf{B}}^{core} \cdot \widetilde{\mathbf{B}}^{core} + \mathbf{A} \cdot \mathbf{A} + 2\mathbf{A} \cdot \widetilde{\mathbf{B}}^{core}} - |\widetilde{\mathbf{B}}^{core}| \tag{82c}$$

$$\approx (\widetilde{\mathbf{B}}^{core} \cdot \widetilde{\mathbf{B}}^{core})^{\frac{1}{2}} + (\widetilde{\mathbf{B}}^{core} \cdot \widetilde{\mathbf{B}}^{core})^{-\frac{1}{2}}(\widetilde{\mathbf{B}}^{core} \cdot \mathbf{A}) - |\widetilde{\mathbf{B}}^{core}| \tag{82d}$$

$$= \mathbf{A}\frac{\widetilde{\mathbf{B}}^{core}}{|\widetilde{\mathbf{B}}^{core}|} \tag{82e}$$

Equation (82d) uses the assumption that the magnitude of the lithospheric field is small compared to the main field intensity, $|\mathbf{A}(\mathbf{r})| \ll |\widetilde{\mathbf{B}}^{core}(\mathbf{r})|$. For a specific location $\mathbf{r}$ it yields

$$\begin{aligned}A(\mathbf{r}) &= \mathbf{A}(\mathbf{r})\frac{\widetilde{\mathbf{B}}^{core}(\mathbf{r}, t)}{|\widetilde{\mathbf{B}}^{core}(\mathbf{r}, t)|} \\ &= \mathbf{A}(\mathbf{r})\hat{\mathbf{b}}(\mathbf{r})\end{aligned} \tag{83}$$

where $\widetilde{\mathbf{B}}^{core}(\mathbf{r}, t)$ is an estimation of the main field at a particular time t based on a certain global geomagnetic field model (e.g. CHAOS or IGRF), and $\hat{\mathbf{b}}(\mathbf{r})$ is the unit vector along the main field direction at location $\mathbf{r}$ (Langel and Hinze, 1998, p. 121).

The scalar version of equation (42) is then

$$
\begin{aligned}
A(\mathbf{r}_i) &= \mathbf{A}(\mathbf{r}_i)\frac{\widetilde{B}^{core}(r_i)\hat{\mathbf{r}} + \widetilde{B}^{core}(\theta_i)\hat{\boldsymbol{\theta}} + \widetilde{B}^{core}(\phi_i)\hat{\boldsymbol{\phi}}}{|\widetilde{\mathbf{B}}^{core}(\mathbf{r}_i,t)|} \\
&= \sum_{k=1}^{K} q_k g_{ik}\frac{\widetilde{B}^{core}(r_i)\hat{\mathbf{r}} + \widetilde{B}^{core}(\theta_i)\hat{\boldsymbol{\theta}} + \widetilde{B}^{core}(\phi_i)\hat{\boldsymbol{\phi}}}{|\widetilde{\mathbf{B}}^{core}(\mathbf{r}_i,t)|} \\
&= \sum_{k=1}^{K} q_k \frac{1}{|\widetilde{\mathbf{B}}^{core}(\mathbf{r}_i,t)|}\sum_{\psi=r,\theta,\phi} g_{ik,\psi}\widetilde{B}^{core}(\psi_i) \\
&= \underline{\underline{\mathbf{G_s}}}\mathbf{q}
\end{aligned} \tag{84}
$$

with $\underline{\underline{\mathbf{G_s}}}$ being a combination of the Green's matrix components used for vector measurements as well as the linearization factor $\hat{\mathbf{b}}$.

2.11 Residual statistics for model comparison

Both global and regional equivalent point source models of this thesis will be assessed by means of the corresponding residual statistics. For a given field component ψ (for $\psi = r, \theta$ or ϕ) the differences between Huber-weighted model predictions ($\mathbf{A}^{\psi}$) and observations ($\mathbf{d}^{\psi}$) are denoted as $\Delta\mathbf{B}^{\psi}$. The associated normalized (by latitude-dependent standard deviation values) and Huber-weighted residual root-mean-square value (RMS) and residual 2-norm are given by

$$
\begin{aligned}
\text{RMS } \Delta\mathbf{B}^{\psi} &= \sqrt{\frac{\sum_{i=1}^{N} h_i^{\psi}\cdot\left(\frac{\Delta B_i^{\psi}}{\sigma_i^{\psi}}\right)^2}{\sum_{i=1}^{N} h_i^{\psi}}} \\
\text{Residual 2-norm } &= \sqrt{\sum_{i=1}^{N}(\Delta B_i^{\psi})^2}
\end{aligned} \tag{85}
$$

3 Global lithospheric magnetic field models using satellite data and equivalent point sources

The global lithospheric field models of this thesis are based on three-component vector data from the CHAMP satellite. Data within the polar gap regions are represented by CHAOS-6 estimates (Finlay et al., 2016a) for the radial field component at 300 km altitude. Section 3.1 starts with a brief introduction to geomagnetic satellite data and mission highlights of the last century. The CHAMP data used, including data error estimates, are presented in section 3.2. Further, the considerations for determining both an appropriate source amount and depth for the global lithospheric field models are given in section 3.3. The effect of polar gaps on global field models based on equivalent sources is found to be limited to regions lacking data. A short discussion of this is given in section 3.4. The remaining part of this chapter focuses on the models derived using the different regularization schemes that were presented in chapter 2. The results are compared to each other and state-of-the-art models MF7 (Maus et al., 2008; Maus, 2010), CHAOS-6 (Finlay et al., 2016a) and CM5 (Sabaka et al., 2015). The comparison is grounded in global and regional field maps, as well as misfit statistics, degree/order matrices, power spectra and degree correlations. A summary of this chapter is given in section 3.9.

Note that the map projections of the presented models are the direct output of the corresponding monopole values rather than an approximation based on a truncated SH expansion.

It should further be noted that the derived models are slightly different from the results of Kother et al. (2015). These differences are due to several factors: a) This thesis works with equal area spaced sources rather than sources placed on an icosahedral grid. b) The source depth of the presented models is 80 km deeper than in the paper version. c) More sources are used in the thesis version. d) A more recent version of the CHAOS model is used for generating synthetic polar gap data and the data error values. e) The large differences in regularization parameters are due to the difference of units used: $g_{ik} = -\hat{\mathbf{e}}_i \cdot \nabla \frac{1}{r_{ik}}$ with source unit being $nT \cdot km^2$ (paper code version) and $g_{ik} = -\hat{\mathbf{e}}_i \cdot \nabla \frac{r_k^2}{r_{ik}}$ with source units in nT (see equation 103).

The global lithospheric field models of this thesis are generated using MATLAB® version 2013a at the DTU Space HPC cluster. Depending on the cluster occupation, the calculation time for one iteration varies between approximately 7 and 36 hours (amount of iterations needed for the final models mono-QR, mono-ER and mono-L1 is 5, 2 and 4, respectively), with the longest time spent on the derivation of $\underline{\underline{\mathbf{G}}}^T \underline{\underline{\mathbf{WG}}}$. The validity of the used mathematical codes has been verified by visual inspection of the derived field prediction maps and by comparison of the respective statistics with already existing lithospheric field models.

3.1 Geomagnetic satellite data

The global coverage of geomagnetic satellite data has contributed enormously to our current knowledge of the geomagnetic source fields, especially the main field and large-wavelength lithospheric field. Regarding the latter, satellites have some advantages compared to near-surface surveys. They provide a global data distribution and are capable of covering large regions of the Earth within a relative short amount of time. Also the prominent data processing problems along survey boundaries vanish when using satellite measurements.

Satellites follow elliptical orbits (with the Earth being in one of the two focus points) with orbital periods ranging typically between 90 and 200 minutes (Langel and Hinze, 1998). Thus, the orbital shape is defined by the ellipse's apogee and perigee points (farthest and closest to the Earth, respectively) as well as the satellite orbit inclination. The latter represents the angle between the Earth's equatorial plane and the satellite path. Thus, a complete global data coverage can only be provided for an inclination of 90 degrees. The magnetometers carried by satellites are of the fluxgate or the proton precession type, sometimes both. The latter, also denoted as scalar magnetometers, measure the field strength only and are not dependent on the information of the satellite's orientation in space. A fluxgate magnetometer, however, is designed to measure the complete vector field. Thus, in order to interpret the respective measurements correctly, it is crucial to know the accurate magnetometer orientation in space. Today this directional information is provided by satellites' on-board star camera observations which are compared with known constellations of fix stars.

The first observations of the Earth's magnetic field from space were provided by *Sputnik 3*. The soviet satellite, launched in 1958, provided three-component geomagnetic measurements with an accuracy of approximately 100 nT for the area of Soviet Union (Langel and Hinze, 1998). Several geomagnetic satellite missions followed, improving both the satellite technology, data quality and coverage. Regarding major contributions to lithospheric field studies, it is worth mentioning *Cosmos 49* (1964), three of the six *POGO* satellites (OGO-2 (1965), OGO-4 (1967) and OGO-6 (1969)) and *Magsat* (1979). While *Cosmos 49* and *POGO* provided measurements for the magnetic field magnitude, the *Magsat* spacecraft was capable of measuring both magnetic field magnitude and direction. Compared to previous missions, POGO and Magsat had the great advantage of on-board data recording devices which enabled full-orbit data coverage (Langel and Hinze, 1998).

The 21st century has been a new era for geomagnetic satellite measurements. Initiated by the launch of the Ørsted satellite in 1999, the International Decade of Geopotential Field Research inspired additional two satellite missions in 2000: CHAMP and Ørsted-2/SAC-C (Friis-Christensen et al., 2008). All three missions provided high-precision geomagnetic data and contributed valuable new knowledge of the Earth's magnetic field. However, being single-satellite missions, none of the generated data was capable in representing the dynamical behaviour of the geomagnetic sources with sufficient accuracy (Thomsen et al., 2003). This fact created the idea of the Swarm mission: Multiple satellites operating at different altitudes and simultaneously recording the geomagnetic vector field at low-Earth, near-polar orbits. The mission was proposed to ESA in 2001, and selected as part of ESA's Earth Explorer Programme in 2004 (Friis-Christensen et al., 2006). The final constellation comprised three identical satellites: *Swarm Alpha*, *Swarm Charlie* and *Swarm Beta*. *Swarm Alpha* and *Swarm Charlie* are flying side-by-side, which is especially favourable for studies of ionospheric currents (Friis-Christensen et al., 2006) and north-south oriented lithospheric features (Olsen et al., 2004), while *Swarm Beta* operates at higher altitude with approximately 3h local time separation. The corresponding initial altitudes were 514 km and 531 km, respectively (Finlay et al., 2016a). But also core field models benefit from the satellite trio, as the constellation enables high resolution models of the secular variation and acceleration which in turn provide insight into the fluid core dynamics (Livermore et al., 2017). Thousands of scientists and enthusiasts followed the launch of the satellite trio on 22/11/2013.
Swarm provides high-precision and high-resolution measurements of the geomagnetic field and its temporal evolution using state-of-the-art navigation, accelerometers and electric field measurements. Combined with the low-altitude orbits, lithospheric field models based on Swarm data are expected to have unprecedented high resolution. So far, the satellite altitudes are still too high for being directly used for lithospheric field modelling (about 450 km). However, Kotsiaros (2016) has demonstrated that vector gradient Swarm data provide lithospheric field models of quality comparable to those based on low-orbit single-missions.

3.2 CHAMP data

The German Challenging Minisatellite Payload (CHAMP) mission, managed by the GeoForschungsZentrum Potsdam (GFZ), was the first of its kind for simultaneous gravity and magnetic field measurements (Reigber et al., 2000). Besides geopotential data, the satellite provided atmospheric and ionospheric information from GPS radio occultation measurements (Reigber et al., 1999).
The satellite was launched on 15/07/2000 designed for a five years mission. Reentry in the atmosphere, however, did not occur till 19/09/2010. CHAMP operated in an almost circular, low Earth orbit with an initial altitude of 454 km. Except for a small range of altitude corrections, the satellite dropped its altitude gradually to values below 340 km in the last period of the mission. The low orbit at the end of its life time makes the CHAMP data especially interesting for lithospheric field investigations.
The current study uses three-component vector data (with a sampling interval of 30 sec) between 01/01/2009 and 02/09/2010. During that period the satellite was at its lowest altitude (below 340 km) and the solar activity was rather low. However, a disadvantage of this low altitude is that the satellite is located within the ionospheric F-region, measuring ionospheric field contributions as internal signals which result in non-potential field conditions. Thus, in order to use the potential field theory for describing the geomagnetic vector field, data measurements have to be selected carefully in order to minimize the influence of ionospheric fields. This is done by selecting data for quiet-time conditions (Kp-index $\leq 2^0$ for quasi-dipole (QD) lati-

tudes equatorward of $\pm 55°$ and the merging electric field at the magnetopause Em $\leq 0.8\frac{mV}{\text{m}}$ for QD latitudes poleward of $\pm 55°$) and dark regions (sun at least 10° below the horizon). Additionally, magnetospheric ring current effects are reduced by only selecting data with hourly RC-index variations smaller than $2\frac{nT}{hr}$ (Olsen et al., 2014). The remaining data selection follows the same criteria as employed in CHAOS-4 (Olsen et al., 2014, 2006). Additionally, data with gross outliers are removed in order to prevent strongly correlated noise from disturbed satellite tracks to effect the lithospheric field models, see Appendix C. The total amount of 3-component satellite vector data is 410,914. The polar gap regions are additionally represented by 12,257 synthetic CHAOS-6 radial field values, see section 3.4.
The final amount of data used for global lithospheric field models of this thesis is thus $3 \cdot 410,914 + 12,257 = 1,244,999$.

3.2.1 Latitude dependent data errors

Recalling equation (1), the observed geomagnetic vector field $\mathbf{B}^{obs}$ from satellite measurements comprises contributions from the core field $\mathbf{B}^{core}$, lithospheric field $\mathbf{B}^{lit}$, external fields $\mathbf{B}^{ext}$ as well as measurement errors $\boldsymbol{\epsilon}^{obs}$,

$$\mathbf{B}^{obs} = \mathbf{B}^{core} + \mathbf{B}^{ext} + \mathbf{B}^{lit} + \boldsymbol{\epsilon}^{obs}. \tag{86}$$

In order to determine the lithospheric signal, core field and external field contributions are removed from the observations by means of CHAOS-6 model estimates $\widetilde{\mathbf{B}}^{core}$ and $\widetilde{\mathbf{B}}^{ext}$ which introduce the corresponding estimation errors $\widetilde{\boldsymbol{\epsilon}}^{core}$ and $\widetilde{\boldsymbol{\epsilon}}^{ext}$. The lithospheric part of the measurements is thus given by

$$\begin{aligned}
\mathbf{B}^{lit} &= \mathbf{B}^{obs} - (\widetilde{\mathbf{B}}^{core} + \widetilde{\mathbf{B}}^{ext} + \boldsymbol{\epsilon}^{obs} + \widetilde{\boldsymbol{\epsilon}}^{core} + \widetilde{\boldsymbol{\epsilon}}^{ext}) && \text{(87a)}\\
&= \mathbf{B}^{obs} - \widetilde{\mathbf{B}}^{core} - \widetilde{\mathbf{B}}^{ext} - \boldsymbol{\epsilon}_{error} && \text{(87b)}\\
&= \mathbf{A}^{obs} - \boldsymbol{\epsilon}_{error} && \text{(87c)}\\
\mathbf{A}^{obs} &= \mathbf{B}^{lit} + \boldsymbol{\epsilon}_{error} && \text{(87d)}
\end{aligned}$$

where $\boldsymbol{\epsilon}_{error}$ combines both measurement and model errors. Thus, the observed lithospheric field $\mathbf{A}^{obs}$ contains also signals which are not based in geological features but rather in inefficient source separation and measurement errors. The accuracy of $\mathbf{A}^{obs}$ is thereby dependent on the estimated models and their ability to describe the field contributions of non-lithospheric origin. Assuming that the "true" lithospheric signal $\mathbf{B}^{lit}$ can be approximated with CHAOS-6 model estimates of the magnetic anomaly field $\mathbf{A}^{CHAOS}$ (for SH degrees $n = 16$ to 120), the data uncertainties $\boldsymbol{\sigma}$ (see Fig.9) can be estimated using the residuals $\boldsymbol{\epsilon} = \mathbf{A}^{obs} - \mathbf{A}^{CHAOS}$ for an approximation of $\boldsymbol{\epsilon}_{error}$. Corresponding covariance matrices are derived by means of the residual mean values $\overline{\boldsymbol{\epsilon}}$ in 2° QD latitudinal bands with the robust algorithm of Driessen and Rombouts (2007). For a given band x which comprises the data indexes $\mathbf{i}$ it yields

$$\begin{aligned}
\overline{\boldsymbol{\epsilon}}_x &= \boldsymbol{\epsilon}(\mathbf{i}) - mean(\boldsymbol{\epsilon}(\mathbf{i}))\\
\underline{\underline{\mathbf{C}}}_x &= cov(\overline{\boldsymbol{\epsilon}}_x)\\
\boldsymbol{\sigma}_x &= \sqrt{\text{diag}(\underline{\underline{\mathbf{C}}}_x)}
\end{aligned} \tag{88}$$

Thus, data values within a given QD latitudinal band are assigned the same uncertainty (standard derivation). Note, that the hemispheric asymmetry in Fig.9 corresponds to an observed phenomenon of the Earth's magnetic field (Laundal et al., 2017).
The QD latitudes are determined using equation (15) of Emmert et al. (2010) and QD Apex coefficients for the period 1995-2015. The QD coordinate system is suitable for describing processes due to unmodelled ionospheric sources, which are assumed to have a major contribution to the derived model residuals (see for instance Fig. 37), especially at polar latitudes.

3.3 Equivalent source distribution for global lithospheric field models

The equivalent sources used for lithospheric field models in this thesis (both global and regional) are distributed on an equal area grid at a certain depth below the Earth's surface, see Fig. 10. The grid is computed

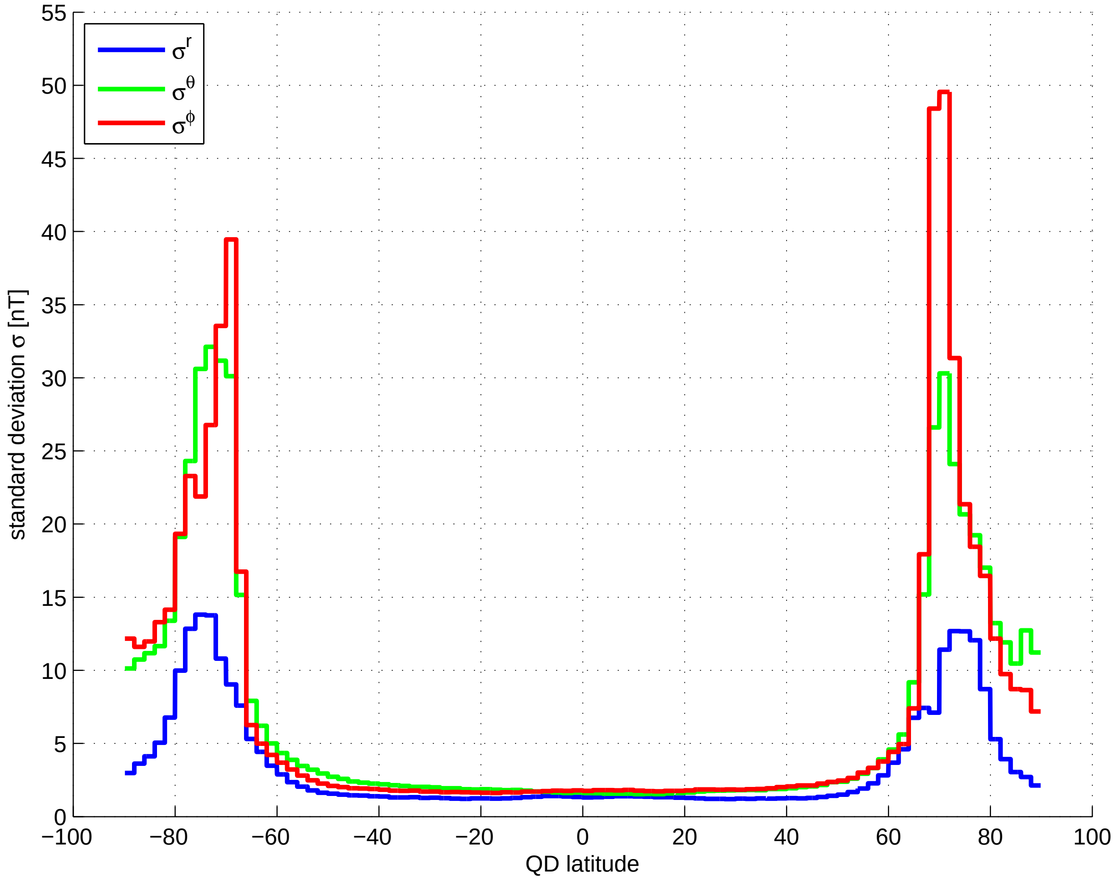

Figure 9 Latitudinal error values for the applied global lithospheric field data from CHAMP.

with a MATLAB® routine based on Saff (2005) and kindly provided by E. Thébault.
Table 2 lists different source grid sizes and corresponding median angular distances d_a between two adjacent sources. The latter are calculated from the distance between each source and its nearest neighbor. Corresponding horizontal distances at the Earth's surface d_s are approximated by dividing the spherical Earth's area with a given amount of globally distributed sources K_g, $d_s = a\sqrt{4\pi/K_g}$, where $a = 6371.2\,\text{km}$ is the Earth's mean radius. Using $n = \frac{2\pi r}{\lambda}$ (based on an approximation of equation (20) for large values of n), the distance d_s (corresponding to a horizontal half wavelength) can be transformed into the respective spherical harmonic degree.
Similar to SH and the other methods mentioned in section 1.3, the monopole representation of the magnetic field is based on harmonic functions. Since the equivalent source potential is undefined for $r_{ik} = 0$, see equation 27, the distance between sources and measurements must be larger than zero. The value should also be larger than the distance between adjacent sources in order to avoid ringing effects in the generated field maps.

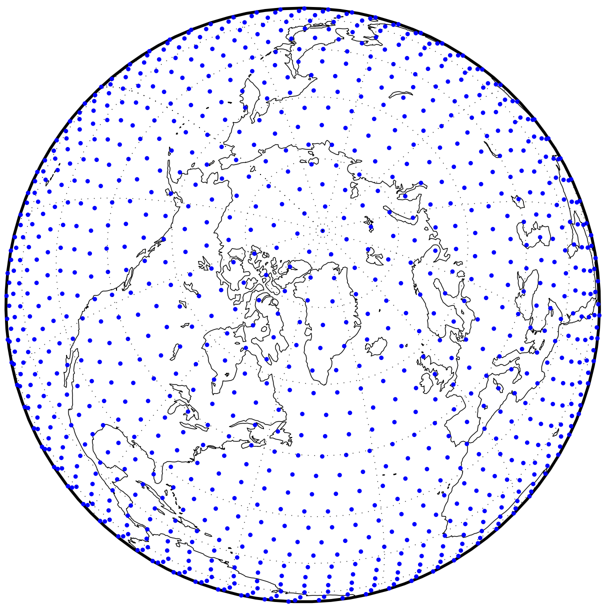

Figure 10 Global source distribution of $K_g = 2000$ equal area spaced sources.

K_g	d_a [deg]	d_s [km]	SH degree
10,000	2.03	225.85	88.62
15,000	1.66	184.41	108.54
30,000	1.17	130.39	153.49
30,722	1.16	128.85	155.33
38,600	1.03	114.96	174.12
45,000	0.96	106.47	187.99
51,000	0.89	100.01	200.14
65,000	0.79	88.59	225.94

Table 2 Global source amount K_g and corresponding median angular distances d_a, surface distances d_s and SH degrees.

3.3.1 Source grid resolution

A horizontal surface distance of approximately 100 km between adjacent sources is expected to be sufficient to represent lithospheric satellite measurements at approximately 300 km altitude. In order to define an appropriate source grid for the global lithospheric field models, un-regularized inversions are computed for five different grid sizes with corresponding surface source distances around 100 km (K_g = 30722, 38600, 45000, 51000, and 65000) and for depth values between 20 km and 200 km. To limit the computation time, only the magnetic field intensity values (scalar data) corresponding to the North American region (ranging from -140 to 60 degrees longitude and from 10 to 60 degrees latitude) of the CHAMP data set are used. The resulting amount of data is 26,009, compared to the original three-component vector data amount of $3 \cdot 410,914$.

The two lowest grid resolutions investigated (K_g = 30722, 38600) result in converging solutions for all investigated depths. Models for $K_g = 45000, 51000, 65000$ converge up to a source depth of 180 km, 140 km, and 80 km, respectively. This is expected from the previous investigations of O'Brien and Parker (1994).

Figure 11 illustrates the derived model misfit statistic by means of the Huber-weighted residual 2-norm and corresponding normalized Huber-weighted residual RMS. Based on these results, no major model improvements can be achieved beyond a global distributed source amount of $K_g = 38,600$, which henceforth is the used grid size for the global lithospheric field models of this thesis. The corresponding median angular distance is $d_a = 1.03°$ which means approximately 115 km distance between two adjacent sources at the Earth's surface. The respective spherical harmonic degree extension is $n = 174$.

3.3.2 Source grid depth

Similar to Ravat et al. (2002), an appropriate source depth for the global lithospheric field models may be found by investigating the residuals derived from un-regularized model inversions of different source depth values. Unfortunately, using equivalent source values generated from the un-regularized inversion scheme, downward continuation of the lithospheric field results in unrealistic large values due to contamination of the short-wavelength fields in the original data set. To prevent this amplification of short wavelength noise, all presented models in this section are derived using quadratic regularization with $\alpha = 900\,\text{nT}^{-2}$.

Equivalent source values have been derived for four different source depths (100 km, 140 km, 180 km and 220 km) using quadratic regularization and the North American region of the three-component CHAMP data set. In order to speed up these tests, only sources with an angular distance of maximal 0.89° to the closest data point are taken into account for the respective model derivations The total number of equivalent sources is thereby reduced from $K_g = 38600$ to $K = 3345$.

The middle part of Fig. 12 illustrates the radial component of the modeled lithospheric field values at data altitude corresponding to an equivalent source depth of 180 km. The right part of the figure indicates that large residual values are mainly caused by uncorrected noise in individual orbits and regions of the auroral oval. As indicated by the similar model statistics in Table 3, the respective figures for the other source depth values (not given here) are very similar.

	100 km	**140 km**	**180 km**	**220 km**
RMS ΔB_r	1.475	1.478	1.481	1.487
RMS ΔB_θ	1.562	1.563	1.563	1.564
RMS ΔB_ϕ	1.316	1.316	1.317	1.319

Table 3 Normalized (by latitude-dependent standard deviation values) RMS values of the *Huber*-weighted residuals between the regional CHAMP observations and quadratic regularized models using $\alpha = 900\,\text{nT}^{-2}$ and different equivalent source altitudes. The used source amount of $K = 3345$ corresponds to a global distribution of $K_g = 38600$ equal area spaced sources.

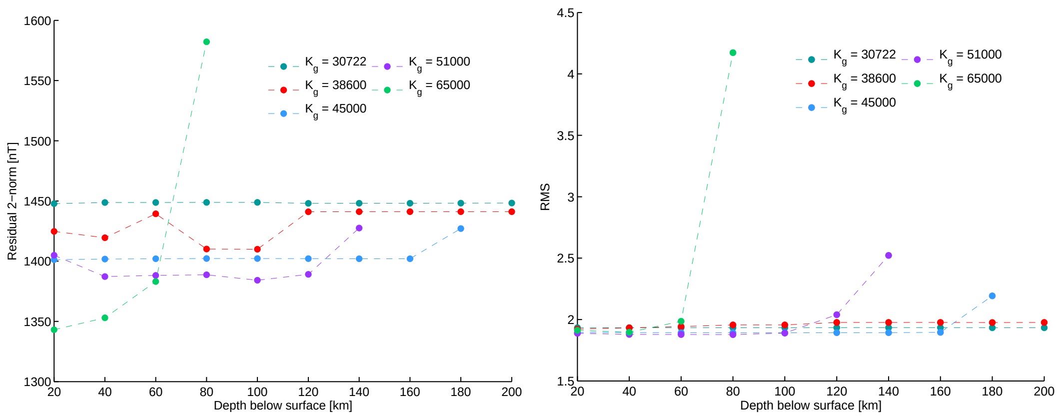

Figure 11 Misfit statistics for the un-regularized equivalent source models corresponding to CHAMP lithospheric intensity data of the North American region. For different grid sizes and source depth values the figure shows *Huber*-weighted residual 2-norm (left) and normalized RMS values of the *Huber*-weighted residuals (right). The chosen grid size of $K_g = 38600$ is given in red.

In order to ease comparison between models of different source depths, the source values are downward continuated to the Earth's surface. Fig. 14 illustrates the corresponding results for the radial field component using the regularizetion parameter $\alpha = 900\,\mathrm{nT}^{-2}$. The general lithospheric behavior is present in all four models. However, distinct north-south striping features appear in the Pacific. According to Fig. 13 these structures are not caused by the used source locations but probably by unmodeled field signals still present in the data. Fig. 14 shows also a clear positive correlation between the amplitude of these structures and the used equivalent source depth. This is, however, also dependent on the type of regularization and the regularization parameters used.
It is noteworthy that deep source locations act as a kind of regularization, as they enhance the long wavelength structures of the lithospheric field. The sources should not be placed too deep in order to represent the satellite measurements, and not too shallow for preventing source signatures on the resulting field maps. Since this is the case for the investigated models, the final source depth for model predictions based on satellite measurements can be chosen below 100 km, as unwanted surface field structures can be avoided using the correct choice of regularization parameter. The source depth used for model predictions based on satellite measurements is henceforth defined to be 180 km. With the regularization parameters used in this section, the surface models reflect the main features of the lithosphere. The striping in the oceanic regions is reduced significantly compared to shallower source depth models. Source values deeper than 180 km risk removing important short wavelength information from the derived models. The precise choice pf depth is not crucial, given our use of regularization to control the power of small length scales, see also O'Brien and Parker (1994) for a range of acceptable depths.

Chapter 4 describes the routine used to determine an appropriate source grid size and depth for regional lithospheric field models based on aeromagnetic data.

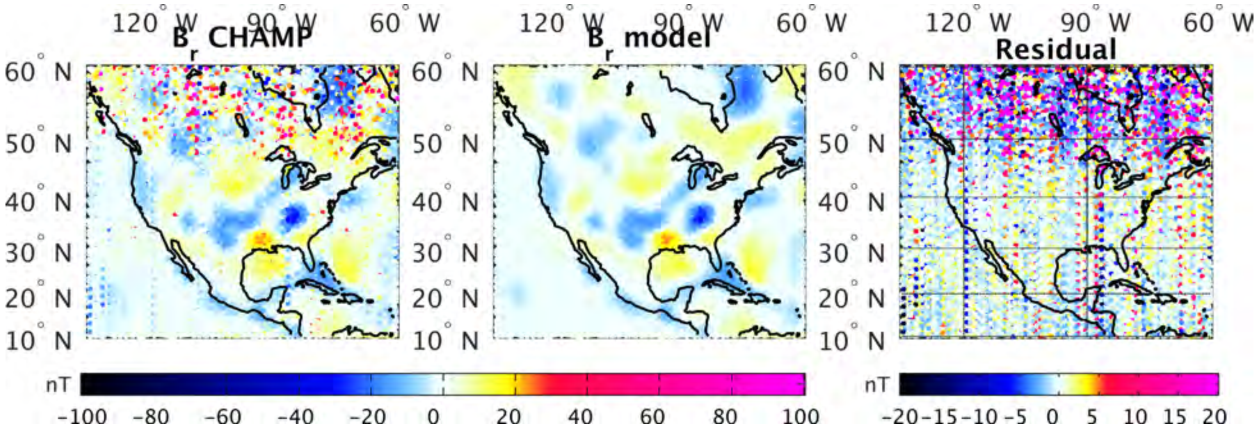

Figure 12 Lithospheric radial magnetic field values corresponding to the CHAMP measurements used (left). The respective model predictions at data altitude (middle) are based on 3345 (corresponding to $K_g = 38,600$) equivalent sources at 180 km depth and quadratic regularization with $\alpha = 900\,\mathrm{nT}^{-2}$. The resulting radial residuals are given in the right part of the figure (note the change of scale). The corresponding normalized (by the latitudinal varying data error) Huber-weighted model residual RMS is 1.48 nT, 1.56 nT and 1.32 nT for the radial, latitudinal and longitudinal field component, respectively. The derived max, min and mean values for the radial residuals are 394 nT, −428 nT and 0.79 nT, respectively.

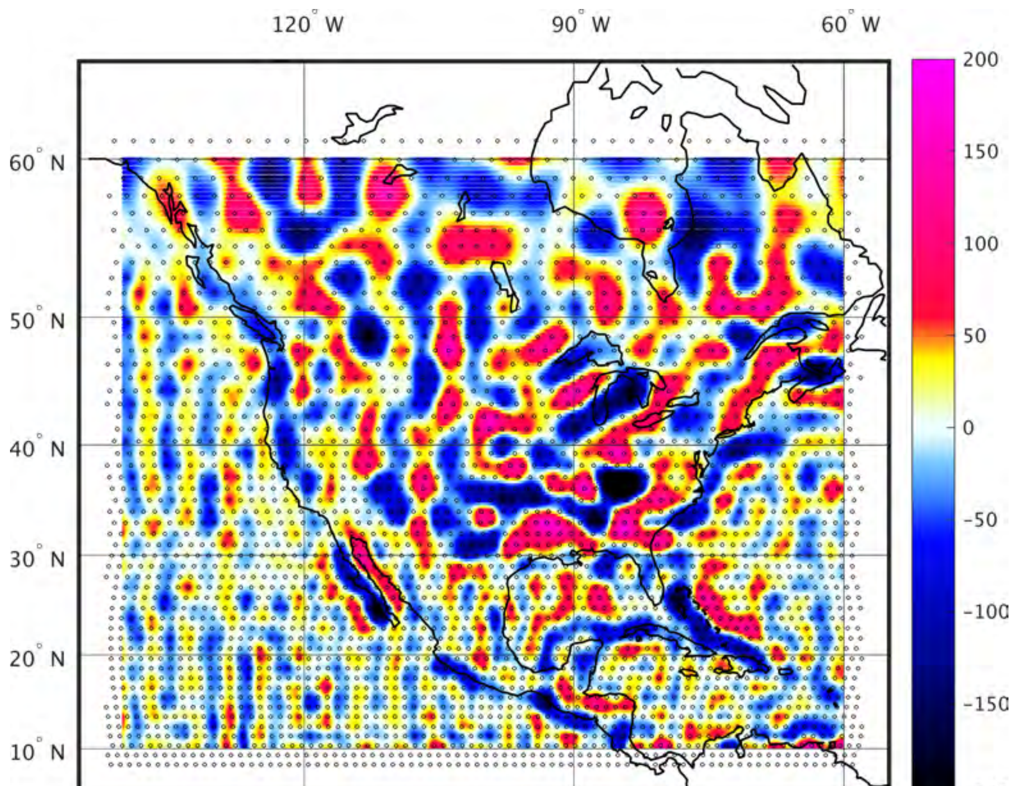

Figure 13 Modelled lithospheric radial magnetic field values at the Earth's surface on a 0.25 degree grid. The respective 3345 (corresponding to $K_g = 38,600$) equivalent source values (black circles) are located at 100 km depth and were derived using regional three-component CHAMP vector data and quadratic regularization with $\alpha = 900\,\mathrm{nT}^{-2}$. The colorbar is given in units of nT. Note that this figure is identical to the upper left part of Fig.14.

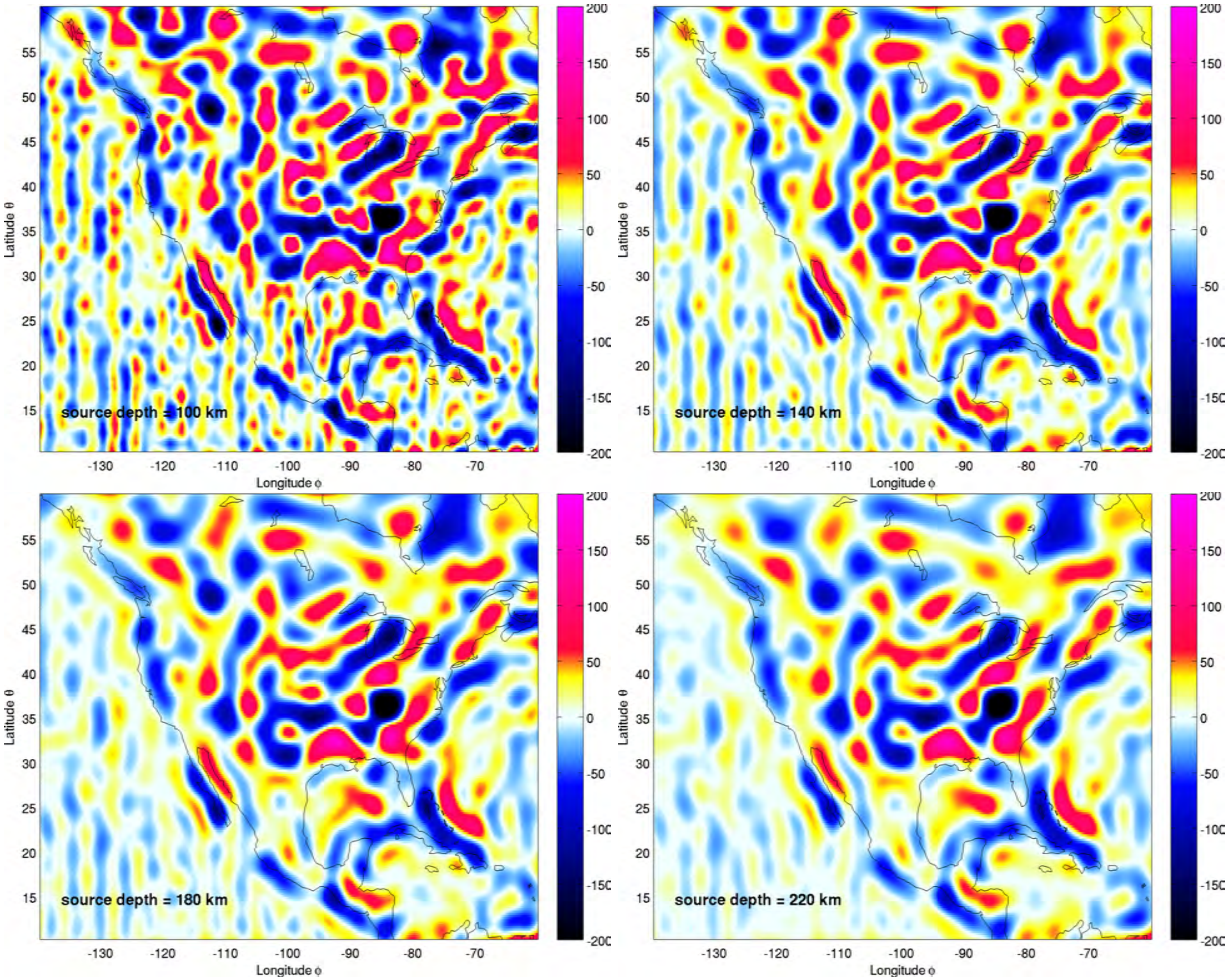

Figure 14 Modelled lithospheric radial magnetic field values at the Earth's surface on a $0.25^\circ \times 0.25^\circ$ grid. The respective 3345 (corresponding to $K_g = 38,600$) equivalent source values are located at 100 km (upper left), 140 km (upper right), 180 km (lower left) and 220 km (lower right) depth and were derived using regional CHAMP vector data and quadratic regularization with $\lambda = 900nT^{-2}$. The colorbar is given in units of nT.

3.4 Polar data gap problem

From an engineering and fuel efficiency perspective, it is more favorable to navigate satellites in near-polar orbits, that involve caps of lacking measurements around the geographic poles, a phenomenon known as "polar gap" (Sneeuw and Van Gelderen, 1997; Simons and Dahlen, 2006). A satellite crossing the poles will rapidly be knocked out of its fixed plane due to the bulge of the equator (the Earth's Bessel function). This is advantageous as it causes satellites to drift in local time, which is necessary to place satellites in sun-synchronous orbits.

Potential field models are often based on spherical harmonic (SH) functions and thereby badly effected by polar gaps, as these are global functions dependent on equally spaced measurements over a sphere. Polar gap effects on potential fields can be seen in both the spatial and spectral domain (Sneeuw and Van Gelderen, 1997). The latter describes instabilities within the low order and zonal spherical harmonic coefficients.

Polar gaps are defined by a half-angle of $|90 - i|$, where i is the satellite orbit inclination.

Since both geodesy and geomagnetism are potential field disciplines, various approaches for dealing with the polar gap effect have been investigated within both communities. One attempt to circumvent the problem has been to fill the satellite data gap with airborne or marine measurements (Koenig et al., 2010).

This thesis always uses measurements from the CHAMP satellite. The corresponding tracks are defined by a near polar orbit with an inclination of 87.3°. The resulting polar gap of 2.7° is counteracted with radial synthetic geomagnetic data in the polar regions for $\theta > 176°$ and $\theta < 4°$ co-latitude. The respective synthetic values are derived on a $0.5° \times 0.5°$ grid using CHAOS-6 model prediction for SH degree $n = [16 : 60]$ at 300 km altitude. The resulting $12,257$ data values represent 2.89% of the total radial data set.

Note that the chosen synthetic data area overlaps with the original measurements, as the latter have a co-latitudinal range of $2.77 - 177.23°$.

Polar gap effect on equivalent source models

In order to investigate the polar gap effect on the equivalent source approach, two synthetic data sets ($\mathbf{d}_{PG}$ and $\mathbf{d}_{all}$) are generated for the north polar region using the CHAOS-6 model up to SH degree $n = 15$ and $n = 60$ for the core field and lithospheric field, respectively. The data altitude is 300 km above the surface and the data interval is 0.5° in both latitudinal and longitudinal directions, resulting in 37,492 three-component geomagnetic field values for co-latitudes $4° < \theta < 30°$. Data set $\mathbf{d}_{all}$ is additionally characterized by 5768 radial field component values for $4° > \theta$, see Fig. 15. In the latter case, the polar gap values account for 13.3 % of the total radial data set.

Since the synthetic data are assumed noise free, all corresponding error values σ are set to unity.

Using the described data above, two un-regularized models are derived ($\mathbf{q}_{all}$ and $\mathbf{q}_{PG}$). The corresponding source depth and global source amount are 180 km and $K_g = 38,600$, respectively. However, since only regional data values are used, only sources for co-latitudes below 35° are taken into account, reducing the total source amount to $K = 3432$.

Figure 16 illustrates the model predictions for the radial magnetic field at the Earth's surface. The right panel of the figure shows that the model differences are limited to the region 0 to 5° co-latitude, which is one degree larger than the tested polar gap region. It is thus concluded that polar data gaps affect equivalent source based models only in a region which is 25% larger than the gap area.

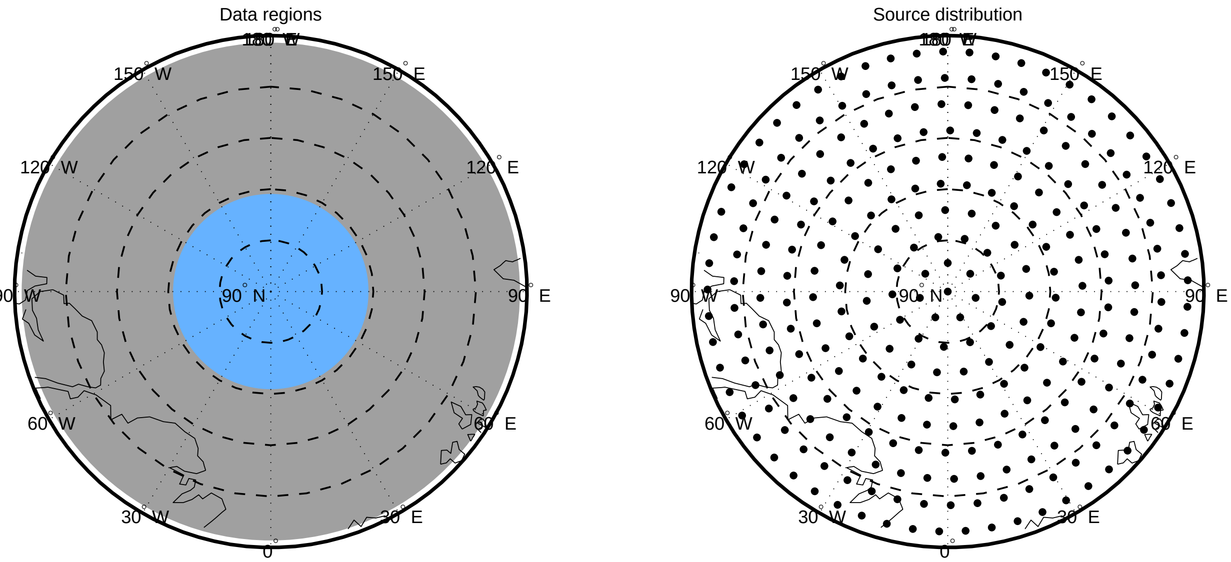

Figure 15 The investigated equivalent source models $\mathbf{q}_{all}$ and $\mathbf{q}_{PG}$ are both based on 3-component synthetic vector data for co-latitude values $4^\circ < \theta < 30^\circ$ (gray area). The first model uses additionally synthetic radial magnetic field data at polar regions (blue area) for $4^\circ > \theta$. The right part of the figure illustrates the source distribution used for co-latitudes below 35°. The latitudinal grid line spacing is 2°.

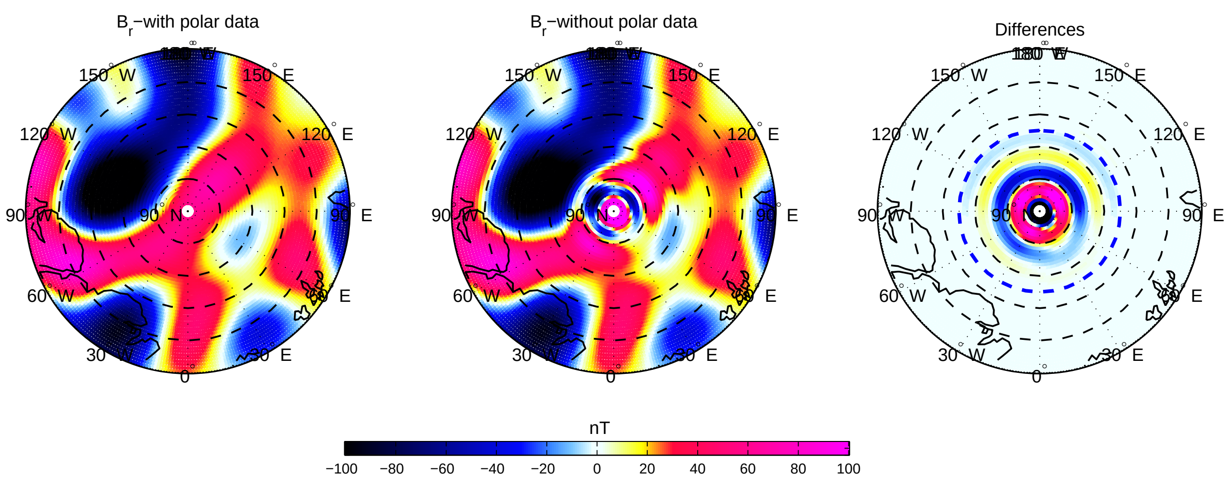

Figure 16 Model predictions (given on a grid of 0.1° latitudinal and 2° longitudinal spacing) of the radial geomagnetic field at the Earth's surface for $\mathbf{q}_{all}$ (left) and $\mathbf{q}_{PG}$ (middle). The corresponding differences (right) are negligible for co-latitudes larger than 5 degrees (blue stipled line). The latitudinal grid line spacing is 2°.

3.5 Quadratic regularized model results

Using $K_g = 38,600$ globally distributed equal area spaced sources at 180 km depth, a wide range of models with different quadratic regularization (QR) parameters are investigated. As described in section 2.8.1, all quadratic regularized models share the same initial equivalent source values and initial *Huber* weights. The former are set to the values obtained in a well-converged but un-regularized ($\alpha = 0$) model solution, while the initial weights are all set to unity. After model convergence (see equation (59)), the derived source values for the different models are transformed into the spherical harmonic Gauss coefficients g_n^m and h_n^m using equations (40) and (41). The resulting power spectra are given in Fig. 17 and compared to the state-of-the-art models CM5 (Sabaka et al., 2015), MF7 (Maus et al., 2008; Maus, 2010) and CHAOS-6 (Finlay et al., 2016a). The figure illustrates clearly the effect of the regularization parameter: increasing values lead to less power for the short wavelength lithospheric features. But despite the very different behavior in power spectra, the investigated QR models share very similar global misfits as given in Table 4 with differences seen mainly in the third and fourth decimal. Here, the different model performances are compared by means of the *Huber*-weighted residual mean values and the normalized *Huber*-weighted root mean square values for the entire data set as well as separately in polar and non-polar regions. The normalization is reached by dividing the residuals with the measurement error standard deviations of Fig. 9. The last two rows of the table give the degree correlation $\rho(n)$ with CHAOS-6 and MF7 for $n = 100$. Apart from model statistics and power spectra, the latter offers an additional method to compare between two different lithospheric field models (having different sets of Gauss coefficients, $[g_n^m, h_n^m]$ and $[g_n^{'m}, h_n^{'m}]$) (Langel and Hinze, 1998, eq. 4.23),

$$\rho(n) = \frac{\sum_{m=0}^{n}(g_n^m g_n^{'m} + h_n^m h_n^{'m})}{\sqrt{\sum_{m=0}^{n}[(g_n^m)^2 + (h_n^m)^2]\sum_{m=0}^{n}[(g_n^{'m})^2 + (h_n^{'m})^2]}}. \tag{89}$$

According to the model misfit statistics, the quadratic regularized model with $\alpha = 30\,\mathrm{nT}^{-2}$ is a good candidate to represent the measurements as it results in the lowest RMS values and the highest degree correlation value for $n = 100$ with respect to both CHAOS-6 and MF7. However, looking at the corresponding power spectrum of Fig. 17, the model seems to give too much power to SH degrees larger than $n > 90$ if compared to MF7, CHAOS-6 and CM5. Differences in power between the latter three models and the investigated QR models as well as the corresponding degree correlation coefficients are given in Fig. 18. Whenever $\rho \geq 0.7$, models are usually considered to be well correlated (Arkani-Hamed et al., 1994; Sabaka and Olsen, 2006). This value is reached at approximately $n = 105$ for the degree correlation between all QR models and CHAOS-6, and at approximately $n = 100$ for the degree correlation between all QR models and MF7. The degree correlations for the different QR models are remarkably similar.

A typical method to determine a reliable regularization parameter is by means of the L-curve (Hansen, 1998), which is given in Fig. 19. The most favorable value for α, providing a balanced treatment of model complexity and misfit, is found in the vicinity of the corresponding knee-point. The quadratic regularization models with $\alpha = 80\,\mathrm{nT}^{-2}, 100\,\mathrm{nT}^{-2}$ and $200\,\mathrm{nT}^{-2}$ are closest to the curve's knee point and are compared by means of plotting the corresponding radial and intensity field maps at the Earth's surface and at 300 km altitude. Respective figures are given in Appendix D.1. Minor model differences can be seen only for the field maps at the Earth's surface, where the increase in regularization parameter leads to a decrease in amplitude, especially in oceanic regions. Compared to the field maps of MF7, CHAOS-6 and CM5, all three QR models show similar lithospheric structures but of generally lower amplitudes as α is increased.

Based on a combination of the above observations, the quadratic regularized model with $\alpha = 80\,\mathrm{nT}^{-2}$ is selected on balance to be the preferred QR model of this study. The corresponding notation is henceforth *mono-QR*. The upper part of Fig. 29 illustrates the corresponding radial field map at the Earth's surface.

$\boldsymbol{\alpha}$ (nT^{-2})	30	50	80	100	200	500
mean ΔB_r (nT)	-0.0703	-0.0694	-0.0685	-0.0681	-0.0667	-0.0642
RMS ΔB_r (-)	1.2883	1.2886	1.2890	1.2892	1.2899	1.2903
RMS ΔB_r polar (-)	1.4301	1.4303	1.4304	1.4305	1.4309	1.4300
RMS ΔB_r non-polar (-)	1.1814	1.1819	1.1824	1.1827	1.1837	1.1851
mean ΔB_θ (nT)	-1.3427	-1.3432	-1.3437	-1.3439	-1.3449	-1.2906
RMS ΔB_θ (-)	1.2627	1.2628	1.2629	1.2630	1.2631	1.2641
RMS ΔB_θ polar (-)	1.3798	1.3798	1.3798	1.3799	1.3799	1.3805
RMS ΔB_θ non-polar (-)	1.1747	1.1748	1.1750	1.1751	1.1753	1.1766
mean ΔB_ϕ (nT)	-0.3625	-0.3623	-0.3622	-0.3621	-0.3617	-0.3614
RMS ΔB_ϕ (-)	1.2727	1.2729	1.2730	1.2731	1.2734	1.2736
RMS ΔB_ϕ polar (-)	1.4266	1.4266	1.4267	1.4267	1.4268	1.4263
RMS ΔB_ϕ non-polar (-)	1.1548	1.1551	1.1554	1.1555	1.1560	1.1568
RMS ΔB (-)	1.2746	1.2748	1.2750	1.2751	1.2755	1.2760
RMS ΔB polar (-)	1.4123	1.4123	1.4124	1.4125	1.4126	1.4124
RMS ΔB non-polar (-)	1.1704	1.1707	1.1710	1.1712	1.1717	1.1729
$\rho_{n=100,CHAOS6}$ (-)	0.7445	0.7332	0.7362	0.7365	0.7343	0.7274
$\rho_{n=100,MF7}$ (-)	0.6872	0.6465	0.6521	0.6536	0.6544	0.6499

Table 4 Huber-weighted residual mean values and Huber-weighted model residual RMS values (normalized by the latitudinally varying error estimates of Fig. 9) for the different investigated QR models at satellite altitude. Here, $\Delta B = \sqrt{\Delta B_r^2 + \Delta B_\theta^2 + \Delta B_\phi^2}$ and the suffixes "polar" and "non-polar" represent data of absolute QD latitudes $\geq 55^\circ$ and $< 55^\circ$, respectively. The last two rows give the degree correlation with CHAOS-6 and MF7 for $n = 100$.

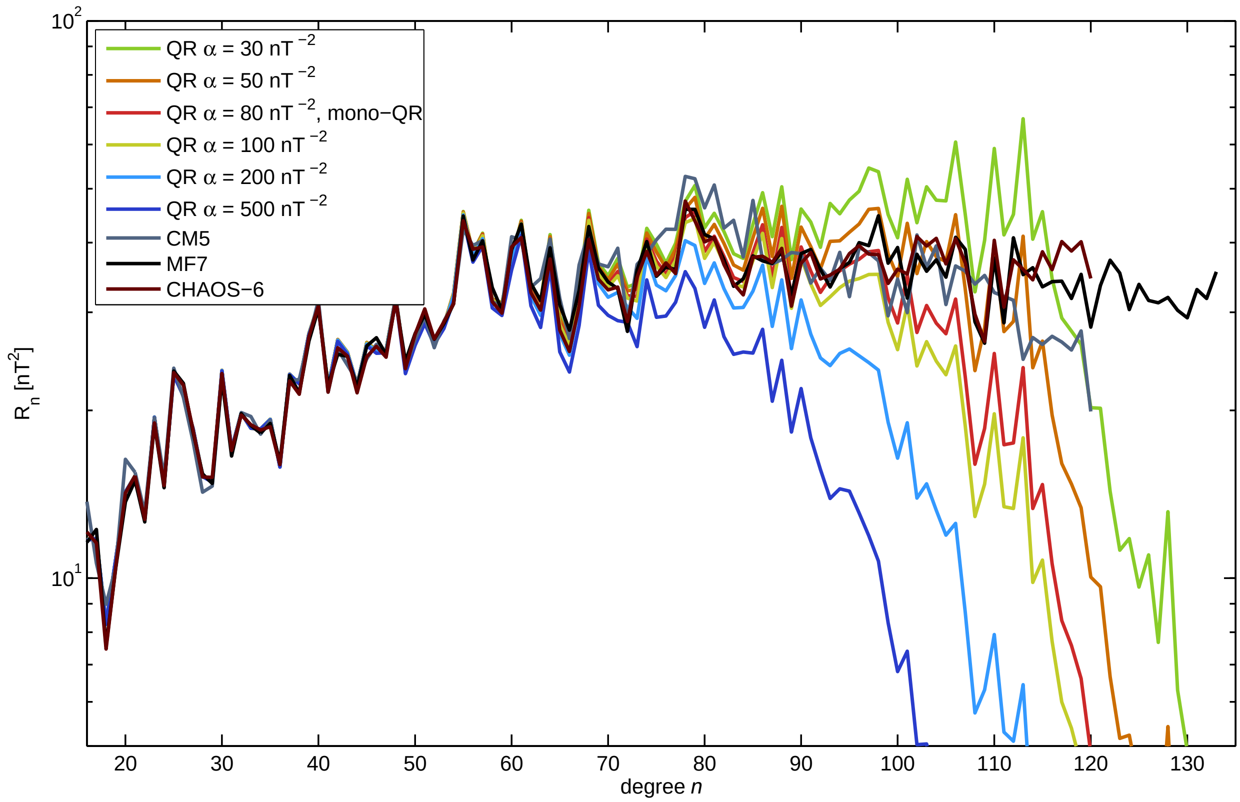

Figure 17 Power spectra for the investigated quadratically regularized (QR) models with different regularization parameters α, compared to some recent lithospheric field models (CM5: (Sabaka et al., 2015), MF7: (Maus et al., 2008; Maus, 2010) and CHAOS-6 (Finlay et al., 2016a)). The model with $\alpha = 80\mathrm{nT}^{-2}$, represented by the red line, is chosen as the preferred model mono-QR. The corresponding lithospheric radial magnetic field at the Earth's surface is illustrated in the upper part of Fig.29.

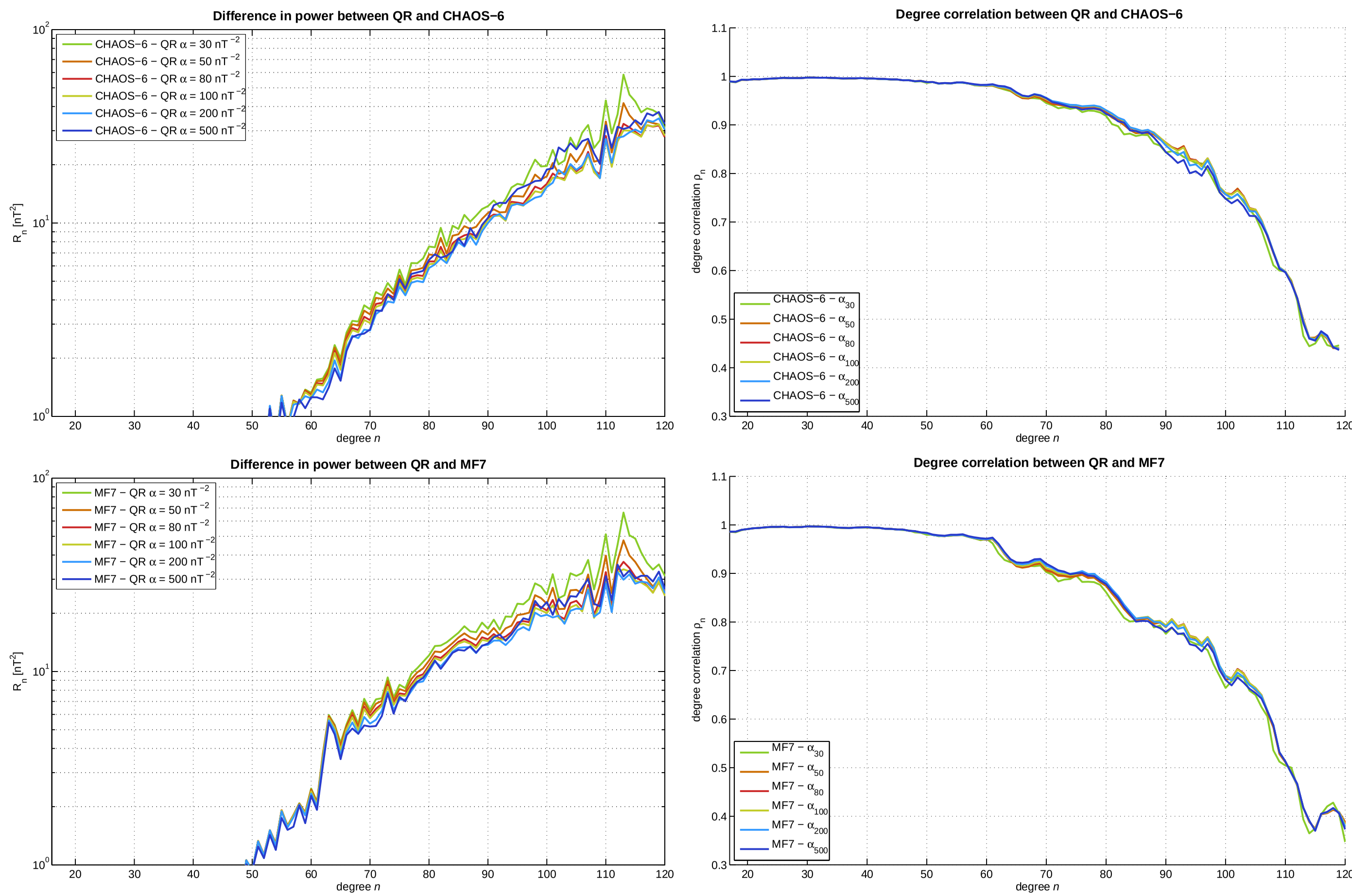

Figure 18 Difference in power (left column) and model correlation coefficients (right column) between CHAOS-6 (upper part), MF7 (lower part) and the quadratic regularized models.

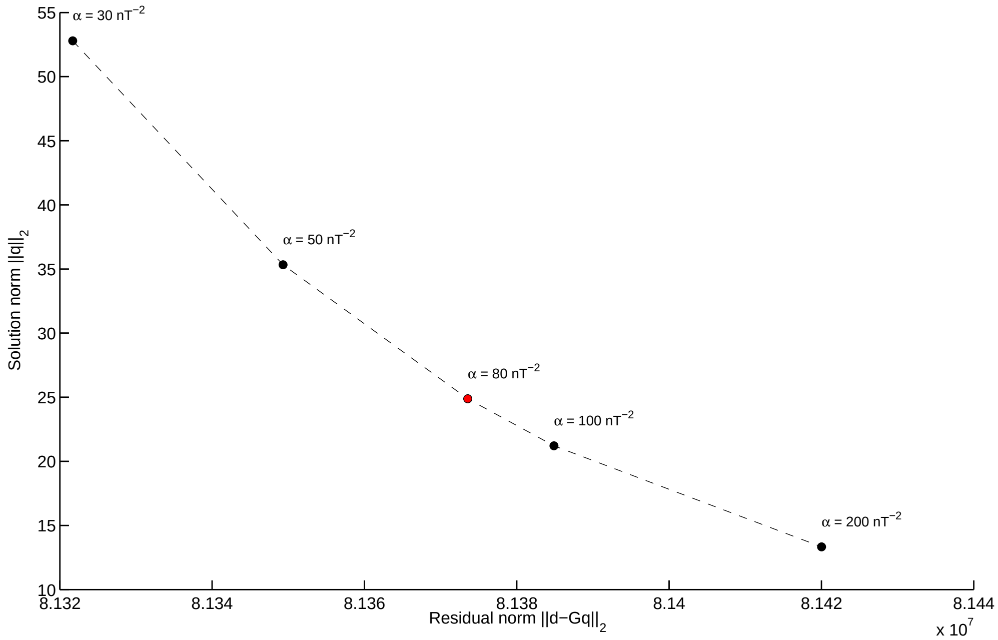

Figure 19 L-curve for quadratic regularized models obtained with different regularization parameters α. The curve shows the trad-off between the residual 2-norm and the source values' 2-norm. The finally preferred QR model is highlighted in red.

3.6 Maximum entropy regularized model results

The method of generating lithospheric field models using the maximum entropy regularization (ER) approach is described in section 2.8.2. In order to demonstrate the effect of the entropy default parameter ω, Table 5 lists the global misfit statistics of four ER models that share the same regularization parameter $\alpha = 30\,\mathrm{nT}^{-2}$ but differ in ω. Similar to the previous section, the table lists the derived *Huber*-weighted residual mean values and the normalized *Huber*-weighted root mean square values for the entire data set as well as for polar and non-polar regions. The four ER models result in very similar misfit statistics. However, it is observed that a decrease in ω reduces the RMS value slightly for all three lithospheric field components. The corresponding power spectra (Fig. 20) show that small-scale lithospheric features above approximately SH degree $n = 90$ gain power for decreasing ω values.

The ER models used for further investigation apply the smallest, largest and mono-QR regularization parameters of the previous section: $\alpha = 30\,\mathrm{nT}^{-2}$, $\alpha = 500\,\mathrm{nT}^{-2}$ and $\alpha = 80\,\mathrm{nT}^{-2}$. The respective QR solutions and corresponding weights are used as starting conditions for the ER model derivations. The initial entropy default parameter ω was set to a large value, and gradually decreased after model convergence. The resulting minimum values reached for ω are chosen for the final ER models. Figure 21 illustrates the power spectra for both these ER models and the corresponding starting condition QR models. Since the ER approach enhances local magnetic field amplitudes, the resulting model predictions for spherical harmonic degrees larger than $n = 70$ have higher power than the corresponding QR counterpart using the same regularization parameter α. Differences in power between the final ER models and the state-of-the-art models MF7 and CHAOS-6, as well as the corresponding degree correlation coefficients are given in Fig. 22.

Similar to the QR results, the derived ER models reach the correlation level of $\rho = 0.7$ at approximately $n = 105$ and $n = 100$ with respect to CHAOS-6 and MF7, respectively. Comparisons of the radial and intensity field maps of these models at the Earth's surface and at 300 km altitude are given in Appendix D.2. Here, the model differences seen for the surface projections are mainly caused by the different damping parameters α, where the ER model with the largest regularization parameter results in the smallest field amplitudes.

A comparison of misfit statistics for the derived ER models is given in Table 6. Like for the QR results, the derived ER models fit the measurements to a similar level, having differences mainly in the third decimal. The final ER-model, henceforth denoted as *mono-ER*, is chosen to have a starting condition which ensures the minimum amount of noise mapped into the monopole sources, corresponding to the largest investigated regularization parameter $\alpha = 500\,\mathrm{nT}^{-2}$. The lower part of Fig. 29 illustrates the corresponding radial field map at the Earth's surface.

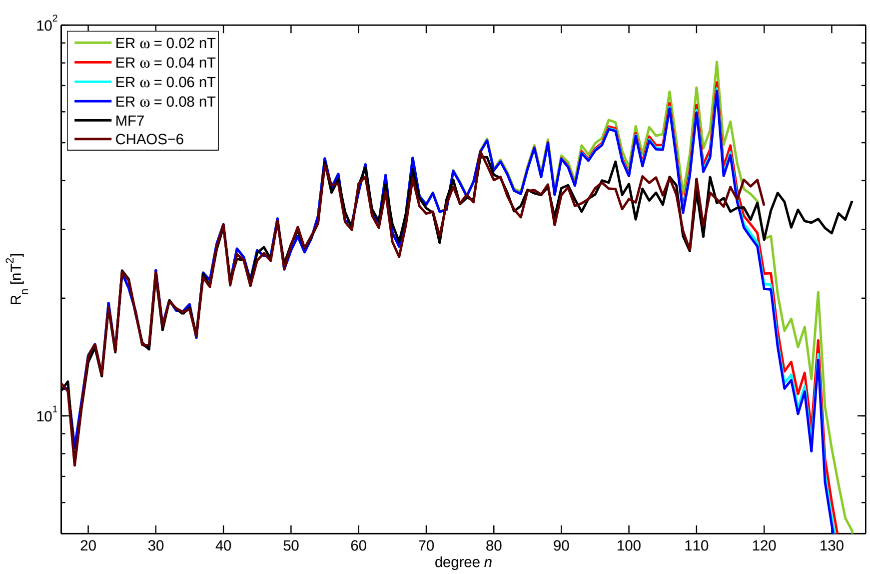

Figure 20 Power spectra for the maximum entropy regularized (ER) models sharing the same regularization parameter $\alpha = 30\,\mathrm{nT}^{-2}$ but having different ER specific parameters ω.

$\boldsymbol{\omega}$ (nT)	0.02	0.04	0.06	0.08
mean ΔB_r (nT)	-0.0697	-0.0695	-0.0695	-0.0694
RMS ΔB_r (-)	1.2863	1.2864	1.2865	1.2865
RMS ΔB_r polar (-)	1.4268	1.4269	1.4269	1.4270
RMS ΔB_r non-polar (-)	1.1805	1.1807	1.1807	1.1807
mean ΔB_θ (nT)	-1.3434	-1.3434	-1.3434	-1.3434
RMS ΔB_θ (-)	1.2625	1.2625	1.2625	1.2625
RMS ΔB_θ polar (-)	1.3793	1.3793	1.3793	1.3794
RMS ΔB_θ non-polar (-)	1.1746	1.1747	1.1747	1.1747
mean ΔB_ϕ (nT)	-0.3625	-0.3625	-0.3625	-0.3625
RMS ΔB_ϕ (-)	1.2723	1.2724	1.2724	1.2724
RMS ΔB_ϕ polar (-)	1.4262	1.4262	1.4262	1.4262
RMS ΔB_ϕ non-polar (-)	1.1545	1.1546	1.1546	1.1547
RMS ΔB (-)	1.2737	1.2738	1.2738	1.2739
RMS ΔB polar (-)	1.4109	1.4109	1.4109	1.4110
RMS ΔB non-polar (-)	1.1699	1.1700	1.1701	1.1701

Table 5 Huber-weighted residual mean values and Huber-weighted model residual RMS values (normalized by the latitudinally varying error estimates of Fig. 9) for four ER models that share the same regularization parameter $\alpha = 30\,\mathrm{nT}^{-2}$ but differ in ω. Here, $\Delta B = \sqrt{\Delta B_r^2 + \Delta B_\theta^2 + \Delta B_\phi^2}$ and the suffixes "polar" and "non-polar" represent data of absolute QD latitudes $\geq 55°$ and $< 55°$, respectively.

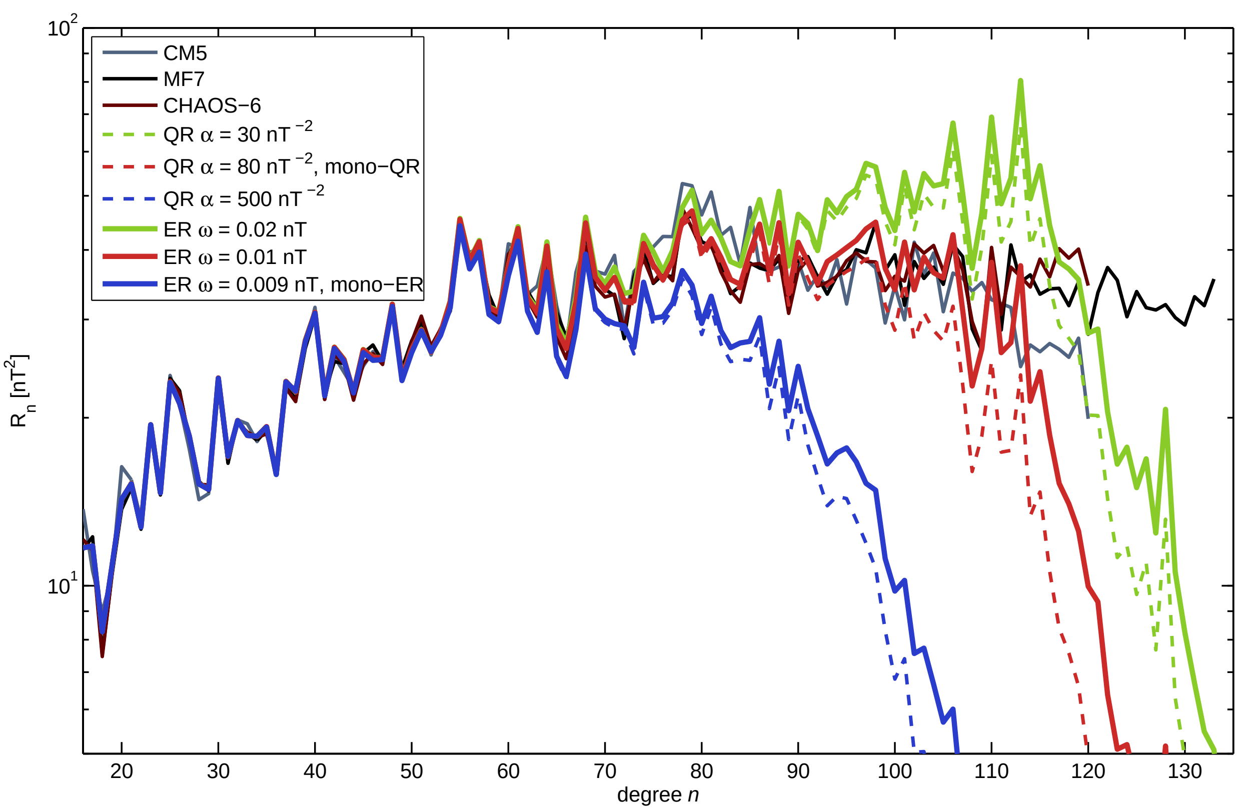

Figure 21 Power spectra for the QR models (thin dashed lines) and maximum entropy regularized (ER) models (thick lines) compared to reference lithospheric field models. Models with the same regularization parameter α are represented with the same color. The preferred ER model is given in dark blue.

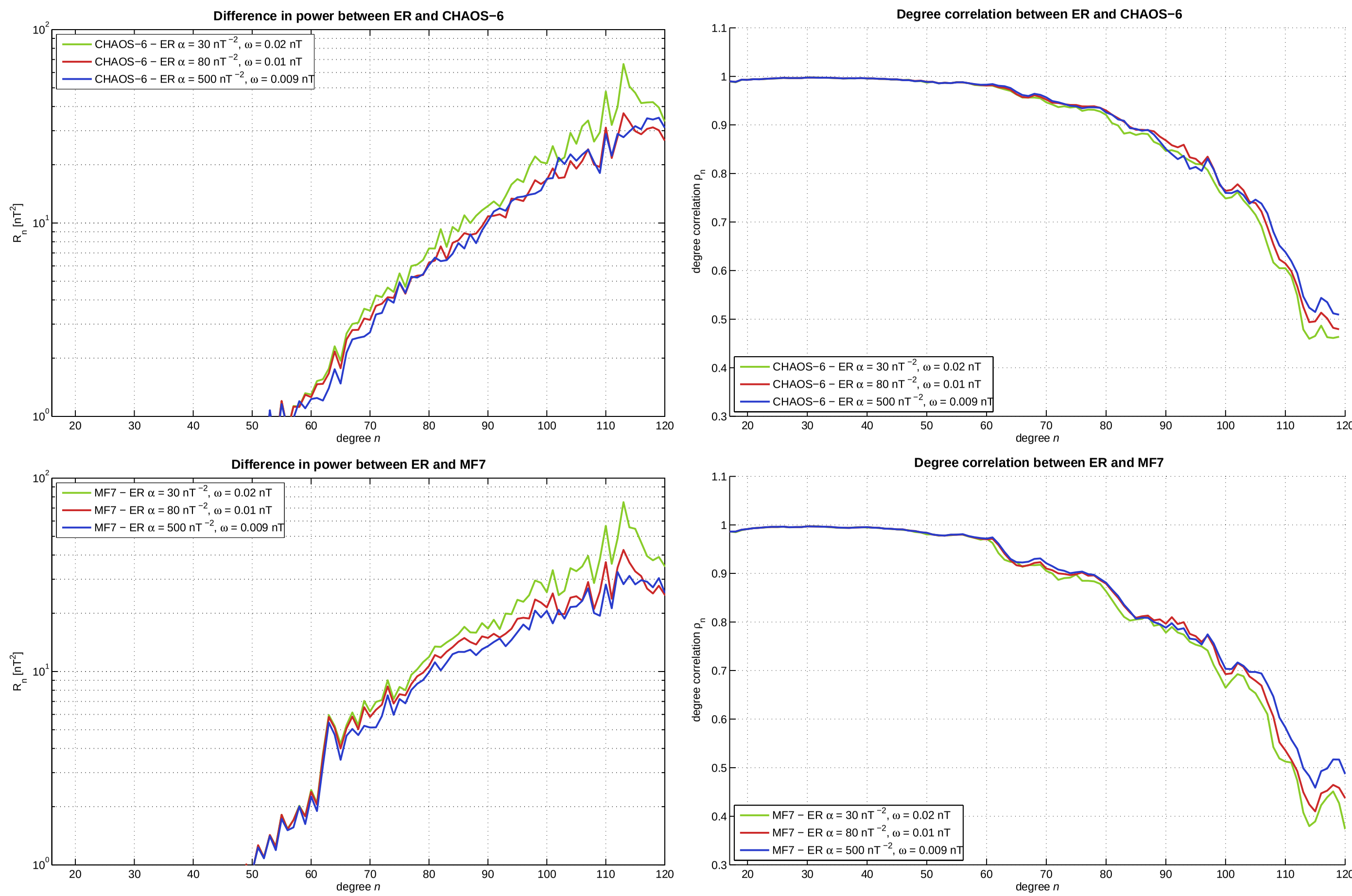

Figure 22 Difference in power (left column) and model correlation coefficients (right column) between CHAOS-6 (upper part), MF7 (lower part) and the maximum entropy regularized (ER) models.

3.7 L_1-norm regularized model results

Instead of regularizing the squared norm of the monopoles or their entropy, this section gives the results of lithospheric field models which were derived by regularizing the L_1-norm of the monopole values. The investigated regularization parameters are $\alpha = 1\,\mathrm{nT}^{-1}$ to $4\,\mathrm{nT}^{-1}$ and the corresponding model statistics are listed in Table 6. As expected, the model with the lowest damping factor results in the smallest residual RMS values for all three field components. However, looking at the corresponding power spectrum in Fig. 23 its seems that this model gives too much power to lithospheric signals beyond SH degree $n = 90$ when comparing with the models MF7 and CHAOS-6. The radial and intensity field maps of all L1 models can be found in Appendix D.3.

Figure 24 illustrates the differences in power and degree correlation values between the L1 models and reference models MF7 and CHAOS-6. The degree correlation curve with respect to CHAOS-6 is very similar to the investigated QR-models and ER-models of the previous sections, reaching the correlation limit of $\rho = 0.7$ at approximately $n = 105$. However, except for the model using $\alpha = 1\,\mathrm{nT}^{-1}$, the L1-models correlate with MF7 up to slightly higher degrees than the models using the quadratic or maximum entropy regularization approach. Here, $\rho = 0.7$ is also given for approximately $n = 105$.

The final L1 model is chosen to be $\alpha = 4\,\mathrm{nT}^{-1}$, which produces the smallest field amplitudes, especially in oceanic regions, compared to the other L1 models, the smallest average radial and longitudinal residuals and the largest degree correlation $\rho_{n=100}$ with respect to both MF7 and CHAOS-6.

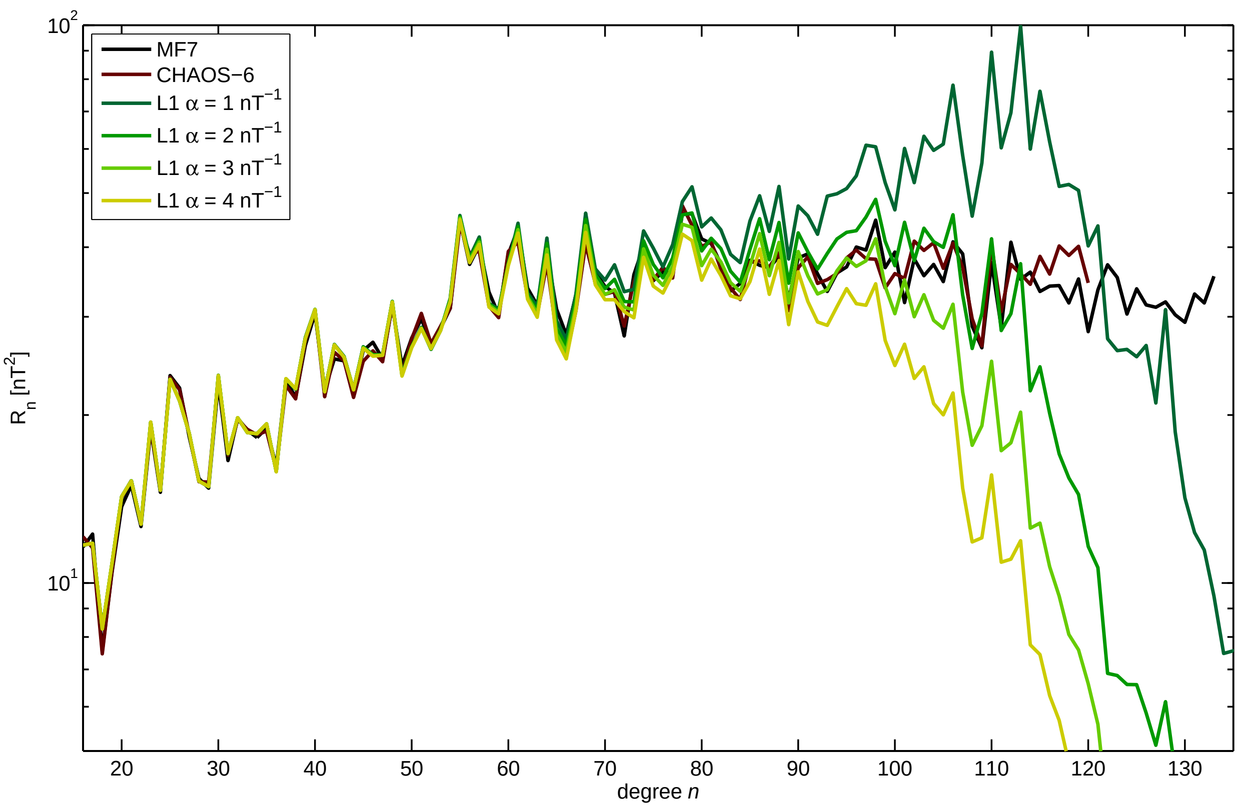

Figure 23 Power spectra for different investigated L1 regularized models. The final model *mono-L1* corresponds to $\alpha = 4\,\mathrm{nT}^{-1}$ and is given in yellow.

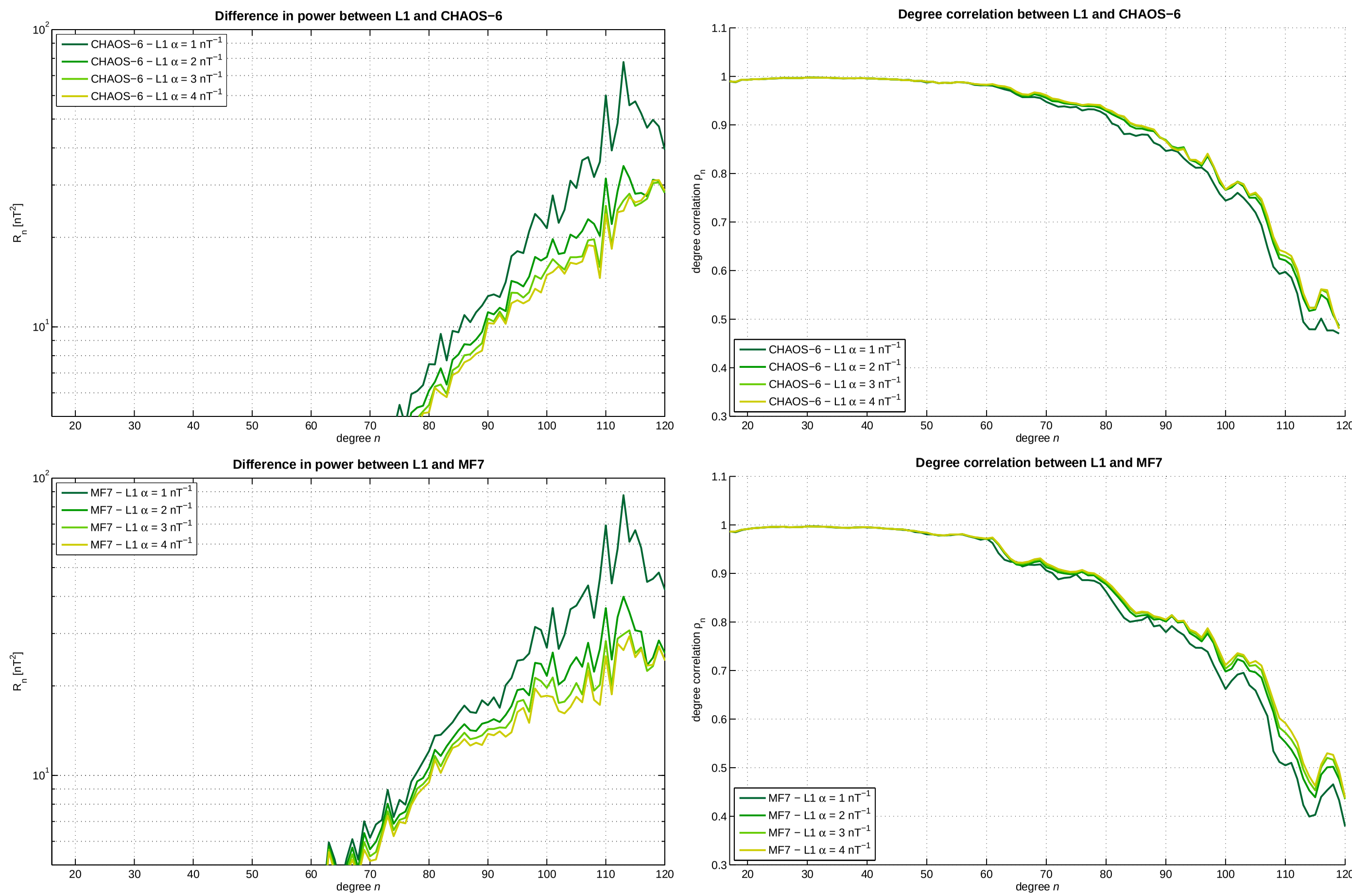

Figure 24 Difference in power (left column) and model correlation coefficients (right column) between CHAOS-6 (upper part), MF7 (lower part) and the L1 regularized models.

3.8 Model comparisons

Having selected a final candidate for each regularization approach, this section compares the corresponding model results by means of misfit, the power spectrum, degree correlation, global and regional plots, degree/order matrices and the effective number of degrees of freedom. Note that both global and regional plots are the direct output of the individual monopole model rather than an approximation based on a truncated SH expansion. Corresponding comparisons with the models MF7, CHAOS-6 and CM5 are collected in Appendix D.

3.8.1 Differences in power spectra and degree correlations

Figure 25 compares the power spectra of the three selected models for the different regularization approaches. The corresponding differences with respect to the models MF7 and CHAOS-6, as well as the respective degree correlation values are given in Fig. 26. The lower right panel of the latter is also given in Fig. 27, along with the degree correlation between MF7 and the spherical harmonic version of mono-QR, mono-ER, mono-L1 and CM5. The monopole based models reach the illustrative correlation limit of $\rho_n = 0.7$ between SH degree $n = 100$ and $n = 105$. According to this measure, CM5 correlates well with MF7 up to SH degree $n = 108$. The light blue and light green lines show the degree correlation for mono-QR/mono-ER and mono-QR/mono-L1, respectively. Figure 27 shows that the selected models correlate well with each other with degree correlation values above 0.7 up to SH degree $n = 121$ (mono-QR/mono-L1) and $n = 130$ (mono-QR/mono-ER). In fact, the models are very similar with $\rho_n = 1$ up to SH degree $n = 60$. It is also interesting to see that model mono-QR correlates slightly better with mono-L1 up to SH degree $n = 100$, whereafter the model is distinctly more congruent with mono-ER.

Despite the good correlation between the selected models, Fig. 25 shows that model mono-ER decreases drastically in power beyond SH degree 90. In fact, the power of this model falls below $5\,\mathrm{nT}^2$, which is an order of magnitude smaller compared to mono-QR and mono-L1. This difference in power will be discussed later in this chapter.

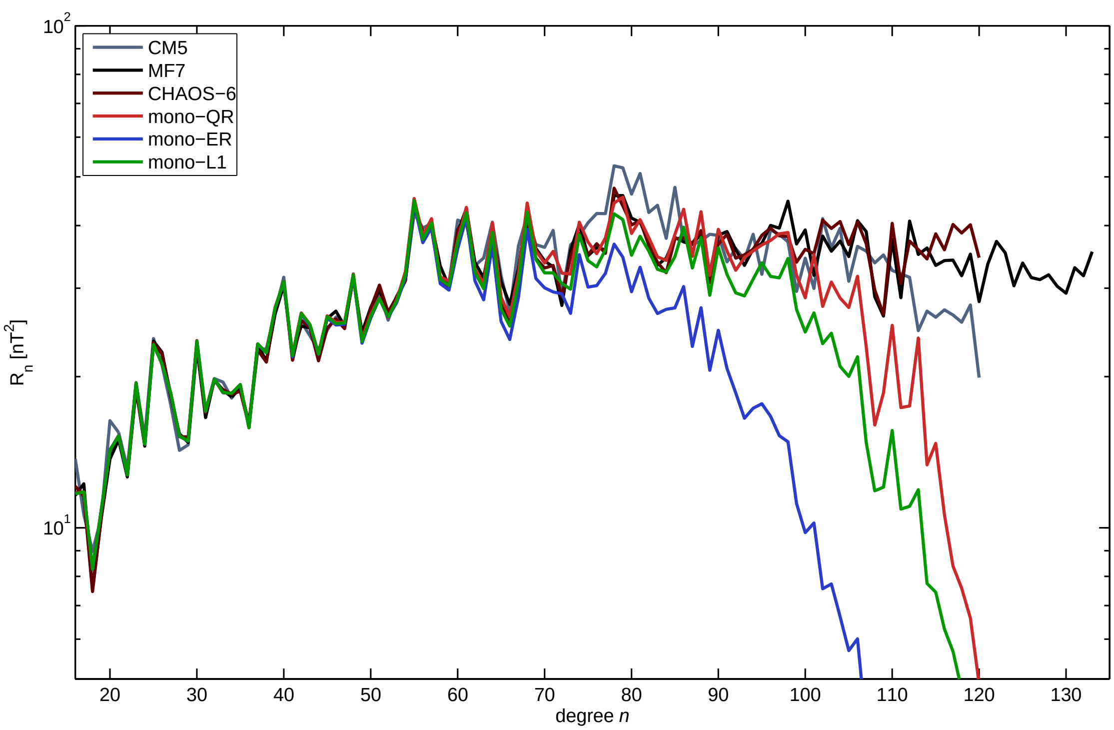

Figure 25 Power spectra for the final models mono-QR (red), mono-L1 (green) and mono-ER (blue) compared to some recent lithospheric field models (CM5: (Sabaka et al., 2015), MF7: (Maus et al., 2008; Maus, 2010) and CHAOS-6 (Finlay et al., 2016a)).

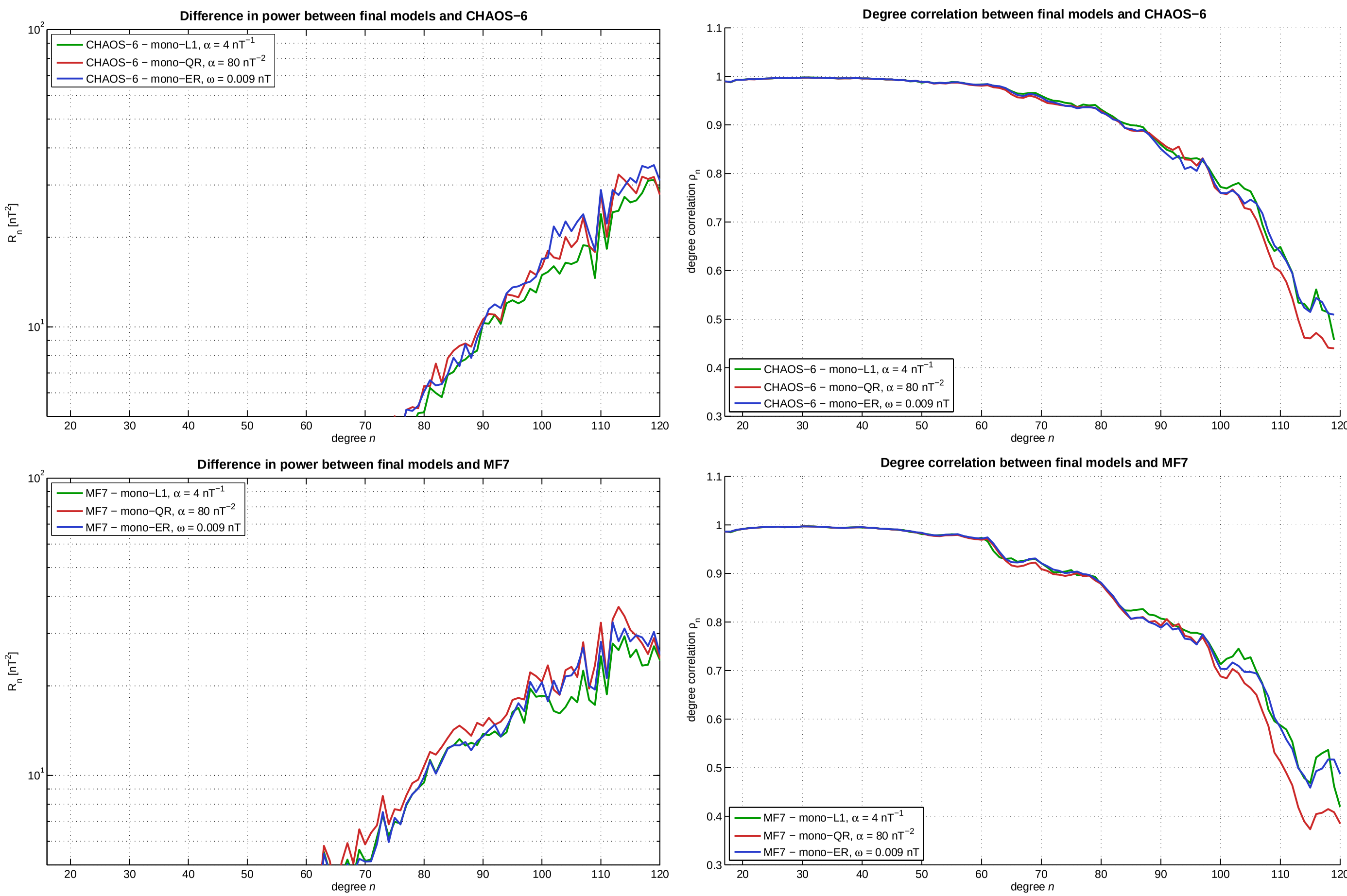

Figure 26 Difference in power (left column) and model correlation coefficients (right column) between CHAOS-6 (upper part), MF7 (lower part) and the final models mono-QR (red), mono-L1 (green) and mono-ER (blue).

	MF7	CM5	CHAOS-6	QR models			ER models			L1 models			
α [nT^{-2}]^{QR,ER}; [nT^{-1}]^{L1}	-	-	-	80	100	200	30	80	500	1	2	3	4
ω [nT]	-	-	-	-	-	-	0.02	0.01	0.009	-	-	-	-
mean ΔB_r (nT)	0.0039	-0.0458	-0.0057	-0.0685	-0.0681	-0.0667	-0.0697	-0.0681	-0.0644	-0.0693	-0.0683	-0.0672	-0.0653
RMS ΔB_r (-)	1.3108	1.3389	1.3025	1.2871	1.2874	1.2881	1.2861	1.2868	1.2891	1.2861	1.2870	1.2875	1.2879
RMS ΔB_r polar (-)	1.4317	1.4458	1.4310	1.4265	1.4266	1.4270	1.4258	1.4263	1.4278	1.4259	1.4265	1.4267	1.4270
RMS ΔB_r non-polar (-)	1.2206	1.2596	1.2063	1.1820	1.1823	1.1833	1.1806	1.1815	1.1845	1.1806	1.1817	1.1823	1.1829
mean ΔB_θ (nT)	-1.5252	-1.4497	-1.4939	-1.3437	-1.3439	-1.3449	-1.3434	-1.3442	-1.3386	-1.3438	-1.3449	-1.3455	-1.3448
RMS ΔB_θ (-)	1.2649	1.2729	1.2645	1.2627	1.2628	1.2630	1.2625	1.2626	1.2632	1.2624	1.2627	1.2628	1.2629
RMS ΔB_θ polar (-)	1.3854	1.3896	1.3846	1.3792	1.3793	1.3793	1.3792	1.3792	1.3795	1.3792	1.3792	1.3793	1.3793
RMS ΔB_θ non-polar (-)	1.1739	1.1851	1.1738	1.1749	1.1750	1.1753	1.1745	1.1747	1.1756	1.1744	1.1748	1.1750	1.1751
mean ΔB_ϕ (nT)	-0.3595	-0.3620	-0.3608	-0.3622	-0.3621	-0.3617	-0.3625	-0.3623	-0.3613	-0.3626	-0.3622	-0.3619	-0.3616
RMS ΔB_ϕ (-)	1.2797	1.2858	1.2750	1.2727	1.2728	1.2731	1.2723	1.2726	1.2734	1.2723	1.2727	1.2729	1.2730
RMS ΔB_ϕ polar (-)	1.4292	1.4286	1.4285	1.4268	1.4269	1.4269	1.4267	1.4268	1.4270	1.4267	1.4268	1.4269	1.4269
RMS ΔB_ϕ non-polar (-)	1.1651	1.1768	1.1572	1.1544	1.1546	1.1550	1.1537	1.1542	1.1555	1.1536	1.1543	1.1546	1.1549
RMS ΔB (-)	1.2852	1.2994	1.2807	1.2742	1.2744	1.2748	1.2736	1.2740	1.2753	1.2737	1.2742	1.2744	1.2747
RMS ΔB polar (-)	1.4155	1.4214	1.4148	1.4110	1.4110	1.4112	1.4107	1.4109	1.4116	1.4107	1.4109	1.4111	1.4112
RMS ΔB non-polar (-)	1.1868	1.2076	1.1793	1.1705	1.1707	1.1713	1.1697	1.1702	1.1720	1.1696	1.1703	1.1707	1.1711
$\rho_{n=100,CHAOS6}$ (-)	0.9054	0.7852	0.0000	0.7362	0.7365	0.7343	0.7466	0.7430	0.7491	0.7461	0.7487	0.7541	0.7614
$\rho_{n=100,MF7}$ (-)	0.0000	0.8182	0.9054	0.6521	0.6536	0.6544	0.6896	0.6590	0.6864	0.6896	0.6666	0.6794	0.6963

Table 6 Residual mean values and normalized (by latitude-dependent standard deviation values) Huber-weighted RMS model residual values between the different investigated QR, ER and L1 models at satellite altitude and the state-of-the-art models MF7 (up to SH degree 133), CHAOS-6 (up to SH degree 120) and CM5 (up to SH degree 120). Here, $\Delta B = \sqrt{\Delta B_r^2 + \Delta B_\theta^2 + \Delta B_\phi^2}$ and the suffixes "polar" and "non-polar" represent data of absolute QD latitudes $> 55°$ and $< 55°$, respectively. $\rho_{n=100,CHAOS6}$ and $\rho_{n=100,MF7}$ represent the degree correlation with respect to CHAOS-6 and MF7 for $n = 100$, respectively. The residual statistics for the final models mono-QR, mono-ER and mono-L1 are highlighted in red, blue and green, respectively.

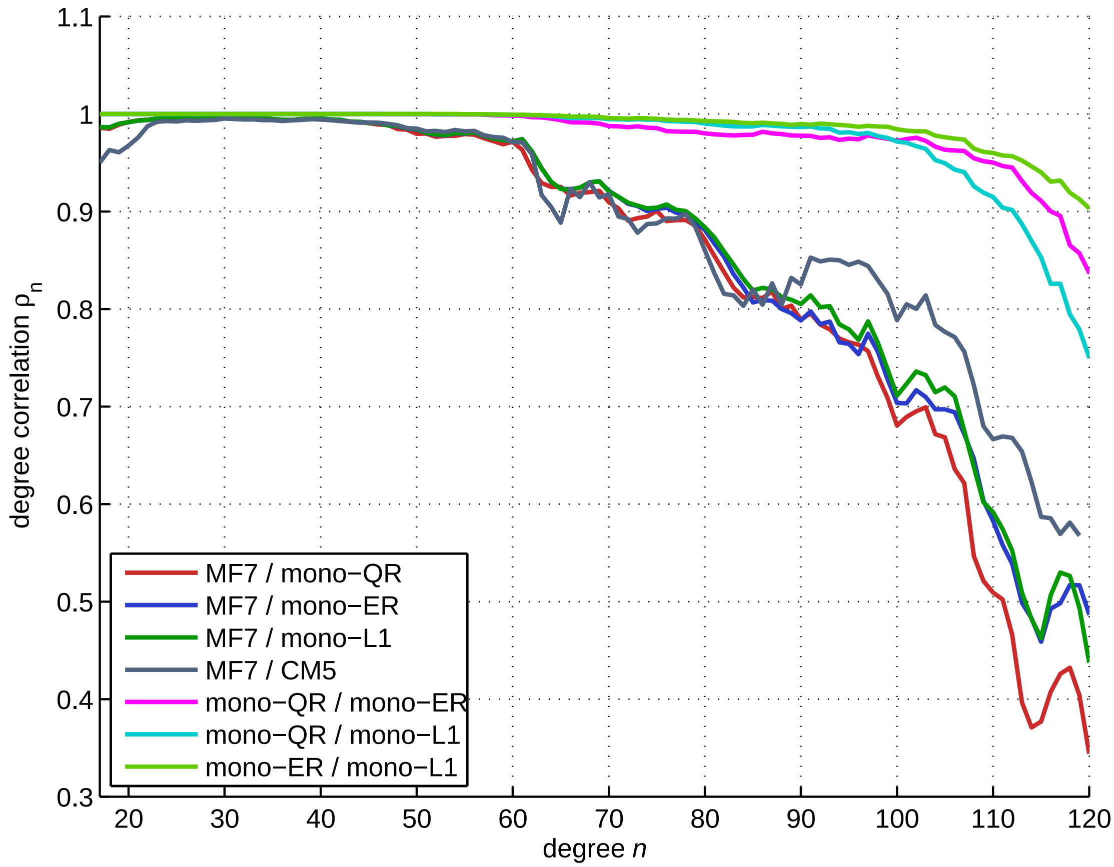

Figure 27 Degree correlation between MF7 and the spherical harmonic degrees of mono-QR ($\alpha = 80\,\mathrm{nT}^{-2}$), mono-ER ($\alpha = 500\,\mathrm{nT}^{-2}$, $\omega = 0.009\,\mathrm{nT}$), mono-L1 ($\alpha = 4\,\mathrm{nT}^{-1}$) and CM5. The light blue and light green lines show the degree correlation for mono-QR/mono-ER and mono-QR/mono-L1, respectively.

3.8.2 Global model differences

Figure 29 illustrates the radial lithospheric field maps at the Earth's surface for the three models selected from the previous sections. Similar figures at 300 km altitude and also for the models MF7, CHAOS-6 and CM5 are given in Appendix D. These figures show that some suspicious north-south directed features appear in all models (incl. MF7, CHAOS-6 and CM5), especially in oceanic regions when downward continuing to the Earth's surface. The amplification of these small-scale features is possibly due to data contamination and noise which are not accounted for in the used models for the external and main field subtractions.
Apart from these structures, the large scale features are equally well represented by all models, which is in good agreement to the similar power spectra behavior for SH degrees $n < 65$ (see Fig. 25).
From all three final models, mono-ER results in the lowest average radial field amplitudes. Using the final source amplitudes to predict the surface lithospheric field on a $1° \times 1°$ grid, the model has a global average absolute radial field value at the Earth's surface of 24.41 nT, which corresponds to 8.56 nT in oceanic regions (topography < -50 m) and 15.85 nT in continental regions (topography ≥ -50 m). For mono-L1, the corresponding values are 26.27 nT, 9.05 nT and 17.21 nT , respectively. The largest global average absolute radial field values are represented by the quadratic regularized model mono-QR, with 29.25 nT, 10.23 nT and 19.02 nT being the respective global, oceanic and continental values at the Earth's surface.
The maximum/minimum values of the radial surface lithospheric field are 521 nT/$-$852 nT, 540 nT/$-$900 nT, 535 nT/$-$1171 nT for mono-QR, mono-ER and mono-L1, respectively. This means that mono-ER has the lowest average radial field amplitudes but larger extremes than mono-QR.
Figures 30 to 32 give the global differences between the three models for all field components at the Earth's

surface. For all model comparisons the differences are globally distributed, with the largest values in the polar regions and around large local lithospheric field anomalies. Regarding the differences between mono-QR and mono-ER, different enhancements are also seen in some specific oceanic regions (e.g. in the mid-Atlantic, north of Brazil and the Indian ocean). For all three model comparisons the differences are most distinct in the radial component, especially between mono-QR and mono-ER. Differences in the other components are mostly connected to large amplitude lithospheric field anomalies (like the Bangui anomaly in central Africa or the Kursk anomaly in Ukraine) and some oceanic regions. Distinct north-south directed features are mostly pronounced in the quadratic regularized model and especially seen in the longitudinal residuals of Figs. 30 and 31.

The right panels of Fig. 28 show a zoomed version of the surface radial model differences for the northwest area of the Indian ocean, as well as the monopole locations projected to the surface of the Earth. The latter clearly illustrates that the distance between individual sources is smaller than length scales of the observed model differences, so the exact monopole positions are not responsible for spurious features.

Further regional comparisons between the surface radial field components of the defined models, MF7, CHAOS-6 and CM5 are given in section 3.8.3.

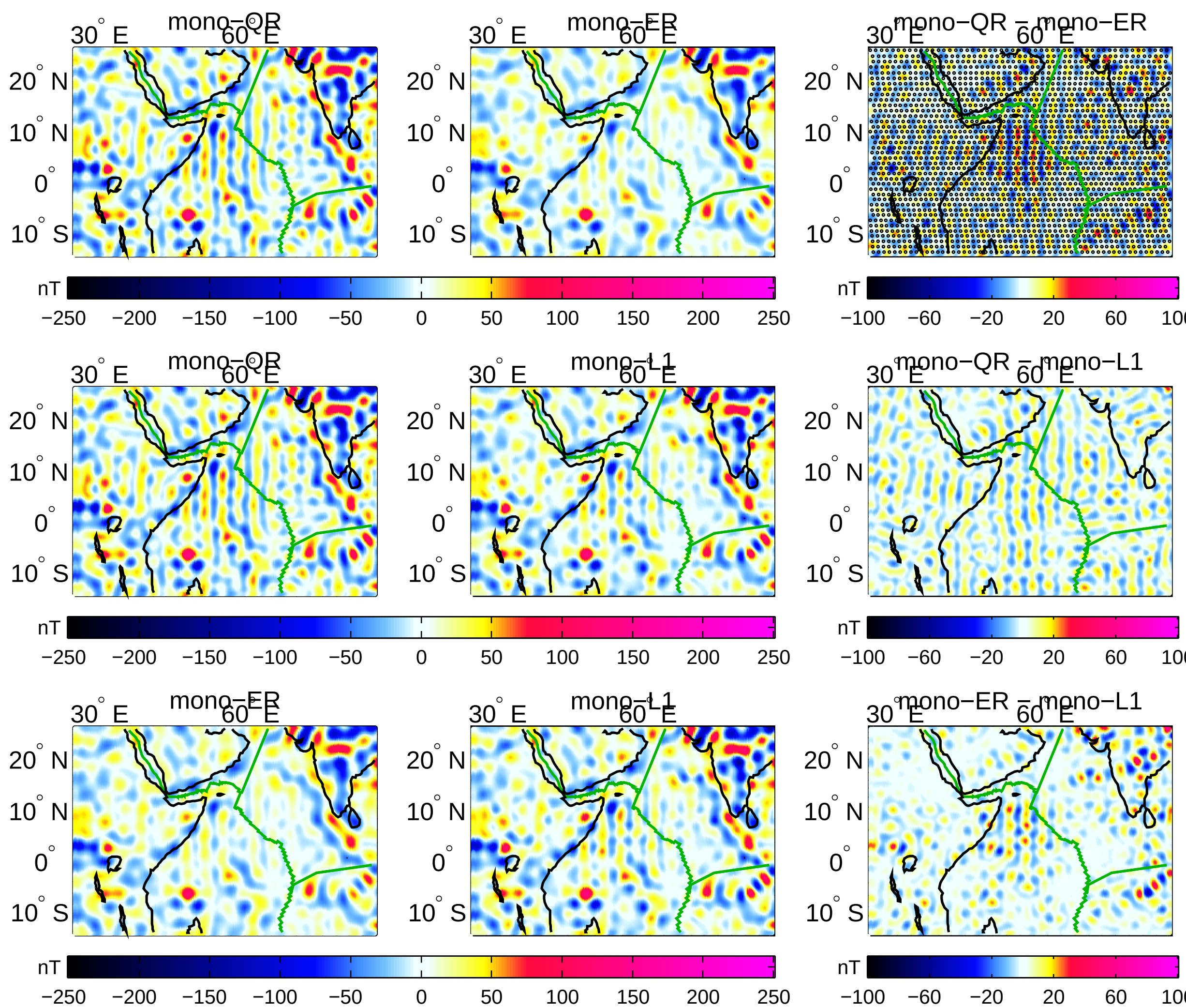

Figure 28 Comparison of the radial field component at the Earth's surface between the three models mono-QR, mono-ER and mono-L1 for the northwest area of the Indian ocean. The individual model differences are given in the right panels of the figures. The upper right panel also includes the source locations (black circles).

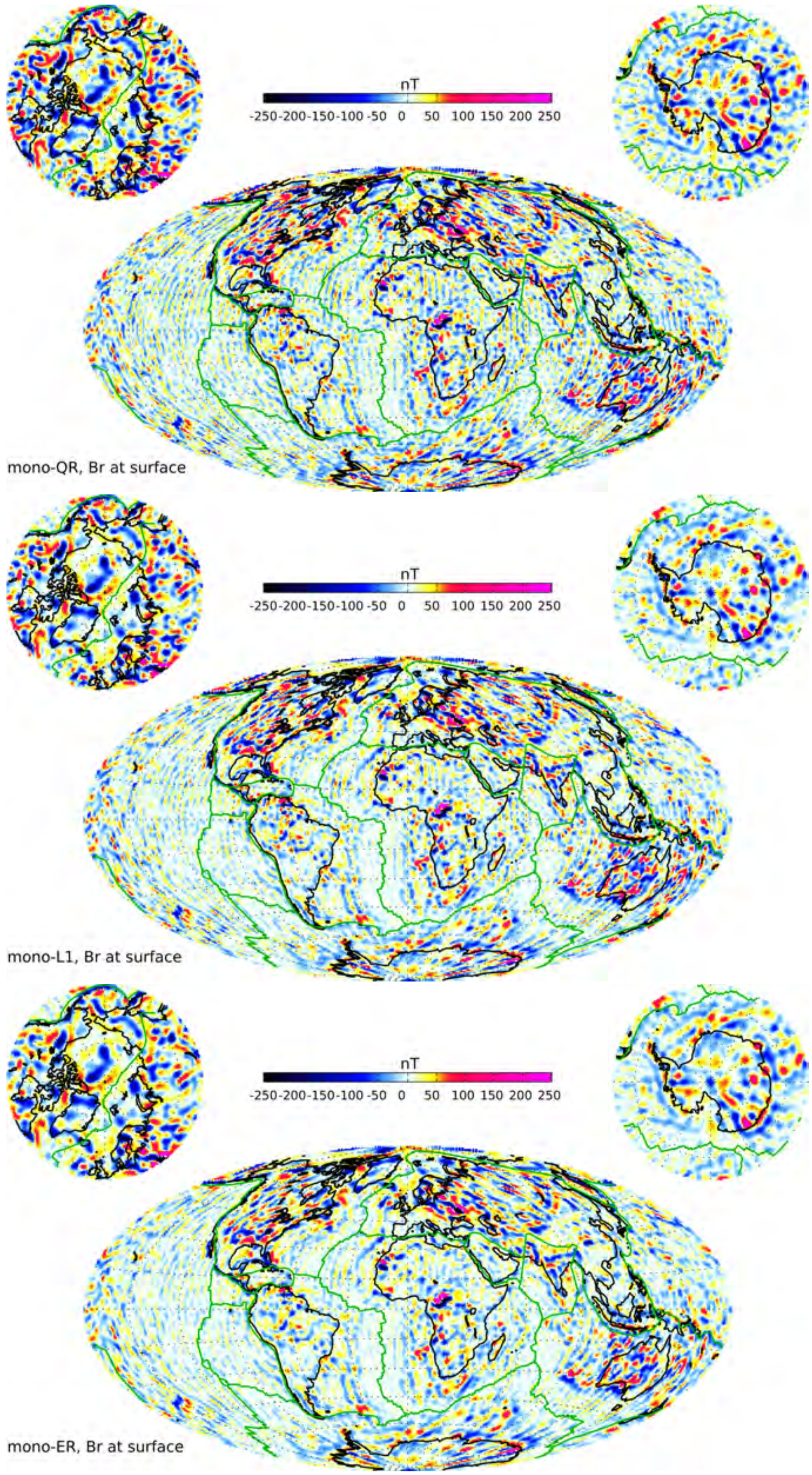

Figure 29 Radial lithospheric field component at the Earth's surface for the preferred models mono-QR (top), mono-L1 (middle) and mono-ER (bottom).

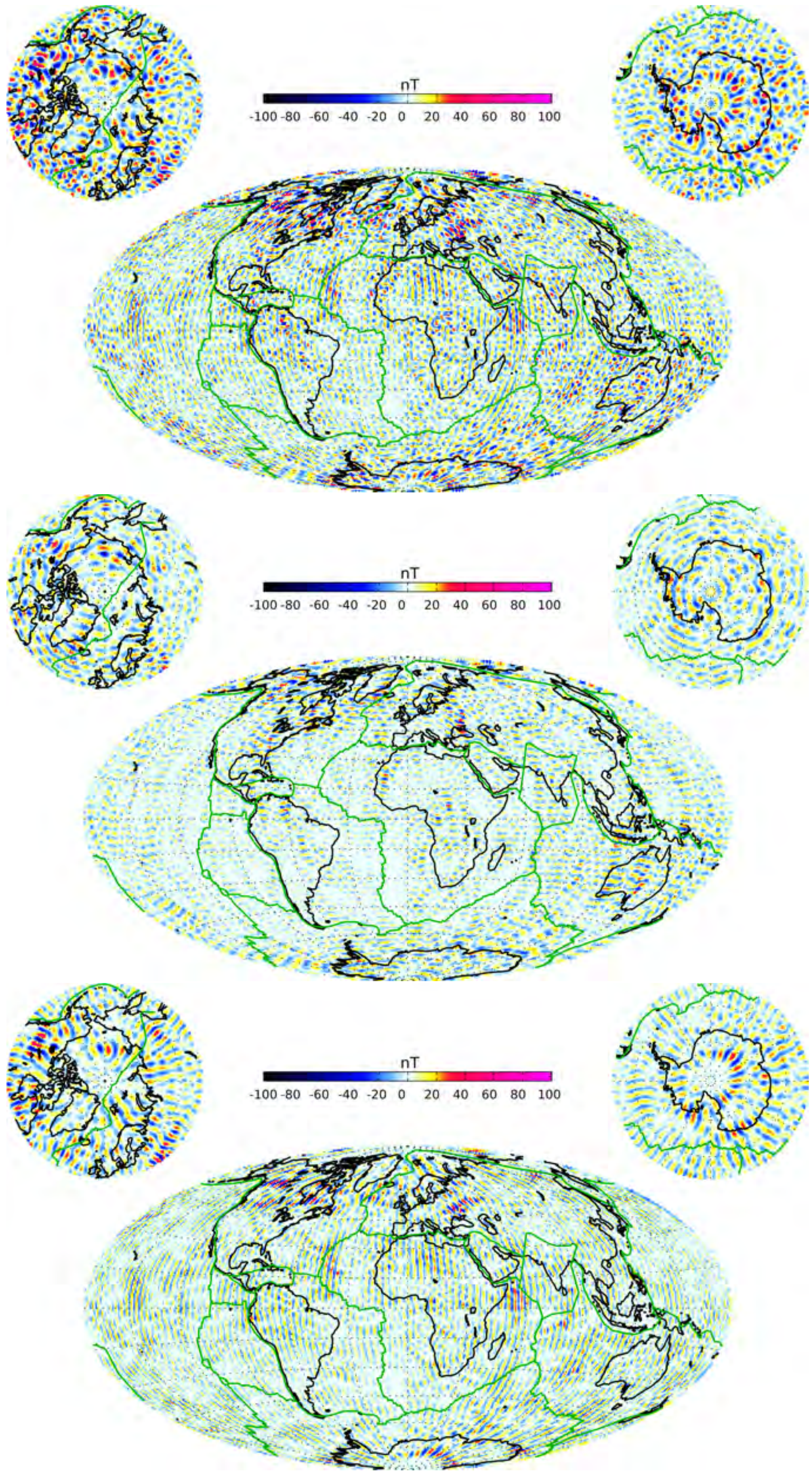

Figure 30 Differences between the two models mono-QR and mono-ER for the radial (top), latitudinal (middle) and longitudinal (bottom) lithospheric field components at the Earth's surface.

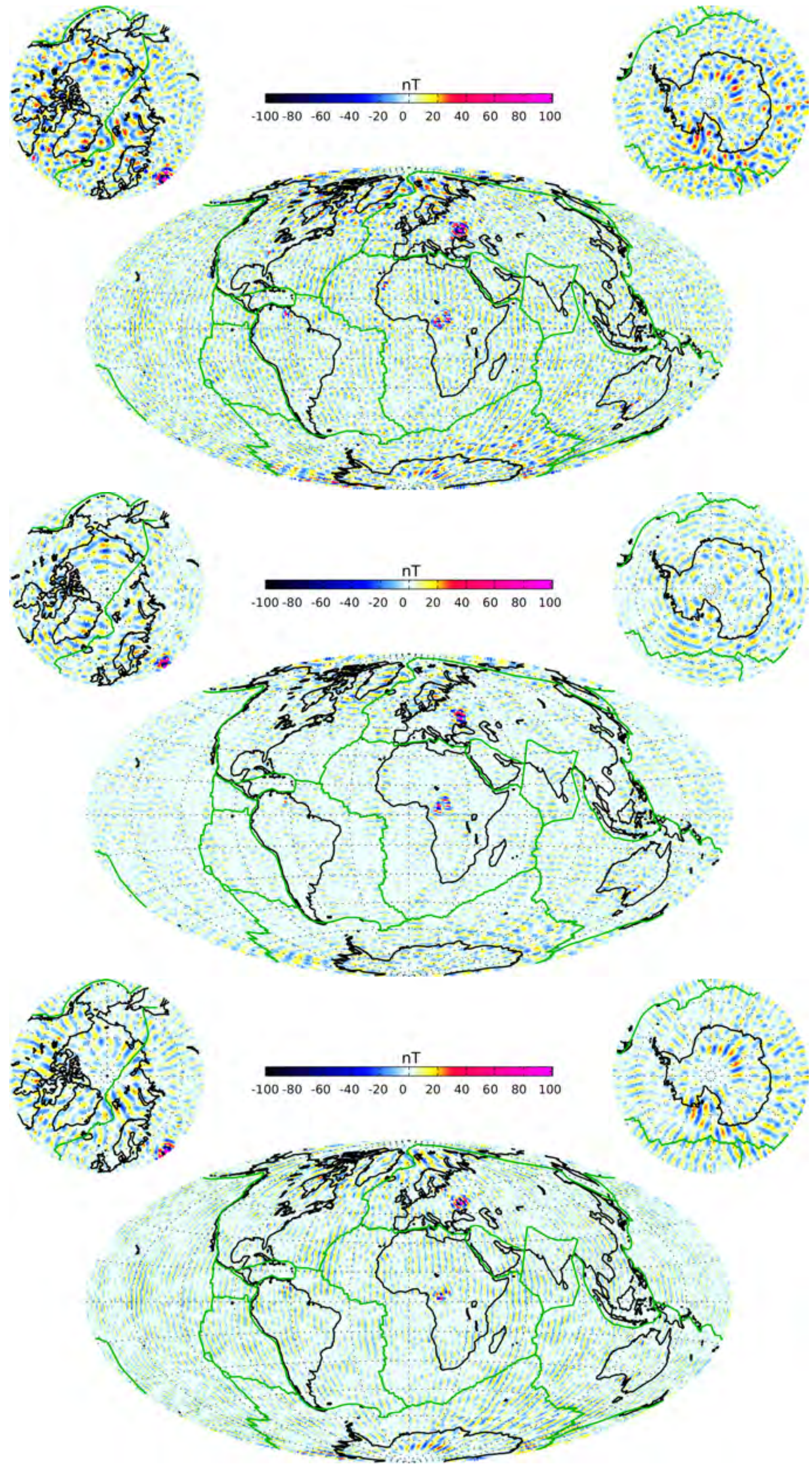

Figure 31 Differences between the two models mono-QR and mono-L1 for the radial (top), latitudinal (middle) and longitudinal (bottom) lithospheric field components at the Earth's surface.

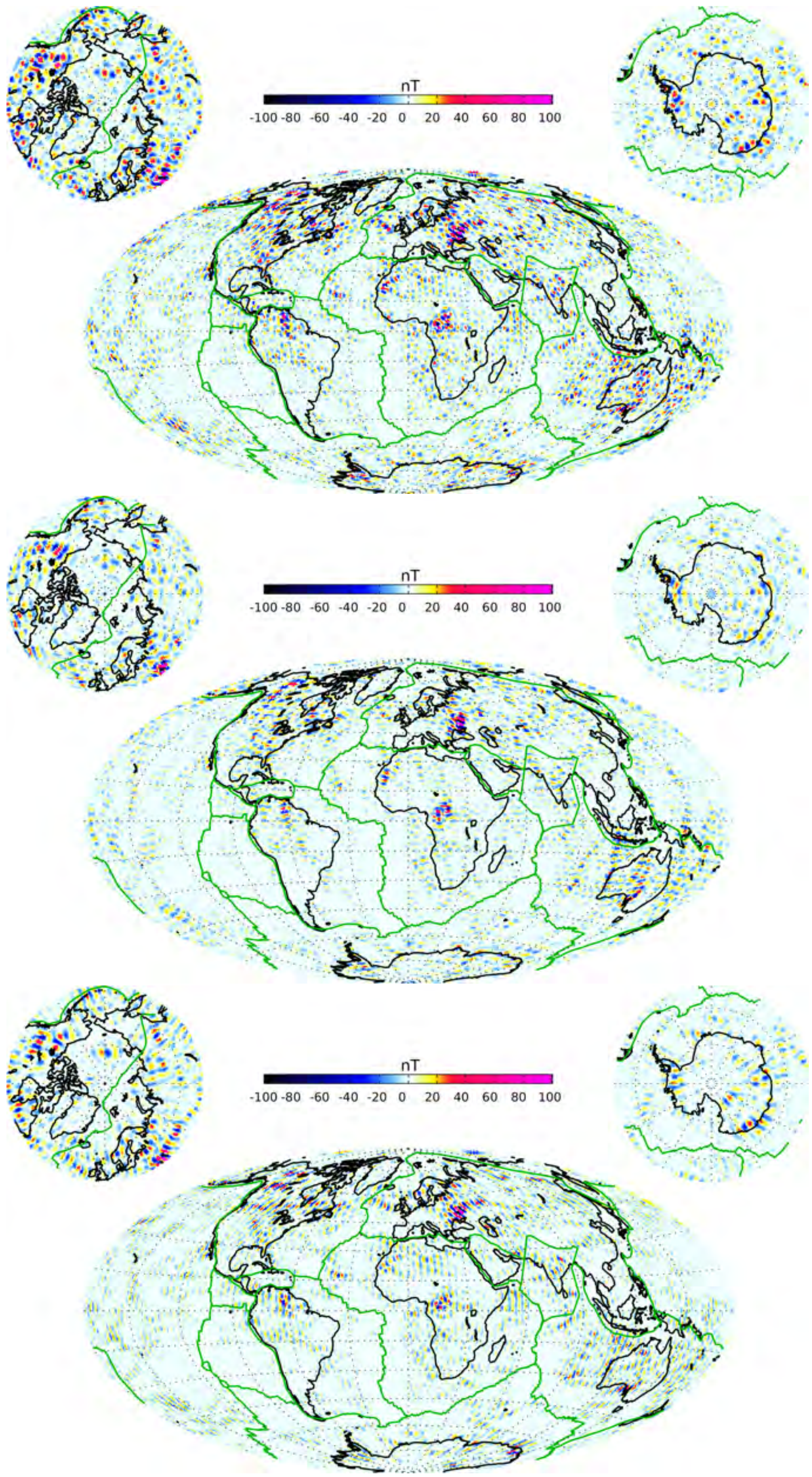

Figure 32 Differences between the two models mono-ER and mono-L1 for the radial (top), latitudinal (middle) and longitudinal (bottom) lithospheric field components at the Earth's surface.

Another method of diagnosing the global differences between models mono-QR, mono-ER and mono-L1 is given in Fig. 33. Here, the corresponding global surface radial magnetic field distributions are illustrated by means of a histogram using surface grid locations identical to the monopole source locations. Compared to mono-QR, both mono-ER and mono-L1 predict more field values closer to zero. The respective maximum and minimum global radial field values are [534.8 nT, −855.4 nT] (mono-QR), [553.2 nT, −913.0 nT] (mono-ER), and [557.9 nT, −1189.9 nT] (mono-L1), respectively. Thus, the maximum entropy and L_1-norm approach follow a more Laplacian distribution, as expected for crustal field anomalies (Walker and Jackson, 2000).
Figure 36 compares the models' surface radial lithospheric magnetic field predictions along a constant longitude crossing the Bangui anomaly. Despite the similar morphology of the anomalies, the smallest amplitudes in regions with weak magnetic anomalies are represented by mono-ER, whereas mono-L1 shows more detailed localized structures in these areas.

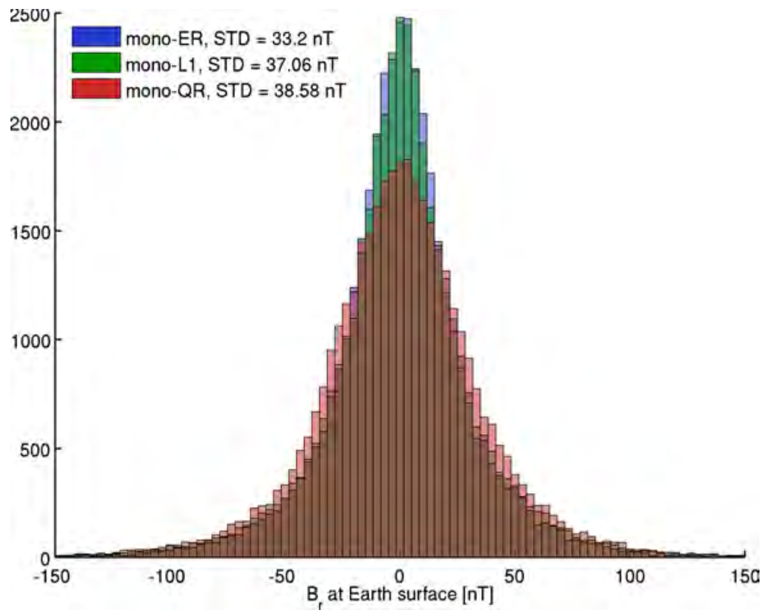

Figure 33 Histogram comparing the modelled lithospheric radial magnetic field amplitude at the Earth's surface predicted by mono-QR (red), mono-ER (blue) and mono-L1 (green). The surface locations used are identical to the monopole locations. Standard deviation values (STD) are given in the upper part of the figure.

3.8.3 Regional model differences

Regional comparisons of the models mono-QR, mono-ER, mono-L1, MF7, CHAOS-6 and CM5 are given in Figs. 34 to 35 by means of the radial component of the surface lithospheric field over North America and the Arctic region, respectively. Appendix D.5 shows the corresponding figures for Europe, Australia and the Antarctic region. The expected characteristic lithospheric features are captured by all models. Differences are mostly observed for the small scale structures such as the positive anomaly band in north Africa, the shape of the Kursk anomaly in Ukraine (Fig. 97) and the positive elongated anomaly structures along the western coast of British Columbia (Fig. 34). In the Arctic region (Fig. 35) models MF7, CHAOS-6 and CM5 show noticeably more small scale features than models mono-QR, mono-ER and mono-L1, especially for the area north of Greenland.

Another regional comparison between the models mono-QR, mono-ER and mono-L1 is given in Fig. 36, which shows the surface radial magnetic field values along a constant longitude crossing the Bangui anomaly in Africa. Despite the similar morphology of the anomalies, the mono-ER model has smaller field amplitudes in regions with weak magnetic anomalies compared to mono-QR and mono-L1. In these regions the latter model predicts more small scale structures, especially north of the Bangui anomaly.

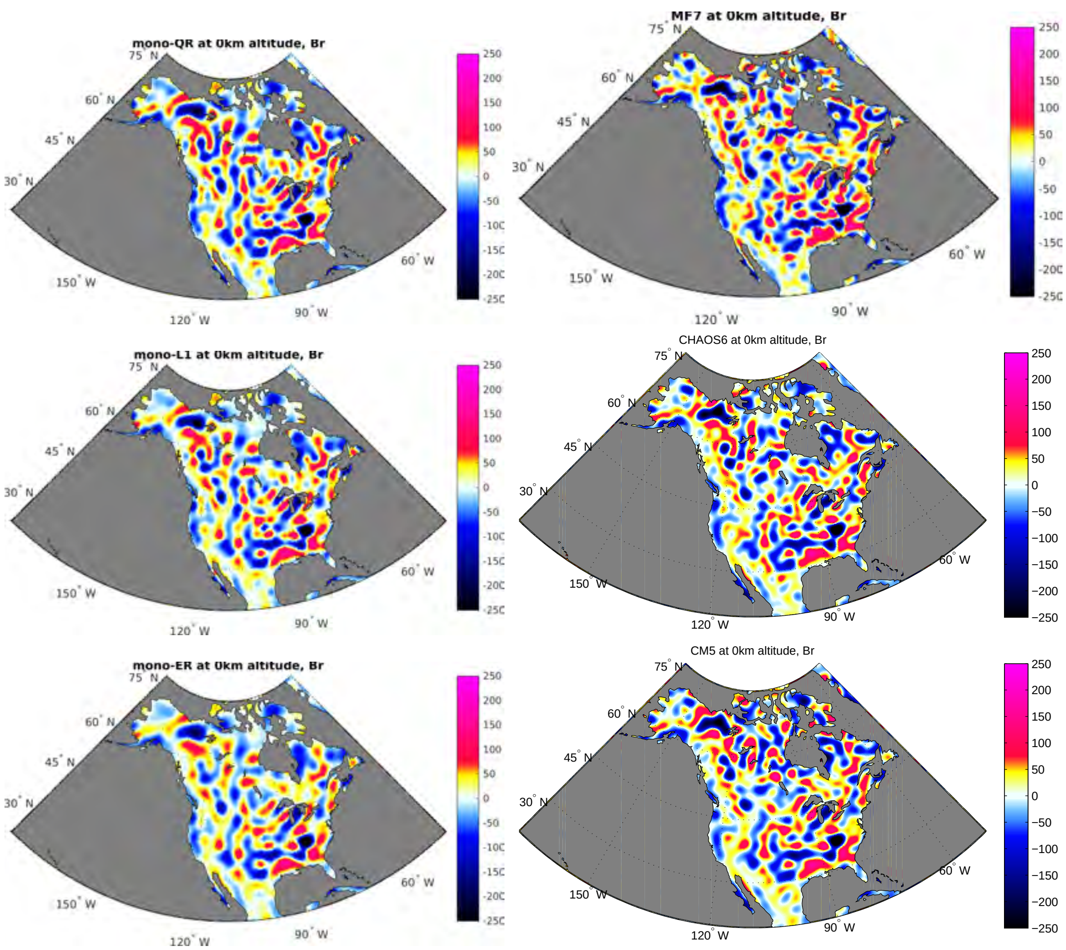

Figure 34 Radial lithospheric field at the Earth's surface over North America for the three models mono-QR (top left), mono-L1 (middle left), mono-ER (bottom left), MF7 up to SH degree $n = 133$ (top right), CHAOS-6 up to SH degree $n = 120$ (middle right) and CM5 up to SH degree $n = 120$ (bottom right). The color scale is given in nT.

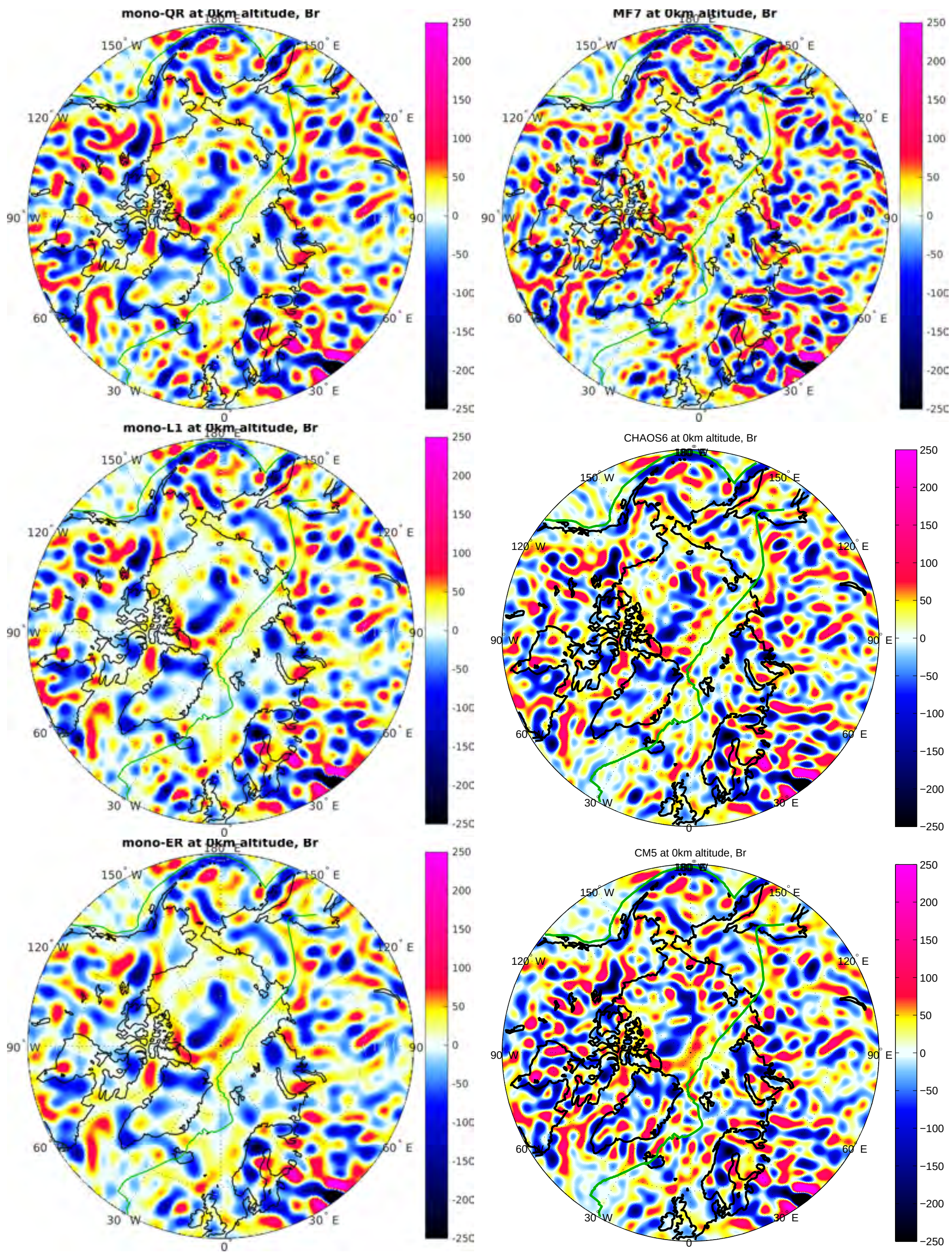

Figure 35 Radial lithospheric field at the Earth's surface over the North Pole for the three models mono-QR (top left), mono-L1 (middle left), mono-ER (bottom left), MF7 up to SH degree $n = 133$ (top right), CHAOS-6 up to SH degree $n = 120$ (middle right) and CM5 up to SH degree $n = 120$ (bottom right). The color scale is given in nT.

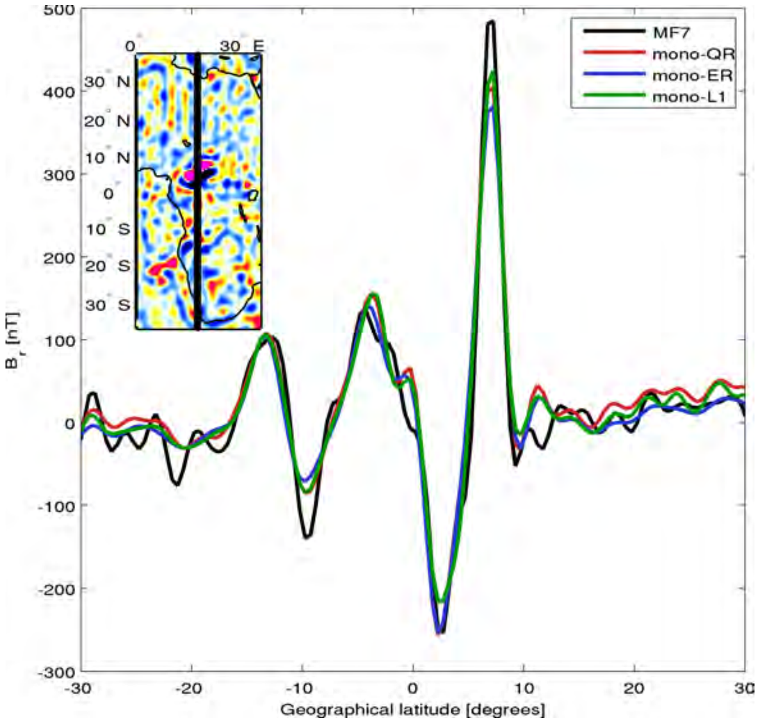

Figure 36 Model prediction for the radial lithospheric magnetic field at the Earth's surface (on a $0.5^\circ \times 0.5^\circ$ grid) along an orbital profile at longitude $\phi = 17.25^\circ$ crossing the Bangui magnetic anomaly (inserted figure, surface radial lithospheric field of model mono-QR). The result is given for MF7 (black), mono-QR (red), mono-ER (blue) and mono-L1 (green) models.

3.8.4 Comparison of model residuals

Despite the differences in both power spectra and field maps discussed above, models mono-QR, mono-ER and mono-L1 fit the measurements to a very similar level, as given in Table 6. The table shows also that, except for the non-polar RMS values of the latitudinal residuals, all investigated models fit the observations used better than MF7, CHAOS-6 and CM5. This is in agreement with the expectations, as the latter three models use either additional or other data than the models of this thesis.

Similar statistics are also displayed by the model residuals: only the corresponding values of model mono-QR are shown in Fig. 37. The residuals are most distinctive in polar regions (absolute QD latitudes $> 50^\circ$), which is assumed to be due to unmodelled signals from the polar electrojet. Ring-like structures at high latitudes are also seen in the global maps of the residuals for mono-QR, mono-ER and mono-L1 (see Appendix D, Figs. 74 to 78, Figs. 84 to 86, and Figs. 91 to 93, respectively). Also the observed shift of the radial residuals in Fig. 37 towards positive values below QD -70°, and towards negative values above QD 70°, is an indication for the polar electrojet. The corresponding westward direction (during night times) enhances and reduces the radial field component in the northern and southern hemisphere, respectively.

Additionally, the global radial residual maps show for all models (incl. MF7, CHAOS-6 and CM5) a distinct pattern along the equator, indicating unmodelled signals still present in the data set.

Figure 38 shows a histogram of the radial residuals between the CHAMP observations and the model predictions of mono-QR. The corresponding distribution is centered on zero, with a Huber weighted residual root-mean-square value of 1.66 nT (see equation (85)).

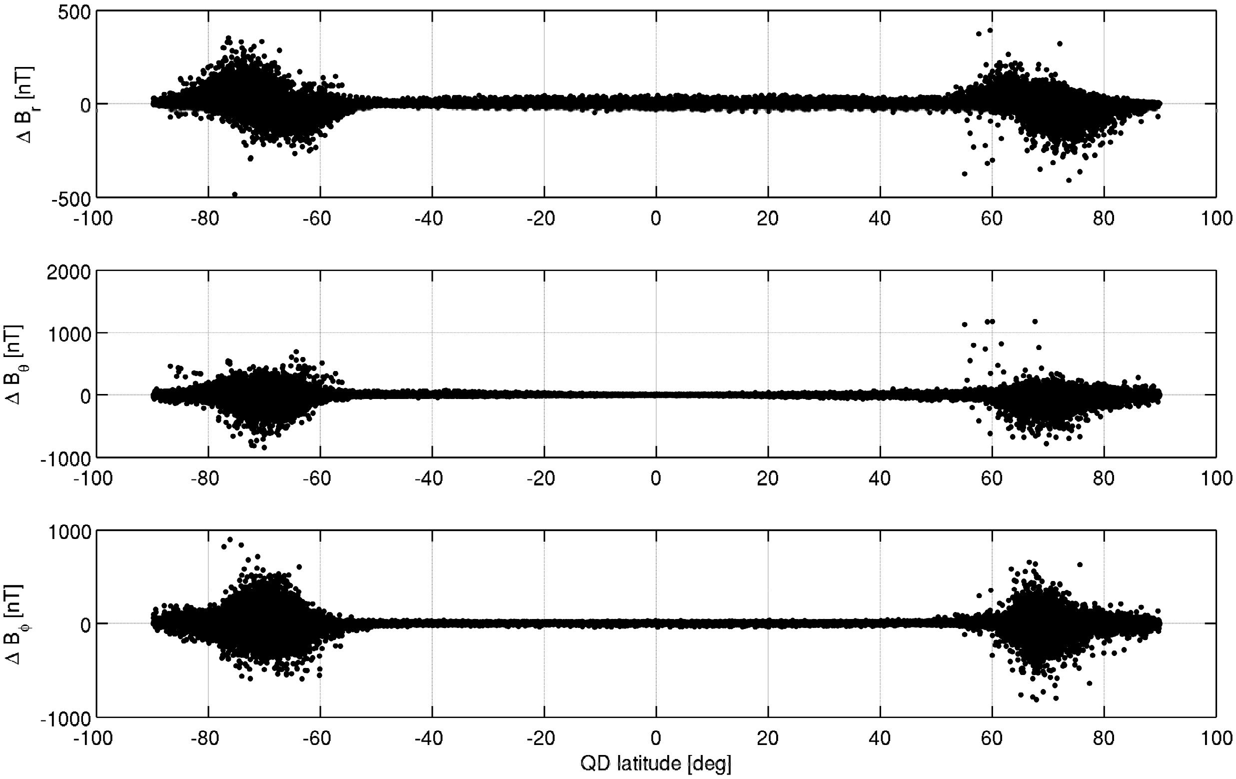

Figure 37 Residuals for the final quadratic regularized model mono-QR.

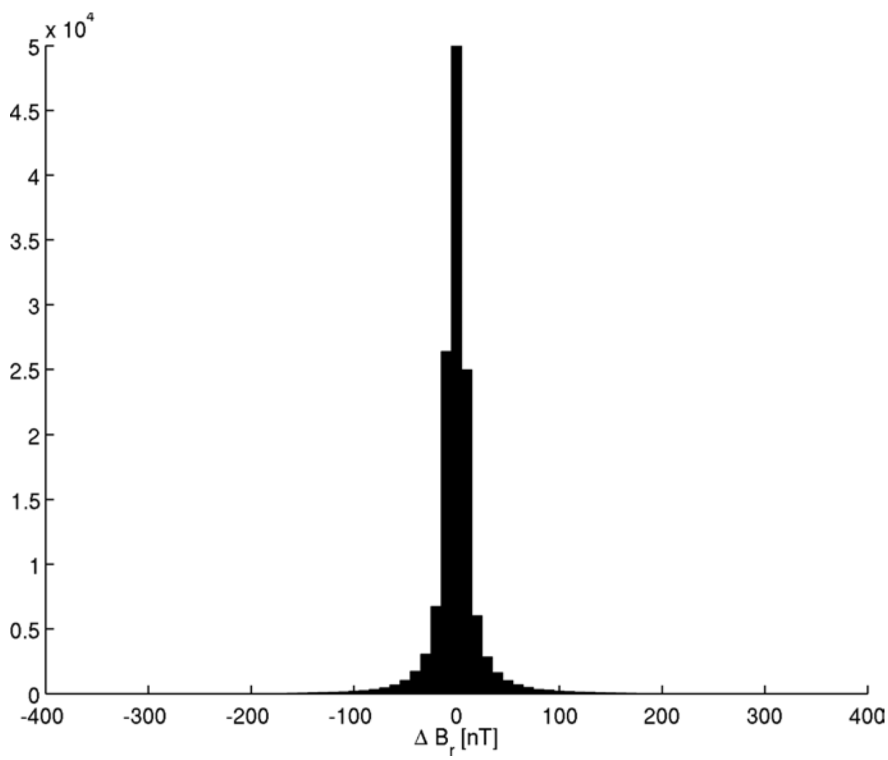

Figure 38 Radial residual histogram of model mono-QR.

3.8.5 Differences in normalized Gauss coefficients

Another way of illustrating the differences between the individual models is illustrated in Fig. 39. Here, the relative differences between two models with corresponding Gauss coefficients $[g_n^m, h_n^m]$ and $[g_n^{'m}, h_n^{'m}]$ are considered in a degree versus order matrix, with elements defined by

$$S(n,m) = 100 \cdot \frac{g_n^m - g_n^{'m}}{\sqrt{\frac{1}{(2n+1)} \sum_{m=0}^{n} [(g_n^{m*})^2 + (h_n^{m*})^2]}}, \tag{90}$$

and similarly for the corresponding h_n^m coefficients. The coefficient differences are normalized with respect to the mean spectral amplitude of a reference model $[g_n^{m*}, h_n^{m*}]$ (Olsen et al., 2005), eq. 5.3), which is defined to be MF7 for all degree/order plots of this thesis. Note that the factor 100 in equation (90) indicates that the normalized coefficient differences are given in %.

Figure 39 shows that the model differences are most notable above SH degree 60, and up to SH degree 80 the differences are almost absent for orders larger than 50. This is in good agreement with the power spectrum and degree correlation results of section 3.8.1. Additionally, interesting vertical stripes are observed especially between degrees 60 and 95, which are assumed to be associated with the observed north–south directed structures in Fig. 29, especially for model-QR.

Degree/order plots showing the differences between mono-QR, mono-ER, mono-L1 and the models MF7, CHAOS-6 and CM5 are given in Appendix D.4.

3.8.6 Model resolution and the effective number of degrees of freedom

An important method of quantitatively assessing inversion results is to compute the model resolution matrix $\underline{\underline{\mathcal{R}}}$, also known as the information density matrix. This represents the mapping between the estimated and true model parameters. Thus, if $\underline{\underline{\mathcal{R}}} = \underline{\underline{\mathbf{I}}}$ the predicted data match the observations perfectly.

For a quadratic regularization, the matrix $\underline{\underline{\mathcal{R}}}$ takes the form (e.g. Bloxham et al., 1989; Menke, 2012)

$$\underline{\underline{\mathcal{R}}}^{QR} = (\underline{\underline{\mathbf{G}}}^T \underline{\underline{\mathbf{WG}}} + \alpha \mathbf{I})^{-1} \underline{\underline{\mathbf{G}}}^T \underline{\underline{\mathbf{WG}}}. \tag{91}$$

The corresponding version for the L_1 approach and the linearized approximation for the maximum entropy approach (assuming that $\alpha \boldsymbol{\gamma} \mathbf{q}^{ER} - 4\alpha\omega\boldsymbol{\beta} \ll 2\underline{\underline{\mathbf{G}}}^T \underline{\underline{\mathbf{W}}}\mathbf{d}$) are

$$\underline{\underline{\mathcal{R}}}^{L1} = (\underline{\underline{\mathbf{G}}}^T \underline{\underline{\mathbf{WG}}} + \alpha \mathbf{T})^{-1} \underline{\underline{\mathbf{G}}}^T \underline{\underline{\mathbf{WG}}} \tag{92}$$

$$\underline{\underline{\mathcal{R}}}^{ER} = (2\underline{\underline{\mathbf{G}}}^T \underline{\underline{\mathbf{WG}}} + \alpha \boldsymbol{\gamma})^{-1} 2\underline{\underline{\mathbf{G}}}^T \underline{\underline{\mathbf{WG}}}, \tag{93}$$

respectively. The resolution of a given regularized model can be described by means of the effective number of degrees of freedom, which corresponds to the trace of the respective resolution matrix. The number of degrees of freedom was found to be 10 819, 15 337 and 8 668 for the models mono-QR, mono-L1 and mono-ER, respectively. This means that model mono-ER requires almost 20% fewer effective degrees of freedom compared to mono-QR, and almost 40% fewer effective degrees of freedom compared to mono-L1, in order to achieve the same level of fit to the observations. The remaining degrees of freedom are controlled by the model regularization.

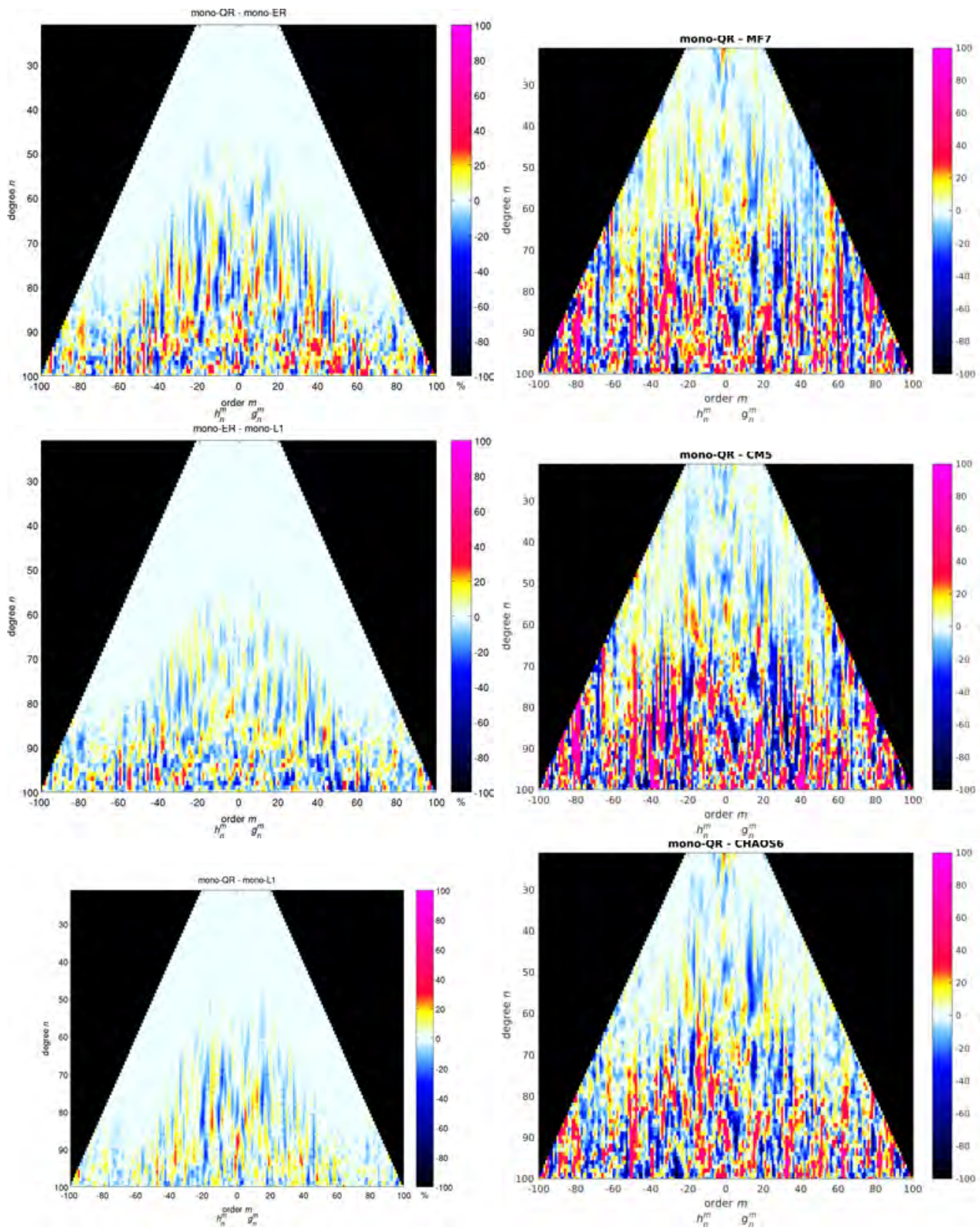

Figure 39 Normalized coefficient differences between mono-QR, mono-ER and mono-L1 (left row) and between mono-QR and the models MF7, CM5 and CHAOS-6 (right row).

3.9 Summary of global models

Global lithospheric magnetic field models were generated using an equal area grid of 38,600 equivalent point sources located at 180 km depth below the Earth's surface.
The generated model solutions were based on iterative least squares, with Huber weighting of misfit values and latitude-dependent data uncertainties implemented for all three vector field components at all latitudes. The approach was tested on lithospheric field measurements from CHAMP observations for the period 01/01/2009 to 02/09/2010. In order to minimize the influence of disturbed satellite tracks and external field signals, data were selected for e.g. geomagnetic quiet time conditions, dark regions, small hourly RC-index variations and model residuals below 100 nT.
Equivalent source models were produced by regularizing either the quadratic norm (QR), the maximum entropy (ER, which is an information-based measure of complexity), or the L_1-norm (L1) of the model parameters. The determination of the final model candidates and the corresponding regularization parameters was based on the Huber-weighted residuals, the corresponding normalized root mean square values, power spectrum comparisons and global maps of the lithospheric field at the Earth's surface. Note that an indirect regularization is also given by the chosen amount of sources and the corresponding depth below the Earth's surface, as decreasing source densities and increasing depth values result in damping of the small-scale lithospheric features.
The final selected models mono-QR ($\alpha = 80\,\mathrm{nT}^{-2}$), mono-ER ($\alpha = 500\,\mathrm{nT}^{-2}$, $\omega = 0.009\,\mathrm{nT}$) and mono-L1 ($\alpha = 4\,\mathrm{nT}^{-1}$) have been compared to each other and the state-of-the-art models MF7, CHAOS-6 and CM5 in terms of residuals and by means of radial magnetic field values globally and locally at the Earth's surface. The models mono-QR, mono-ER and mono-L1 agree very well with each other up to SH degree 60, whereupon the differences increase gradually with degree based on the various regularization parameters. However, the respective degree correlation values remain above the correlation limit of $\rho_n = 0.7$ up to at least SH degree 120. Additionally, the models correlate satisfactorily with MF7 and CHAOS-6 up to approximately SH degree $n = 100$ and $n = 105$, respectively.
The similarity of the models was also exhibited in the derived model residuals and corresponding statistics. Despite the fact that all three models achieve the same level of global fit to the observations, both the ER and L1 approach produce models which are more congruent with geological expectations: the corresponding lithospheric magnetic fields have large amplitudes locally where there are strong anomalies, and weaker amplitudes in oceanic regions.
From all investigated models, mono-ER uses the largest regularization parameter, which results in the strongest damping of the small-scale lithospheric signals. The corresponding global and regional maps are also characterized by a distinctly lower field complexity compared to the other model results. It is also interesting to notice that mono-ER has a much smaller number of degrees of freedom than mono-QR and mono-L1, despite the same level of fit to the data.

The quality of the derived field predictions is dependent on the used data and the adequate removal of non-lithospheric field signals. Thus, increasing knowledge of the external source behavior and the temporal and spatial variations of the core field, as well as the use of more recent Swarm satellite measurements and magnetic gradient data will increase both the data quality and the modeled lithospheric field resolution remarkably. The latter has been demonstrated by Olsen et al. (2017), who used a similar equivalent point source routine and L_1-norm regularization for generating a high resolution map of the global lithospheric field based on combined along-track differences from CHAMP and across-track differences from Swarm. Further model enhancements are expected once Swarm reaches an altitude below 350 km.

4 Regional lithospheric magnetic field models of aeromagnetic data using equivalent point sources

The history of aeromagnetic surveys reaches back to the first decades of the 1900s where different magnetometers were invented for the use of airborne surveys (Reford and Sumner, 1964). The corresponding measurements reveal information for geologic mapping, the depth to magnetic basement rocks in sedimentary basins (important for oil surveys), and subsurface susceptibilities and dips (important for mineral surveys) (Reford and Sumner, 1964). Compared to other geophysical approaches, aeromagnetic measurements are less time consuming and more cost effective per unit area explored (Hamoudi et al., 2011). In that sense it is a favorable technique to use in the early stages of finding interesting exploration areas, after which other methods are applied for more detailed investigations (Reford and Sumner, 1964; Grant, 1985).
This chapter focuses on the generation of regional lithospheric field models based on equivalent point sources using the inversion scheme of chapter 2.3. The derived models are based on three aeromagnetic surveys from offshore Norway, kindly provided by the Norwegian Geological Survey (NGU). The derived model resolution is highly dependent on the chosen equivalent source density and depth. Additional investigations concern the influence of regularization and the models' ability for upward and downward continuation. The latter is a crucial criterion for using the equivalent source application for directional drilling, which will be discussed in the final part of this chapter.

4.1 Aeromagnetic data from offshore Norway

Regional lithospheric field models based on equivalent point sources are investigated using aeromagnetic survey data kindly provided by NGU. All provided data are corrected by NGU for aircraft effects, main field contributions and temporal field variations. The corresponding data processing routines have been performed by NGU applying statistical and micro-levelling algorithms from Geosoft OASIS Montaj (Geosoft 2010a, 2010; Geosoft 2010b, 2010). A general introduction to these routines is given in Appendix A.
The used surveys were acquired between 1971 and 1990 and differ in size, line spacing, and processed data elevation. Table 7 lists the corresponding survey information and the covered survey area is illustrated in Fig. 40.
NGU-74-75 is the oldest data set and covers the Norwegian continental shelf in the Norwegian North Sea. This data set is the largest of all three provided surveys, comprising of 42 000 km survey length. The survey was flown at approximately 280 m altitude and with line spacings ranging between 1 km and 7 km.
Between 1971 and 1973, Fairey has performed several aeromagnetic surveys covering the Viking Graben (Fairey-71a) and the Shetland Basin (Fairey-71b, Fairey-72, Fairey-73). This thesis uses the former data set, containing 11 000 km line volume. The corresponding flight altitude ranges between 300 m and 500 m.
Similar to Fairey-71a, the Viking Aeromagnetic Survey 1993 (Viking-93) covers the northern part of the Viking Graben. This survey was flown between April and June 1993 with a mean altitude of about 240 m and maximal line spacings and tie-line spacings of 2 km and 5 km, respectively.
All provided survey data contain lithospheric intensity values given in geodetic coordinates with elevations relative to the mean sea level. These orthometric heights are transformed into the WGS84 ellipsoidal (geodetic) heights using the ellipsoid egm-84 and the MATLAB® function *geoid_height.m*. The equivalent source modelling scheme uses the corresponding geocentric coordinates $\mathbf{r} = (r, \theta, \phi)$.

	Fairey-71a	NGU-74-75	Viking-93
Year	1971	1974-1975	1993
Contractor	NGU	NGU	NGU
Operator	NGU	Fairey	NGU
Flight altitude [m]	300-500	333/239/279*	405/36/238*
Line spacing [km]	2	1-7	0.5-2 (1.25-5)△
Line volume [km]	11,100	42,000	28,000
Subtracted IGRF model	DGRF-1975	IGRF-1975	DGRF-1990
Processed data altitude [m]⋆	300	300	150
Reference	Åm (1973); Olesen et al. (1997, 2010)	Olesen et al. (1997, 2010)	Smethurst (2000), Viking-93

Table 7 Aeromagnetic survey data applied for the present study.
* Flight altitudes are given in max/min/mean values.
⋆ Processed data altitude values are given in geodetic coordinates above sea level.
△ Tie-line spacings are given in parenthesis.

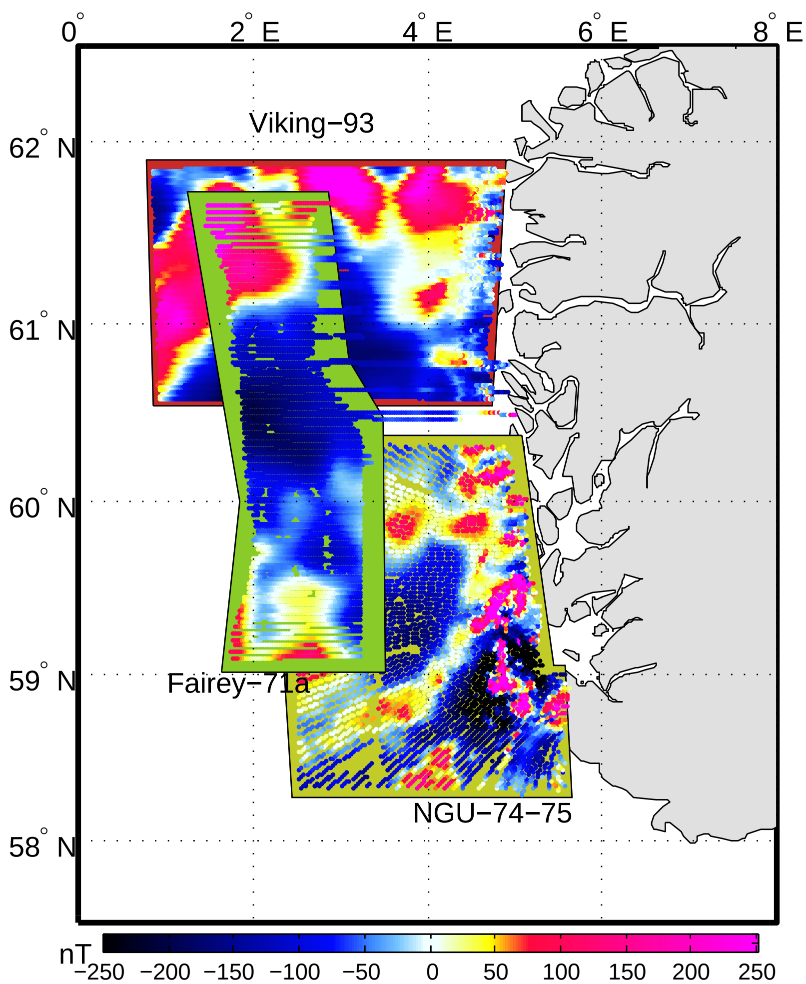

Figure 40 Aeromagnetic intensity data (every 10th point), displayed in geocentric coordinates, corresponding to the surveys Fairey-71a, NGU-74-75 and Viking-93. Note that the data elevations differ between the individual surveys as indicated in Table 7. Each survey is emphasized by a certain background color (red = Viking-93, green = Fairey-71a and yellow = NGU-74-75).

4.2 Equivalent source distribution for regional lithospheric field models

Compared to satellite data, airborne and marine magnetic measurements are closer to the respective sources and provide more information on the small-scale features of the lithospheric field. Producing corresponding high resolution regional lithospheric field models based on equivalent sources thus requires a larger grid resolution than found for the global models in section 3.3.

Similar to the global models of chapter 3.3, the regional lithospheric field models of this thesis are based on equal area distributed equivalent point sources located at a certain depth below the Earth's surface. Different source grid sizes are tested for a range of source depth values and corresponding un-regularized *Huber*-weighted equivalent source models are derived for each of the aeromagnetic surveys (corresponding results are not given here). Table 8 gives the respective grid specifications. Note that the used data error values are defined to be unity instead of being latitude dependent.

Compared to models based on globally distributed data, not all sources given in the second column are applied for regional model investigations. Since aeromagnetic surveys only cover a fracture of the globe, only sources in the survey vicinity are used for the respective model derivations. Projecting all sources and data points to the Earth's surface, only sources for which the distance to the closest data point does not exceed 20 km are approved for the model inversions, see Fig. 41. The resulting source amount for the individual surveys is given in the last columns of the table.

The positive correlation between grid resolution and a model's ability to represent the measurements stops at a certain level. This level can be found based on the investigated model's residual 2-norm, correlation coefficient and residual RMS. A further increase in grid resolution will not improve the corresponding values or can even cause model convergence problems.

The preferred grid resolution should be large enough for deriving reasonable models with statistical parameters within an acceptable range, and small enough for minimizing calculation time and convergence problems. Having this in mind, the maximal possible source amount for the individual surveys (highlighted in bold in the last three columns of Table 8) are used for further model investigations.

L	# global sources (K_g)	Surface source distance [km]	# Local sources (K) **Fairey-71a**	**NGU-74**	**Viking-93**
1	500000	31.94	43	45	44
2	1000000	22.58	93	91	87
3	1500000	18.44	136	144	134
4	2000000	15.97	172	184	185
5	2500000	14.28	226	237	224
6	3000000	13.04	270	275	264
7	3500000	12.07	**313**	325	305
14	7000000	8.53		**644**	608
16	8000000	7.98			**708**

Table 8 Investigated grid sizes L and corresponding regional source amount K for the individual aeromagnetic survey models. Bold values correspond to the chosen amount of sources for further model investigations. The surface distance between two sources (third column) is estimated with $\sqrt{\frac{4\pi a^2}{K_g}}$, where $a = 6371.2km$ is the Earth's mean radius and K_g represents the global amount of sources (second column).

4.2.1 Source depth estimate from Metropolis-Hastings algorithm

After choosing the source grid density, the next step prior to model inversion is to determine an appropriate source depth. For the global field models of section 3.3.2, the preferred source depth was subjectively chosen since the major model features were highly dependent on the used regularization type and corresponding parameter. However, for the used regional surveys it yields that regularization does not have the same effect on the final model predictions of the lithospheric scalar field. In fact, regional model regularization is mainly necessary for generating realistic field components for upward and downward continuation (see Appendix

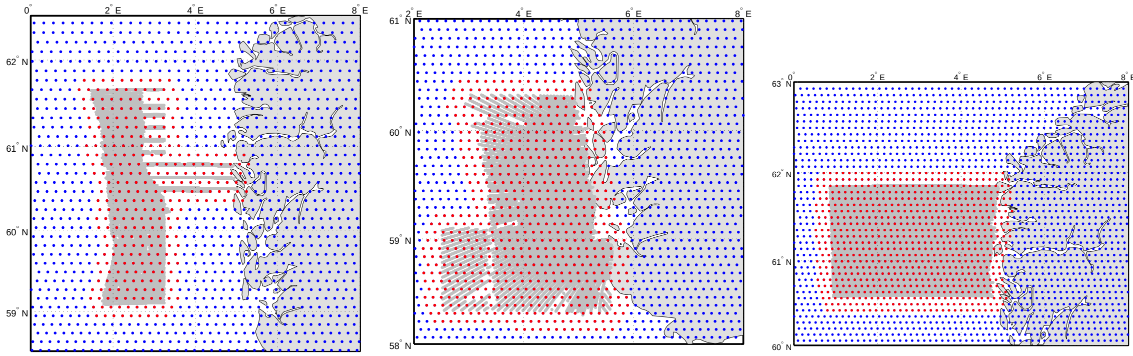

Figure 41 Global source distribution (blue) and corresponding source locations (red) used for generating lithospheric field models of the aeromagnetic survey (grey) Fairey-71a (left), NGU-74-75 (middle) and Viking-93 (right).

E.1). But apart from the vector field predictions, the source depth, rather than regularization, plays the key role for defining the level of model accuracy.
This thesis uses a Monte Carlo Metropolis Hastings algorithm for nominating the source depth of regional lithospheric field models based on aeromagnetic data. The corresponding code is easy to implement but expensive in calculation time. In order to reduce the calculation time of the algorithm, the largest possible source depth values need to be determined for local field models of a given aeromagnetic survey. For this purpose, un-regularized inversions are performed using the maximal source densities of Table 8 and source depth values between 0 and 100 km. Figure 42 illustrates the corresponding Euclidean norm of the model residuals at data altitude. For the surveys Fairey-71a, NGU-74-75 and Viking-93 no model convergence could be reached beyond 65 km, 45 km and 40 km, respectively.

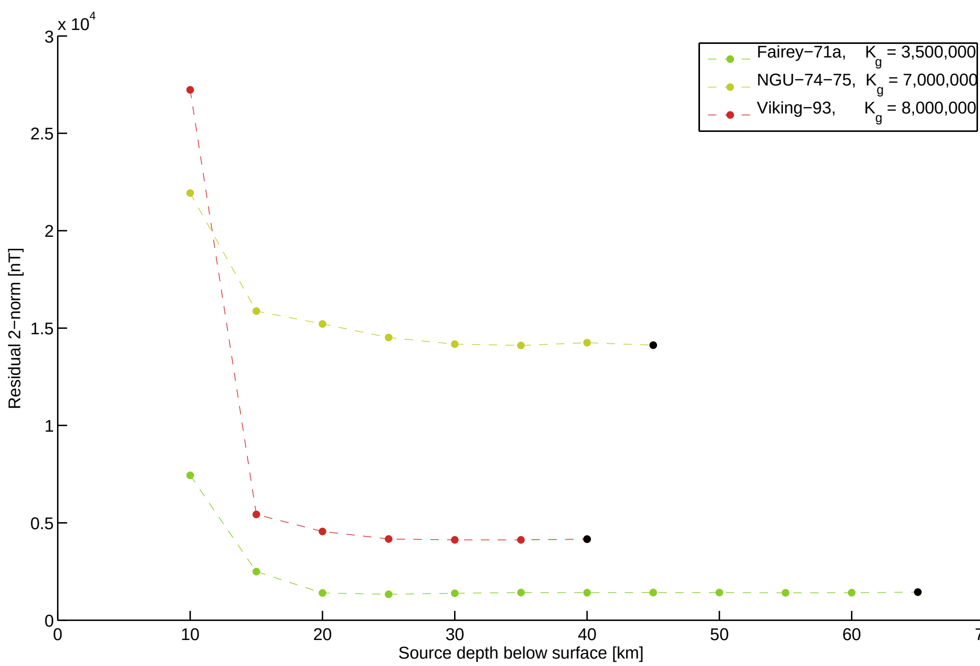

Figure 42 Un-regularized model residual 2-norm at data altitude corresponding to the aeromagnetic surveys of Table 7. The different source grid resolutions are indicated in the legend and Table 8. The black colored circles represent the maximum allowed depth values for model convergence and for the Metropolis Hastings algorithm. Note that the minimum investigated source depth is 10 km as the geocentric data altitude is around 9 km, see Table 9.

The used source depth is now determined by performing 560 (due to expensive computations) un-regularized inversion runs with depth values randomly chosen by a Metropolis Hastings algorithm. The maximum allowed source depth values are as indicated in Fig. 42
For a given run ζ (for $\zeta = 1, ..., 560$) the depth value is derived as follows,

$$\delta_\zeta = \delta^{org}_{\zeta-1} + \beta \Delta\delta \tag{94}$$

where $\Delta\delta = 20\,\text{km}$ represents the maximum perturbation in depth, δ^{org} is the initial depth value derived in the previous run and $\beta = 1$. For $\zeta = 1$ the initial depth value is defined to $\delta^{org}_0 = 10\,\text{km}$.
The probability for the chosen source depth value is defined to be based on the corresponding Euclidean norm of the model residuals $\nu(\delta_\zeta)$,

$$p_{acc,\zeta} = \begin{cases} e^{-(\nu(\delta_\zeta) - \nu(\delta^{org}_{\zeta-1}))}, & \text{for } \nu(\delta_\zeta) > \nu(\delta^{org}_{\zeta-1}) \\ 1, & \text{otherwise} \end{cases} \tag{95}$$

Depending on $p_{acc,\zeta}$, the depth candidate δ_ζ is either accepted or rejected for the next inversion run,

$$\delta^{org}_\zeta = \begin{cases} \delta_\zeta, & \text{for } \gamma \leqslant p_{acc,\zeta} \\ \delta^{org}_{\zeta-1}, & \text{otherwise.} \end{cases} \tag{96}$$

Here, γ is a uniformly distributed random number in the interval (0,1).
Using the residual 2-norm as statistical parameter is an individual choice. It is assumed that the derived source depth values may differ when applying another statistical parameter as basis for the model selection routine.
Figure 43 shows the proposed and accepted source depth values for the three NGU survey models. The probability density functions (PDF) for the corresponding normal distributions are given in the lower right part of the figure. The respective peak values are found for 23 km (Fairey-71a), 37 km (NGU-74-75) and 39 km (Viking-93). Please note, that the latter value is only based on a fraction of the original survey area ($\theta > 61.5°$ and $\phi < 3°$) due to heavy computation time.

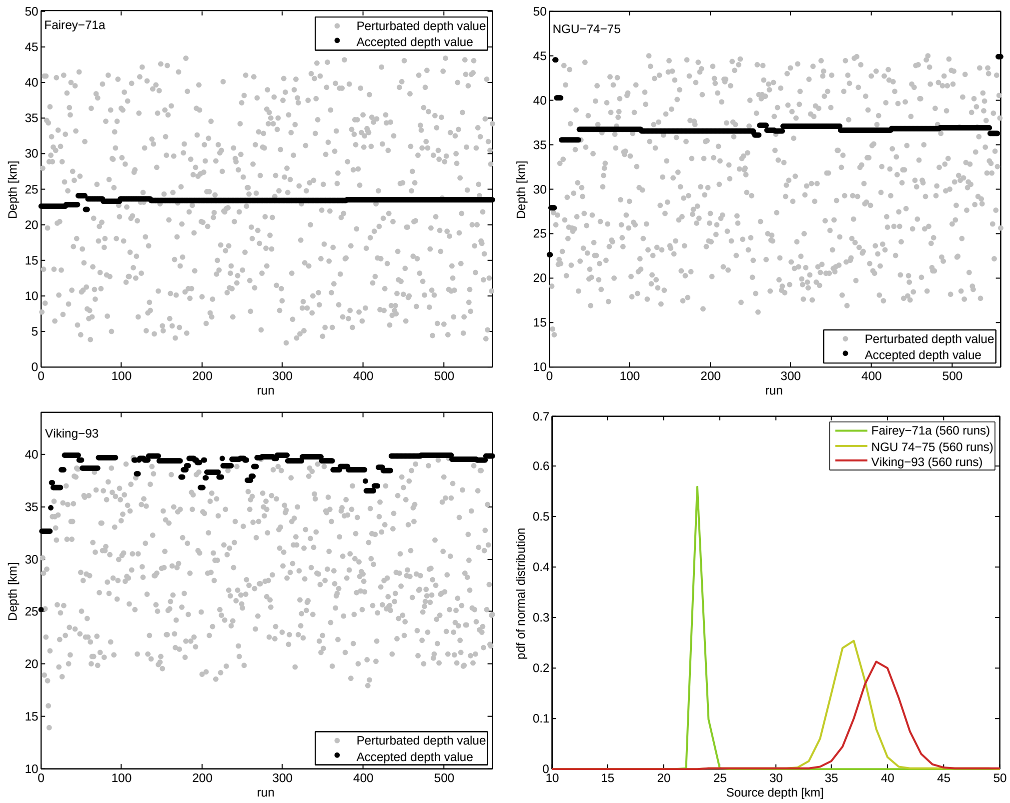

Figure 43 Perturbated (grey) and accepted (black) depth values due to the Metropolis Hastings algorithm for 560 un-regularized model inversions of the Fairey-71a (upper left), NGU-74-75 (upper right) and Viking-93 (lower left) surveys. The corresponding source grid sizes are $L = 6$, $L = 7$ and $L = 14$, respectively. The initial depth is 10 km and maximum allowed perturbation in depth is $\Delta\delta = 20$ km. The lower right part of the figure gives the PDF for the normal distributions corresponding to the accepted source depth values for the surveys Fairey-71a (green), NGU-74-75 (yellow) and Viking-93 (red). The corresponding peaks are derived for 23 km, 37 km and 39 km source depth, respectively.

4.2.2 Model regularization

Figure 44 illustrates the quadratic regularized L-curve for the different aeromagnetic surveys using the source depth values defined in the previous section. Corresponding model statistics are given in Tables 20, 21 and 22 in Appendix E.1. These latter two tables demonstrate that regularization has no major effect on the field intensity predictions, but is crucial for the derivation of realistic values for the vector components when performing upward or downward continuation.
For the survey Fairey-71a, all investigated quadratic regularization parameters result in stable conditions for upward and downward continuation. The preferred value is thus defined to $\alpha = 400\,\mathrm{nT}^{-2}$, which is close to the knee-point of the respective L-curve.
For survey Viking-93 it is found that the small-scale spatial features along the coastline cannot be captured by the chosen source density. This results in large residual values and unrealistic vector field predictions in these regions. By generating these model prediction maps for various altitudes using different regularization parameters (corresponding results are not given here), the preferred damping for survey Viking-93 is defined to $\alpha = 600\,\mathrm{nT}^{-2}$. This value is larger than the knee-point of the corresponding L-curve, thus giving more importance to the model norm than the residuals.
Despite the well shaped L-curve of Fig. 44, no suitable regularization parameter value was found for survey NGU-74-75. Visual inspection of vector field maps revealed that a regularization parameter of minimum $\alpha = 2000\,\mathrm{nT}^{-2}$ is necessary to ensure reasonable field predictions for both upward and downward continuation, therefore this value will be used in the following.
Table 9 summarizes the derived model details.

	Fairey-71a	**NGU-74-75**	**Viking-93**
# sources	313	644	708
# Field intensity data	89,186	57,270	294,910
Data altitude [km]*,*	-8.9	-8.5	-9.3
Max. source depth [km]*	65	45	40
Model source depth [km]*	23	37	39
α_{L2} [nT^{-2}]	400	2000	600
IGRF$^{\triangle}$	DGRF-1970	DGRF-1975	DGRF-1990

Table 9 Defined source grid, depth and regularization parameters for the model inversions of individual aeromagnetic surveys.
$^{\triangle}$ IGRF version used for the core field predictions necessary for generating the scalar version of the Greens' matrix $\underline{\underline{\mathbf{G_s}}}$ (see equation 84). The IGRF versions are not necessarily identical to the date of data collection, but have been used to generate the processed data provided by NGU.
* Both data and source depth values are with respect to the Earth's mean surface with radius 6371.2 km.
* Mean value for geocentric data altitude.

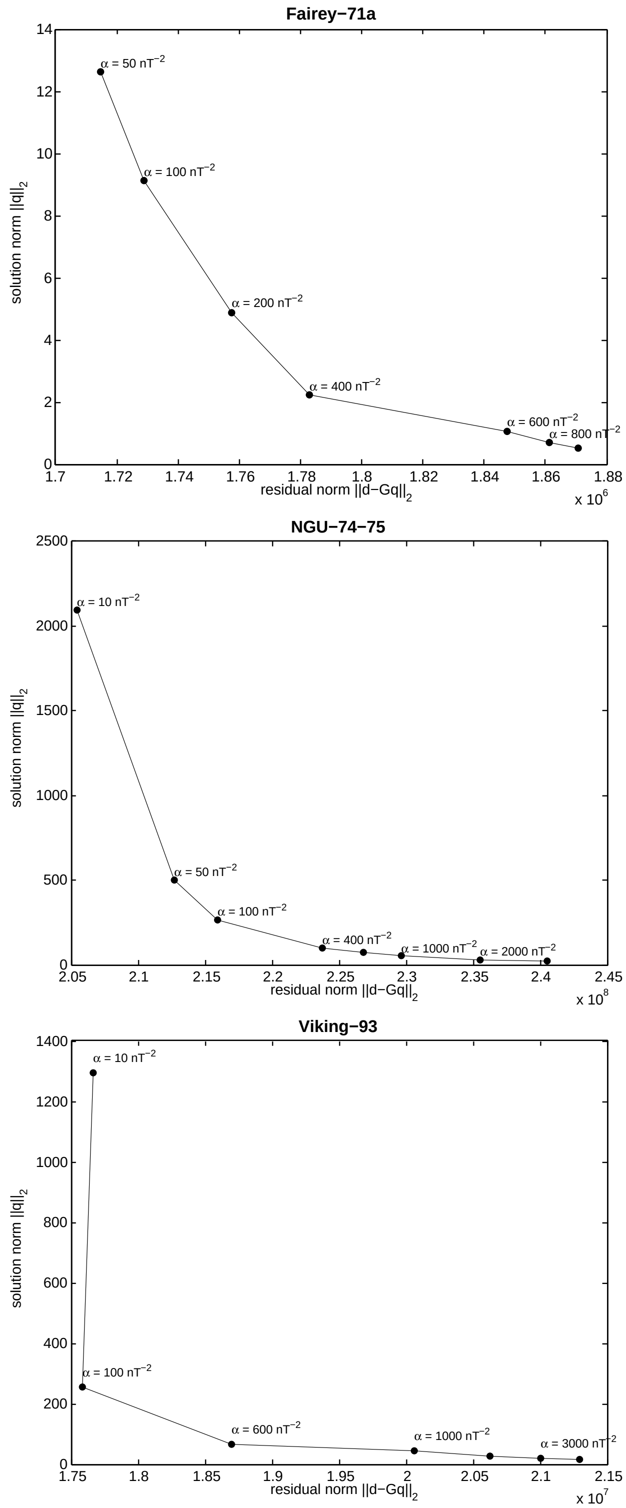

Figure 44 L-curve for quadratic regularized models using aeromagnetic surveys Fairey-71a, NGU-74-75 and Viking-93 and the source depth values of 23 km, 37 km, and 39 km, respectively. Corresponding model statistics are given in Appendix E.1.

4.3 Regional model results

Using the above described regularization parameters, Figs. 45 to 47 illustrate the field predictions and corresponding residuals for the three surveys.
The absolute residual values are typically around 5 nT. For especially the surveys NGU-74-75 and Viking-93 the figures show clearly that the chosen source distances are too large in order to capture the detailed field structures along the coastline. These areas are characterized by absolute residual values beyond 50 nT.
Both the models for surveys Fairey-71a and Viking-93 fit the observations with residual RMS values of about 2.3 nT. However, for the oldest data set NGU-74-75 it seems that the small source density value compared to the coastal field structures and possible noise in the data which has not been accounted for, result in a residual RMS value as large as 9.5 nT.
The equivalent source method does not deal well with regional small-scale structures. Higher source grid densities are required to solve this problem. This, however, can have large effects on the computation time or result in memory issues.

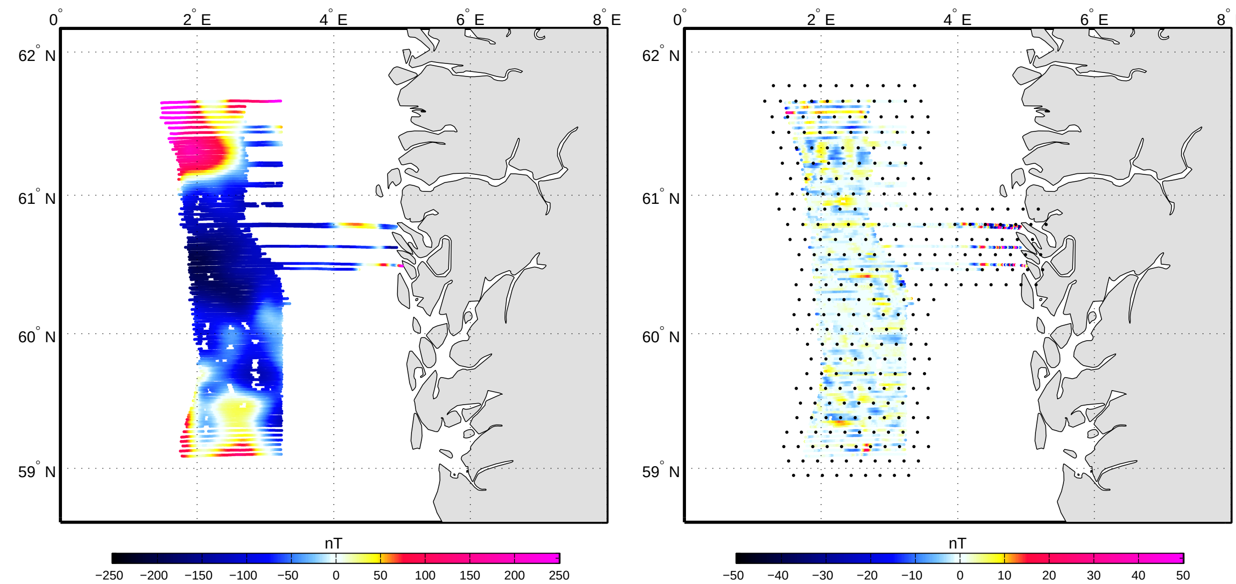

Figure 45 Model predictions of the lithospheric field intensity at data locations (left) and corresponding residuals (right) for Fairey-71a. The used quadratic regularization parameter, source amount and favorite depth is $\alpha = 400\,\mathrm{nT}^{-2}$, 313 (black dots) and 23 km, respectively. The weighted residual RMS is of 2.29 nT. The corresponding max, min and mean values of the residuals are 115.99 nT, −120.84 nT and 0.09 nT, respectively. Using initial source values of zero nT, model convergence was reached after 12 iterations.

4.4 Downward continuation

Having determined the source values, the equivalent source approach allows for upward and downward continuation, predicting the geomagnetic field at any location above the source grid.
Applying the model results of survey Fairey-71a for grid size $L = 7$ and a source depth of 23 km, Fig. 48 illustrates the corresponding intensity predictions for four different depth values below the Earth's surface, utilizing the core field values from DGRF-1970 for degrees $n = 1 : 10$. The figure shows smooth field variations with depth.
Even if the original data does only provide information of the field intensity, model predictions can be given for all three vector components using equation 29. This is demonstrated in Fig. 49, which illustrates all vector components and field intensity at 10 km depth based on the quadratic regularized model result using $\alpha = 400\,\mathrm{nT}^{-2}$, a grid size of $L = 7$ and a source depth of 30 km. Compared to Fig. 48, these model predictions are not given at data locations but rather on a $0.01° \times 0.02°$ grid. Areas outside the original

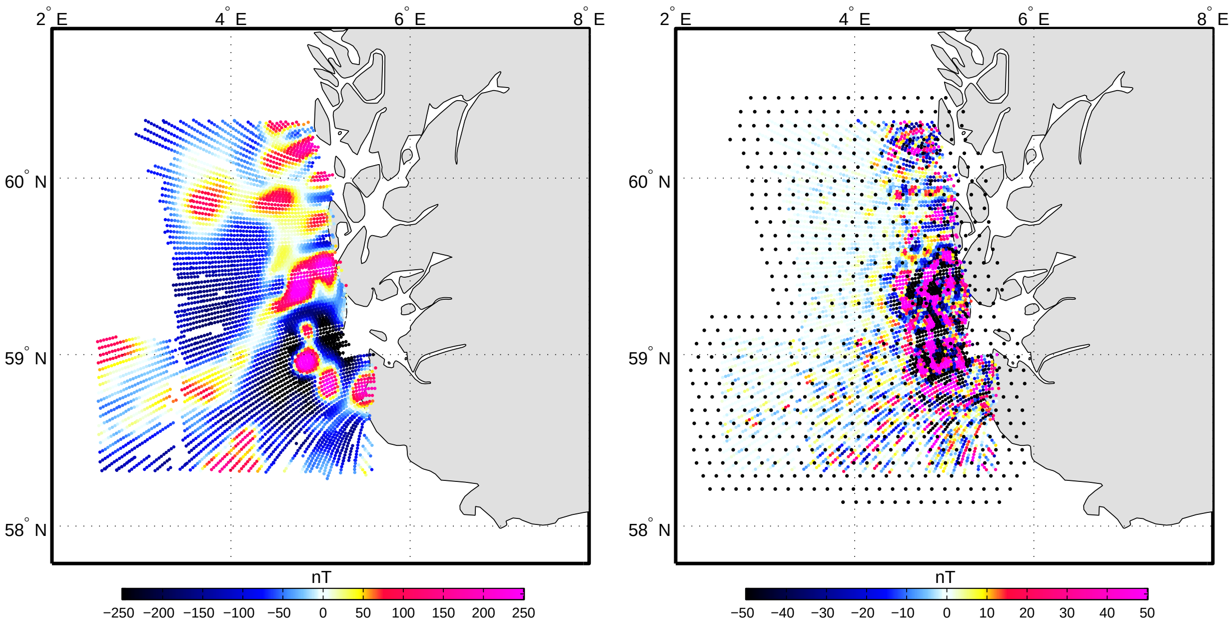

Figure 46 Model predictions of the lithospheric field intensity at data locations (left) and corresponding residuals (right) for NGU-74-75. The used quadratic regularization parameter, source amount and favorite depth is $\alpha = 2000\,\mathrm{nT}^{-2}$, 644 (black dots) and 37 km, respectively. The weighted residual RMS is of 9.55 nT. The corresponding max, min and mean values of the residuals are 1125.6 nT, −411.22 nT and 4.47 nT, respectively. Using initial source values of zero nT, model convergence was reached after 18 iterations.

survey coverage are not shown, as corresponding model predictions are non-reliable.
Appendix E.2 gives the corresponding results for the remaining surveys NGU-74-75 and Viking-93.

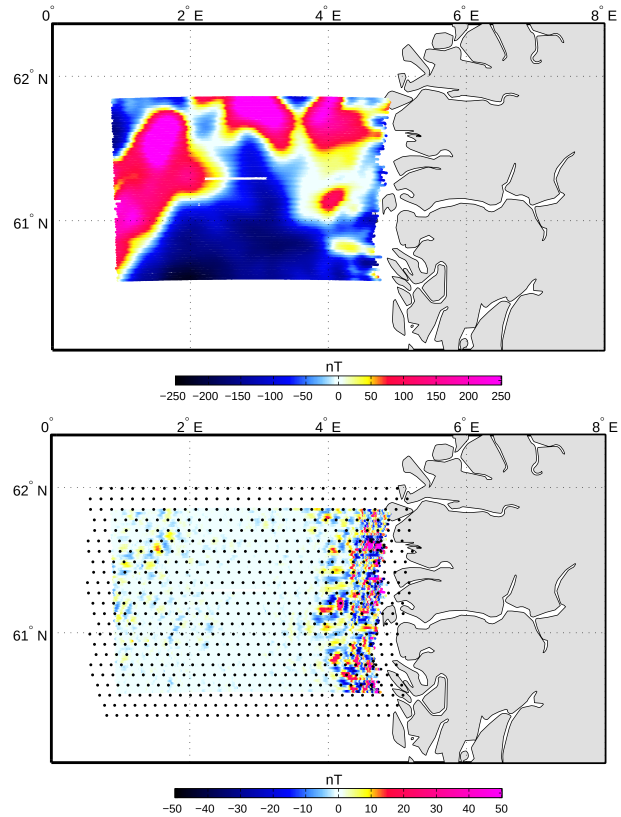

Figure 47 Model predictions of the lithospheric field intensity at data locations (top) and corresponding residuals (bottom) for Viking-93. The used quadratic regularization parameter, source amount and favorite depth is $\alpha = 600\,\mathrm{nT}^{-2}$, 708 (black dots) and 39 km, respectively. The weighted residual RMS is of 2.25 nT. The corresponding max, min and mean values of the residuals are 301.5 nT, −334.35 nT and 0.27 nT, respectively. Using initial source values of zero nT, model convergence was reached after 12 iterations.

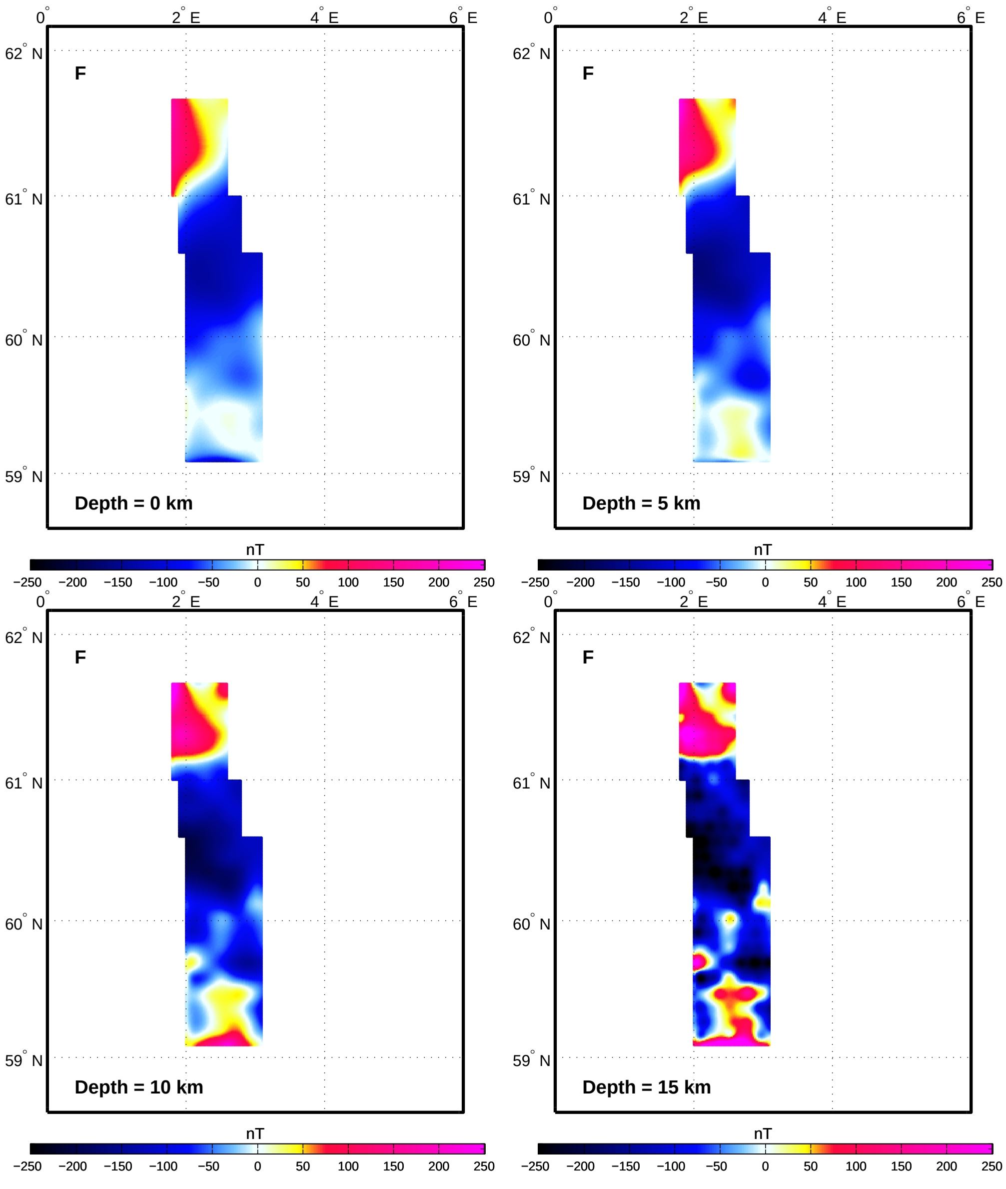

Figure 48 Model estimation of the Fairey-71a lithospheric field intensity for different depth values below the Earth's surface $a = 6371.2\,\mathrm{km}$. The corresponding model values are based on the quadratic regularized ($\alpha = 400\,\mathrm{nT}^{-2}$) model results with $L = 7$ and a source depth of $23\,\mathrm{km}$.

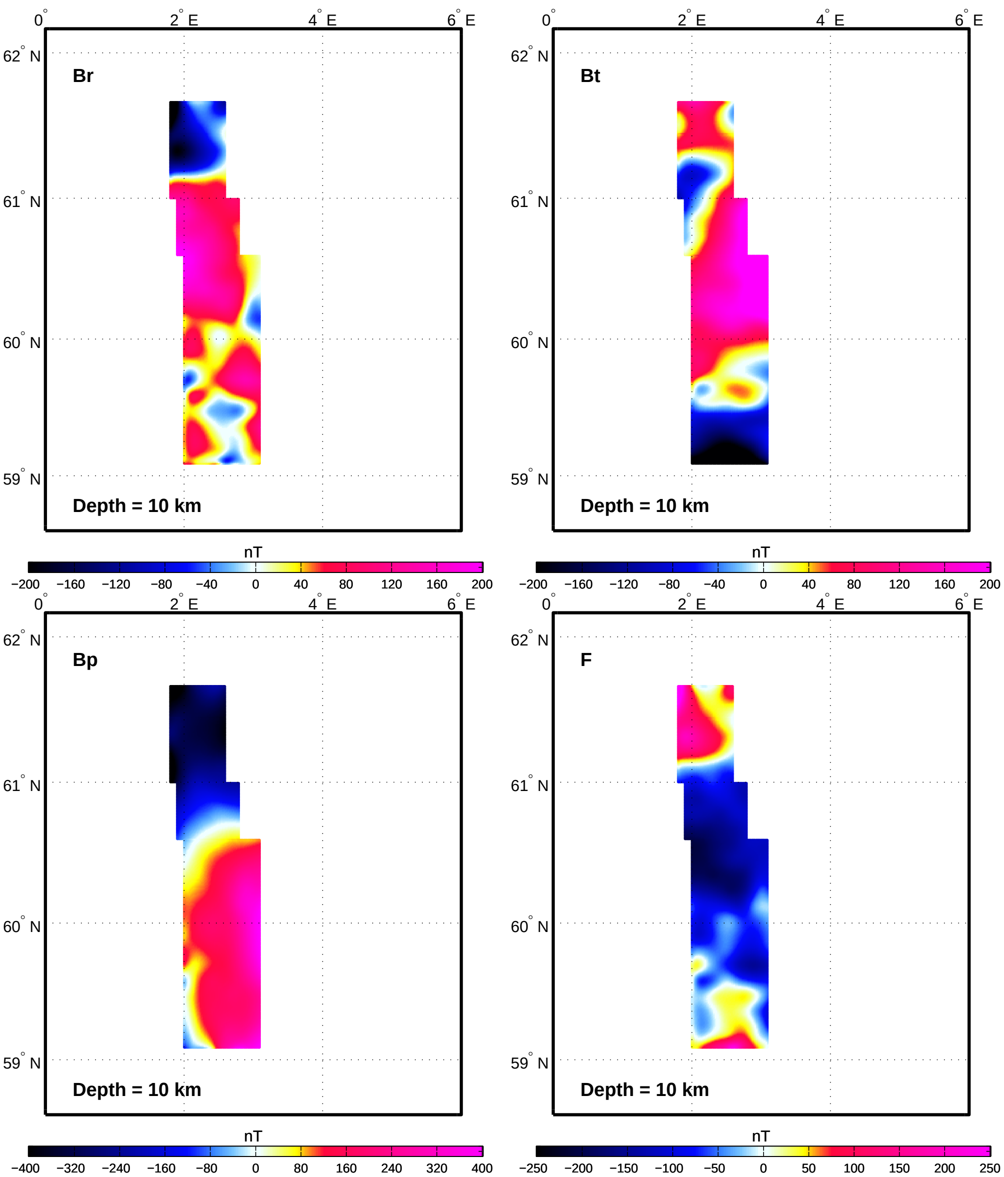

Figure 49 Fairey-71a model estimations of the three lithospheric field components and the field intensity at 10 km depth below the Earth's surface $a = 6371.2$ km. The corresponding model values are based on the quadratic regularized ($\alpha = 400\,\mathrm{nT}^{-2}$) results with $L = 7$ and a source depth of 23 km. B_t and B_p correspond to B_θ and B_ϕ, respectively.

4.5 Comparison of regional lithospheric magnetic field models for directional surveying using an equivalent source based DTU model and BGGM2016: A case study at one specific Ekofisk well

This final section of the chapter demonstrates the applicability of the equivalent source method for directional wellbore surveying. For that purpose, DTU model predictions for the total field intensity, magnetic declination and inclination are compared to corresponding values from the British Geological Survey (BGS) industry standard BGGM2016 model at one specific well of the Ekofisk field. The DTU model uses predictions from the CHAOS-6 geomagnetic field model (Finlay et al., 2016a) for the large-scale field, together with predictions from an equivalent source model, derived from aeromagnetic data, for the local crustal signal.
The application of actual geomagnetic well data was kindly authorized by ConocoPhillips. The provided well locations are confidential and have been anonymized in this section.
The use of DTU's global geomagnetic reference field model is described in section 4.5.1. Sections 4.5.2 and 4.5.3 present the aeromagnetic data and resulting equivalent source model for the local lithospheric field predictions. The final model predictions for the given Ekofisk well are presented in section 4.5.4, along with comparisons to respective model predictions from BGGM2016. Section 4.5.6 summarizes the results in the same form as the BGS predictions provided to ConocoPhillips by Halliburton.

4.5.1 DTU global geomagnetic reference model, CHAOS-x

The global geomagnetic reference field $\mathbf{B}^{main}$ is based on the latest version of the CHAOS-x field model, CHAOS-6 (Finlay et al., 2016a). This global geomagnetic field model applies ground observatory data as well as satellite data from both Ørsted, SAC-C, CHAMP and Swarm (from 26 November 2013 to 30 March 2016). An additional feature is the inclusion of along-track field differences for both CHAMP and Swarm as well as east-west gradients derived from *Swarm Alpha* and *Swarm Charlie*. For the present case, both CHAOS-6 time-dependent internal field for spherical harmonic degrees 1-20, its static internal field for spherical harmonic degrees 21-110 and its external field prediction for the daily mean value of the 1st of May 2016 are used. Fully advantage cannot be taken of the CHAOS-6 external field model (with hourly resolution) and no estimate of the solar-quiet diurnal variation can be included (despite this being available within the extended CHAOS-x framework) due to the lack of time-stamp associated with the provided dates and locations.

4.5.2 Aeromagnetic data from the specific Ekofisk well

The local crustal field model is based on final processed geomagnetic intensity observations (F_{MAGAN}) from the aeromagnetic surveys CGAM-95 and HDCG-95 (MAGAN). The respective survey area is located in the North Sea, along the British-Norwegian off-shore border line, see Fig.50. Data were acquired between June and July 1995 and provided by TGS-NOPEC Geophysical Company ASA (TGS). This data set was recommended as the most appropriate by ConocoPhillips and had all the required location and processing data available. The altitude of the processed gridded data used is 400 ft above mean sea level (MSL). Similar to section 4.1, this orthometric height and the corresponding locations were transformed into geocentric coordinates $\mathbf{r} = (r, \theta, \phi)$ for the modelling scheme.

As part of the original data processing, the large-scale internal field signal was removed from the data using IGRF-90 for spherical harmonic degrees n = 1:10. This reference field is hereafter denoted as $\mathbf{B}_{main90}(\mathbf{r})$. F_{MAGAN} are the data, reduced using $\mathbf{B}_{main90}(\mathbf{r})$, provided by ConocoPhillips. In addition, for consistency with the CHAOS-6 model, a prediction for the scalar component of the large scale crustal field is removed from the data. The respective values are denoted $A(\mathbf{r})$ and obtained from the CHAOS-6 vector field for SH degrees n = 11:110, $\mathbf{A}(\mathbf{r})$, projected onto the IGRF-90 main field direction (see equation 83),

$$\begin{aligned} A(\mathbf{r}) &= \frac{\mathbf{B}_{main90}(\mathbf{r}) \cdot \mathbf{A}(\mathbf{r})}{|\mathbf{B}_{main90}(\mathbf{r})|} \\ F_{crust}(\mathbf{r}) &= F_{MAGAN}(\mathbf{r}) - A(\mathbf{r}) \end{aligned} \tag{97}$$

Figure 51 illustrates the resulting crustal field intensity values $F_{crust}(\mathbf{r})$ that are used as input to the equivalent source modelling scheme.

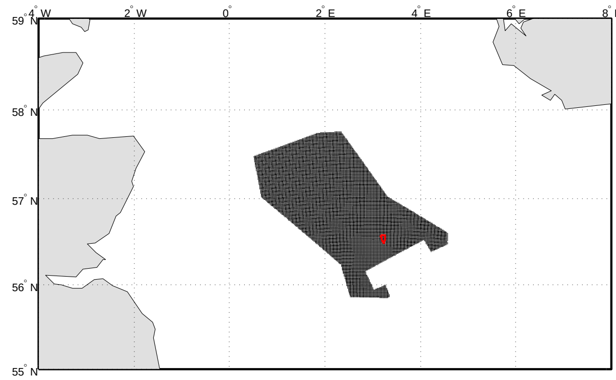

Figure 50 Geodetic coordinates of the MAGAN survey (black) and Ekofisk field (red).

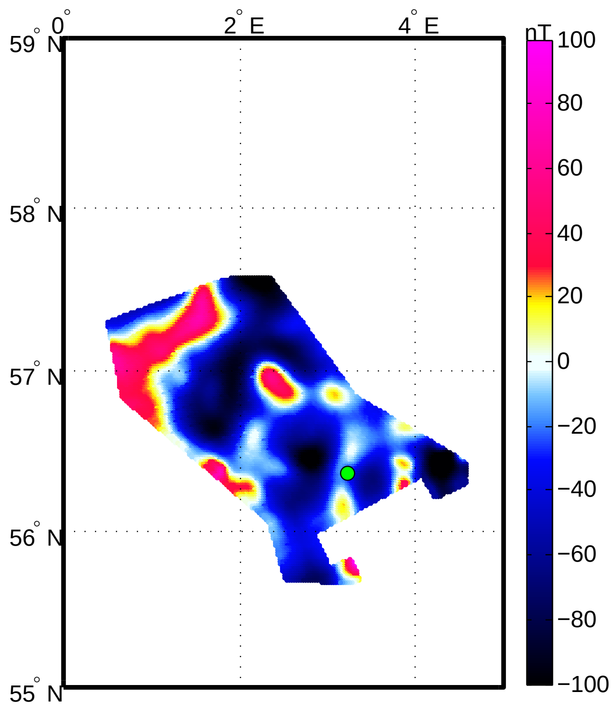

Figure 51 Aeromagnetic intensity data (F_{crust}) used in this study, displayed in geocentric coordinates. Large scale internal field signals for SH degrees n = 11:110 have been subtracted using CHAOS-6 model predictions aligned with the IGRF-90 main field. The green circle represents the approximate location of the specific Ekofisk well.

4.5.3 Equivalent source model of the local crustal field

In order to minimize wellbore navigation errors due to spatial variations of the nearby geology, local crustal field estimations based on marine- and/or aeromagnetic data are often included in the final magnetic field predictions for a directional wellbore survey. The mathematical method used here corresponds to the equivalent source based routine already described in the previous sections of this chapter. More details regarding the

derivation of the used source amount (K = 285), depth (53 km below the Earth's surface) and regularization (quadratic regularization parameter $\alpha = 300\,\mathrm{nT}^{-2}$) are given in Appendix F. The appendix demonstrates also the derived model's capability for stable downward continuation, which is the basis for geomagnetic field predictions at different depth values at the given Ekofisk well.
Figure 52 illustrates the derived model predictions at data locations.

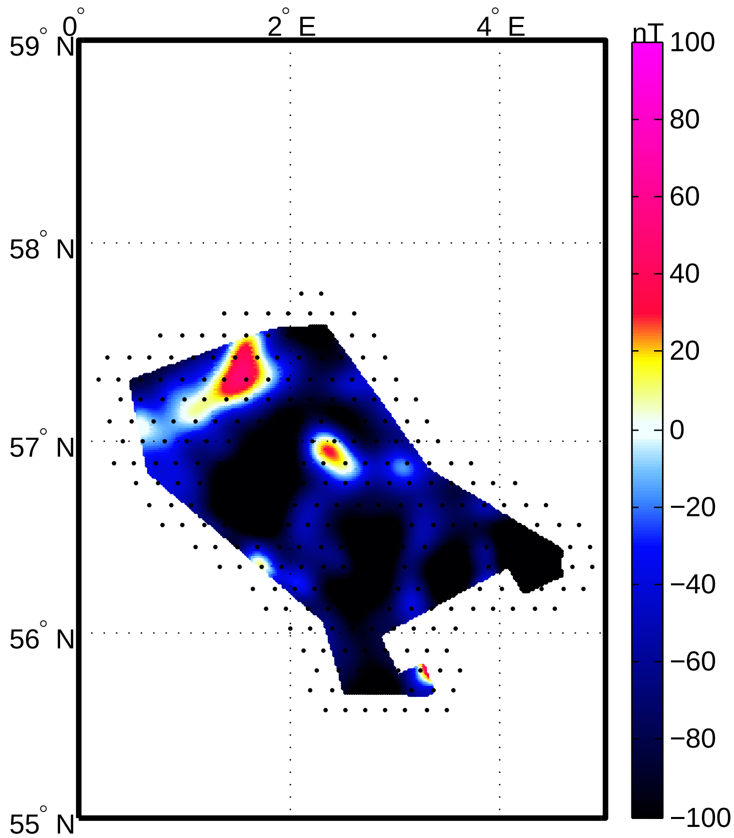

Figure 52 Quadratic regularized model values based on equivalent sources. The applied regularization parameter, source depth and source amount are $\alpha = 300\,\mathrm{nT}^{-2}$, 53 km and 285, respectively. Black circles indicate the location for the equivalent sources. The max, min and mean values for the corresponding residuals are 27.37 nT, −32.94 nT and 0.03 nT, respectively. The *Huber* weighted residual rms is 1.62 nT.

4.5.4 Detailed results at the specific Ekofisk well

In this section the geomagnetic field predictions from the DTU model and the BGS model (BGGM2016 with IFR) are compared for various depth values of the well at the Ekofisk field. Note that the depth values used are given relative to the geocentric coordinate system, and are thus not identical to true vertical depth (TVD), which refers to the mean sea level. The predictions of the BGS model and DTU model are listed in Table 10 and Table 11, respectively. In-field referencing (IFR) values of the latter are based on the combined magnetic field components from the CHAOS-6 large-scale geomagnetic model $\mathbf{B}^{main}$ and the equivalent source based model of the local lithospheric field $\mathbf{B}^{loc}$. Given a spherical polar coordinate system, the IFR components for the total field intensity F^{IFR}, declination D and inclination I are

$$\begin{aligned}
\mathbf{B}^{IFR} = (B_r^{IFR}, B_\theta^{IFR}, B_\phi^{IFR}) = (B_r^{main} + B_r^{loc}, B_\theta^{main} + B_\theta^{loc}, B_\phi^{main} + B_\phi^{loc})& \\
F^{IFR} = \sqrt{(B_r^{IFR})^2 + (B_\theta^{IFR})^2 + (B_\phi^{IFR})^2}& \\
D^{IFR} = \tan^{-1}\left(\frac{B_\phi^{IFR}}{-B_\theta^{IFR}}\right)& \\
I^{IFR} = \tan^{-1}\left(\frac{-B_r^{IFR}}{\sqrt{(B_\theta^{IFR})^2 + (B_\phi^{IFR})^2}}\right).&
\end{aligned} \tag{98}$$

Differences in the combined IFR baseline values are illustrated in Fig.53 and corresponding background values are listed in Table 12. Care should be taken when comparing crustal models due to possible differences in the corresponding reference values.
For all tables in this section, the first column refers to a specific location along the well path with increasing values indicating increasing depths.

Hole pt	**Main Field Values (BGS)**			**Crustal Field Values**			**IFR Baseline Values**		
	Decl.	Incl.	Intensity	Decl.	Incl.	Intensity	Decl.	Incl.	Intensity
	[deg]	[deg]	[nT]	[deg]	[deg]	[nT]	[deg]	[deg]	[nT]
0	0.114	70.365	50149.6	-0.010	-0.005	-2.1	0.104	70.360	50147.5
1	0.115	70.365	50160.4	-0.016	-0.005	-1.7	0.099	70.360	50158.7
2	0.116	70.365	50165.6	-0.019	-0.005	-1.6	0.097	70.360	50164.0
3	0.117	70.365	50170.9	-0.018	-0.003	0.9	0.099	70.362	50171.8
4	0.118	70.364	50177.4	-0.024	-0.003	0.9	0.094	70.361	50178.3
5	0.119	70.362	50183.2	-0.030	-0.003	0.9	0.089	70.359	50184.1
6	0.120	70.360	50190.5	-0.038	-0.002	1.1	0.082	70.358	50191.6
7	0.121	70.358	50199.0	-0.047	-0.001	1.3	0.074	70.357	50200.3
8	0.122	70.356	50207.1	-0.057	0.001	1.5	0.065	70.357	50208.6
9	0.123	70.353	50213.0	-0.067	0.002	1.3	0.056	70.355	50214.3
10	0.124	70.352	50214.6	-0.071	0.003	1.1	0.053	70.355	50215.7
11	0.124	70.350	50214.4	-0.073	0.004	0.7	0.051	70.354	50215.1
12	0.124	70.349	50214.0	-0.074	0.005	0.7	0.050	70.354	50214.7
13	0.124	70.347	50213.6	-0.076	0.006	0.7	0.048	70.353	50214.3

Table 10 IFR values at one specific Ekofisk well. Corresponding main field and crustal field values were estimated using the BGGM2016 predictions for 01-05-2016.

Hole pt	Main Field Values (DTU)			Crustal Field Values			IFR Baseline Values		
	Decl.	Incl.	Intensity	Decl.	Incl.	Intensity	Decl.	Incl.	Intensity
	[deg]	[deg]	[nT]	[deg]	[deg]	[nT]	[deg]	[deg]	[nT]
0	0.122	70.561	50159.4	0.120	0.128	-77.1	0.242	70.689	50082.3
1	0.123	70.562	50170.4	0.114	0.127	-77.6	0.237	70.689	50092.8
2	0.123	70.562	50175.7	0.111	0.127	-78.0	0.234	70.689	50097.7
3	0.124	70.562	50181.1	0.107	0.127	-78.6	0.232	70.689	50102.5
4	0.126	70.561	50187.8	0.102	0.127	-79.7	0.228	70.688	50108.1
5	0.127	70.559	50193.8	0.098	0.128	-81.0	0.225	70.687	50112.8
6	0.128	70.557	50201.3	0.092	0.129	-82.3	0.220	70.686	50119.0
7	0.129	70.555	50210.0	0.085	0.130	-83.8	0.214	70.685	50126.2
8	0.130	70.553	50218.3	0.078	0.132	-85.4	0.208	70.685	50132.9
9	0.131	70.550	50224.3	0.072	0.134	-87.3	0.203	70.685	50137.1
10	0.132	70.549	50226.0	0.070	0.135	-88.1	0.202	70.685	50137.9
11	0.132	70.547	50225.9	0.070	0.137	-88.7	0.202	70.685	50137.1
12	0.132	70.546	50225.4	0.071	0.139	-89.0	0.204	70.685	50136.4
13	0.133	70.544	50225.1	0.072	0.141	-89.2	0.205	70.685	50135.9

Table 11 Column 2-4: DTU model predictions for 01-05-2016. Main field values include contributions from the CHAOS-6 time-dependent internal field (up to SH degree 20), large-scale external field and large scale lithospheric field (up to SH degree 110). **Column 5-7:** Crustal field contribution is defined as the difference between the main field values (column 2-4) and the IFR baseline values (column 8-10). **Column 8-10:** IFR baseline values apply the combined main field and local crustal model derived from aeromagnetic data.

Hole pt	Main Field Values			Crustal Field Values			IFR Baseline Values		
	Decl.	Incl.	Intensity	Decl.	Incl.	Intensity	Decl.	Incl.	Intensity
	[deg]	[deg]	[nT]	[deg]	[deg]	[nT]	[deg]	[deg]	[nT]
0	0.008	0.196	9.8	0.130	0.133	-75.0	0.138	0.329	-65.2
1	0.008	0.197	10.0	0.130	0.132	-75.9	0.138	0.329	-65.9
2	0.007	0.197	10.1	0.130	0.132	-76.4	0.137	0.329	-66.3
3	0.007	0.197	10.2	0.125	0.130	-79.5	0.133	0.327	-69.3
4	0.008	0.197	10.4	0.126	0.130	-80.6	0.134	0.327	-70.2
5	0.008	0.197	10.6	0.128	0.131	-81.9	0.136	0.328	-71.3
6	0.008	0.197	10.8	0.130	0.131	-83.4	0.138	0.328	-72.6
7	0.008	0.197	11.0	0.132	0.131	-85.1	0.140	0.328	-74.1
8	0.008	0.197	11.2	0.135	0.131	-86.9	0.143	0.328	-75.7
9	0.008	0.197	11.3	0.139	0.132	-88.6	0.147	0.330	-77.2
10	0.008	0.197	11.4	0.141	0.132	-89.2	0.149	0.330	-77.8
11	0.008	0.197	11.5	0.143	0.133	-89.4	0.151	0.331	-78.0
12	0.008	0.197	11.4	0.145	0.134	-89.7	0.154	0.331	-78.3
13	0.009	0.197	11.5	0.148	0.135	-89.9	0.157	0.332	-78.4

Table 12 Differences between geomagnetic field predictions of the DTU model and BGGM2016 at the specific Ekofisk well. The last three columns are illustrated in Fig. 53.

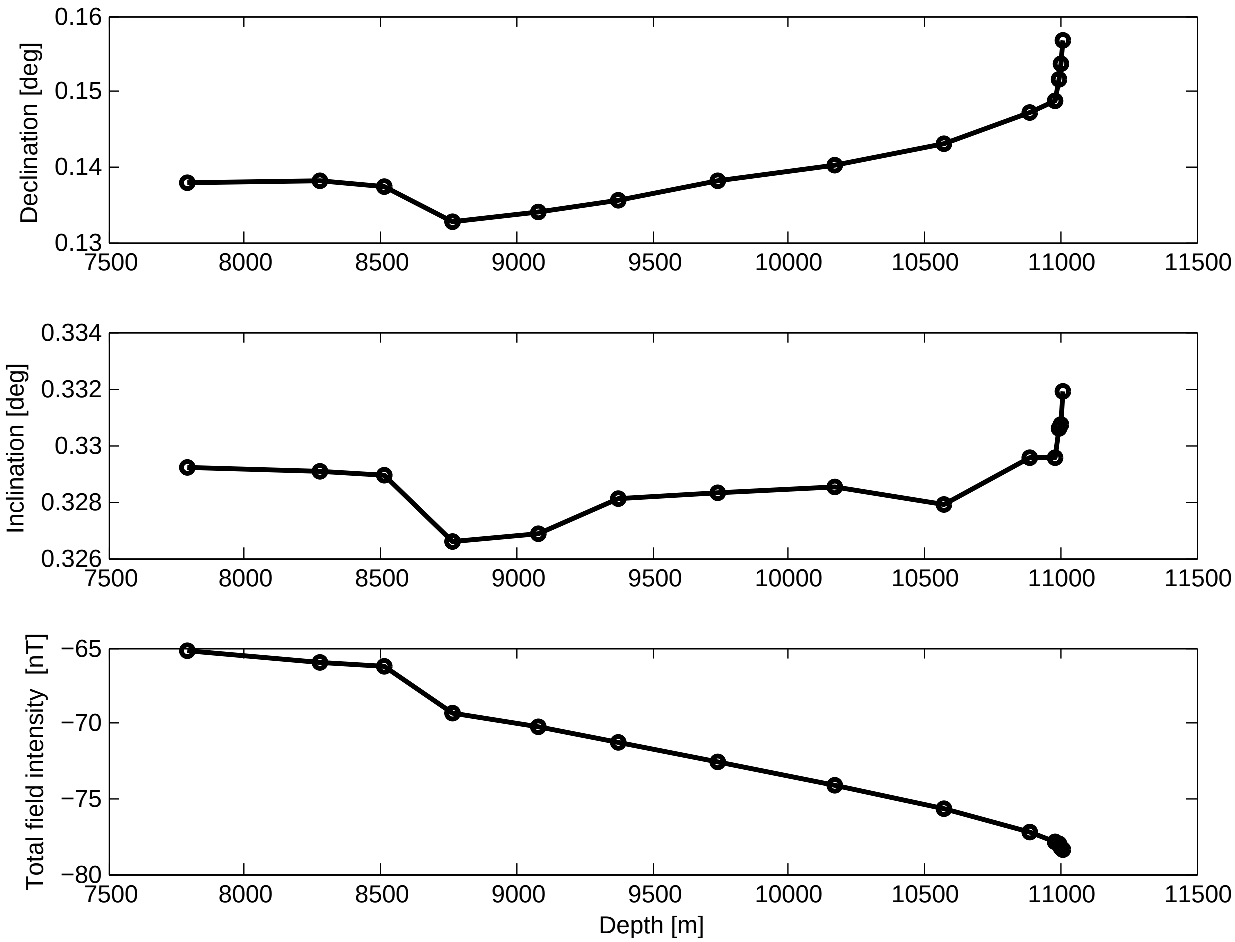

Figure 53 Differences between IFR baseline predictions for the DTU method and BGGM2016 for magnetic declination (top), magnetic inclination (middle) and the total magnetic field intensity (bottom) for the specific Ekofisk well. Note that the depth values are given in meters below the Earth's surface.

The large-scale field agrees rather well between the two models (magnitude of differences around 0.008° in declination, 0.197° in inclination and 10 nT in the field intensity). Differences in the crustal field part are larger regarding both the declination (about 0.13°), inclination (about 0.13°) and field intensity (around 80 nT). As shown in Fig.53 the differences between the models change only gradually with the depth of the well, except for the deepest positions.
There are several possible reasons for the observed differences between the model predictions from BGS and DTU. First, concerning the large-scale magnetic field predictions, the differences are most likely linked to alternative approaches for modelling the secular variations, external field and large-scale crustal field, and perhaps also different selections of ground and satellite data. Another contribution to the model differences comes from the fact that BGGM2016 and CHAOS-6 represent the geomagnetic field up to SH degree 133 and 120, respectively.
Regarding differences in the regional crustal field models from BGS and DTU, one possible reason is that BGS works with a Fourier technique for downward continuation while DTU has implemented an equivalent source model. The former is characterized by only one free parameter, which is damping or smoothing of the solution between upward and downward continuation.
In order to have a fair comparison between the two methods, it is crucial that the corresponding modelling routines are applied on the same aeromagnetic data set. This is however not the case in the current study. In addition to the MAGAN survey data, BGS uses a large and complete compilation for the entire North Sea, including at least 50 km of aeromagnetic data in each direction around the well (C. Beggan, private communication, 2017). Thus, since the used Ekofisk well is at the edge of the MAGAN survey area, possible anomalies to the south of the aeromagnetic grid are more likely to be captured by the BGS model.
A rigorous assessment of the differences between the approaches would involve both BGS and DTU working on exactly the same data set, and setting out in detail all the processing and modelling procedures. Additionally, for a reasonable comparison of the two model performances, it is necessary to consider a statistical representable and significant sample of bore holes.

4.5.5 Model comparison with actual well measurements

The used Ekofisk well consists of five different sections, each defined by a specific hole section diameter, see Table 13. Model values corresponding to the highlighted hole points represent the predictions for the respective well section. Differences between actual measurements within a well section and the respective model values for total field intensity and magnetic inclination are not allowed to exceed certain limits, which are defined by the individual drilling companies or operators. However, the limits are typically dependent on location, wellbore direction and the type of positional uncertainty error model assigned to the directional surveys.

The first two hole sections were drilled using Gyro MWD, determining the wellbore inclination and azimuth with accelerometer and gyroscopic measurements, respectively. In the third and fourth hole section the axial magnetometer readings were heavily disturbed by drill string interference and a correction algorithm was applied to optimize the azimuth values. Thus, the downhole magnetic measurements are not directly comparable to the modeled predictions of the geomagnetic field parameters. The last section of the well was drilled with uncorrected azimuths, using quality control limits as indicated in Table 14. An overview of how the acceptance limits for the magnetic inclination and total field intensity is achieved can be found at http://www.iscwsa.net/ (Error Model Sub-Comittee). The former is set to 0.6° (for 3σ), while the uncertainty in total field intensity is given by 165 nT (for 3σ, including IFR). Table 14 gives the mean differences between hole section measurements and model predictions of BGS and DTU where uncorrected azimuths were used. All differences are well within the Baker Hughes' defined error margins with (apart for the magnetic intensity for well section 8.5") BGS having the smallest differences to actual measurements. Especially the BGS differences for the magnetic inclination are surprisingly low and presumes additional data and/or model treatments which we are not aware of (e.g. assumptions regarding the spectral gap). It should be noted that the error margins defined by Baker Hughes include error sources such as drillstring interference, sag, misalignment and depth.
In order to have more data for model comparisons, Table 14 includes measurement from a 9.5" section of another Ekofisk well (also drilled with uncorrected azimuths by Baker Hughes).

Well section	Hole pt
26 inch	0
20 inch	1
	2
16 inch	3
	4
12.25 inch	5
	6
	7
	8
8.5 inch	9
	10
	11
	12
	13

Table 13 Ekofisk well sections and hole points within. Model predictions corresponding to the highlighted hole points are used for determining the differences to respective section measurements.

If the difference between model predictions and actual measurements exceeds the predefined limit, more conservative uncertainty models are used which widen the acceptance range of difference.
Note that only model predictions for the total magnetic field and magnetic inclination are compared to actual measurements. MWD provides no quality control of model predictions for the magnetic declination.

Well section	Fourier Transform		Monopoles	
	Magn. intensity [nT]	**Magn. inclination** [deg]	**Magn. intensity** [nT]	**Magn. inclination** [deg]
26 inch	-	-	-	-
8.5 inch	-24.62	0.02	11.76	-0.34
9.5 inch	-24.27	-0.01	61.73	-0.35
Baker Hughes limits	318.86	0.59	318.86	0.59

Table 14 Mean differences between actual measurements in the 8.5" and 9.5" sections and corresponding geomagnetic model predictions. The last row gives the (absolute) mean Baker Hughes acceptance limits for the same hole sections.

4.5.6 Summary in standard industrial format

The results from the previous sections are now summarized in a more standard industrial format. Tables 15, 16 and 17 give the corresponding values for the BGS model, DTU model and differences, respectively. The specific selection of hole points corresponds to the different well sections which are characterized by certain thickness values.
The grid convergence λ_{gc} (column 6) describes the angular deviation between the true north and grid north for this location. These two values are equal to each other at the applied UTM zone's central meridian. The respective formula is

$$\lambda_{gc} = (\phi - \phi_{cm}) \cdot \sin(\theta), \tag{99}$$

with (θ,ϕ) representing the well coordinates and $\phi_{cm} = 3°$E the central meridian longitude of the applied UTM zone 31N (0°E to 6°E).
The total corrections (column 4) are derived by subtracting the grid convergence from the combined large-scale and regional crustal field declinations of column 5.

Hole pt	Magnetic Field Values			Azimuth Corr. Values		Depth
	Inclination	Intensity	Total Corr.	Declination	λ_{gc}	TVD
	[deg]	[nT]	[deg]	[deg]	[deg]	ft
2	70.360	50164.0	-0.093	0.097	0.190	2126.8
4	70.361	50178.3	-0.097	0.094	0.191	3993.2
7	70.357	50200.3	-0.115	0.074	0.189	7562.7
11	70.354	50215.1	-0.136	0.051	0.187	10300.3

Table 15 Geomagnetic reference and azimuth correction data for BGGM2016 + crustal on 1st of May 2016 for the different hole sections of the specific Ekofisk well.

Hole pt	Magnetic Field Values			Azimuth Corr. Values		Depth
	Inclination	Intensity	Total Corr.	Declination	λ_{gc}	TVD
	[deg]	[nT]	[deg]	[deg]	[deg]	ft
2	70.689	50097.7	0.045	0.234	0.190	2126.8
4	70.688	50108.1	0.037	0.228	0.191	3993.2
7	70.685	50126.2	0.026	0.214	0.189	7562.7
11	70.685	50137.1	0.016	0.202	0.187	10300.3

Table 16 Geomagnetic reference and azimuth correction data for DTU model + equivalent source crustal model on 1st of May 2016 for the different hole sections of the specific Ekofisk well.

Hole pt	Magnetic Field Values			Azimuth Corr. Values		Depth
	Inclination	Intensity	Total Corr.	Declination	λ_{gc}	TVD
	[deg]	[nT]	[deg]	[deg]	[deg]	ft
2	0.329	-66.3	0.137	0.137	0.190	2126.8
4	0.327	-70.2	0.134	0.134	0.191	3993.2
7	0.328	-74.1	0.140	0.140	0.189	7562.7
11	0.331	-78.0	0.151	0.151	0.187	10300.3
mean	0.329	-72.1	0.141	-	-	-

Table 17 Difference between geomagnetic reference and azimuth correction data of the DTU model and BGGM2016. The last row gives the corresponding mean values.

There is a general satisfactory agreement between the predictions of the two models with absolute mean differences for the total correction, inclination (or dip angle) and intensity of magnitude 0.14°, 0.3° and 72 nT, respectively. These are within or close to respective values in the ISCWSA error model for BGGM of 0.36°, 0.2° and 130 nT (Williamson et al., 2000; Herland et al., 2017).

4.6 Summary of regional models

This chapter has shown that the equivalent point source routine is also applicable for regional lithospheric field investigations. Near-surface measurements of the magnetic anomaly field intensity have been used to estimate all components of the vector field. The method has been tested on three aeromagnetic surveys from offshore Norway which differ in both period, area and altitude. For chosen quadratic regularization parameters, the corresponding model predictions are stable for downward continuation. This is a necessary requirements for a successful application of the equivalent source routing in directional drilling. Based on aeromagnetic measurements in the vicinity of the Ekofisk field in the North Sea, a geomagnetic vector field was estimated using both CHAOS-6 predictions for the large-scale signals and an equivalent source model for the small-scale variations of the lithospheric field. This combined model was compared to the industry standard BGGM2016 model and actual measurements from an Ekofisk well. The two models have differences for the total correction, inclination (or dip angle) and intensity of magnitude 0.14°, 0.3° and 72

nT, respectively. Additionally, both models are capable to represent the measurements within the industry standard error margins.
The excellent model predictions from BGGM2016 + IFR for the Ekofisk well data are due to additional data.
Better regional model predictions are assumed when using a method similar to the one presented in the following chapter, taking advantage of both satellite and near-surface measurements.
Generally, it is difficult to determine a precise absolute level of the magnetic field based on scalar anomaly data. This yields especially when there is no information given on the performed data processing, e.g. the original survey with the raw magnetic measurements, magnetic diurnal correction, IGRF values, line leveling, etc. Additionally, arbitrary offsets are typically added into the later processing stages in order to make the data "look" nice. It is thus important to have independent measurements from the same data area (aeromagnetic or marine magnetic) or repeat stations for comparison and validation of the provided data.

5 Joint inversion of satellite and near-surface measurements

Satellites have the great advantage of global data coverage, allowing the resulting lithospheric field models to possess wavelengths between approximately 350 km and 3000 km (Langel and Hinze, 1998). Near-surface measurements, on the other hand, conducted from ships or airplanes, are characterized by wavelengths smaller than 200 km and provide lithospheric field models more suitable for geologic interpretation. Thus, models based on satellite measurements are only able to capture the large-scale lithospheric structures, while models obtained from near-surface surveys also provide information of the small-scale features. Combining both types of data would enable models to cover the entire spatial spectra of lithospheric signals. Unfortunately, such a combination is wishful thinking as there exist a systematic disagreement between global satellite-based field models and small regional magnetic anomaly maps for the SH degree range 15-100 (Thébault et al., 2010). Spectral gap problems appear especially when the near-surface data area is small. The resulting effect can be reduced by including either model predictions of the large scale lithospheric features or satellite measurements. Thus, high precision satellites with low altitudes as well as large-area near-surface surveys are necessary for better data compilations.

The previous two chapters have demonstrated the successful application of the equivalent point sources routine for generating global and regional lithospheric field models based on satellite and aeromagnetic measurements, respectively. This chapter provides a proof of concept study, where monopole based regional lithospheric field models are generated by jointly inverting satellite and near-surface measurements. The former are represented by radial field measurements from the CHAMP data set presented in section 3.2 (upper part of Fig. 54), whereas the near-surface measurements are given by magnetic intensity values from the North-American geomagnetic map NURE-NAMAM2008 (lower part of Fig. 54). The latter is described in more detail in section 5.1. The used joint inversion routine is explained in section 5.2 and respective model results are presented in section 5.3.

5.1 Regional near-surface data

The regional geomagnetic intensity data of NURE-NAMAM2008 were kindly provided by D. Ravat and comprises both marine and aeromagnetic surveys from North America. The corresponding values are defined on a grid of 1.25 km spacing. For data reduction purposes in the combined inversion routine, only measurements within $20°$ to $50°$ latitude and $-70°$ to $-130°$ longitude are used, which reduces the data amount from 28,276,304 to 10,131,220. Further data reduction to $337,708$ is achieved by using every 30th data point in order to speed up the calculation time. The data altitude is 1000 ft above mean sea level.
NURE-NAMAM2008 combines long-wavelength magnetic anomalies obtained as part of the U.S. National Uranium Resource Evaluation (NURE) program with short-wavelength anomalies from the North American Magnetic Anomaly Map (NAMAM). The former is based on $2° \times 1°$ aeromagnetic surveys flown from 1975 to 1981 with a line spacing of 4.8 to 9.6 km and variable tie-line spacing. Except for the oceanic regions, Alaska, Mexico and Canada, the NURE data are reduced for core field contributions based on model predictions of CM4 up to spherical harmonic degree 13. External field contributions are removed using either base stations or estimates from CM4. Further, the data are low-pass filtered to retain wavelengths > 50 km (Ravat et al., 2009).
The NAMAM2002 data are based on the same near-Earth survey measurements as NURE. However, different data processing routines result in more high resolution magnetic anomaly maps. For instance, the short-wavelength noise, due to e.g. unaccounted external field sources, anthropogenic sources or base-station offsets, is reduced using leveling and micro-leveling. More details about the different processing steps are given in Bankey et al. (2002). The data are provided on a grid of 1 km spacing and characterized by a poor representation of the long wavelength lithospheric signals, especially in the U.S. and the marine regions.
A full spectrum geomagnetic anomaly map is created by combining the altered NURE data ($\lambda > 50$ km) with short-wavelength anomalies ($\lambda < 50$ km) from NAMAM2002. The final measurements are projected to WGS84 locations and 0.01 ° block-averaged using GMT (Wessel et al., 2013).
Similar to the aeromagnetic survey data of section 4, the used NURE-NAMAM2008 magnetic intensity values are projected into geocentric coordinates prior to model inversion.

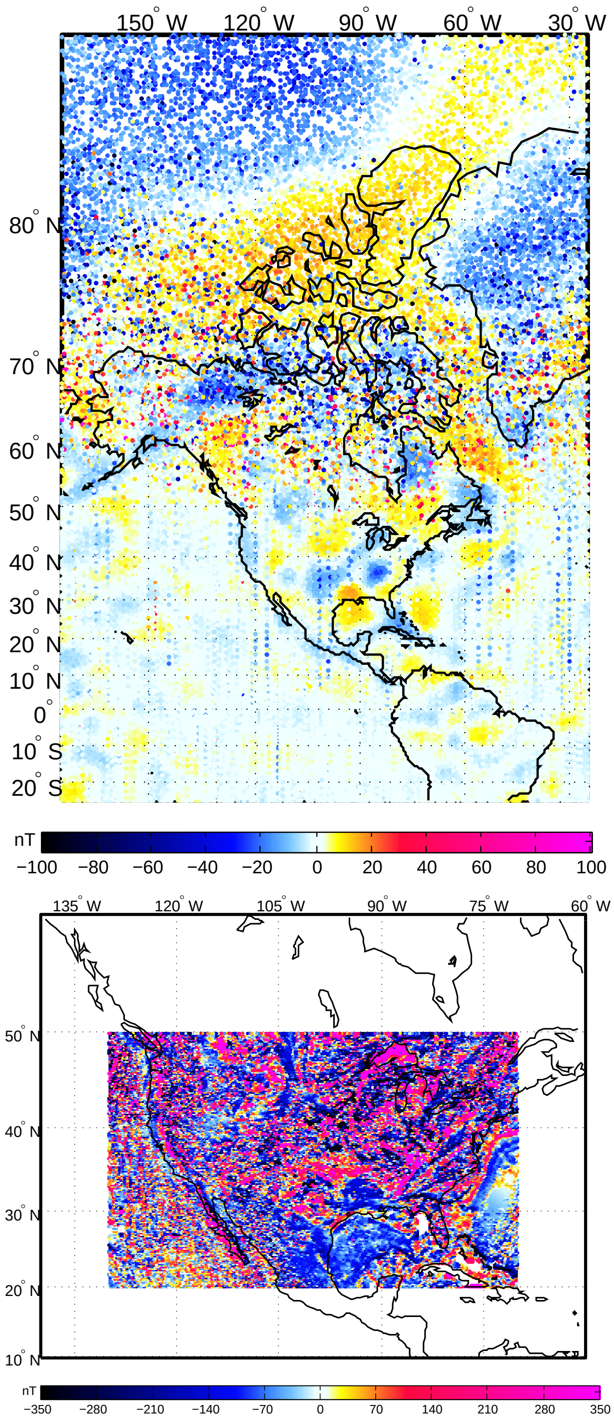

Figure 54 Radial lithospheric field data from CHAMP (top) and geomagnetic intensity data from NURE-NAMAM2008 (bottom, every 30th data point) used for the joint inversion routine.

5.2 Model derivation

The near-surface measurements $\mathbf{d}_1$ are given by every 30th magnetic intensity value of NURE-NAMAM2008 in the area between 20° to 50° latitude and −70° to −130° longitude ($N_1 = 337,708$). The respective error values $\boldsymbol{\sigma}_1$ are chosen as 1 nT. The largest possible number of sources and corresponding source depth for representing these near-surface measurements are $K_1 = 29,846$ and 60 km, respectively (see Appendix G.1). These values correspond to a global source amount of $K_g = 700,000$ (which is equivalent to a source distance of approximately 27 km at the Earth's surface) and a source area between 18° to 52° latitude and −68° to −132° longitude (±2° in both latitude and longitude around the regional near-surface data area).
For the long-wavelength signal of the joint inversion scheme, every radial CHAMP measurement $\mathbf{d}_2$ within the area between −25° to 90° latitude and −25° to −175° longitude is used (±45° in both latitude and longitude around the regional near-surface data area). This corresponds to $N_2 = 104,143$ satellite measurements and respective errors $\boldsymbol{\sigma}_2^r$ (see Fig. 9). Using the same source grid parameters as the global lithospheric field models of chapter 3 and a source area defined to be ±50° in both latitude and longitude around the regional near-surface data area, the number of equivalent point sources representing the satellite measurements is $K_2 = 12,937$.
Both data sets are combined into a data vector $\mathbf{d} = [\mathbf{d}_1, \mathbf{d}_2]$ of length $N = N_1 + N_2 = 441,851$ with corresponding locations $\mathbf{r}_i = [r_i, \theta_i, \phi_i]$ (for $i = 1, ..., N$) and error values $\boldsymbol{\sigma} = [\boldsymbol{\sigma}_1, \boldsymbol{\sigma}_2^r]$. The sources of both grids (having different depths and densities as illustrated in Fig. 55) are collected in a combined model vector of length $K = K_1 + K_2 = 42,783$ with corresponding locations $\mathbf{s}_k = [r_k, \theta_k, \phi_k]$ (for $k = 1, ..., K$). The remaining inversion scheme follows the same equations as already presented in chapter 2, using quadratic regularization with $\alpha = 80\,\mathrm{nT}^{-2}$ (equivalent to the global lithospheric field model mono-QR).
The major difference for the joint inversion scheme lies in the fact that $\underline{\underline{\mathbf{G}}}^T\underline{\underline{\mathbf{W}}}\underline{\underline{\mathbf{G}}}$ and $\underline{\underline{\mathbf{G}}}^T\underline{\underline{\mathbf{W}}}\mathbf{d}$ are derived individually for the different data sets. The respective values are weighted by an additional factor ϱ and added together prior to the usage of equation (61). As pointed out by Ravat et al. (2002), an inversion scheme which combines satellite and near-surface measurements should weight the two data sets differently when there is not enough information on the attributed uncertainties. The different weighting accounts also for differences in the data sets' amplitude and source-data distances r_{ik}. The latter are used to define the Green's matrix of the inversion scheme (see equation (103)) which automatically weights large source-data distances less than small distances. An un-weighted joint inversion scheme will thus mostly build on the near-surface measurements. In order to account for both data sets approximately equally, the joint inversion scheme of this study uses $\varrho_1 = 0.001$ and $\varrho_2 = 1$ for near-surface and satellite measurements, respectively. This is equivalent to NURE-NAMAM2008 error values being on the order of 32 nT.
Due to limited computational resources, only satellite data which extend up to $\eta = \pm 40°$ in longitude and latitude around a given source are taken into account in the joint inversion scheme. The corresponding value for the near-surface data is $\eta = \pm 15°$. The reasoning for these specific data ranges is given in Appendix G.2.

5.3 Joint inversion model results

Figure 56 illustrates the jointly estimates anomaly field at the Earth's surface. Corresponding model predictions at satellite and near-surface altitude are given in the left panels of Figs. 57 and 58, respectively. The associated residuals are illustrated in the figures' right panels.
In order to assess the derived joint inversion model result, two additional models are generated using only radial CHAMP data or NURE-NAMAM2008 data. Except for the regularization parameter, the corresponding inversion schemes differ in the following input parameters (here the subscripts $_1$ and $_2$ refer to the NURE-NAMAM2008 and radial CHAMP data, respectively):

Model 1:	$\mathbf{d}$ = radial CHAMP data	$N = 104,143$	$K = 12,937$	$\eta = 40°$	$\varrho = 1$
Model 2:	$\mathbf{d}$ = NURE-NAMAM2008	$N = 337,708$	$K = 29,846$	$\eta = 15°$	$\varrho = 1$
Model 3:	$\mathbf{d}$ = NURE-NAMAM2008 and radial CHAMP	$N = 441,851$	$K = 42,783$	$\eta_1 = 15°$, $\eta_2 = 40°$	$\varrho_1 = 0.001$, $\varrho_2 = 1$

Table 18 lists the *Huber*-weighted residuals and *Huber*-weighted normalized residual RMS values for the derived model predictions at CHAMP (upper part of the table) and NURE-NAMAM2008 altitude (lower part of the table). For the combined inversion scheme (Model 3), the *Huber*-weighted residuals at satellite

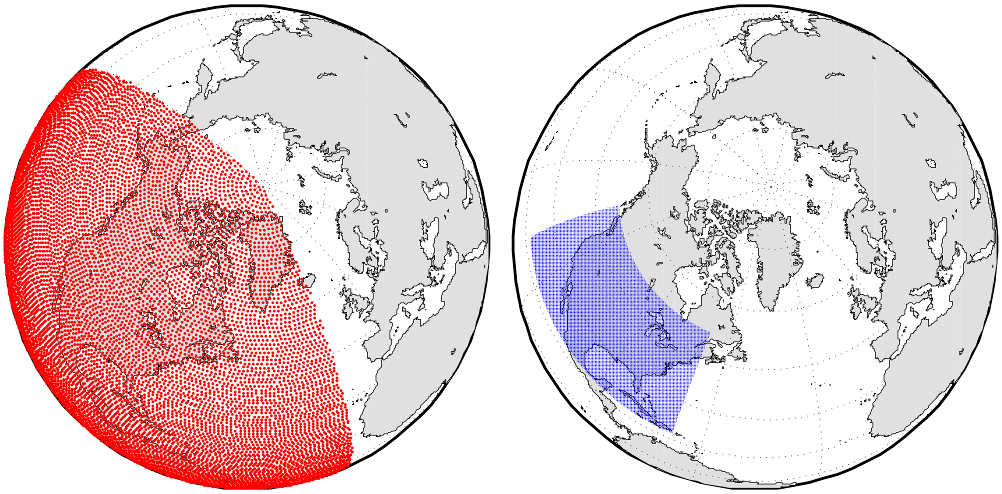

Figure 55 Source distribution for combined inversion scheme. Left: 12,937 sources (corresponding to a global source amount of $K_g = 38,600$) at 180 km depth. Right: 29,846 sources (corresponding to a global source amount of $K_g = 700,000$) at 60 km depth.

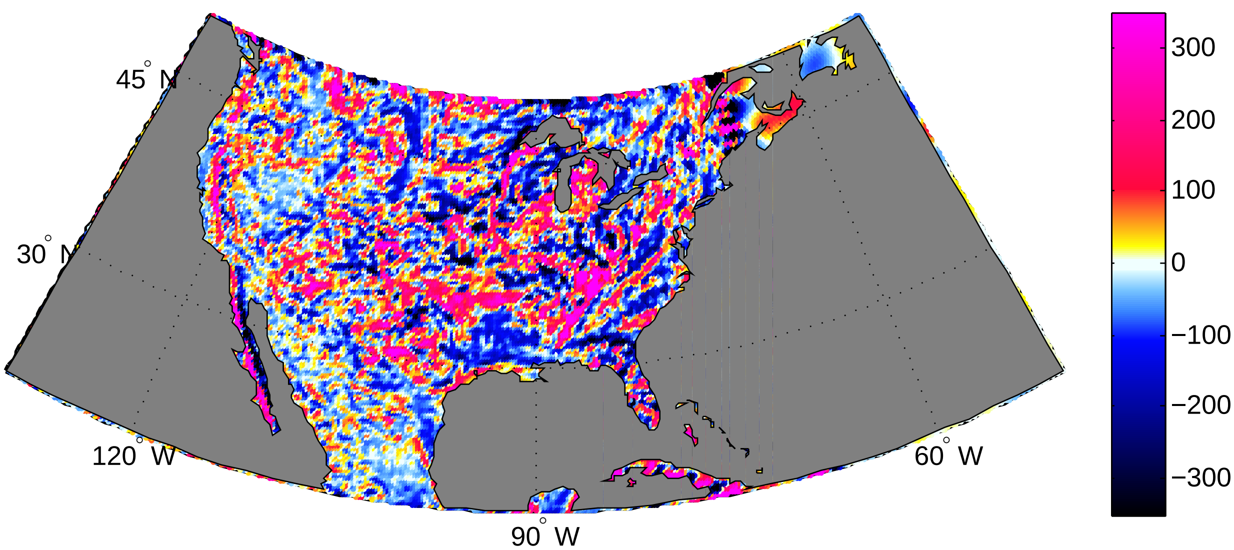

Figure 56 Joint inversion model predictions of the lithospheric magnetic intensity field at the Earth's surface.

altitude range between $-401\,\mathrm{nT}$ and $394\,\mathrm{nT}$ with a median value of $0.01\,\mathrm{nT}$. The corresponding *Huber*-weighted normalized residual RMS value is 1.28. All of these values are similar to model results which are based on radial CHAMP data only (Model 1).

The joint inversion model predictions at NURE-NAMAM2008 altitude are characterized by a larger RMS value than the predictions at satellite altitude. This, however, is expected when looking at the purely near-surface based model results (Model 2) and knowing that the used source resolution in the near-surface area is lower than the corresponding data resolution. The latter enables the model to represent the measurements only to a certain level of accuracy.

The derived results are compared with the high-resolution lithospheric field models EMM215, developed by Stefan Maus and co-workers (`www.ngdc.noaa.gov/geomag/EMM/`), and WDMAM2 (Lesur et al., 2016). Looking at Table 18, the Gauss coefficients of these global lithospheric field models result in radial field predictions at satellite altitude which represent the measurements to a similar level of accuracy as the joint inversion predictions (Model 3). The misfits due to near-surface measurements, on the other hand, are distinctly smaller for the joint inversion model. This is also clearly seen in the corresponding residual maps given in the right panels of Fig. 58. Here, the residual values of model 3 are generally smaller than EMM2015 and WDMAM over most parts of the used near-surface data area, especially in the regions of Lake Superior, the Gulf of Mexico and the North Atlantic ocean.

	Model 1	**Model 2**	**Model 3**	**MF7**	**EMM2015**	**WDMAM**
max ΔB_r (nT)	393.97	1771.14	394.07	394.00	394.16	394.02
min ΔB_r (nT)	-401.25	-2072.54	-400.79	-410.35	-409.70	-410.31
median ΔB_r (nT)	0.01	-0.06	0.01	-0.06	-0.09	-0.06
RMS ΔB_r (-)	1.29	-	1.28	1.33	1.46	1.33
max ΔF (nT)	9499.73	9447.92	9569.98	9575.16	9582.28	9549.91
min ΔF (nT)	-8683.88	-8497.79	-8590.41	-8665.23	-8626.05	-8652.94
median ΔF (nT)	-25.70	-0.01	-2.20	-22.51	-23.91	-24.85
RMS ΔF (-)	-	21.31	27.42	52.07	52.62	57.93

Table 18 *Huber*-weighted model residuals and normalized *Huber*-weighted residual RMS values for three different combinations of data and source distribution. Shaded areas represent the results due to upward or downward continued model predictions. The last three columns present corresponding statistics for the models MF7 (up to SH degree 133), EMM2015 (up to SH degree 720) and WDMAM (up to SH degree 800), using CHAOS-6 for the core field predictions (SH degree 1 to 15).

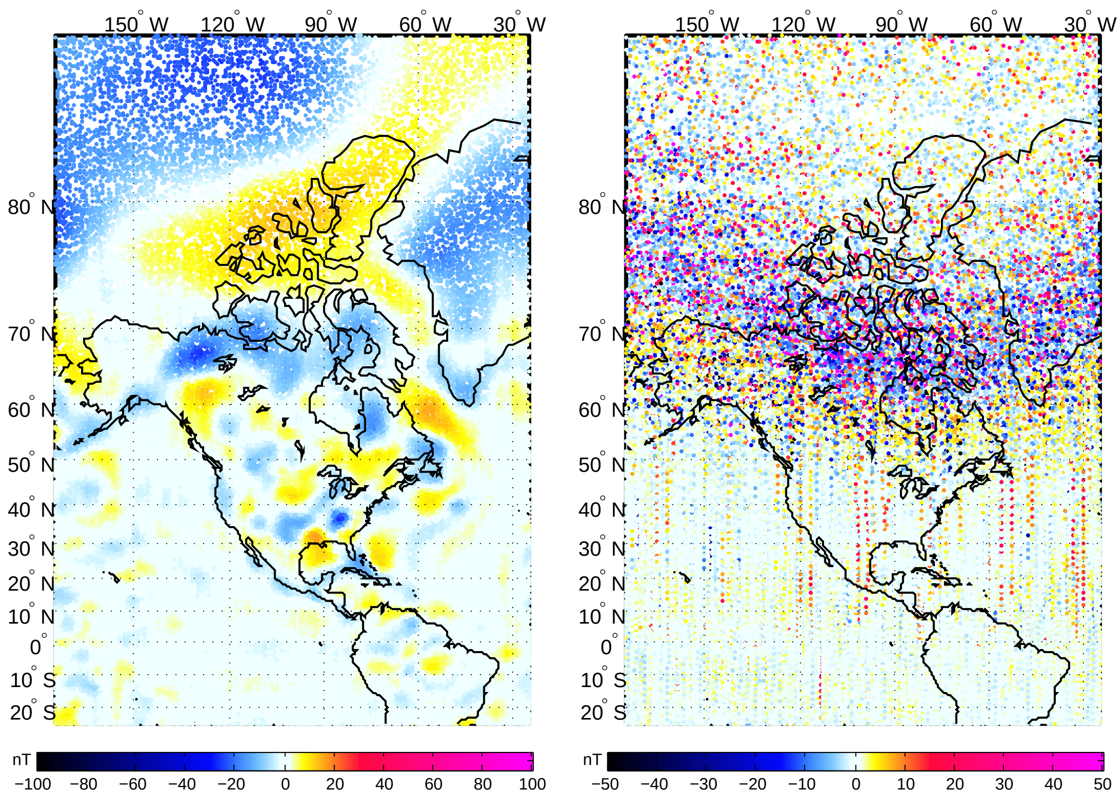

Figure 57 Radial lithospheric field predictions (left) and corresponding residuals (right) at satellite altitude for the joint inversion scheme using quadratic regularization ($\alpha = 80\,\mathrm{nT}^{-2}$) and the weighting factors $\varrho_1 = 0.001$ and $\varrho_2 = 1$ for near-surface and satellite measurements, respectively.

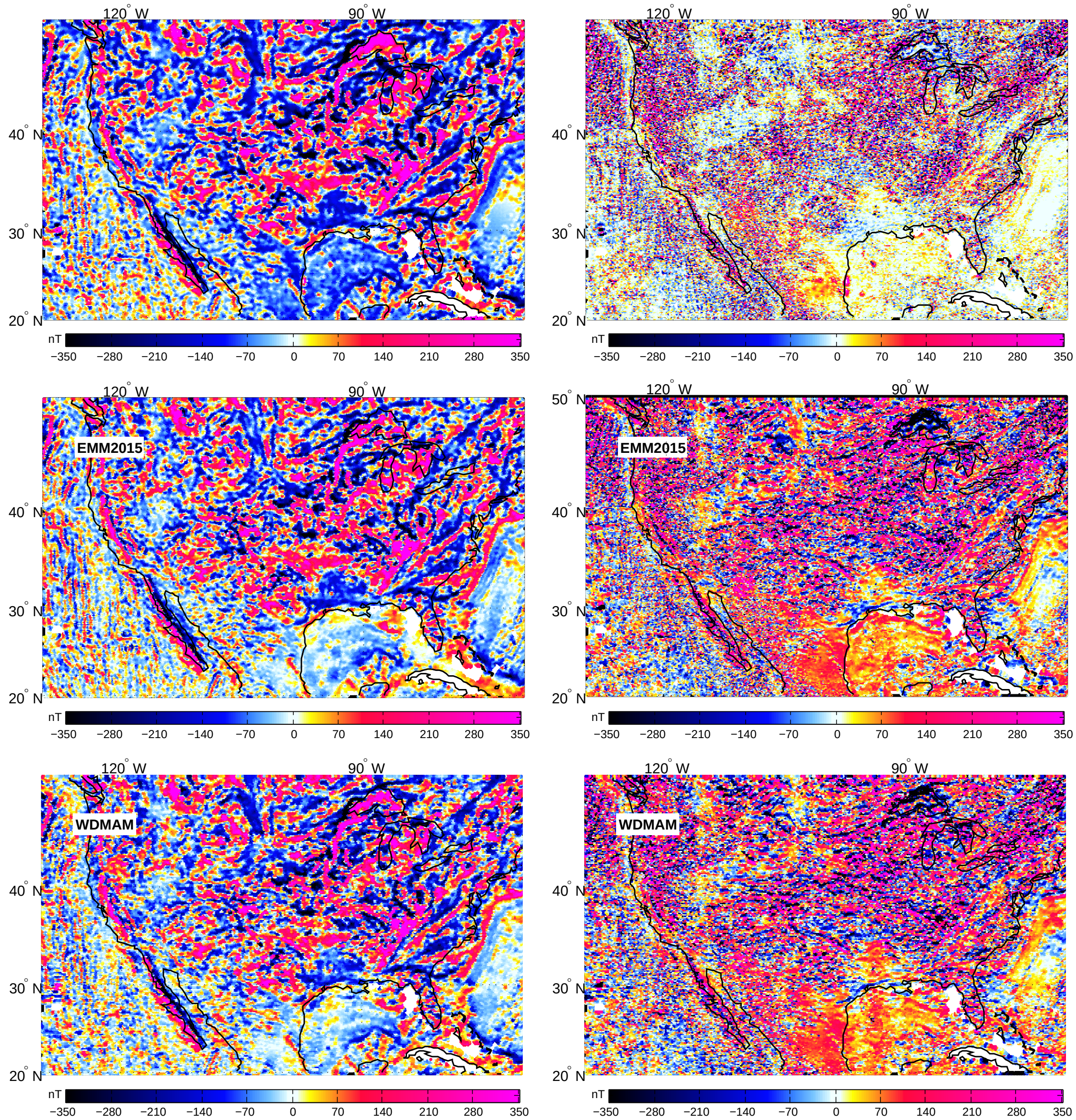

Figure 58 Lithospheric field intensity predictions (left) and corresponding residuals (right) at NURE-NAMAM2008 altitudes for the joint inversion scheme (upper row), models EMM2015 (up to SH degree 720) and WDMAM (up tp SH degree 800).

5.3.1 Regional power spectra

Since the monopole amplitudes are easily transformed into spherical harmonic coefficients (see section 2.2), the equivalent point sources method possesses the possibility of estimating regional power spectra. This can be achieved by retaining only the sources inside the region of interest, implicitly setting the amplitude of the remaining sources to zero and renormalizing the power spectrum accounting only for the area considered.

Regional lithospheric field models based on the equivalent point source routine are generated using the same input parameters as models 1-3 of the previous section. However, instead of the previously used source area of Fig. 55, only sources inside a spherical cap with center-point $C = [35°N, 100°W]$ and half angle $\theta_0^s = 20°$, and data inside a cap with the same center-point and half angle $\theta_0^d = 15°$ are used for the inversions. The sum of the resulting source amplitudes is zero for preventing aliased regional power spectra. The derived model predictions of the lithospheric field intensity at the Earth's surface (using CHAOS-6 for the core field estimations) are given in panels (a),(c) and (e) of Fig. 60 along with the corresponding model predictions of MF7, EMM2015 and WDMAM.

Using a global source distribution and defining only source amplitudes inside a cap (C, θ_0^s) to be non-zero and equivalent to the model results of the previous paragraph (see Fig. 59), regional power spectra are derived using equations (40) and (41). Respective values are multiplied with $\frac{4\pi a^2}{2\pi a^2(1-\cos\theta_0^s)}$ (for $a = 6371.2\,\mathrm{km}$) in order to account for the caps' surface area with respect to the surface area of the Earth. Unfortunately, no realistic regional power spectra could be achieved using this approach and it is concluded that the corresponding methodology needs to be investigated further. For this reason, the vector field predictions corresponding to Fig. 60 are used to generate regional power spectra based on the R-SCHA routine of Vervelidou and Thébault (2015). Figure 61 displays the respective values, which were kindly derived by Fotini Vervelidou. For regional R-SCHA power spectra the distance between two spectral terms is dependent on the cap's half-angle and thus only equal to 1, as it is the case for power spectra of the conventional spherical harmonic analysis, for $\theta_0^d = \pi$. In the present case, the spectral bin size corresponds to $\pi/\theta_0^d = 12$. The derived R-SCHA regional power spectra are rescaled by this number in order achieve a meaningful comparison to global power spectra. Additionally, the spectra are normalized by $2\pi a^2(1 - \cos\theta_0^s)$ (for $a = 6371.2\,\mathrm{km}$) in order to account for the caps' surface area with respect to the surface area of the Earth.

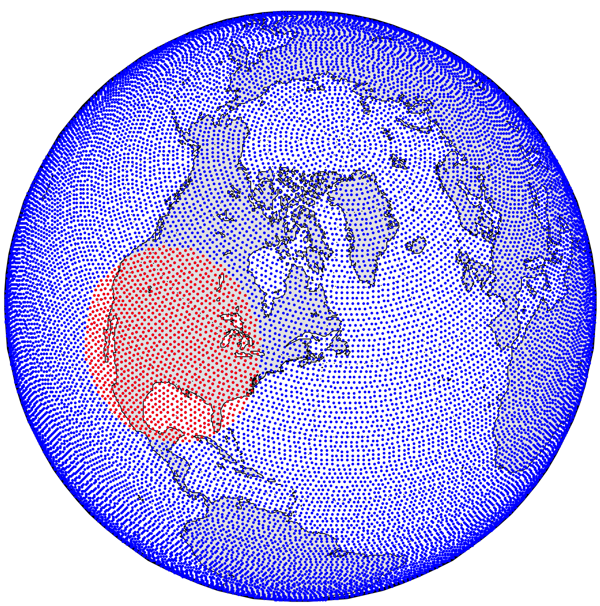

Figure 59 Regional power spectra of the equivalent point source routine are derived using equations (40) and (41), with globally equal-area distributed sources having non-zero amplitudes (indicated in red) only within the region of interest.

Figure 61 shows that the used data sets are compatible. As expected, the highest power for all degrees is provided by the regional power spectrum which is based solely on near-surface data (panel (c) of Fig. 60), whereas the regional power spectrum from the satellite measurements (panel (a) of Fig. 60) results in the lowest power amplitudes (especially for small wavelengths). The power spectra corresponding to the radial CHAMP- and combined radial CHAMP and NURE-NAMAM2008 data (panel (a) and (e) of Fig. 60) are of similar amplitudes up to spherical harmonic degree $n = 80$, whereafter the former experiences a significant decrease in amplitude, reaching a value of $1\,\mathrm{nT}^2$ at $n = 230$. The regional power spectrum of panel (e) reaches this level at $n = 790$. It is this power spectrum, which corresponds remarkably well with the results of WDMAM and EMM2015 up to SH degree $n = 600$. It should be noted that the joint inversion model has higher power than the global lithospheric field models up to approximately SH degree $n = 550$.

All derived regional power spectra are characterized by larger amplitudes compared to power spectrum based on globally distributed measurements (black curve in Fig. 61, corresponding to the model results of mono-QR).

5.4 Summery of joint equivalent point source inversion

High-resolution global lithospheric field models (i.e. WDMAM and EMM2015) are usually based on a combination of satellite and near-surface data, using satellite measurements or global field models to replace the large-wavelength features in near-surface survey areas as well as in regions of missing near-surface data. A joint inversion of satellite and near-surface data is, however, barely used for global applications, and seldom seen for the generation of high-resolution regional lithospheric field models. For instance, Thébault et al. (2006a) used the R-SCHA method for jointly inverting measurements of repeat stations, observatories, aeromagnetic surveys and CHAMP for lithospheric magnetic field predictions over France. Ravat et al. (2002) used equivalent dipole sources for generating a joint inversion lithospheric field model over Canada based on aeromagentic intensity data and Magsat measurements.

This chapter has shown that the equivalent point source routine is also capable of generating joint inversion models combining satellite and near-surface data. Using the North American region as a test case, the regional power spectrum of the derived joint inversion model corresponds well to the results of the high-resolution global lithospheric field models WDMAM and EMM2015, having slightly higher power values up to SH degree $n = 550$. All of these models result in similar misfit values with respect to the used radial CHAMP data. The corresponding model predictions for the NURE-NAMAM2008 data set, on the other hand, result in remarkably smaller misfit values for the joint inversion model than for WDMAM and EMM2015.

The presented case study used only every 30th near-surface measurement point due to computational limitations. Future improvements of the joint inversion method should, however, investigate a better way to implement all available data. The same is valid for the current approach of only using a limited amount of data around a given source for the joint inversion routine. Also the weighting between satellite and near-surface measurements should be based on a better quantitative justification.

The derived jointly inverted source values show distinct edge effects around the source area corresponding to the near-surface data. These effects could be reduced by replacing the abrupt change in source depth with a more gradual transition zone.

So far, only radial satellite measurements have been used for the generation of jointly inverted field predictions. Future applications of the corresponding routine should make use of the entire vector field and/or gradient measurements.

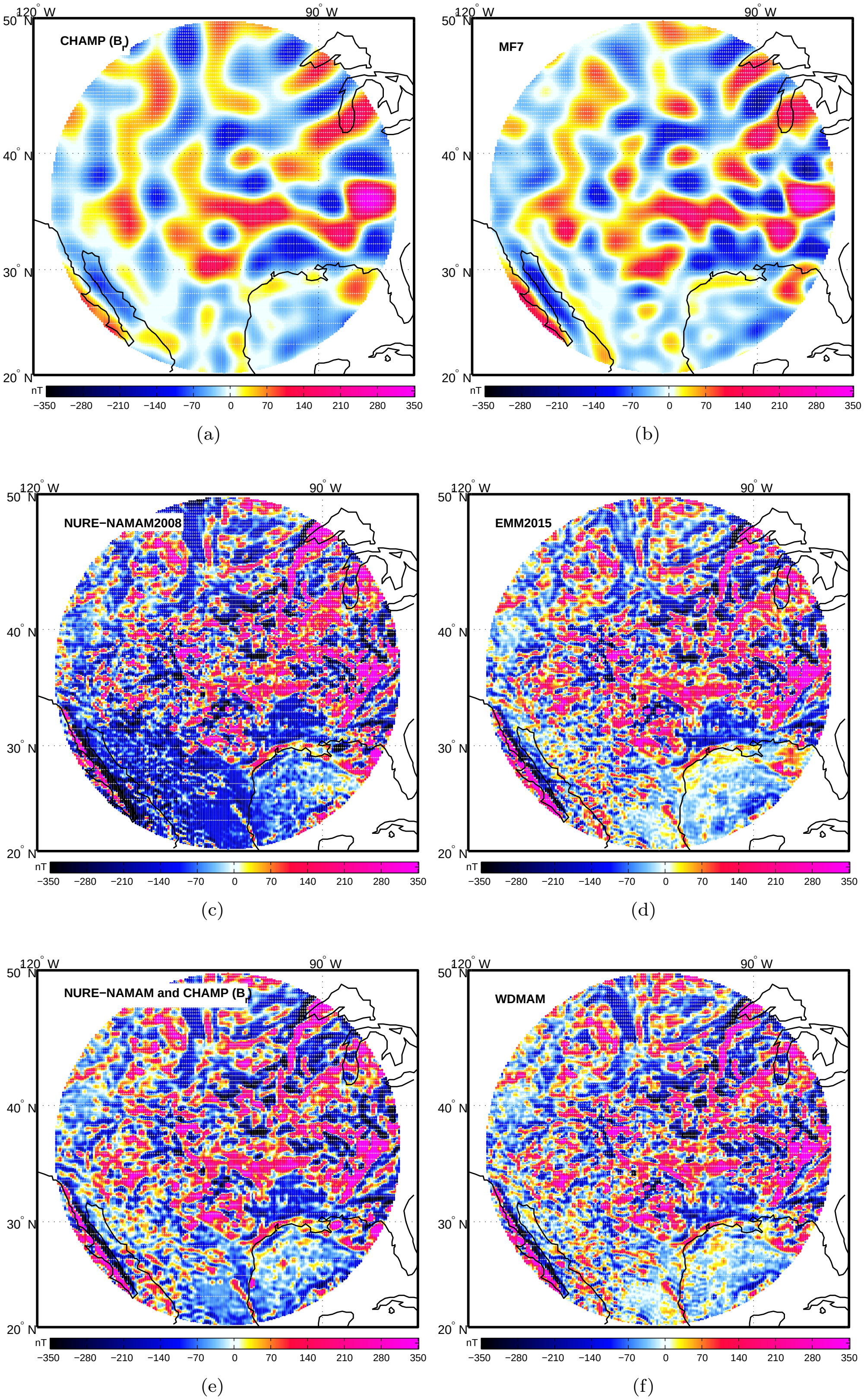

Figure 60 Lithospheric field intensity predictions at the Earth's surface for equivalent point source models based on radial CHAMP data (a), NURE-NAMAM2008 (c) and the combined observations of radial CHAMP and NURE-NAMAM2008 data (e). Additionally, field intensity predictions are given for the models MF7 (up to SH degree 133) (b), EMM2015 (up to SH degree 720) (d) and WDMAM (up to SH degree 800) (f). The field predictions are derived on a grid of 0.1° latitude × 0.2° longitude and within a cap of half angle 15°, centered at 35°N and 100°W. The CHAOS-6 model was used for respective core field estimations. The sources used to generate panels (a),(c) and (e) are located inside a cap with half angle 20° and centered at 35°N and 100°W.

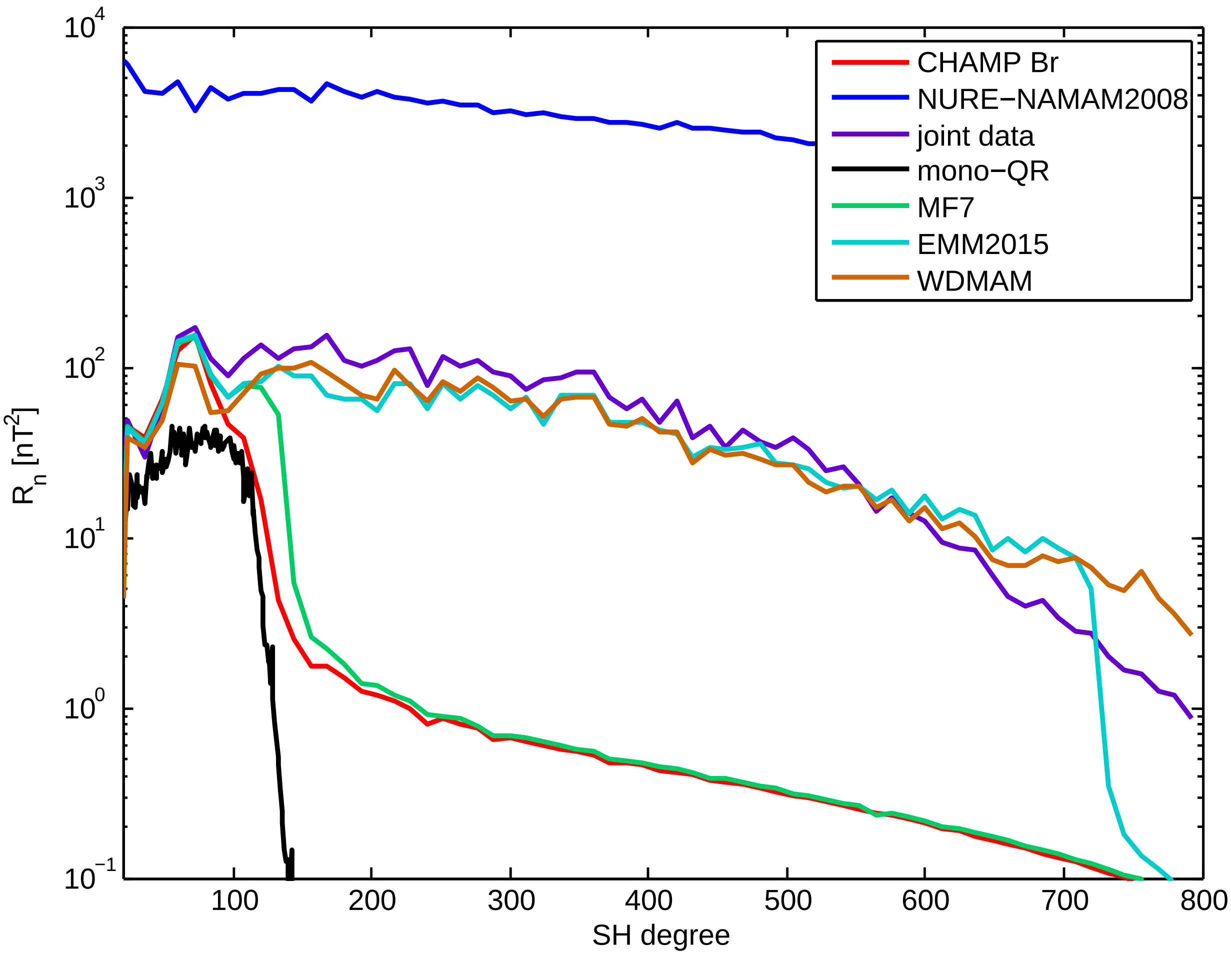

Figure 61 Regional power spectra corresponding to panels (a)-(f) of Fig. 60. Respective values were kindly derived by Fotini Vervelidou using the R-SCHA based routine of Vervelidou and Thébault (2015). For comparison, the global power spectrum of the quadratic regularized model mono-QR is given in black.

6 Summary and conclusion

This thesis presents the successful development and application of a potential field modeling method based on equivalent point sources to problems on both global and regional scales. Field predictions are derived from global satellite measurements from CHAMP and regional near-surface measurements from offshore Norway and North America. The employed inversion scheme considers the residuals in a least squares sense but handles outliers using a robust approach. Stable model solutions at the Earth's surface and below are derived by the additional implementation of model regularization.

The first part of the thesis focuses on global lithospheric field models derived from CHAMP satellite vector magnetic field data and using an IRLS algorithm, with Huber weighting of residuals and latitude-dependent data uncertainties implemented for all three field components at all latitudes. Three different regularization approaches are tested: quadratic regularization (QR), maximum entropy regularization (ER) and L_1-norm regularization (L1). The first approach results in models which have the smallest possible sum of squares of the source values for a chosen level of misfit. The resulting damping of the field amplitudes is not always in agreement with the geology, as the lithospheric field is characterized by several large amplitude local magnetic field anomalies like the Kursk anomaly in Ukraine and the Bangui anomaly in central Africa. Both the L_1-norm regularization and the entropy regularization allow higher amplitude localized anomalies. The final models representing the quadratic, entropy and L_1-norm regularization scheme are denoted as mono-QR, mono-ER and mono-L1, respectively. The corresponding regularization parameters are chosen according to the model misfits and by considering field predictions at the Earth's surface. The final models represent the global observations to a similar level of accuracy. Model differences are more distinct in the spectral domain and in visual inspection of the radial field predictions at the Earth's surface. There is excellent agreement between the various models for spherical harmonic degrees up to $n = 60$. The models show also good agreement with MF7 and CHAOS-6, with degree correlations above 0.7 for degrees $n < 100$ and $n < 105$, respectively. The entropy regularized model mono-ER has the lowest power for spherical harmonic degrees $n > 65$, whereas the power of mono-L1 is slightly less than that of the quadratic regularized model mono-QR, although this depends on the precise choice of the regularization parameter. In these tests, the entropy regularized model requires fewer effective degrees of freedom and its predictions at the Earth's surface have the smallest global average absolute radial field value.

The equivalent source routine is based on local basis functions, so the technique is also suitable for regional geomagnetic field investigations. The second part of this thesis concentrates on regional lithospheric field models applying a quadratic regularized IRLS scheme to aeromagentic scalar data from offshore Norway. The corresponding routine uses only sources in the vicinity of the survey and does not account for latitude dependent data errors. With suitable regularization parameters, the model predictions of all three field components are stable when performing downward continuation. By comparing an equivalent source based regional model with the industry standard model BGGM20016 and real well data from the Ekofisk field in the North Sea, the equivalent source routine is demonstrated to be suitable for directional drilling applications.

The final part of this thesis shows that the equivalent point source routine is capable of generating joint inversion models of satellite and near-surface data. Radial CHAMP data with near-surface field intensity data from NURE-NAMAM2008 are used to generate a high resolution regional map of North America. The resulting field predictions as well as regional power spectra are found to be in good agreement with the lithospheric field models EMM2015 and WDMAM. Corresponding residual values with respect to the NURE-NAMAM2008 data are smallest for the joint inversion model.

The above results suggest that the equivalent point source inversion routine is a flexible method for generating both global and regional lithospheric field models. The benefit of the used approach is its mathematical simplicity and useful application for data at any altitude and spatial extension. The equivalent source values can also be easily transformed into spherical harmonics, allowing for comparisons with SH based models and the possibility to generate approximate regional power spectra. The main advantage of the equivalent point source routine lies in the local parametrization of the source model, compared with the global nature of standard spherical harmonic basis functions. When using global basis functions, noise focused at a particular location (e.g. polar latitudes) contaminates all model parameters and is hard to control. This problem is particularly noticeable for zonal terms in spherical harmonic models. However, in the presented approach only the equivalent sources located close to the disturbed regions are affected. A further advantage that follows from the local parametrization is the ability to apply model regularization (or other a priori information) locally. The adopted method is also not dependent on injecting synthetic data with the satellite polar gap regions, as is necessary in the standard spherical harmonic modeling framework.

Since the launch of the satellite trio Swarm, geomagnetic data quality has improved significantly. The methodology presented here needs further improvement in order to take full advantage from the satellites' constellation. In particular, the data error covariance matrix will need to be extended to handle field differences, approximating NS and EW gradients, and related error correlations. With these methodological improvements the lithospheric field models are also expected to improve (Olsen et al., 2017).
In addition, the method of using only a limited amount of measurements close to a given source to improve the efficiency of the regional and combined inversion routine is promising and should be investigated further in order to ensure that as much data as possible is used when deriving regional lithospheric field models.

Having established the technique in this thesis and demonstrated its application in case studies, a wide range of future applications is now possible. For instance, the combined inversion routine can be used to produce full spectrum model predictions, which are valuable for directional surveying and lithospheric studies in particular regions (e.g. Australia). The method also possesses the possibility for magnetization studies. Further, the local parametrization of the method can be an advantage for lithospheric field studies of other terrestrial planets and the Moon (e.g. Toyoshima et al., 2008).

References

Aakjær, C. D., Olsen, N., and Finlay, C. C. (2016). Determining polar ionospheric electrojet currents from Swarm satellite constellation magnetic data. *Earth, Planets and Space*, 68(1):140.

Allen, F., Tooms, P., Conran, G., Lesso, B., and Van de Slijke, P. (1997). Extended-reach drilling: breaking the 10-km barrier. *Oilfield Review*, 9:32–47.

Åm, K. (1973). Tolkning av magnetiske og gravimetriske data: Kontinentalsokkelen. Stavanger/Stad (59°–62°N). *Norges geologiske undersøkelse Report*, 1175:18.

Arkani-Hamed, J., Langel, R. A., and Purucker, M. (1994). Scalar magnetic anomaly maps of Earth derived from POGO and Magsat data. *Journal of Geophysical Research: Solid Earth*, 99(B12):24075–24090.

Aster, R., Borchers, B., and Thurber, C. (2013). *Parameter estimation and inverse problems. Second Edition.* Elsevier Academic Press: Burlington.

Backus, G., Parker, R. L., and Constable, C. (1996). *Foundations of geomagnetism.* Cambridge University Press.

Bankey, V., Cuevas, A., Daniels, D., Finn, C., et al. (2002). U.S. Geological Survey special map. *available at: https://pubs.usgs.gov/sm/mag_map/*.

Beamish, D. et al. (2015). Levelling aeromagnetic survey data without the need for tie-lines. *Geophysical Prospecting*, 63(2):451–460.

Beggan, C., Macmillan, S., Clarke, E., and Hamilton, B. (2014). Improving models of the Earth's magnetic field for directional drilling applications. *First Break*, 32(3):53–60.

Beiki, M., Bastani, M., and Pedersen, L. B. (2010). Leveling HEM and aeromagnetic data using differential polynomial fitting. *Geophysics*, 75(1):L13–L23.

Berger, A. L., Pietra, V. J. D., and Pietra, S. A. D. (1996). A maximum entropy approach to natural language processing. *Computational linguistics*, 22(1):39–71.

BGS (2016). BGS Global Geomagnetic Model. *available at: http://www.geomag.bgs.ac.uk/data_service/directionaldrilling/bggm.html, last accessed 01 May 2017.*

Blakely, R. (1996). *Potential Theory in Gravity and Magnetic Applications.* Cambridge University Press.

Bloxham, J., Gubbins, D., and Jackson, A. (1989). Geomagnetic secular variation. *Philosophical Transactions of the Royal Society of London A: Mathematical, Physical and Engineering Sciences*, 329(1606):415–502.

Chambodut, A., Panet, I., Mandea, M., Diament, M., Holschneider, M., and Jamet, O. (2005). Wavelet frames: an alternative to spherical harmonic representation of potential fields. *Geophysical Journal International*, 163(3):875–899.

Cheatham, C., Shih, S., Churchwell, D., Woody, J., Rodney, P., et al. (1992). Effects of magnetic interference on directional surveys in horizontal wells. In *SPE/IADC Drilling Conference*. Society of Petroleum Engineers.

Constable, C. (1988). Parameter estimation in non-Gaussian noise. *Geophysical Journal International*, 94(1):131–142.

Cowles, L. G. (1938). The adjustment of misclosures. *Geophysics*, 3(4):332–339.

Cox, A. (1969). Geomagnetic reversals. *Science*, 163(3864):237–245.

Cramer, N. F. (2001). *The Physics of Alfvén Waves.*

Dampney, C. (1969). The equivalent source technique. *Geophysics*, 34(1):39–53.

Driessen, K. and Rombouts, R. (2007). Matlab Library for Robust Analysis. *available at: http://wis.kuleuven.be/stat/robust.html*.

Dyment, J., Choi, Y., Hamoudi, M., Lesur, V., and Thébault, E. (2015). Global equivalent magnetization of the oceanic lithosphere. *Earth and Planetary Science Letters*, 430:54–65.

Edvardsen, I., Hansen, T. L., Gjertsen, M., Wilson, H., et al. (2013). Improving the accuracy of directional wellbore surveying in the Norwegian Sea. *SPE Drilling & Completion*, 28(02):158–167.

Edvardsen, I., Nyrnes, E., Johnsen, M. G., Hansen, T. L., Løvhaug, U. P., Matzka, J., et al. (2014). Improving the accuracy and reliability of MWD/magnetic-wellbore-directional surveying in the Barents Sea. *SPE Drilling & Completion*, 29(02):215–225.

Emmert, J., Richmond, A., and Drob, D. (2010). A computationally compact representation of magnetic-Apex and quasi-dipole coordinates with smooth base vectors. *Journal of Geophysical Research: Space Physics*, 115(A8).

Farquharson, C. G. and Oldenburg, D. W. (1998). Non-linear inversion using general measures of data misfit and model structure. *Geophysical Journal International*, 134(1):213–227.

Fedi, M. and Florio, G. (2003). Decorrugation and removal of directional trends of magnetic fields by the wavelet transform: application to archaeological areas. *Geophysical Prospecting*, 51(4):261–272.

Finlay, C. C., Olsen, N., Kotsiaros, S., Gillet, N., and Tøffner-Clausen, L. (2016a). Recent geomagnetic secular variation from Swarm. *Earth, Planets and Space*, 68(1):1–18.

Finlay, C. C., Olsen, N., and Tøffner-Clausen, L. (2015). DTU candidate field models for IGRF-12 and the CHAOS-5 geomagnetic field model. *Earth, Planets and Space*, 67(1):1.

Finlay, C. C., Vorgel, C., and Olsen, N. (2016b). Separation of core and lithospheric magnetic fields by co-estimation of equivalent source models from Swarm data. AGU Fall Meeting in San Francisco, USA.

Fox, J. and Weisberg, S. (2002). Robust regression. *An R and S-Plus companion to Applied Regression*.

Friis-Christensen, E., Lühr, H., and Hulot, G. (2006). Swarm: A constellation to study the Earth's magnetic field. *Earth, planets and space*, 58(4):351–358.

Friis-Christensen, E., Lühr, H., Knudsen, D., and Haagmans, R. (2008). Swarm–an Earth observation mission investigating Geospace. *Advances in Space Research*, 41(1):210–216.

Geosoft 2010a (2010). Montaj MAGMAP filtering, 2-D frequency domain processing of potential field data, extension for OASIS Montaj v7.1. Geosoft Incorporated.

Geosoft 2010b (2010). OASIS Montaj v7.2 Mapping and processing system, The core software platform for working with large volume spatial data. Quick start tutorials. Geosoft Incorporated.

Gillet, N., Jackson, A., and Finlay, C. C. (2007). Maximum entropy regularization of time-dependent geomagnetic field models. *Geophysical Journal International*, 171(3):1005–1016.

Glatzmaier, G. A., Coe, R. S., Hongre, L., and Roberts, P. H. (1999). The role of the Earth's mantle in controlling the frequency of geomagnetic reversals. *Nature*, 401(6756):885–890.

Grant, F. (1985). Aeromagnetics, geology and ore environments, i. magnetite in igneous, sedimentary and metamorphic rocks: an overview. *Geoexploration*, 23(3):303–333.

Green, A. (1983). A comparison of adjustment procedures for leveling aeromagnetic survey data. *Geophysics*, 48(6):745–753.

Gull, S. and Skilling, J. (1989). Maximum entropy and Bayesian methods. *J. Skilling*.

Gull, S. F. and Daniell, G. J. (1978). Image reconstruction from incomplete and noisy data.

Gull, S. F. and Skilling, J. (1999). Quantified maximum entropy MemSys5 users' manual. *Royston: Maximum Entropy Data Consultants Ltd.*

Haines, G. (1985). Spherical cap harmonic analysis. *Journal of Geophysical Research: Solid Earth (1978–2012)*, 90(B3):2583–2591.

Halliburton (2001). *Directional Surveying Fundamentals. Document Number: TDTM0106A*. Sperry-Sun, a Halliburton Company.

Hamilton, B., Ridley, V. A., Beggan, C. D., and Macmillan, S. (2015). The BGS magnetic field candidate models for the 12th generation IGRF. *Earth, Planets and Space*, 67(1):1.

Hammer, M. D. (2011). Master's thesis: Lithospheric contributions to the geomagnetic field as measured with satellites - spatial representation using monopoles. *Faculty of Science at the University of Copenhagen*.

Hamoudi, M., Quesnel, Y., Dyment, J., and Lesur, V. (2011). Aeromagnetic and marine measurements. In *Geomagnetic Observations and Models*, pages 57–103. Springer.

Hansen, P. C. (1998). *Rank-deficient and discrete ill-posed problems: numerical aspects of linear inversion*. SIAM.

Hanson, K. M. and Silver, R. N. (2012). *Maximum Entropy and Bayesian Methods: Santa Fe, New Mexico, USA, 1995 Proceedings of the Fifteenth International Workshop on Maximum Entropy and Bayesian Methods*, volume 79. Springer Science & Business Media.

Hauta-niemi, H., Kurimo, M., Multala, J., Levaniemi, H., and Vironmaki, J. (2005). The "Three In One" aerogeophysical concept of GTK in 2004. *Special paper-Geological survey of Finland*, 39:21.

Herland, E. V., Finlay, C. C., Olsen, N., Edvardsen, I., Nordgård-Hansen, E., Laundal, K. M., and Waag, T. I. (2017). The CHAOS-X model and uncertainty values for magnetic directional surveying. *Society of Petroleum Engineers*.

Hodder, B. M. (1982). Monopoly. *Geophysical Journal International*, 70(1):217–228.

Holschneider, M., Chambodut, A., and Mandea, M. (2003). From global to regional analysis of the magnetic field on the sphere using wavelet frames. *Physics of the Earth and Planetary Interiors*, 135(2):107–124.

Huang, H. (2008). Airborne geophysical data leveling based on line-to-line correlations. *Geophysics*, 73(3):F83–F89.

Inglis, T. (2013). *Directional drilling*, volume 2. Springer Science & Business Media.

Ishihara, T. (2015). A new leveling method without the direct use of crossover data and its application in marine magnetic surveys: weighted spatial averaging and temporal filtering. *Earth, Planets and Space*, 67(1):1–14.

Jackson, A., Constable, C., and Gillet, N. (2007). Maximum entropy regularization of the geomagnetic core field inverse problem. *Geophysical Journal International*, 171(3):995–1004.

Jacobs, J. A. (1994). *Reversals of the Earth's magnetic field*, volume 63. Cambridge University Press.

Jamieson, A., McGregor, A., Stigant, J., and Weston, J. (2016). *Introduction to Wellbore Positioning*. *https://www.uhi.ac.uk/en/research-enterprise/wellbore-positioning-download*. University of the Highlands and Islands.

Kan, J. R., Zhu, L., Lui, A. T. Y., and Akasofu, S.-I. (1991). A Magnetosphere-Ionosphere Coupling Theory of Substorms Including Magnetotail Dynamics. In Meng, C.-I., Rycroft, M. J., and Frank, L. A., editors, *Auroral Physics*, page 311.

Koenig, L., Martin, S., Studinger, M., and Sonntag, J. (2010). Polar airborne observations fill gap in satellite data. *Eos, Transactions American Geophysical Union*, 91(38):333–334.

Kother, L., Hammer, M. D., Finlay, C. C., and Olsen, N. (2015). An equivalent source method for modelling the global lithospheric magnetic field. *Geophysical Journal International*, 203(1):553–566.

Kotsiaros, S. (2016). Toward more complete magnetic gradiometry with the Swarm mission. *Earth, Planets and Space*, 68(1):130.

Kuvshinov, A. and Olsen, N. (2005). 3-d modelling of the magnetic fields due to ocean tidal flow. In *Earth observation with CHAMP*, pages 359–365. Springer.

Langel, R. A. and Hinze, W. J. (1998). *The magnetic field of the Earth's lithosphere: The satellite perspective*. Cambridge University Press.

Laundal, K., Cnossen, I., Milan, S. E., Haaland, S. E., Coxon, J., Pedatella, N., Förster, M., and Reistad, J. (2017). North–South asymmetries in Earth's magnetic field. *Space Science Reviews*, 206(1–4):225–257.

Lesur, V., Hamoudi, M., Choi, Y., Dyment, J., and Thébault, E. (2016). Building the second version of the World Digital Magnetic Anomaly Map (WDMAM). *Earth, Planets and Space*, 68(1):1–13.

Livermore, P., Hollerbach, R., and Finlay, C. (2017). An accelerating high-latitude jet in Earth's core. *Nature Geoscience*, 10:62–68.

Lowes, F. (1974). Spatial power spectrum of the main geomagnetic field, and extrapolation to the core. *Geophysical Journal International*, 36(3):717–730.

Lowrie, W. (2007). *Fundamentals of geophysics*. Cambridge university press.

Luenberger, D. G. (1969). *Optimization by vector space methods*. John Wiley & Sons.

Luyendyk, A. (1997). Processing of airborne magnetic data. *AGSO Journal of Australian Geology and Geophysics*, 17:31–38.

Lysak, R. (1990). Electrodynamic coupling of the magnetosphere and ionosphere. *Space Science Reviews*, 52:33–87.

Macmillan, S. and Finlay, C. (2011). The international geomagnetic reference field. *IAGA Special Sopron Book Series - Chapter 10*, 5:265 – 276.

Macmillan, S. and Grindrod, S. J. (2010). Confidence limits associated with values of the Earth's magnetic field used for directional drilling. *SPE Drilling and Completion*, 25(2):230–238.

Maisinger, K., Hobson, M. P., and Lasenby, A. (2004). Maximum-entropy image reconstruction using wavelets. *Monthly Notices of the Royal Astronomical Society*, 347(1):339–354.

Matzka, J., Rasmussen, T., Olesen, A., Nielsen, J., Forsberg, R., Olsen, N., Halpenny, J., and Verhoef, J. (2010). A new aeromagnetic survey of the North Pole and the Arctic Ocean north of Greenland and Ellesmere island. *Earth Planets Space*, 62:829 – 832.

Mauersberger, P. (1956). Das Mittel der Energiedichte des geomagnetischen Hauptfeldes. *Gerlands Beiträge*, 65:207.

Mauring, E., Beard, L. P., Kihle, O., and Smethurst, M. A. (2002). A comparison of aeromagnetic levelling techniques with an introduction to median levelling. *Geophysical Prospecting*, 50(1):43–54.

Maus, S. (2010). Magnetic field model MF7. *available at: http://geomag.org/models/MF7.html, last accessed 30 January 2017.*

Maus, S., Nair, M. C., Poedjono, B., Okewunmi, S., Fairhaid, D., Barckhausen, U., Milligan, P. R., Matzka, J., et al. (2012). High-definition geomagnetic models: A new perspective for improved wellbore positioning. In *IADC/SPE Drilling Conference and Exhibition*. Society of Petroleum Engineers.

Maus, S., Rother, M., Hemant, K., Stolle, C., Lühr, H., Kuvshinov, A., and Olsen, N. (2006). Earth's lithospheric magnetic field determined to spherical harmonic degree 90 from CHAMP satellite measurements. *Geophysical Journal International*, 164(2):319–330.

Maus, S., Yin, F., Lühr, H., Manoj, C., Rother, M., Rauberg, J., Michaelis, I., Stolle, C., and Müller, R. (2008). Resolution of direction of oceanic magnetic lineations by the sixth-generation lithospheric magnetic field model from CHAMP satellite magnetic measurements. *Geochemistry, Geophysics, Geosystems*, 9(7).

McLeod, M. G. and Coleman, P. J. (1980). Spatial power spectra of the crustal geomagnetic field and core geomagnetic field. *Physics of the Earth and Planetary Interiors*, 23(2):P5–P19.

Menke, W. (2012). *Geophysical data analysis: Discrete inverse theory*, volume 45. Academic press.

Merrill, R. T. and McFadden, P. L. (1999). Geomagnetic polarity transitions. *Reviews of Geophysics*, 37(2):201–226.

Nelson, J. B. (1994). Leveling total-field aeromagnetic data with measured horizontal gradients. *Geophysics*, 59(7):1166–1170.

NOAA (2016). High Definition Geomagnetic Model. *available at: https://ngdc.noaa.gov/geomag/HDGM/index.html, last accessed 01 May 2017*.

O'Brien, M. S. and Parker, R. L. (1994). Regularized geomagnetic field modelling using monopoles. *Geophysical Journal Internatinoal*, 118.3:566–578.

Olesen, O., Brönner, M., Ebbing, J., Gellein, J., Gernigon, L., Koziel, J., Lauritsen, T., Myklebust, R., Pascal, C., Sand, M., et al. (2010). New aeromagnetic and gravity compilations from Norway and adjacent areas: methods and applications. In *Geological Society, London, Petroleum Geology Conference series*, volume 7, pages 559–586. Geological Society of London.

Olesen, O., Gellein, J., Håbrekke, H., Kihle, O., Skilbrei, J., and Smethurst, M. (1997). Magnetic anomaly map Norway and adjacent ocean areas, scale 1: 3 million. *Geological Survey of Norway, Trondheim*.

Olsen, N. (2002). A model of the geomagnetic field and its secular variation for epoch 2000 estimated from Ørsted data. *Geophysical Journal International*, 149(2):454–462.

Olsen, N. and Finlay, C. C. (2012). Geomagnetism. *Lecture notes*.

Olsen, N. and Finlay, C. C. (2016). Inverse problems. *Lecture notes*.

Olsen, N., Friis-Christensen, E., Hulot, G., Korte, M., Kuvshinov, A., Lesur, V., Lühr, H., Macmillan, S., Mandea, M., Maus, S., et al. (2004). Swarm end-to-end mission performance simulator study. *DSRI Report*, 1.

Olsen, N., Friis-Christensen, E., Hulot, G., Korte, M., Kuvshinov, A., Lesur, V., Lühr, H., Macmillan, S., Mandea, M., Maus, S., Purucker, M., Reigber, C., Ritter, P., Rother, M., Sabaka, T., Tarits, P., and Thomson, A. (2005). *Swarm end-to-end mission performance simulator study*. DSRI Report 1/2004, ISSN 1602-527X.

Olsen, N., Hulot, G., and Sabaka, T. J. (2010a). Sources of the geomagnetic field and the modern data that enable their investigation. In *Handbook of geomathematics*, pages 105–124. Springer.

Olsen, N., Lühr, H., Finlay, C. C., Sabaka, T. J., Michaelis, I., Rauberg, J., and Tøffner-Clausen, L. (2014). The CHAOS-4 geomagnetic field model. *Geophysical Journal International*, 197(2):815–827.

Olsen, N., Lühr, H., Sabaka, T. J., Mandea, M., Rother, M., Tøffner-Clausen, L., and Choi, S. (2006). CHAOS—a model of the Earth's magnetic field derived from CHAMP, Ørsted, and SAC-C magnetic satellite data. *Geophysical Journal International*, 166(1):67–75.

Olsen, N., Mandea, M., Sabaka, T. J., and Tøffner-Clausen, L. (2009). CHAOS-2—a geomagnetic field model derived from one decade of continuous satellite data. *Geophysical Journal International*, 179(3):1477–1487.

Olsen, N., Mandea, M., Sabaka, T. J., and Tøffner-Clausen, L. (2010b). The CHAOS-3 geomagnetic field model and candidates for the 11th generation IGRF. *Earth, Planets and Space*, 62(10):719–727.

Olsen, N., Ravat, D., Finlay, C. C., and Kother, L. (2017). A new lithospheric field model based on CHAMP and Swarm magnetic satellite data. Fourth Swarm Science Meeting and Geodetic Missions Workshop. Banff, Alberta, Canada.

Olsen, N. and Stolle, C. (2012). Satellite geomagnetism. *Annual Review of Earth and Planetary Sciences*, 40:441–465.

Olson, P. and Amit, H. (2006). Changes in Earth's dipole. *Naturwissenschaften*, 93(11):519–542.

Parker, R. L. and Shure, L. (1982). Efficient modeling of the Earth's magnetic field with harmonic splines. *Geophysical Research Letters*, 9(8):812–815.

Purucker, M. and Whaler, K. (2007). Crustal magnetism. *Treatise on geophysics*, 5:195–237.

Ravat, D., Finn, C., Hill, P., Kucks, R., Phillips, J., Blakely, R., Bouligand, C., Sabaka, T., Elshayat, A., Aref, A., and Elawadi, E. (2009). A preliminary, full spectrum, magnetic anomaly grid of the united states with improved long wavelengths for studying continental dynamics: A website for distribution of data. *U.S. Geological Survey Open-File Report 2009-1258*, pages 1–7.

Ravat, D., Whaler, K., Pilkington, M., Sabaka, T., and Purucker, M. (2002). Compatibility of high-altitude aeromagnetic and satellite-altitude magnetic anomalies over Canada. *Geophysics*, 67(2):546–554.

Reeves, C. (2005). Aeromagnetic surveys: principles, practice and interpretation. *Earthworks - Geosoft*.

Reeves, C. V. (1993). Limitations imposed by geomagnetic variations on high quality aeromagnetic surveys. *Exploration Geophysics*, 24(2):115–116.

Reford, M. and Sumner, J. (1964). Aeromagnetics. *Geophysics*, 29(4):482–516.

Reigber, C., Lühr, H., and Schwintzer, P. (2000). Status of the CHAMP mission. In *Towards an Integrated Global Geodetic Observing System (IGGOS)*, pages 63–65. Springer.

Reigber, C., Schwintzer, P., and Lühr, H. (1999). The CHAMP geopotential mission. *Boll. Geof. Teor. Appl*, 40:285–289.

Sabaka, T. J. and Olsen, N. (2006). Enhancing comprehensive inversions using the Swarm constellation. *Earth, planets and space*, 58(4):371–395.

Sabaka, T. J., Olsen, N., and Purucker, M. E. (2004). Extending comprehensive models of the Earth's magnetic field with Ørsted and CAMP data. *Geophysical Journal International*, 159(2):521–547.

Sabaka, T. J., Olsen, N., Tyler, R. H., and Kuvshinov, A. (2015). CM5, a pre-Swarm comprehensive geomagnetic field model derived from over 12 yr of CAMP, Ørsted, SAC-C and observatory data. *Geophysical Journal International*, 200(3):1596–1626.

Saff, E. (2005). Points on spheres and manifolds. *available at: https://my.vanderbilt.edu/edsaff/spheres-manifolds/, last accessed: 30 June 2015.*

Schmidt, M. (2005). Least squares optimization with l1-norm regularization. *CS542B Project Report*, pages 14–18.

Schott, J.-J. and Thébault, E. (2011). Modelling the Earth's magnetic field from global to regional scales. In *Geomagnetic Observations and Models*, pages 229–264. Springer.

Serson, P. and Hannaford, W. (1957). A statistical analysis of magnetic profiles. *Journal of Geophysical Research*, 62(1):1–18.

Shure, L., Parker, R. L., and Backus, G. E. (1982). Harmonic splines for geomagnetic modelling. *Physics of the Earth and Planetary Interiors*, 28(3):215–229.

Simons, F. J. and Dahlen, F. (2006). Spherical slepian functions and the polar gap in Geodesy. *Geophysical Journal International*, 166(3):1039–1061.

Smethurst, M. (2000). Land–offshore tectonic links in western Norway and the northern North Sea. *Journal of the Geological Society*, 157(4):769–781.

Smith, C. R. and Grandy, W. (2013). *Maximum-Entropy and Bayesian methods in inverse problems*, volume 14. Springer Science & Business Media.

Sneeuw, N. and Van Gelderen, M. (1997). The polar gap. In *Geodetic boundary value problems in view of the one centimeter geoid*, pages 559–568. Springer.

Stockmann, R., Finlay, C. C., and Jackson, A. (2009). Imaging Earth's crustal magnetic field with satellite data: a regularized spherical triangle tessellation approach. *Geophysical Journal International*, 179(2):929–944.

Tarantola, A. (2005). *Inverse problem theory and methods for model parameter estimation*. SIAM.

Thébault, E. (2006). Global lithospheric magnetic field modelling by successive regional analysis. *Earth, planets and space*, 58(4):485–495.

Thébault, E. (2008). A proposal for regional modelling at the Earth's surface, R-SCHA2D. *Geophysical Journal International*, 174(1):118–134.

Thébault, E., Finlay, C. C., Beggan, C. D., Alken, P., Aubert, J., Barrois, O., Bertrand, F., Bondar, T., Boness, A., Brocco, L., et al. (2015). International geomagnetic reference field: the 12th generation. *Earth, Planets and Space*, 67(1):1–19.

Thébault, E., Lesur, V., Kauristie, K., and Shore, R. (2017). Magnetic field data correction in space for modelling the lithospheric magnetic field. *Space Science Reviews*, 206(1):191–223.

Thébault, E., Mandea, M., and Schott, J. (2006a). Modeling the lithospheric magnetic field over France by means of revised spherical cap harmonic analysis (R-SCHA). *Journal of Geophysical Research: Solid Earth (1978–2012)*, 111(B5).

Thébault, E. and Mandea-Alexandrescu, M. (2007). *The changing faces of the Earth's magnetic field: a glance at the magnetic lithospheric field, from local and regional scales to a planetary view*. Commission for the Geological Map of the World.

Thébault, E., Purucker, M., Whaler, K. A., Langlais, B., and Sabaka, T. J. (2010). The magnetic field of the Earth's lithosphere. *Space Science Reviews*, 155(1-4):95–127.

Thébault, E., Schott, J., and Mandea, M. (2006b). Revised spherical cap harmonic analysis (R-SCHA): Validation and properties. *Journal of Geophysical Research: Solid Earth (1978–2012)*, 111(B1).

Thébault, E., Schott, J., Mandea, M., and Hoffbeck, J. (2004). A new proposal for spherical cap harmonic modelling. *Geophysical Journal International*, 159(1):83–103.

Thomsen, P. L., Hansen, F., Olsen, N., and Christensen, E. F. (2003). Swarm-a constellation to study the dynamics of the Earth's magnetic field and its interactions with the Earth system. In *Recent Advances in Space Technologies, 2003. RAST'03. International Conference on. Proceedings of*, pages 194–201. IEEE.

Tikhonov, A. and Arsenin, V. (1977). *Solution of Ill-posed problems*. V. H. Winston and Sons.

Torge, W. (2001). *Geodesy*. Walter de Gruyter.

Torkildsen, T., Edvardsen, I., Fjogstad, A., Saasen, A., Amundsen, P. A., Omland, T. H., et al. (2004). Drilling fluid affects MWD magnetic azimuth and wellbore position. In *IADC/SPE Drilling Conference*. Society of Petroleum Engineers.

Toyoshima, M., Shibuya, H., Matsushima, M., Shimizu, H., and Tsunakawa, H. (2008). Equivalent source mapping of the lunar crustal magnetic field using ABIC. *Earth, Planets and Space*, 60(4):365–373.

Tyler, R. H., Maus, S., and Lühr, H. (2003). Satellite observations of magnetic fields due to ocean tidal flow. *Science*, 299(5604):239–241.

Vervelidou, F. and Thébault, E. (2015). Global maps of the magnetic thickness and magnetization of the Earth's lithosphere. *Earth, Planets and Space*, 67(1):173.

von Frese, R., Ravat, D., Hinze, W., and McGue, C. (1988). Improved inversion of geopotential field anomalies for lithospheric investigations. *GEOPHYSICS,*, 53(3):375–385,.

Von Frese, R. R., Hinze, W. J., and Braile, L. W. (1981). Spherical Earth gravity and magnetic anomaly analysis by equivalent point source inversion. *Earth and Planetary Science Letters*, 53(1):69–83.

Walker, M. and Jackson, A. (2000). Robust modelling of the Earth's magnetic field. *Geophysical Journal International*, 143:799–808.

Wendler, J. (2004). External forcing of the geomagnetic field? Implications for the cosmic ray flux - climate variability. *Journal of Atmospheric and Solar-Terrestrial Physics*, 66(13):1195–1203.

Wessel, P., Smith, W. H., Scharroo, R., Luis, J., and Wobbe, F. (2013). Generic mapping tools: Improved version released. *Eos, Transactions American Geophysical Union*, 94(45):409–410.

Williamson, H. S. et al. (2000). Accuracy prediction for directional measurement while drilling. *SPE Drilling & Completion*, 15(04):221–233.

Winch, D., Ivers, D., Turner, J., and Stening, R. (2005). Geomagnetism and Schmidt quasi-normalization. *Geophysical Journal International*, 160(2):487–504.

A Aeromagnetic data processing

For getting a better understanding of the used aeromagnetic data sets of this thesis, this chapter provides a brief introduction to a typical aeromagnetic data processing sequence, involving the correction for temporal field variations, main field subtraction, line leveling and micro leveling. Note that the common final processing steps of gridding and contouring will not be discussed here.

A.1 Error sources

Before starting the processing procedure, raw measurements are checked for spikes, gaps, instrument noise and other data irregularities (Luyendyk, 1997). Other severe contributions to error sources are due to magnetometer drift, aircraft effects, navigational effects, temporal magnetic field variations, ground clearance variations, altitude variations, and wave noise. The former contribute with very small noise levels (ca 0.1 nT) applying modern magnetometers (e.g. helium magnetometers (Reeves, 1993) and cesium magnetometers (Matzka et al., 2010)).
Aircraft effects are due to the aircraft's permanent magnetization (heading error) and its movement dependent magnetization (maneuver noise). The latter comprises of the Earth's magnetic field induced magnetization and a magnetization induced by currents within the aircraft. Maneuver noise is commonly removed from the measurements by performing a compensation flight prior to a survey. In this procedure the aircraft performs different roll, pitch and yaw maneuvers at high altitude and in a region of low magnetic signature, see Fig. 62.
Navigational effects are caused by inaccurate positioning of the different measurement points. Modern GPS systems have positional accuracies of ± 5 m, while pre-GPS techniques (radio-beacons and the comparison of video recordings with aerial photographs and topographical maps) were characterized by values of ± 50 to 500 m. In combination with the navigational data control, it is important to take the *cable length* into account: the distance between the aircraft's navigational reference point and the recording magnetometer. Hereafter the navigational data and raw measurements are merged for the following data processing.
Ground clearance effects are due to the fact that the measured amplitude of magnetic anomalies varies with the distance to the measuring device. A related error source is the altitude variation, magnetic field changes with height above the ellipsoid (ca. 0.025 nT/m).
Wave noise is created by secondary induced magnetic fields due to surface waves on large bodies of water. Values up to 1.5 nT have been recorded for this error source (at 80 m altitude) (Luyendyk, 1997).
The mentioned error sources have to be reduced as much as possible prior to aeromagentic data investigation, as the noise envelope limits the amplitude of geological anomalies that can be detected in a survey (Reeves, 1993).

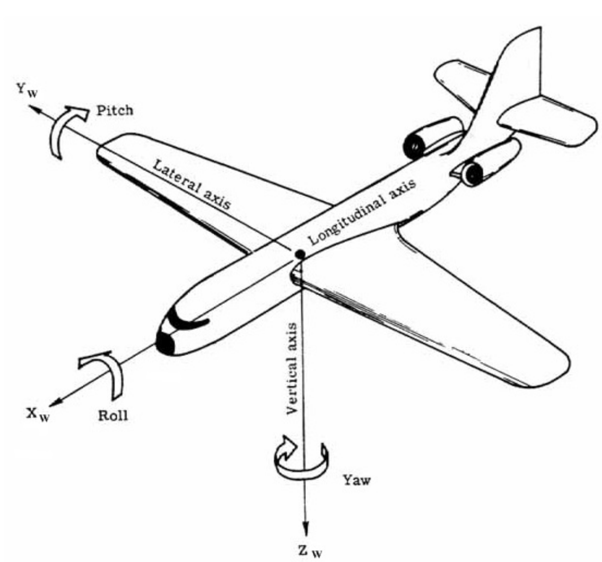

Figure 62 Roll, pitch and yaw maneuvers applied for the maneuver noise compensation. http://blog.tkjelectronics.dk/2012/03/quadcopters-how-to-get-started/

A.2 Main field corrections

In this processing step the survey time equivalent IGRF model of the Earth's regional field is subtracted from the measurements. The corresponding values are internationally agreed and derived using both satellite and observatory magnetic measurements. It should be noted that the model field is mainly based on the magnetic field arising from electric currents in the outer Earth's core and does not include rapid field fluctuations and small scale fields due to magnetized crustal rocks (Macmillan and Finlay, 2011).
For the data processing approach, secular variations are neglected as the mean date for the survey (and measurement locations above the ellipsoid) is used for deriving the corresponding model values (Luyendyk, 1997).

A.3 Removal of temporal variations

Current systems in the ionosphere and magnetosphere introduce rapid fluctuations in magnetic field measurements on Earth: micropulsations, diurnal variations and magnetic storms. The corresponding variations can be of a few seconds, minutes or hours - shorter than a typical aeromagnetic survey duration. The recorded magnetic fluctuations in an aeromagnetic missions have thus both temporal and spatial reasons - they are dependent on morphology changes due to the movement from one measurement point to another, and the field fluctuations due to the corresponding traveling period. Before further investigations of the data, the magnetic time variations, as well as instrumental drift, have to be removed from the measurements (Reford and Sumner, 1964).
Field variations which last a day or more can easily be quantified with repeating measurements. More complicated is the assessment of rapid fluctuations, especially in polar regions.
There exist three common approaches to deal with rapid time variations. The first one applies base station measurements to correct the airborne records, while the second approach uses tie-lines and corresponding cross-over corrections (see section A.3). The last method involves micro-leveling (Reeves, 1993). Most aeromagnetic surveys apply all three approaches in order to achieve the best possible data quality (Reeves, 2005).
Compared to the tie-line approach, base stations (at a fixed location on the ground) provide field corrections at every measurement point - not only at cross-over locations. However, the approach assumes that field variations on the ground are representative for the entire survey area. This assumption is not strictly true, especially for base station - aircraft distances of $> 50\,\mathrm{km}$, and can introduce high-frequency errors into the measurements (Luyendyk, 1997).
In order to minimize the effect of temporal field variations as much as possible, ground measurements are used to determine magnetic undisturbed days for the airborne mission.

Magnetic leveling

Aeromagnetic surveys consist of flight-lines covering the area of investigation. These lines are approximately parallel to each other. However due to e.g. weather conditions, orientation of the magnetic region of interest and topography changes, different line configurations exist. The flight-line spacing is defined individually for the different surveys and depend mainly on the mean depth to the crystalline basement, the required mapping resolution, the size of the target to detect and financial resources (Hamoudi et al., 2011). Typical spacing values range from $50 - 1500$ m. It is common to fly control lines (tie-lines) perpendicular to the flight lines at distances of typically 10 times the flight-line spacing (Hamoudi et al., 2011). This rate is often reduced to 5 for high latitude regions and 3 for some petroleum explorations (Hamoudi et al., 2011). After having removed the time dependent magnetic variations described in the above sections, flight lines and tie-lines should record identical values at their crossover points (Beamish et al., 2015). This is however not the case due to e.g. incomplete diurnal corrections, flight altitude variations, navigational errors, magnetometer drift or random noise (Mauring et al., 2002; Beamish et al., 2015). Before performing data gridding and interpretation, the measured differences at crossover points have to be minimized in order to remove the observed short-period magnetic variations from the data (Mauring et al., 2002). This procedure is commonly known as "leveling" and different empirical strategies have been developed throughout the last century for its optimization (Luyendyk, 1997). Differences between tie-lines and flight-lines at crossover points have got various names in the literature: mis-ties, crossover errors, misclosure errors and intersection errors. The former will be applied in the following.

Since mis-ties are typically much larger ($10-100$ nT) than modern aeromagnetic survey resolution, leveling becomes especially important when resolving anomalies in the range of $0.5-1$ nT (Mauring et al., 2002; Beamish et al., 2015). The general aim of leveling is to reduce the mis-ties to an amplitude below the noise envelope (Reeves, 1993).

Leveling of aeromagnetic surveys is typically performed by either least square methods or techniques based on fitting smooth functions to the observed mis-tie values (Mauring et al., 2002). Two techniques of the first category are the "method of condition equations" and the "method of observation equations". The reader is referred to Cowles (1938) and Green (1983) for further details of these techniques.
Typical techniques of the last category (all based on tie-line leveling) are polynomial leveling, B-spline leveling, low-pass filter leveling and median leveling (Mauring et al., 2002). The following sections will focus on the former two techniques. Additionally, a short list of literature suggestions for tie-line independent methods is given at the end of this section.

Adjustment of intersection locations

Most leveling methods assume accurate intersection locations along the flight pattern (Reeves, 2005). In order to ensure this condition, crossover locations are often adjusted prior to leveling. This adjustment can be performed by minimizing the sum of squares of the closure errors around the individual crossover points (Green, 1983). Except for the survey boundaries, each crossover point is surrounded by four loops of intersection lines, each defined by a closure error C

$$C = \eta_a - \eta_b + \eta_c - \eta_d, \tag{100}$$

where η_x represents the mis-tie (magnetic intensity difference between flight-line and tie-line) at crossover point x. Note that the signs are dependent on the chosen flight path, see Fig. 63. More details on reducing the closure errors of a given aeromagnetic survey can be found in (Green, 1983).

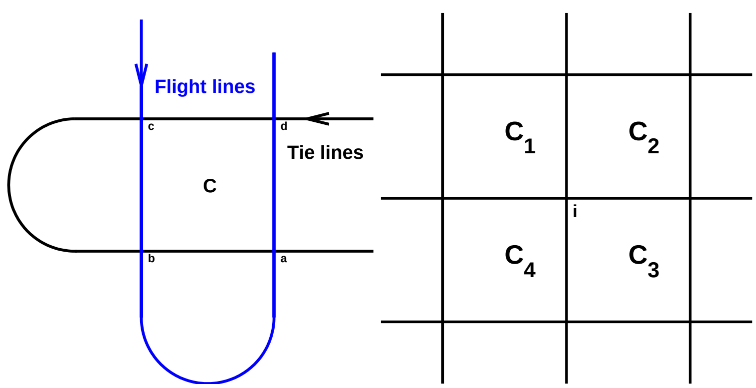

Figure 63 Left: The closure error C is dependent on the mis-ties at crossover points $a-d$. The arrows indicate the flight path. **Right:** A crossover point i is surrounded by four loops of intersection lines. Each loop is defined by a closure error. The figure is an adjusted version of Fig.1 in Green (1983).

Tie-line processing using polynomial leveling

Polynomial leveling is a standard procedure for reducing mis-ties below the noise envelope (Reeves, 2005). The method is based on the technique of fitting a polynomium $p(x)$ (or spline) to the N measured mis-tie values $e(x)$ along a survey line, where x represents the corresponding distance in time (Mauring et al., 2002). The desired polynomium is derived using the least squares method and minimizes the function $\sum_j [e(x_j) - p(x_j)]^2$ for $j = [1, N]$. It is common to apply low order polynomial functions (1-3) with orders less than $(N-1)/2$ (Luyendyk, 1997).
The tie-line processing is based on the assumption that the measured magnetic intensity is directionally invariant. In that sense flight lines and tie-lines should record equivalent values at crossover points, which

justifies that flight lines are adjusted to the tie-lines (Beamish et al., 2015).
Figure 64 illustrates the typical steps within polynomial leveling. Here the flight-lines are represented by horizontal lines $1-4$, while the perpendicular tie-lines are denoted $A-C$. Crossover locations are indicated by the letters $a-p$ Prior to the leveling steps the principal tie-line (T in the figure) is defined by the operator. This will be the absolute reference for the leveling process. The measurement period of T is often characterized by low geomagnetic activity, while the respective covered area shows a low magnetic profile (Reeves, 2005).
In the first polynomial leveling step all tie-lines are leveled with respect to T, determining the tie drift curves. The measured differences between a given tie-line C and T are calculated for intersections of the same flight-line $(C_d - T_b, C_h - T_f, C_l - T_j, ...)$. Plotting the corresponding values against their respective times, a polynomial fit is derived and subtracted from the data set of C. This results in the leveled tie-line C^*. This procedure is repeated for all tie-lines.
The next step describes the leveling of all combined flight-lines to the now adjusted tie-lines. The mis-ties between the flight-lines $(1-4)$ and tie-lines $(A^* - C^*)$ are calculated and sorted with respect to their measurement time along the flight-lines $(1_a - A^*_a, 1_b - T_b, 1_c - B^*_c, ...)$. The corresponding polynomial fit is subtracted from the original flight-line measurements resulting in the adjusted version $1^* - 4^*$.
Remaining residual values at cross-over points can be removed by two further steps (Luyendyk, 1997): i) a second flight-line leveling $(1^{**} - 4^{**})$ where the individual adjusted flight lines are leveled to the adjusted tie-lines (i.e. $3^*_i - A^*_i, 3^*_j - T_j, 3^*_k - B^*_k, 3^*_l - C^*_l$);
ii) The adjusted tie-lines are leveled to $1^{**} - 4^{**}$.

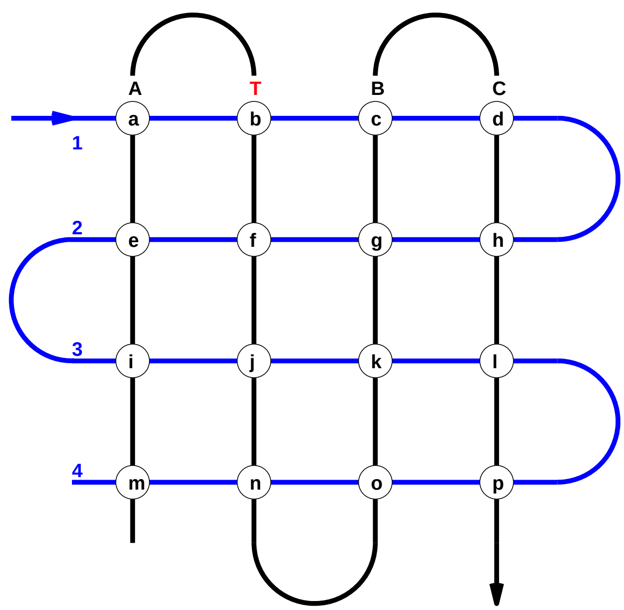

Figure 64 Idealistic illustration of flight-lines (blue) and tie-lines (black). Crossover points (white circles) appear whenever the two lines meet.

Leveling has no distorting effect on the original data as the respective flight-lines and tie-lines are only exposed to a constant shift (Mauring et al., 2002).
The polynomial leveling approach assumes smooth temporal variations of the mis-ties. This is indeed the case for most tie-lines which have a dense coverage of crossover points.
It is noteworthy that all mis-ties are weighted equally in the above presented procedure. This makes the polynomial leveling approach sensitive to outliers, a disadvantage which can be avoided by using piecewise low-order polynomial fitting (Mauring et al., 2002). The same authors give a good description of the sensitivity of the polynomial fit to the amount of applied mis-ties.

Leveling without tie-lines

Tie-line correction looses its efficiency for areas with large lithospheric gradients and for low flight altitudes (Beamish et al., 2015). Also, typical mis-tie errors are larger than modern aeromagnetic survey resolution. Having this in mind, and due to the fact that flying tie-lines is very expensive, different alternatives for tie-line corrections have been developed throughout the last decades. Some of the proposed leveling methods without the use of tie-lines are: synthetic tie lines (Hauta-niemi et al., 2005), wavelet transform (Fedi and Florio, 2003), horizontal gradient (Nelson, 1994), 1D and 2D polynomial data fitting (Beiki et al., 2010), line-to-line correlation (Huang, 2008), bi-directional gridding scheme (Beamish et al., 2015), weighted spatial averaging, and temporal filtering (Ishihara, 2015). The reader is referred to the mentioned literature for further details.

Micro leveling

Residual errors remaining after the above presented procedures are removed using micro-leveling. These errors become visible when the processed data is gridded and displayed as enhanced images (Luyendyk, 1997). Micro-leveling is a filtering process for removing across-line wavelengths equal to twice the line spacing and along-line wavelengths equal to the tie-line spacing (Reeves, 1993).

B Green's matrix for equivalent point source representation

The lithospheric field potential at a given position $\mathbf{r}_i = (r_i, \theta_i, \phi_i)$ can be expressed by means of K equal area distributed equivalent sources with individual positions $\mathbf{s}_k = (r_k, \theta_k, \phi_k)$ and source amplitudes q_k (in nT)

$$\begin{aligned} \mathbf{A}(\mathbf{r}_i) &= -\nabla\Phi(\mathbf{r}_i) \\ &= -\sum_{k=1}^{K} q_k \frac{r_k^2}{r_{ik}} \\ &= -\sum_{k=1}^{K} q_k \hat{\mathbf{e}}_i \cdot \nabla \frac{r_k^2}{r_{ik}} \\ &= \sum_{k=1}^{K} q_k g_{ik} \\ &= \underline{\underline{\mathbf{G}}}\mathbf{q}, \end{aligned} \tag{101}$$

where r_{ik} and μ_{ik} are the distance and angle between the position vectors of the location of interest i and source k, respectively:

$$\begin{aligned} r_{ik} &= |\mathbf{r}_i - \mathbf{s}_k| \\ &= \sqrt{r_i^2 + r_k^2 - 2r_i r_k \cos(\mu_{ik})} \\ \cos(\mu_{ik}) &= \cos(\theta_i)\cos(\theta_k) + \sin(\theta_i)\sin(\theta_k)\cos(\phi_i - \phi_k). \end{aligned} \tag{102}$$

where $\hat{\mathbf{e}}_i$ represents the unit vector, $\mathbf{q}$ is a vector of source amplitudes and $\underline{\underline{\mathbf{G}}}$ is an $N \times K$ Green's matrix with elements g_{ik} that are directional derivatives of source k evaluated at the location and measurement direction i,

$$g_{ik} = -\hat{\mathbf{e}}_i \cdot \nabla \frac{r_k^2}{r_{ik}}. \tag{103}$$

Applying $r_{ik} = \sqrt{u}$ with

$$\begin{aligned} u &= r_i^2 + r_k^2 - 2r_i r_k \cos(\mu_{ik}) \\ \cos(\mu_{ik}) &= \cos(\theta_i)\cos(\theta_k) + \sin(\theta_i)\sin(\theta_k)\cos(\phi_i - \phi_k) \\ \cos(\phi_i - \phi_k) &= \cos(\phi_i)\cos(\phi_k) + \sin(\phi_i)\sin(\phi_k) \\ \sin(\phi_i - \phi_k) &= \sin(\phi_i)\cos(\phi_k) - \cos(\phi_i)\sin(\phi_k) \\ \frac{\delta}{\delta x}\Big(\frac{1}{\sqrt{u}}\Big) &= -\frac{1}{2} \cdot u^{-3/2} \cdot \frac{\delta u}{\delta x}, \end{aligned} \tag{104}$$

the radial, latitudinal and longitudinal parts of the Green's matrix can be derived as follows,

$$\begin{aligned} g_{ik}^r &= -\frac{\partial}{\partial r_i}\Big(\frac{r_k^2}{r_{ik}}\Big) \\ &= -\frac{\partial}{\partial r_i}\Big(\frac{r_k^2}{\sqrt{u}}\Big) \\ &= -r_k^2 \cdot \Big[-\frac{1}{2} u^{-3/2} \cdot \Big(2r_i - 2r_i \cos(\mu_{ik})\Big)\Big] \\ &= r_k^2 \cdot \Big[u^{-3/2} \cdot (r_i - r_i \cos(\mu_{ik}))\Big] \\ &= \frac{r_k^2}{r_{ik}^3}\Big[r_i - r_k \cos(\mu_{ik})\Big] \end{aligned} \tag{105}$$

$$
\begin{aligned}
g_{ik}^{\theta} &= -\frac{1}{r_i}\frac{\partial}{\partial\theta_i}\Big(\frac{r_k^2}{r_{ik}}\Big) \\
&= -\frac{r_k^2}{r_i}\Big[-\frac{1}{2}u^{-3/2}\cdot\Big(-2r_ir_k(-\sin(\theta_i)\cos(\theta_k)+\cos(\theta_i)\sin(\theta_k)\cos(\phi_i-\phi_k))\Big)\Big] \\
&= \frac{r_k^3}{r_{ik}^3}\Big[\sin(\theta_i)\cos(\theta_k)-\cos(\theta_i)\sin(\theta_k)\cos(\phi_i-\phi_k)\Big]
\end{aligned}
\tag{106}
$$

$$
\begin{aligned}
g_{ik}^{\phi} &= -\frac{1}{r_i\sin(\theta_i)}\frac{\partial}{\partial\phi_i}\Big(\frac{r_k^2}{r_{ik}}\Big) \\
&= -\frac{r_k^2}{r_i\sin(\theta_i)}\Big[-\frac{1}{2}u^{-3/2}\cdot\Big(-2r_ir_k\sin(\theta_i)\sin(\theta_k)\cdot(-\sin(\phi_i)\cos(\phi_k)+\cos(\phi_i)\sin(\phi_k))\Big)\Big] \\
&= \frac{r_k^3}{r_{ik}^3}\Big[\sin(\theta_k)\cdot\Big(\sin(\phi_i)\cos(\phi_k)-\cos(\phi_i)\sin(\phi_k)\Big)\Big] \\
&= \frac{r_k^3}{r_{ik}^3}[\sin(\theta_k)\sin(\phi_i-\phi_k)].
\end{aligned}
\tag{107}
$$

C Removal of gross outliers

The quadratic regularized model with $\alpha = 900\,\mathrm{nT}^{-2}$ is used to identify disturbed satellite tracks by means of large residual values. In order to prevent these tracks to have an influence on the equivalent source models, days where at least one of the residual components $> 100\,\mathrm{nT}$ are removed from the data set, see Fig. 65. For the used CHAMP data set (from 01/01/2009 to 02/09/2010) this corresponds to 30 days. Please note that this additional data selection is only performed on non-polar data values (QD latitude $|\theta| < 55°$).
The removal of gross outliers has almost no influence on the resulting power spectrum (see Fig. 66), and minimal variations are observed for the corresponding radial field maps (see Fig. 67). However, clear differences are given in the corresponding model statistics of Table 19.

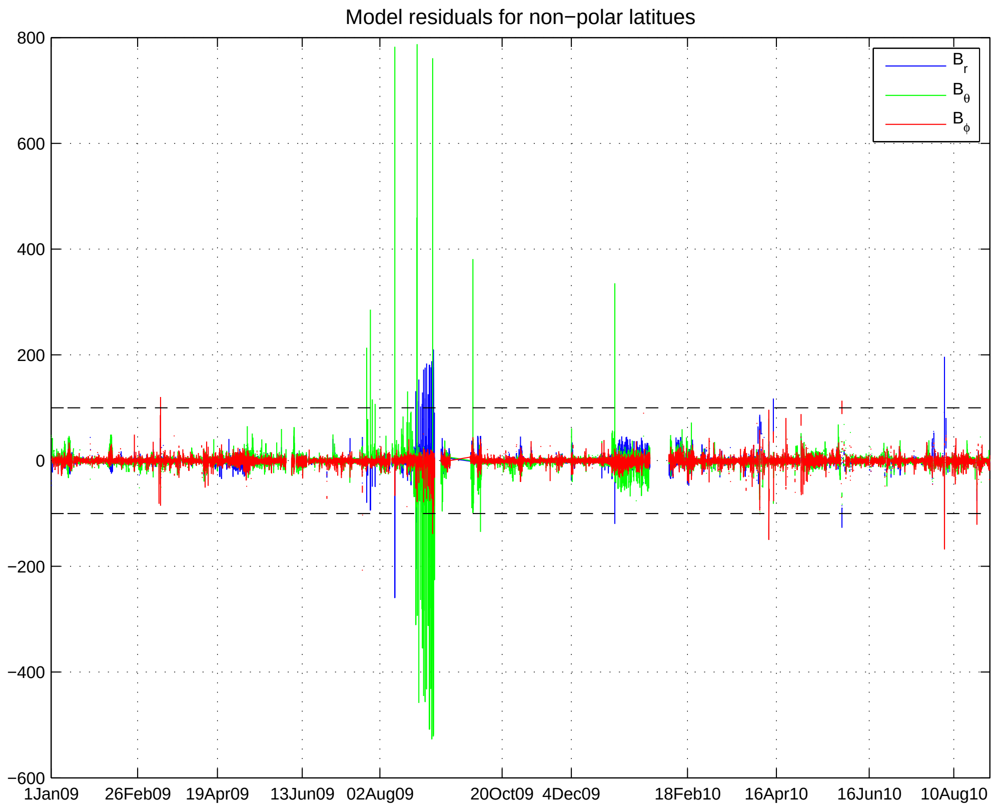

Figure 65 Non-polar residual values corresponding to the quadratic regularized model with $\alpha = 900\,\mathrm{nT}^{-2}$. Days where at least one of the residual components $> 100\,\mathrm{nT}$ are removed from the data set.

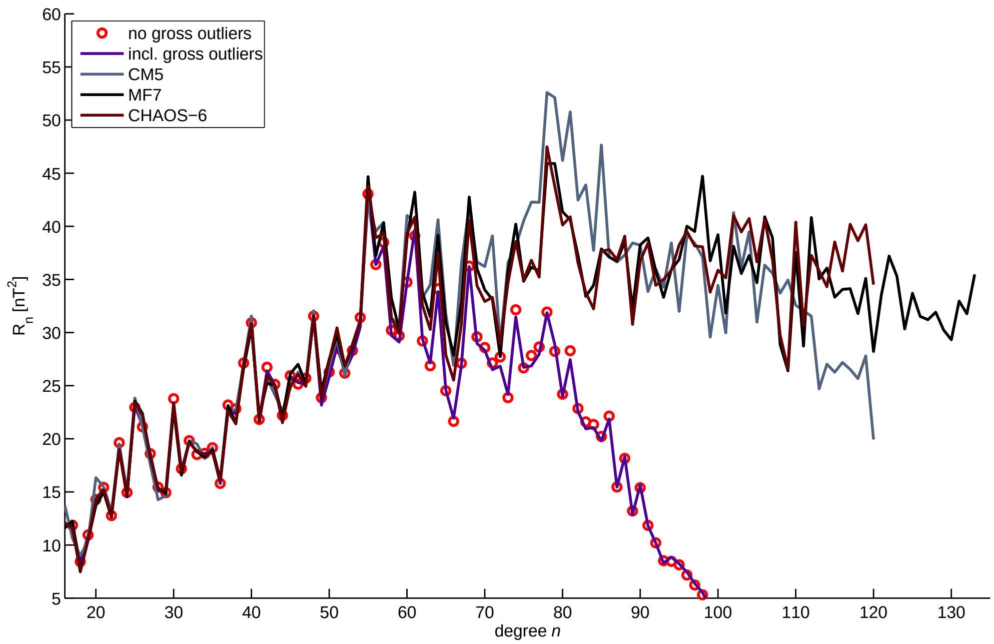

Figure 66 Power spectrum corresponding to equivalent source models with (purple) and without (red circles) gross outliers

	no gross outliers	**incl. gross outliers**
mean ΔB_r (nT)	-0.07	0.06
RMS ΔB_r (-)	1.30	1.33
RMS ΔB_r polar (-)	1.46	1.49
RMS ΔB_r non-polar (-)	1.19	1.21
mean ΔB_θ (nT)	-1.34	-1.54
RMS ΔB_θ (-)	1.27	1.32
RMS ΔB_θ polar (-)	1.38	1.46
RMS ΔB_θ non-polar (-)	1.18	1.21
mean ΔB_ϕ (nT)	-0.36	-0.36
RMS ΔB_ϕ (-)	1.28	1.30
RMS ΔB_ϕ polar (-)	1.43	1.48
RMS ΔB_ϕ non-polar (-)	1.16	1.17
RMS ΔB (-)	1.28	1.32
RMS ΔB polar (-)	1.42	1.48
RMS ΔB non-polar (-)	1.17	1.20

Table 19 Model statistics for investigation of gross outliers.

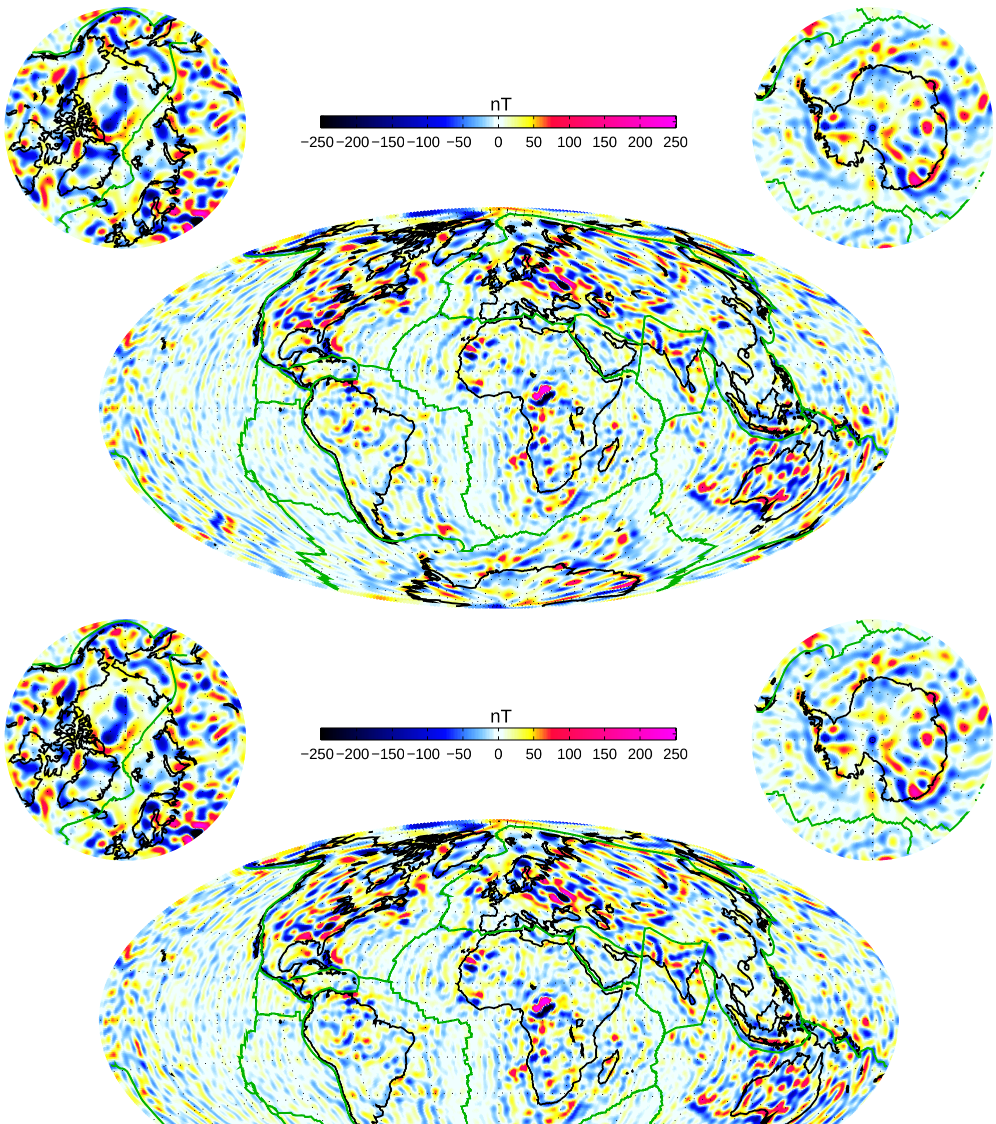

Figure 67 Radial lithospheric field component at the Earth's surface for the quadratic regularized model ($\alpha = 900\,\mathrm{nT}^{-2}$) with (top) and without (bottom) gross outliers in the data set.

D Additional material for the analysis of global lithospheric field models

D.1 Quadratic regularized models

Maps of the radial field component at the Earth's surface

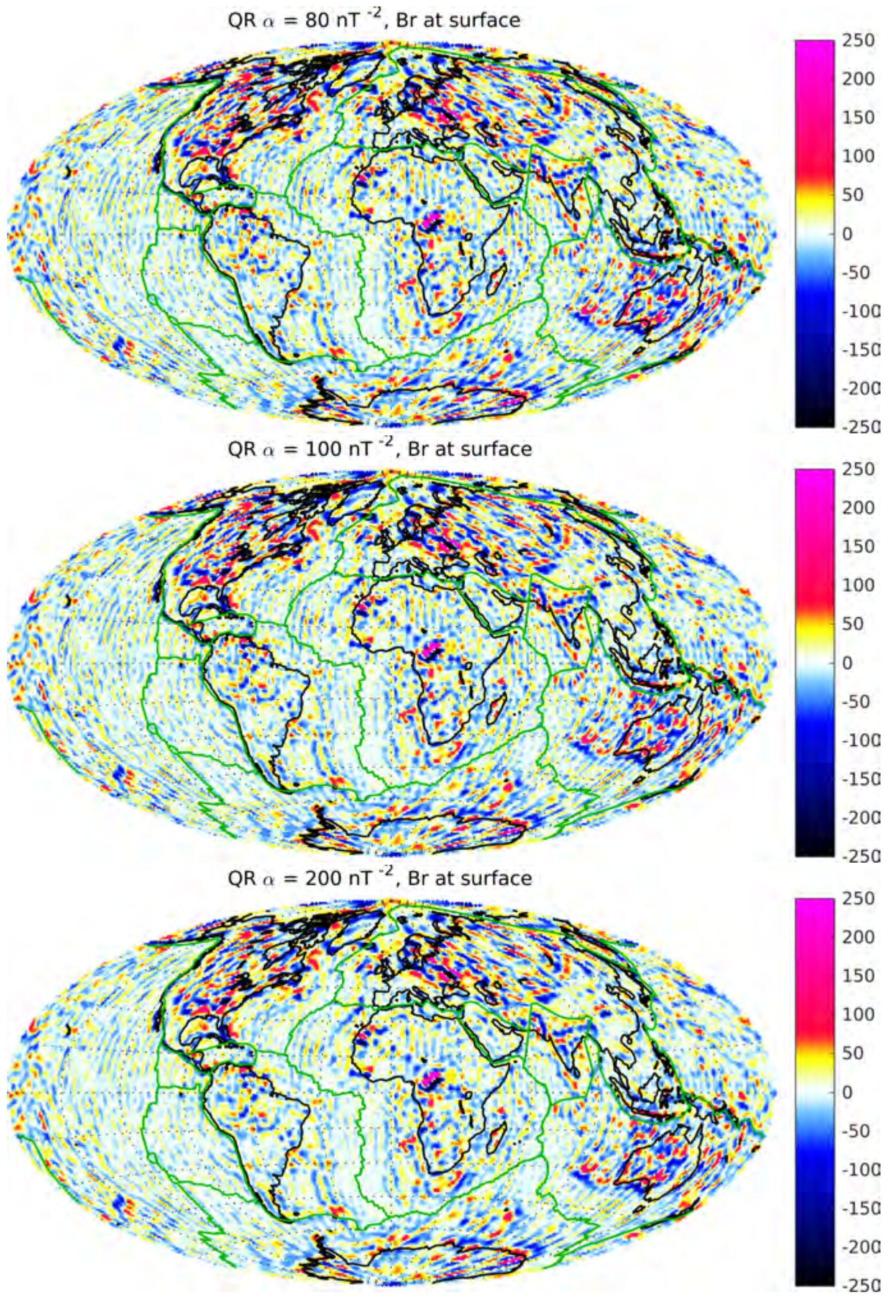

Figure 68 Radial lithospheric field component at the Earth's surface for the quadratic regularized models using $\alpha = 80\,\mathrm{nT}^{-2}$ (top), $\alpha = 100\,\mathrm{nT}^{-2}$ (middle) and $\alpha = 200\,\mathrm{nT}^{-2}$ (bottom). The color bar is given in nT.

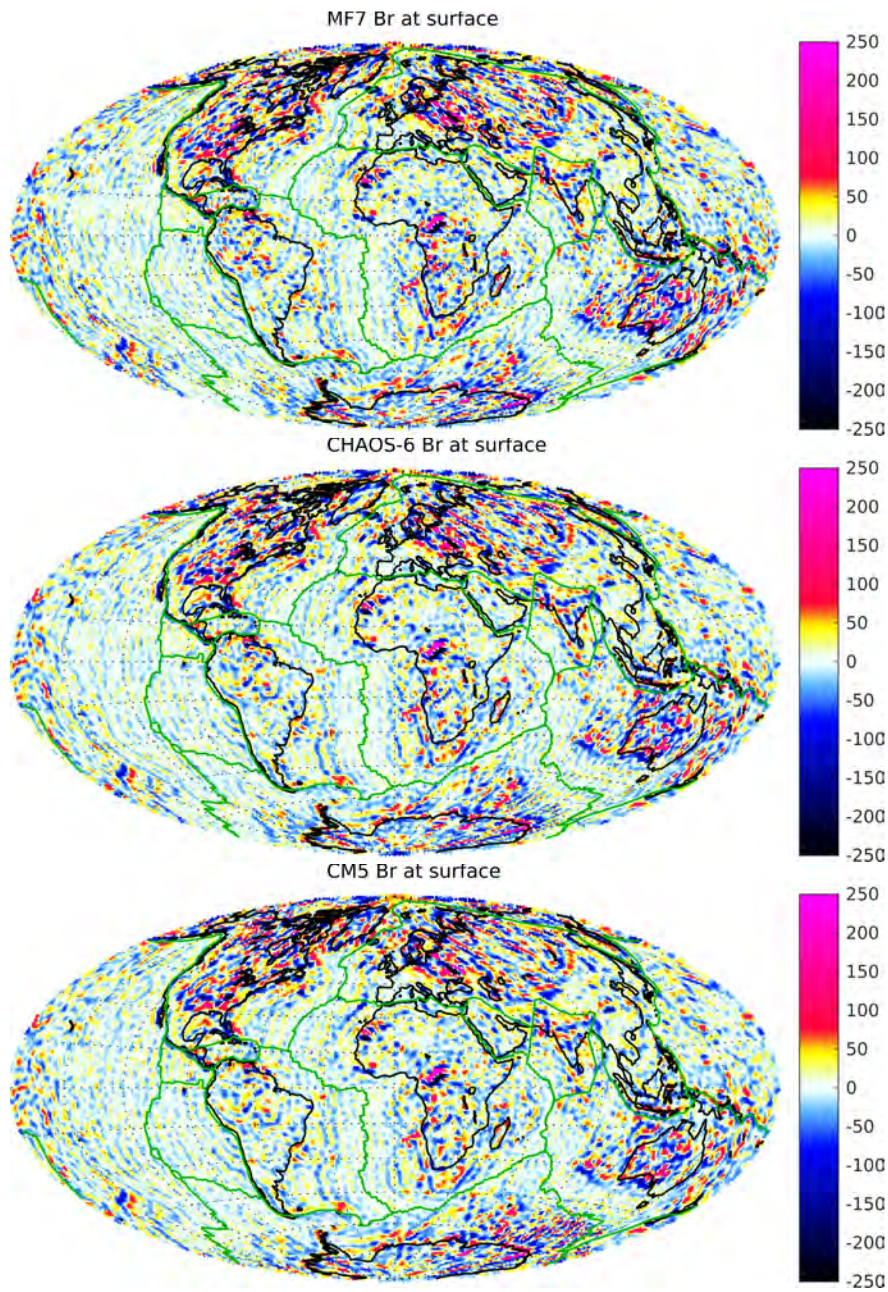

Figure 69 Radial lithospheric field component at the Earth's surface for the models MF7 (top), CHAOS-6 (middle) and CM5 (bottom). The color bar is given in nT.

Maps of the intensity field at the Earth's surface

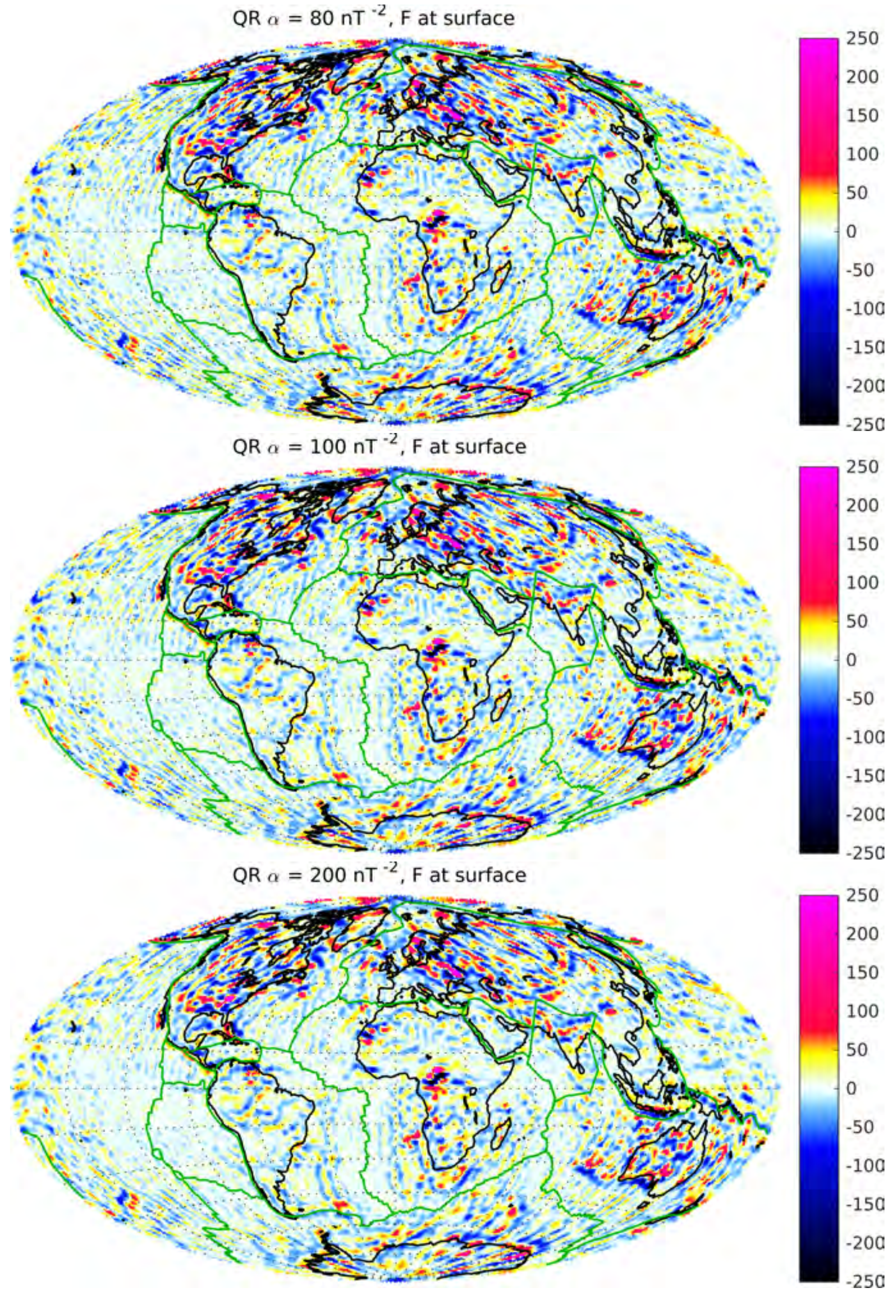

Figure 70 Lithospheric field intensity at the Earth's surface for the quadratic regularized models using $\alpha = 80\,\mathrm{nT}^{-2}$ (top), $\alpha = 100\,\mathrm{nT}^{-2}$ (middle) and $\alpha = 200\,\mathrm{nT}^{-2}$ (bottom). The color bar is given in nT.

Maps of the radial field component at $300\,\mathrm{km}$ altitude

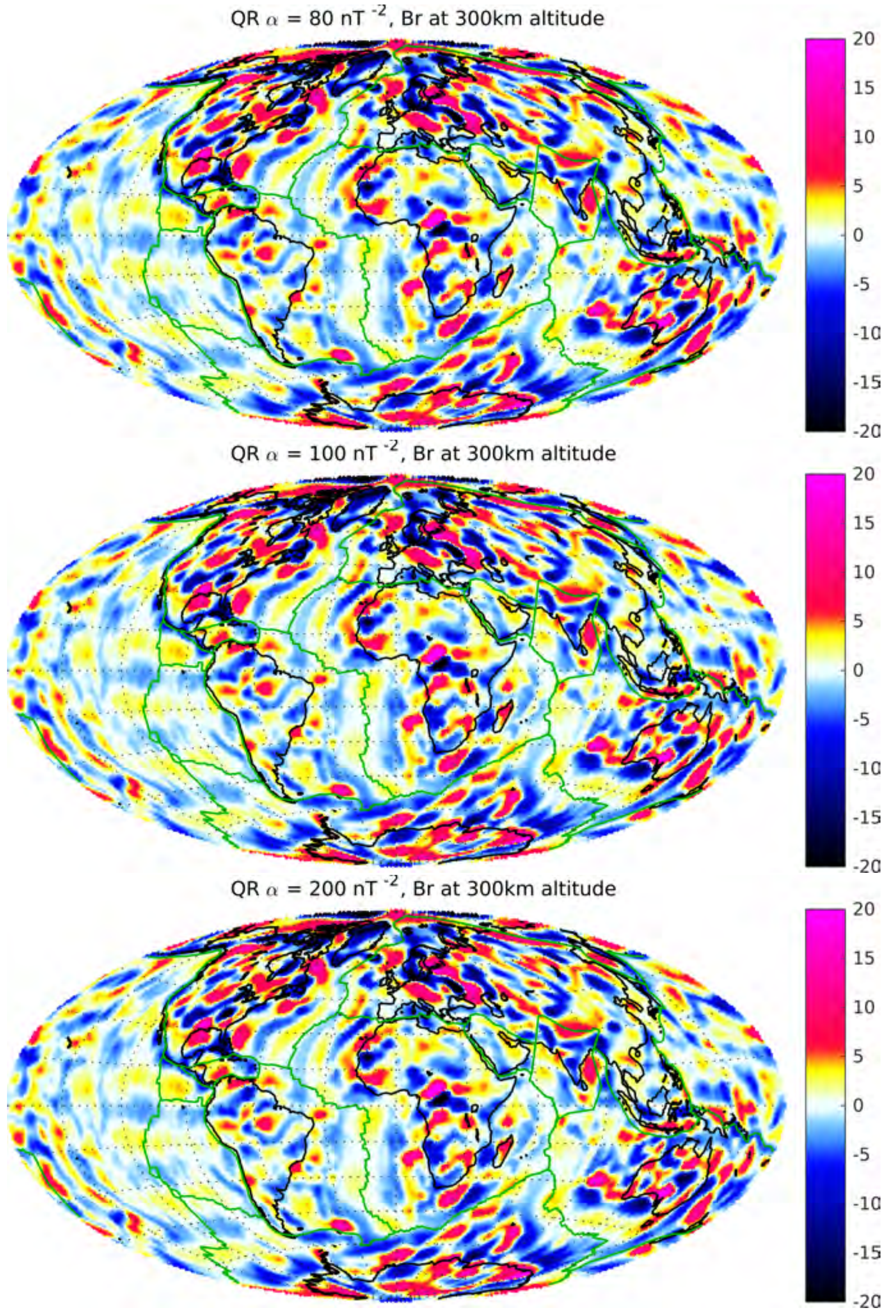

Figure 71 Radial lithospheric field component at 300 km altitude for the quadratic regularized models using $\alpha = 80\,\mathrm{nT}^{-2}$ (top), $\alpha = 100\,\mathrm{nT}^{-2}$ (middle) and $\alpha = 200\,\mathrm{nT}^{-2}$ (bottom). The color bar is given in nT.

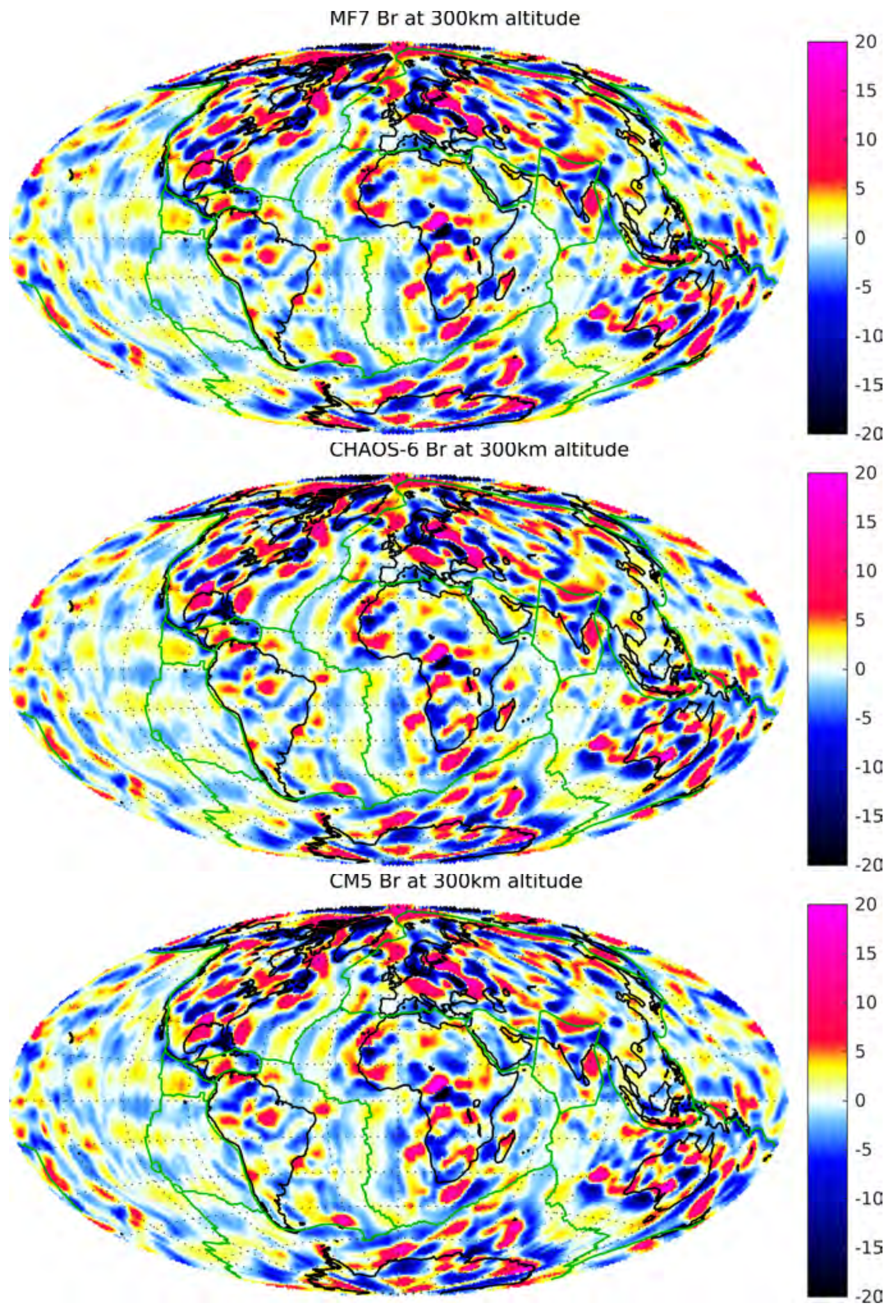

Figure 72 Radial lithospheric field component at 300 km altitude for the models MF7 (top), CHAOS-6 (middle) and CM5 (bottom). The color bar is given in nT.

Maps of the intensity field at 300 km altitude

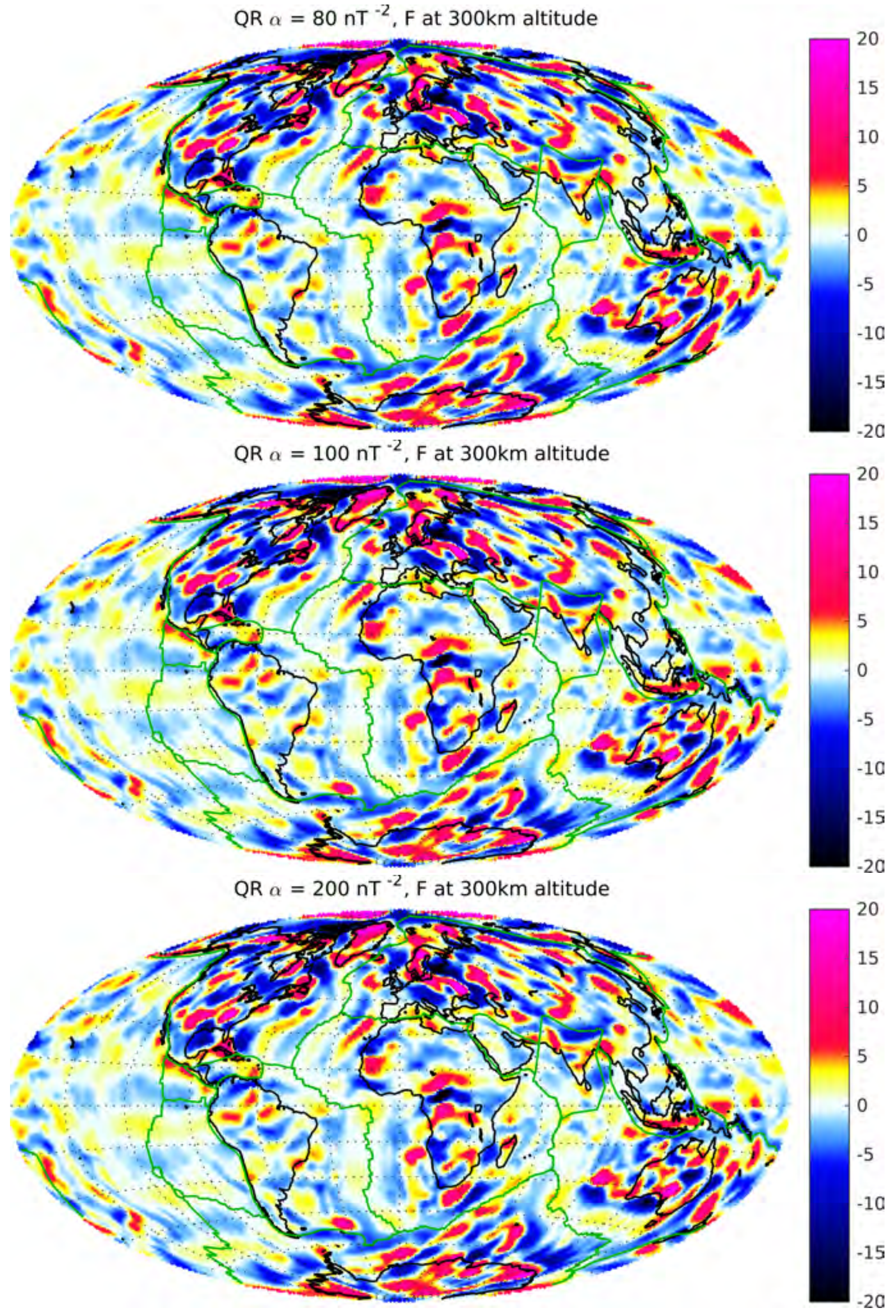

Figure 73 Lithospheric field intensity at 300 km altitude for the quadratic regularized models using $\alpha = 80\,\mathrm{nT}^{-2}$ (top), $\alpha = 100\,\mathrm{nT}^{-2}$ (middle) and $\alpha = 200\,\mathrm{nT}^{-2}$ (bottom). The color bar is given in nT.

Residual maps at data altitude

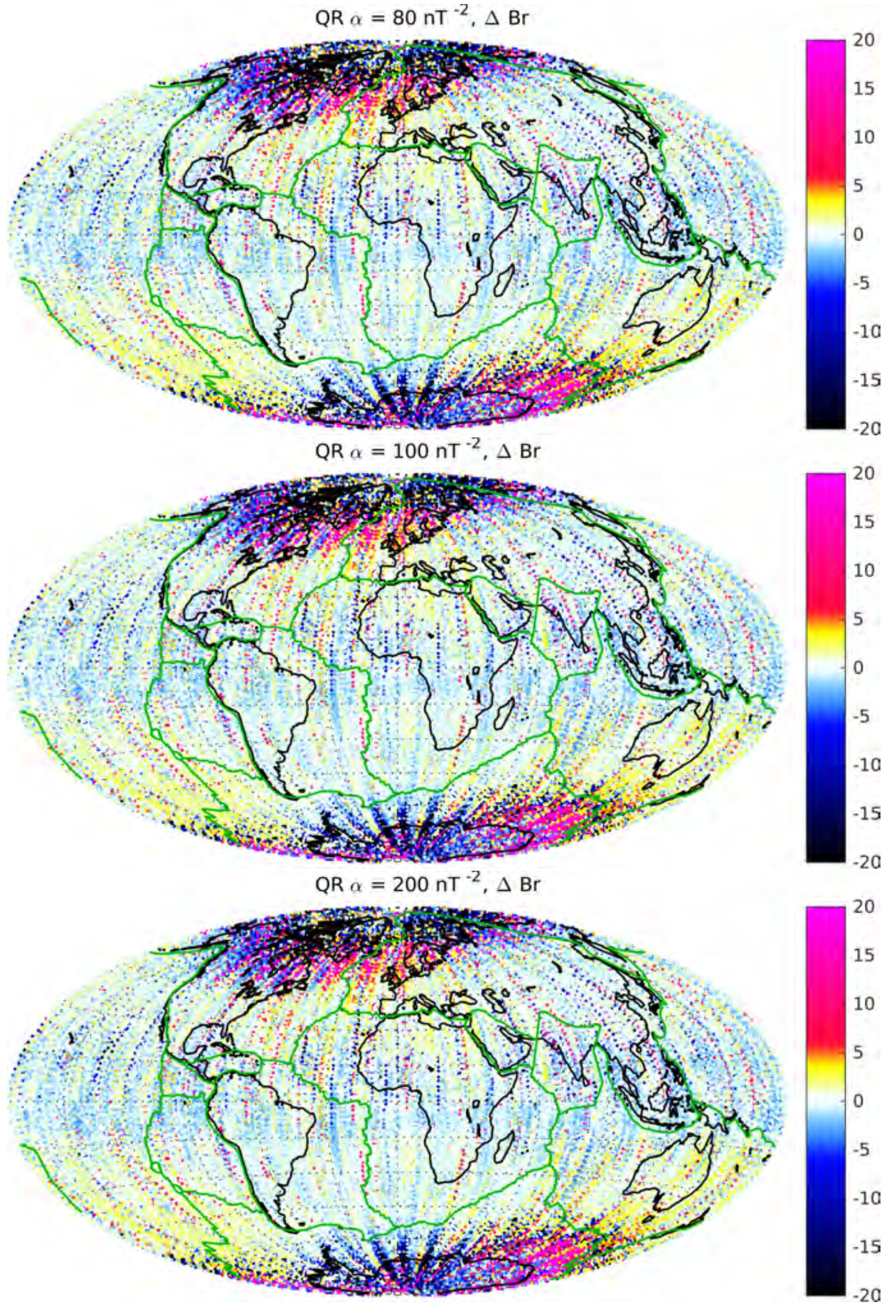

Figure 74 Radial residuals at data altitude for the quadratic regularized models using $\alpha = 80\,\mathrm{nT}^{-2}$ (top), $\alpha = 100\,\mathrm{nT}^{-2}$ (middle) and $\alpha = 200\,\mathrm{nT}^{-2}$ (bottom). The colorbar is given in nT.

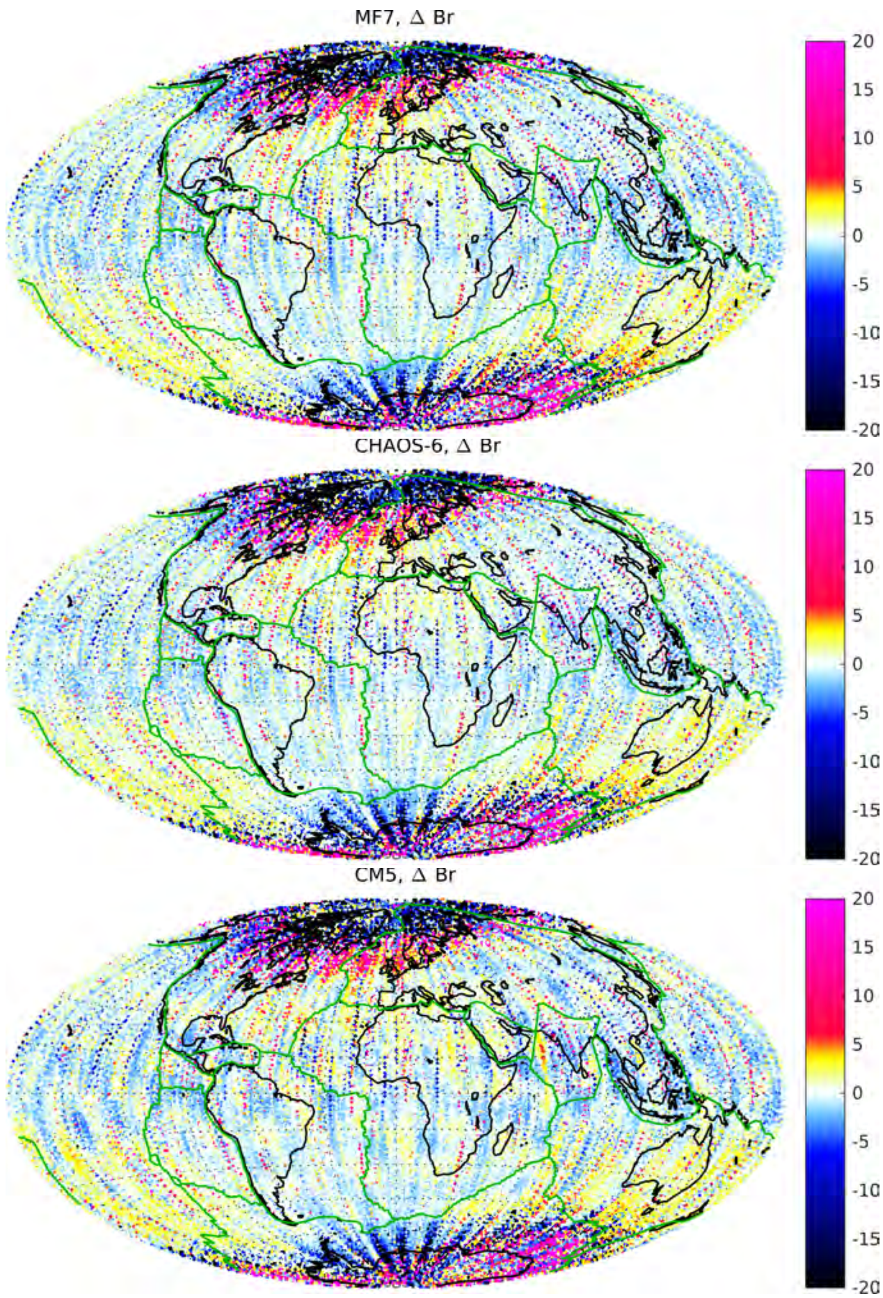

Figure 75 Radial residuals at data altitude for the models MF7 (top), CHAOS-6 (middle) and CM5 (bottom). The colorbar is given in nT.

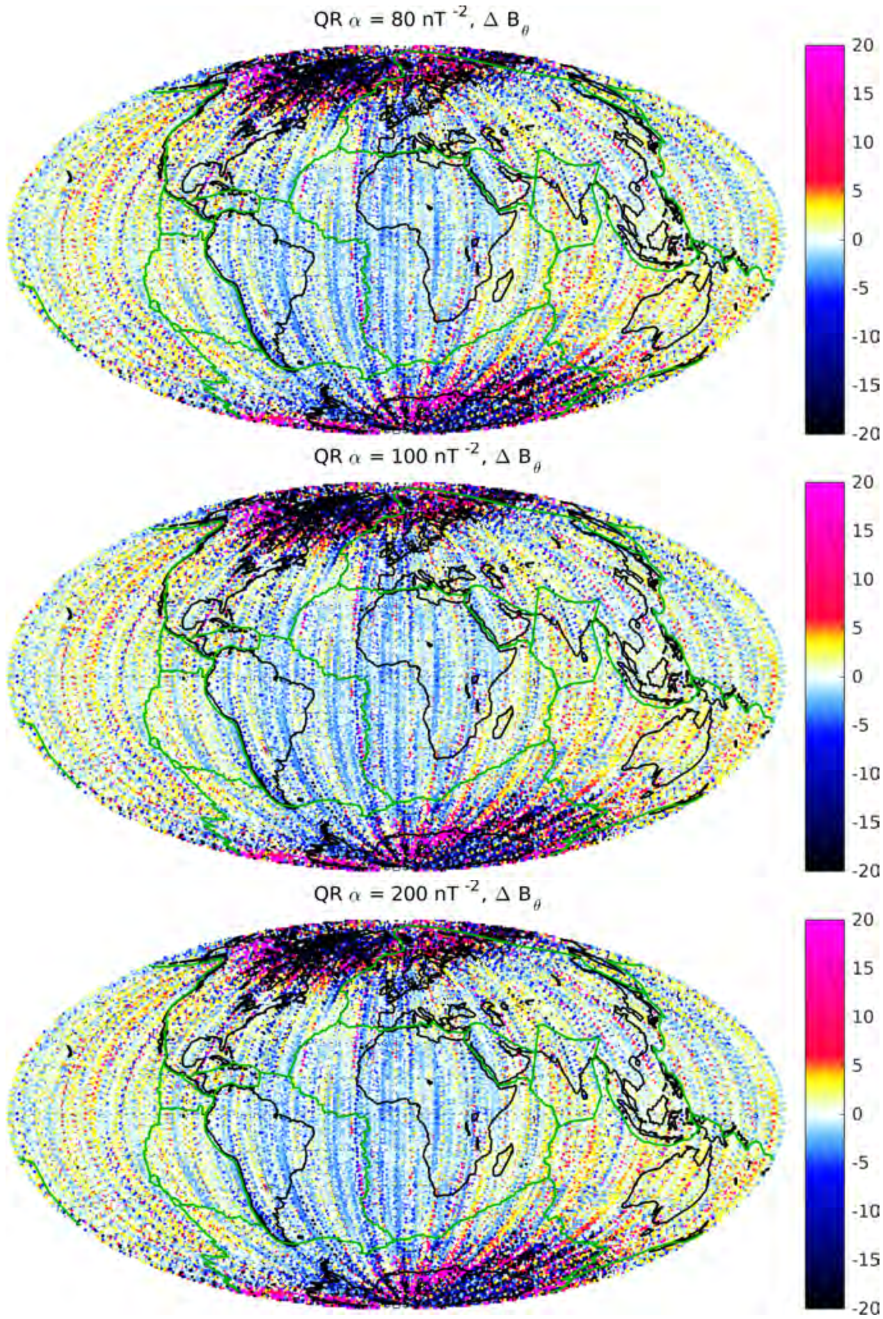

Figure 76 Latitudinal residuals at data altitude for the quadratic regularized models using $\alpha = 80\,\mathrm{nT}^{-2}$ (top), $\alpha = 100\,\mathrm{nT}^{-2}$ (middle) and $\alpha = 200\,\mathrm{nT}^{-2}$ (bottom). The colorbar is given in nT.

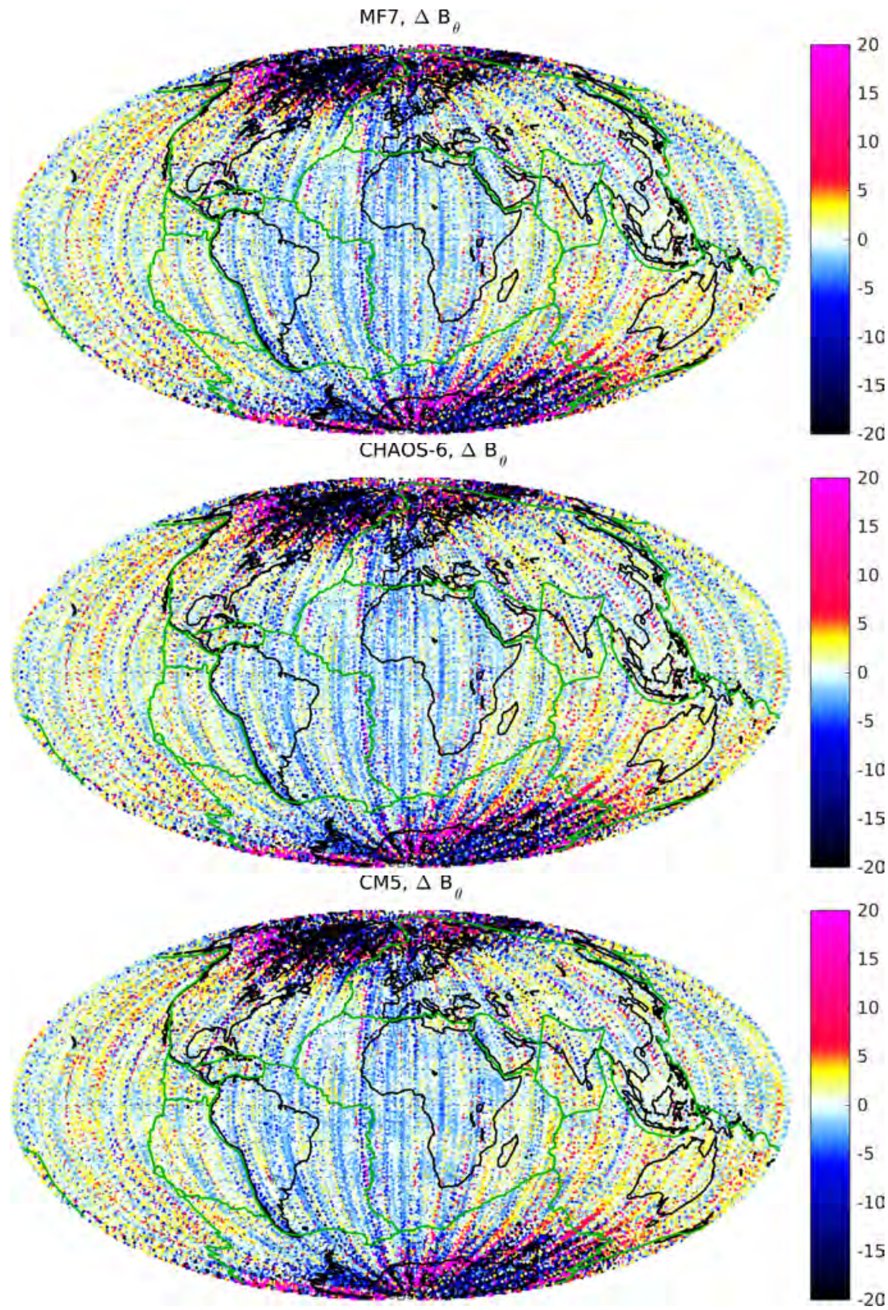

Figure 77 Latitudinal residuals at data altitude for the models MF7 (top), CHAOS-6 (middle) and CM5 (bottom). The colorbar is given in nT.

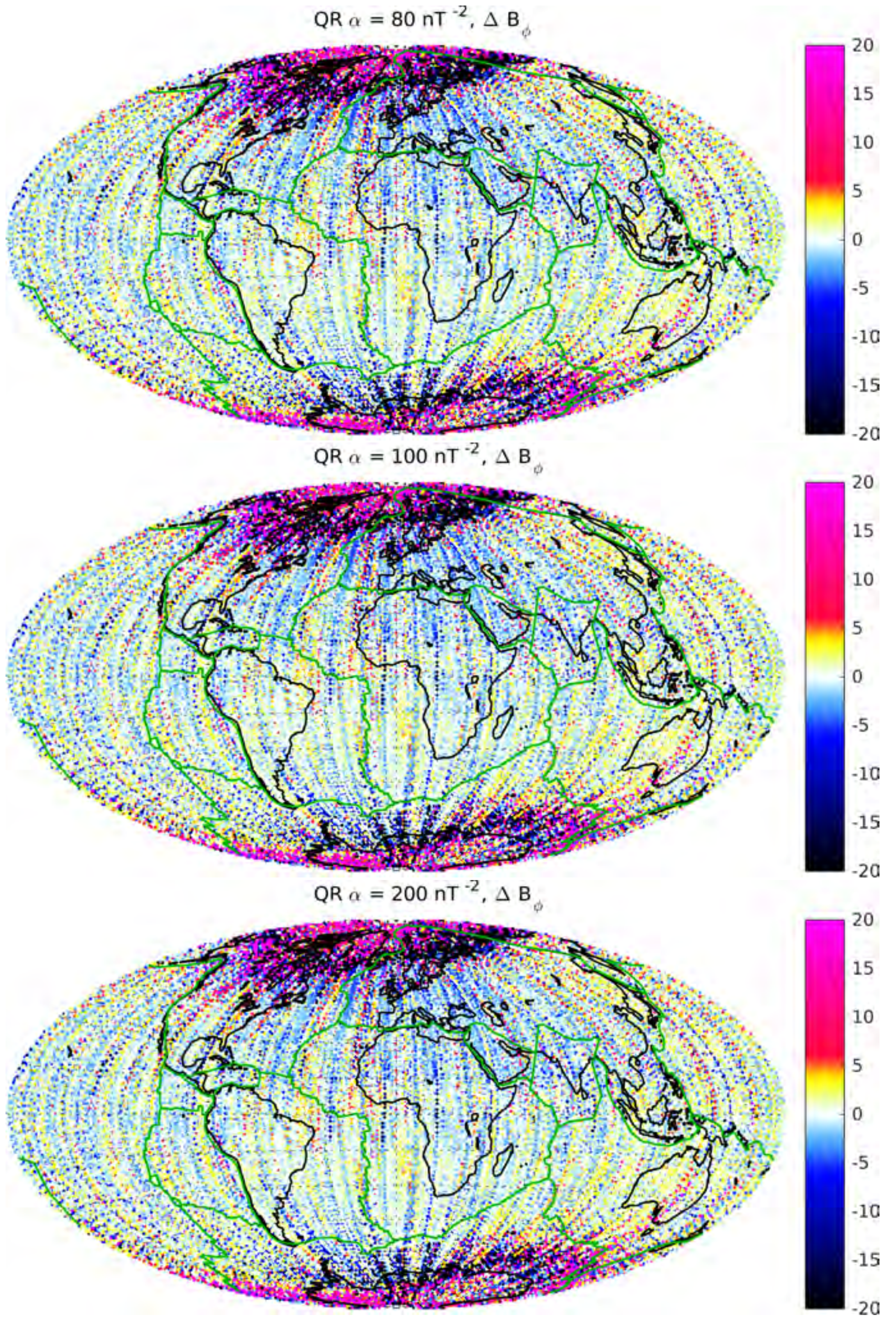

Figure 78 Longitudinal residuals at data altitude for the quadratic regularized models using $\alpha = 80\,\mathrm{nT}^{-2}$ (top), $\alpha = 100\,\mathrm{nT}^{-2}$ (middle) and $\alpha = 200\,\mathrm{nT}^{-2}$ (bottom). The colorbar is given in nT.

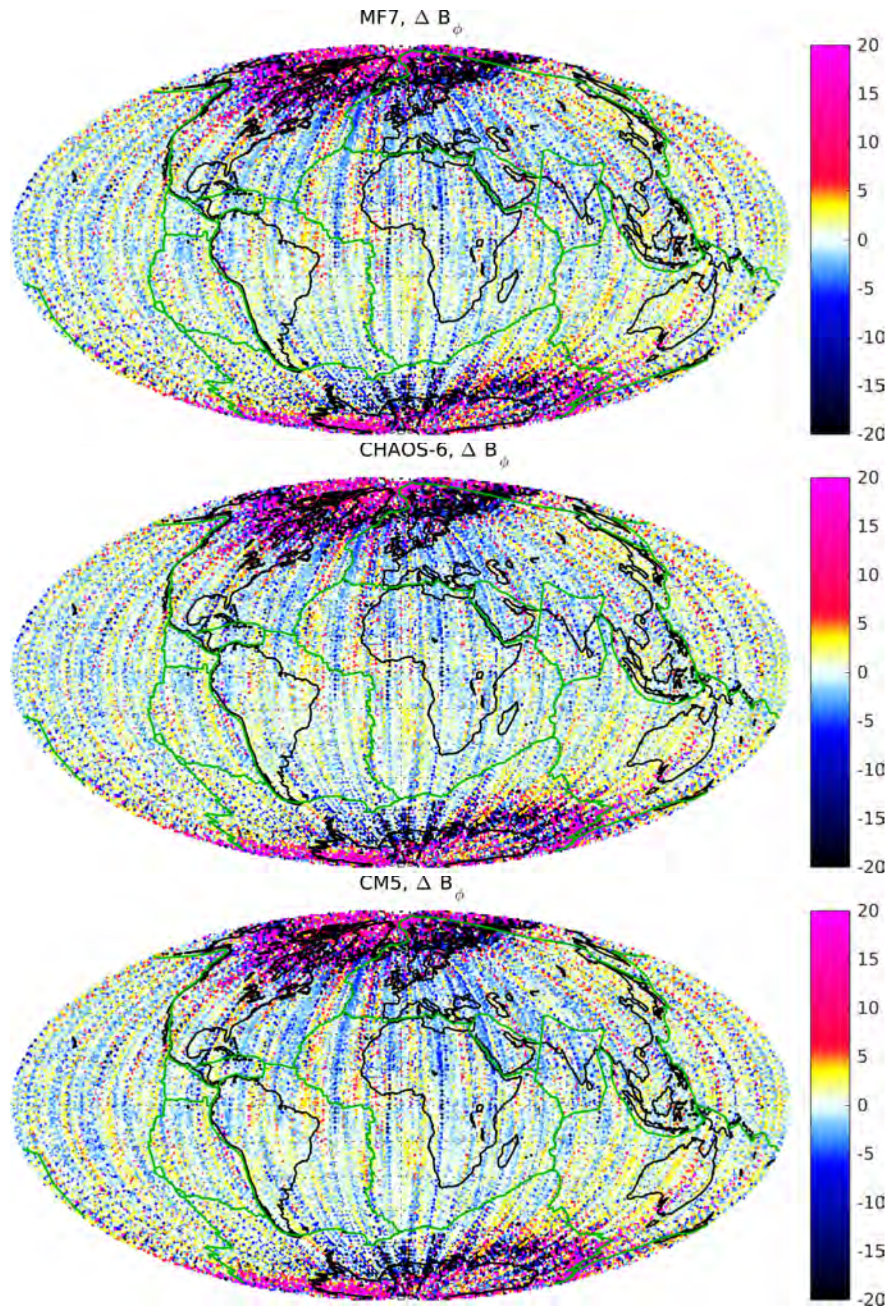

Figure 79 Longitudinal residuals at data altitude for the models MF7 (top), CHAOS-6 (middle) and CM5 (bottom). The colorbar is given in nT.

D.2 Maximum entropy regularized models

Maps of the radial field component at the Earth's surface

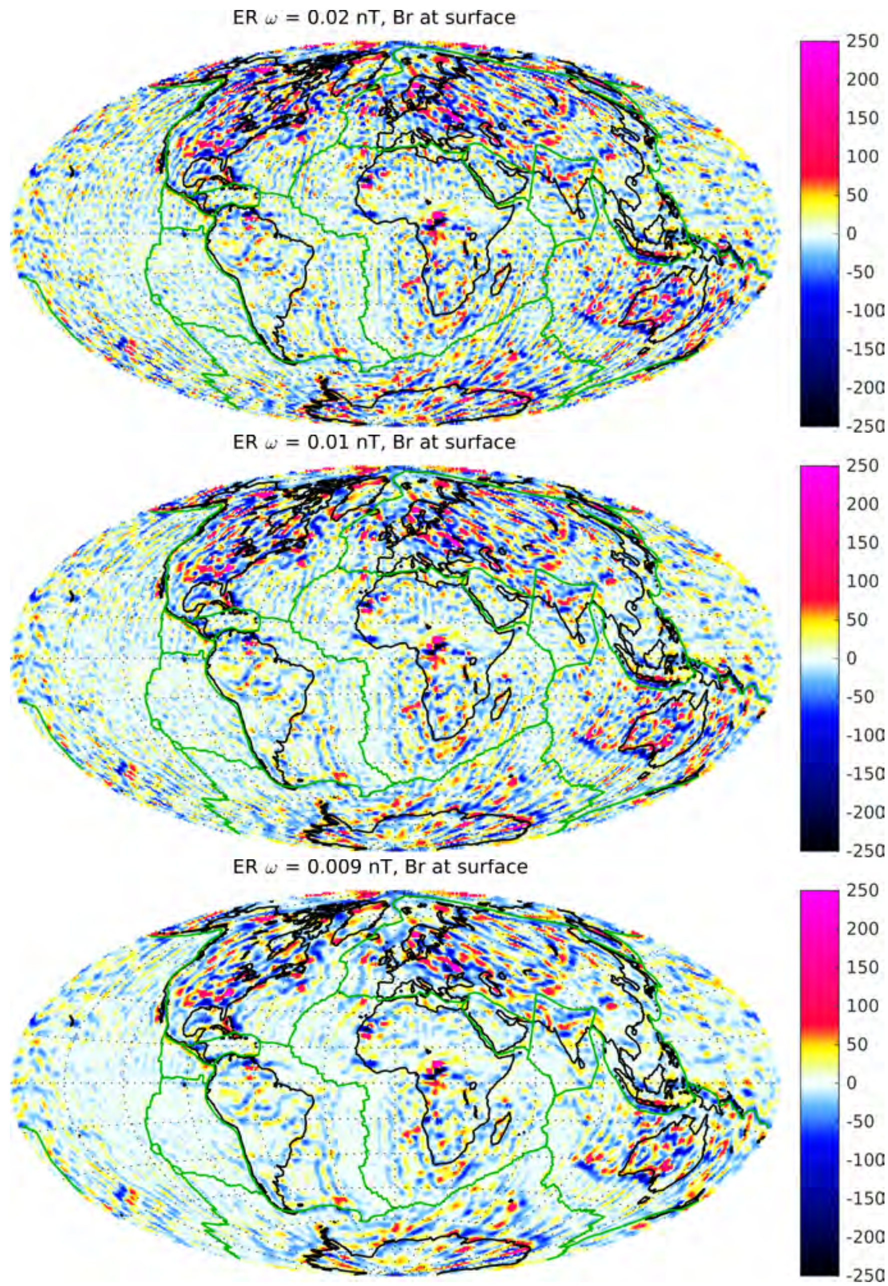

Figure 80 Radial lithospheric field component at the Earth's surface for the maximum entropy regularized models using $\alpha = 30\,\mathrm{nT}^{-2}$ and $\omega = 0.02\,\mathrm{nT}$ (top), $\alpha = 80\,\mathrm{nT}^{-2}$ and $\omega = 0.01\,\mathrm{nT}$ (middle) and $\alpha = 500\,\mathrm{nT}^{-2}$ and $\omega = 0.009\,\mathrm{nT}$ (bottom). The colorbar is given in nT.

Maps of the intensity field at the Earth's surface

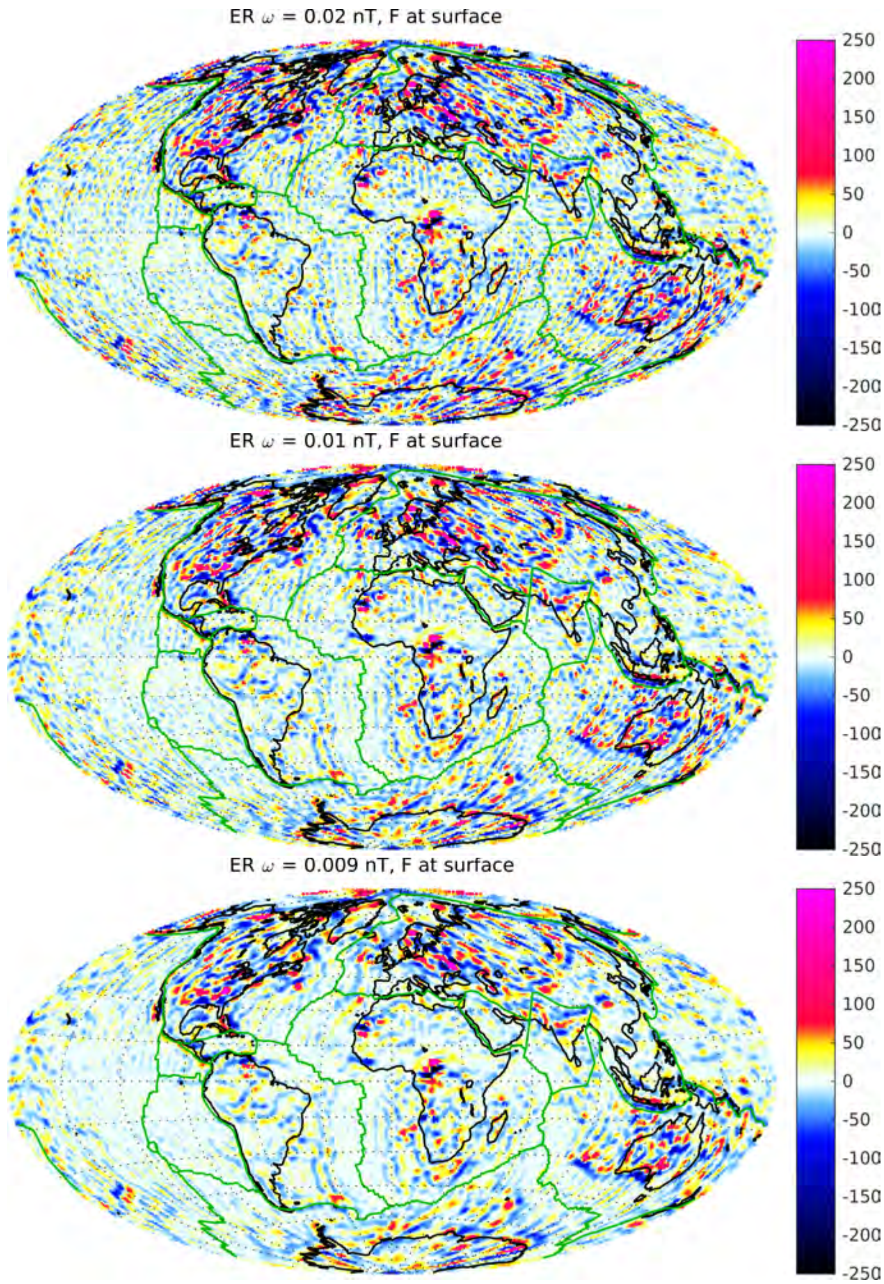

Figure 81 Lithospheric field intensity at the Earth's surface for the maximum entropy regularized models using $\alpha = 30\,\mathrm{nT}^{-2}$ and $\omega = 0.02\,\mathrm{nT}$ (top), $\alpha = 80\,\mathrm{nT}^{-2}$ and $\omega = 0.01\,\mathrm{nT}$ (middle) and $\alpha = 500\,\mathrm{nT}^{-2}$ and $\omega = 0.009\,\mathrm{nT}$ (bottom). The colorbar is given in nT.

Maps of the radial field component at 300 km altitude

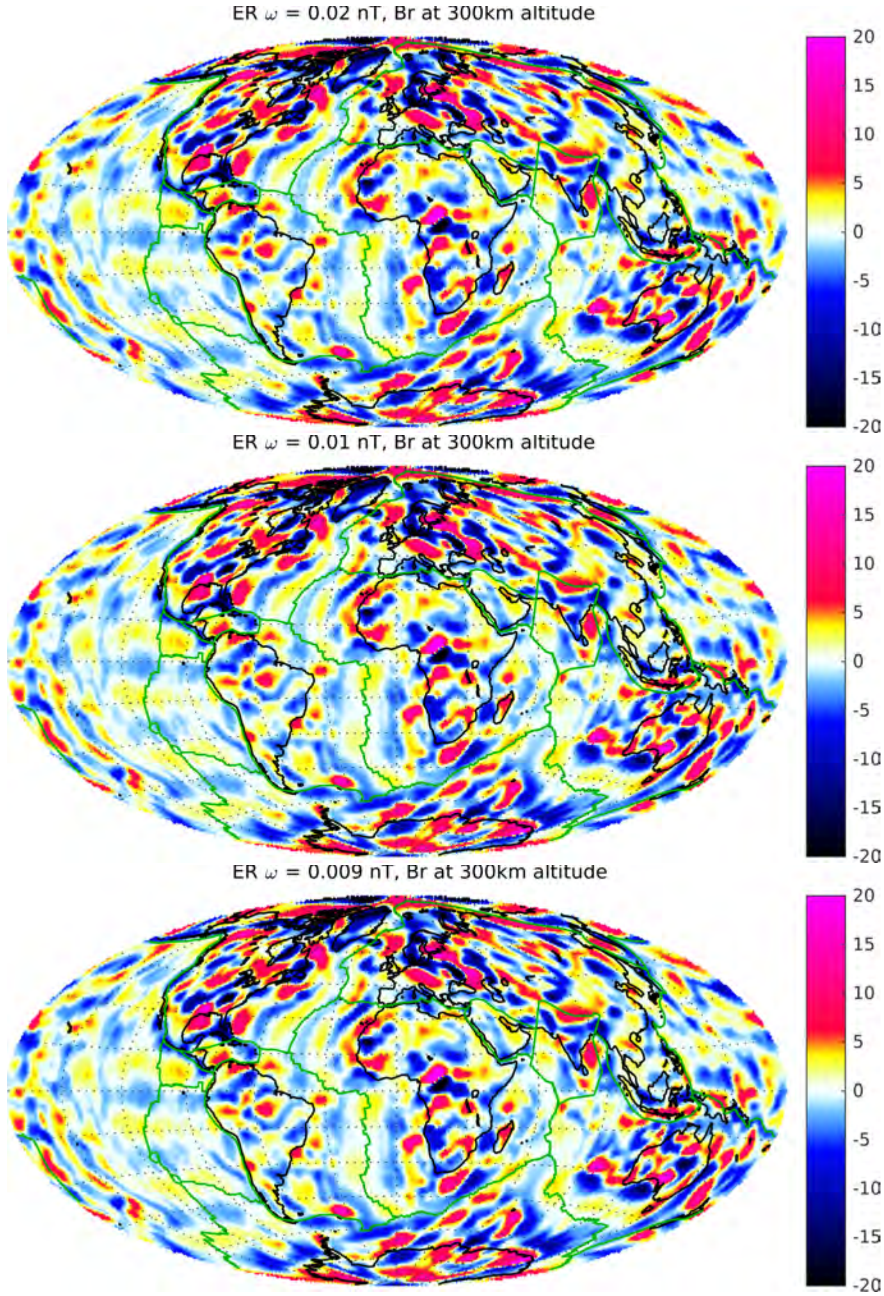

Figure 82 Radial lithospheric field component at 300 km altitude for the maximum entropy regularized models using $\alpha = 30\,\mathrm{nT}^{-2}$ and $\omega = 0.02\,\mathrm{nT}$ (top), $\alpha = 80\,\mathrm{nT}^{-2}$ and $\omega = 0.01\,\mathrm{nT}$ (middle) and $\alpha = 500\,\mathrm{nT}^{-2}$ and $\omega = 0.009\,\mathrm{nT}$ (bottom). The colorbar is given in nT.

Maps of the intensity field at $300\,\mathrm{km}$ altitude

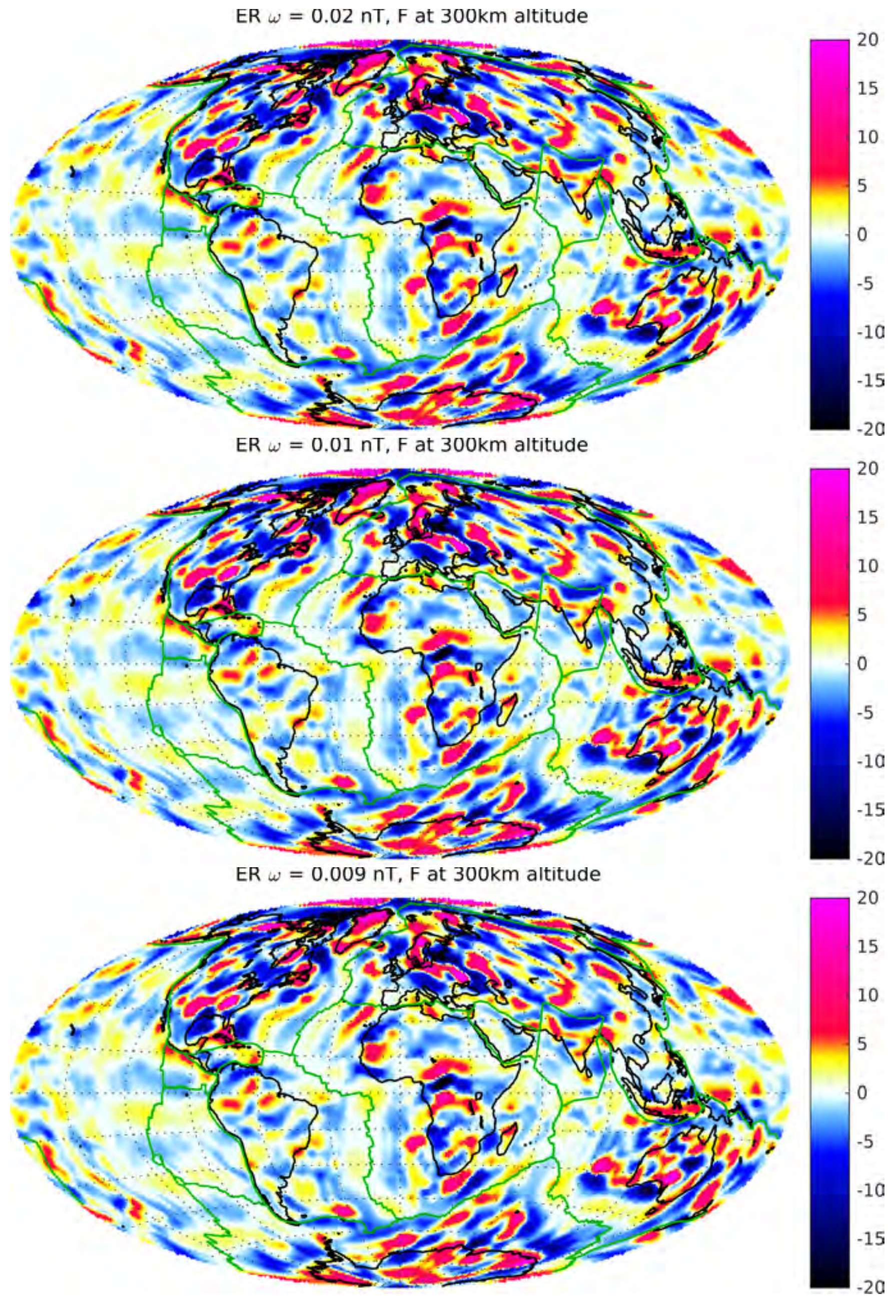

Figure 83 Lithospheric field intensity at $300\,\mathrm{km}$ altitude for the maximum entropy regularized models using $\alpha = 30\,\mathrm{nT}^{-2}$ and $\omega = 0.02\,\mathrm{nT}$ (top), $\alpha = 80\,\mathrm{nT}^{-2}$ and $\omega = 0.01\,\mathrm{nT}$ (middle) and $\alpha = 500\,\mathrm{nT}^{-2}$ and $\omega = 0.009\,\mathrm{nT}$ (bottom). The colorbar is given in nT.

Residual maps at data altitude

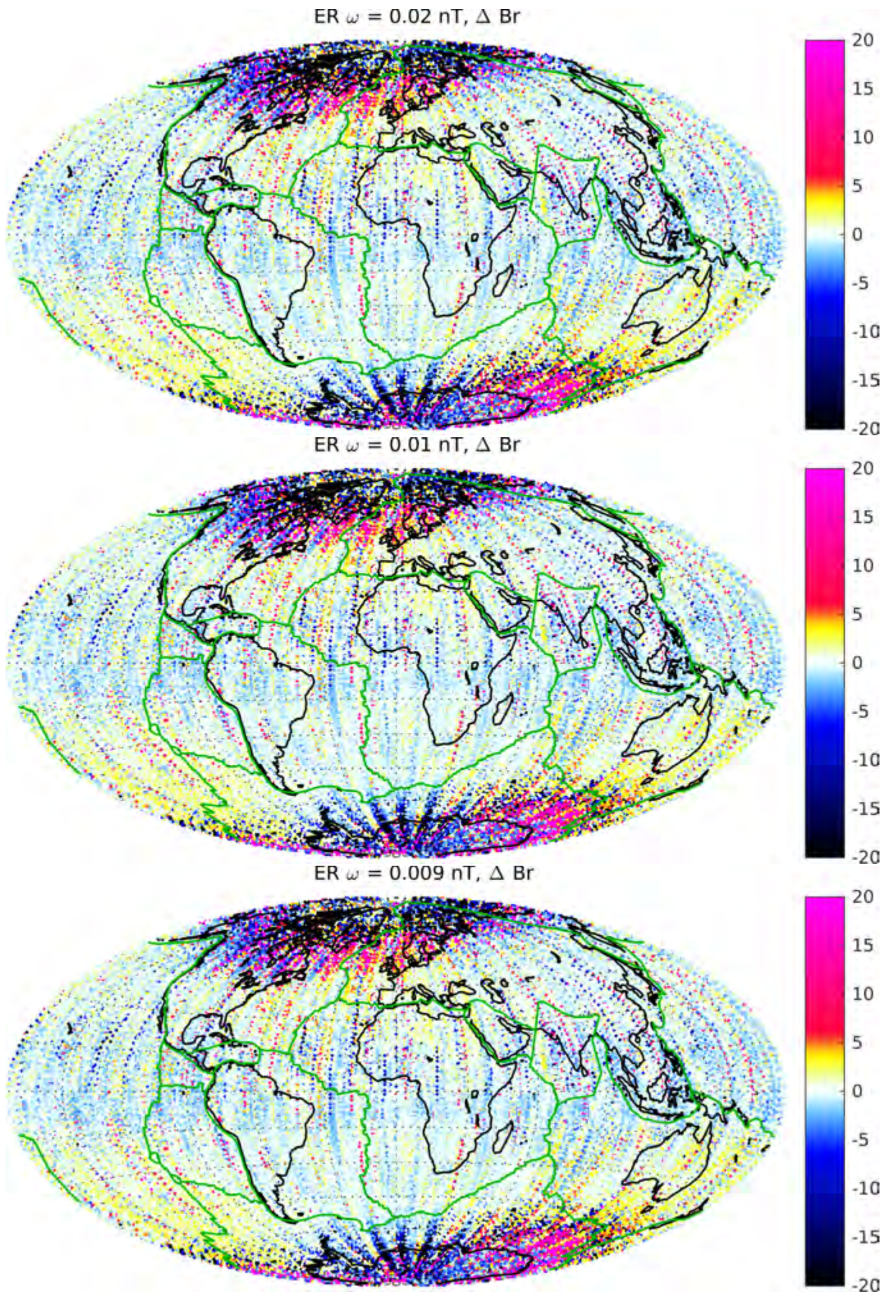

Figure 84 Radial residuals at data altitude for the maximum entropy regularized models using $\alpha = 30\,\mathrm{nT}^{-2}$ and $\omega = 0.02\,\mathrm{nT}$ (top), $\alpha = 80\,\mathrm{nT}^{-2}$ and $\omega = 0.01\,\mathrm{nT}$ (middle) and $\alpha = 500\,\mathrm{nT}^{-2}$ and $\omega = 0.009\,\mathrm{nT}$ (bottom). The colorbar is given in nT.

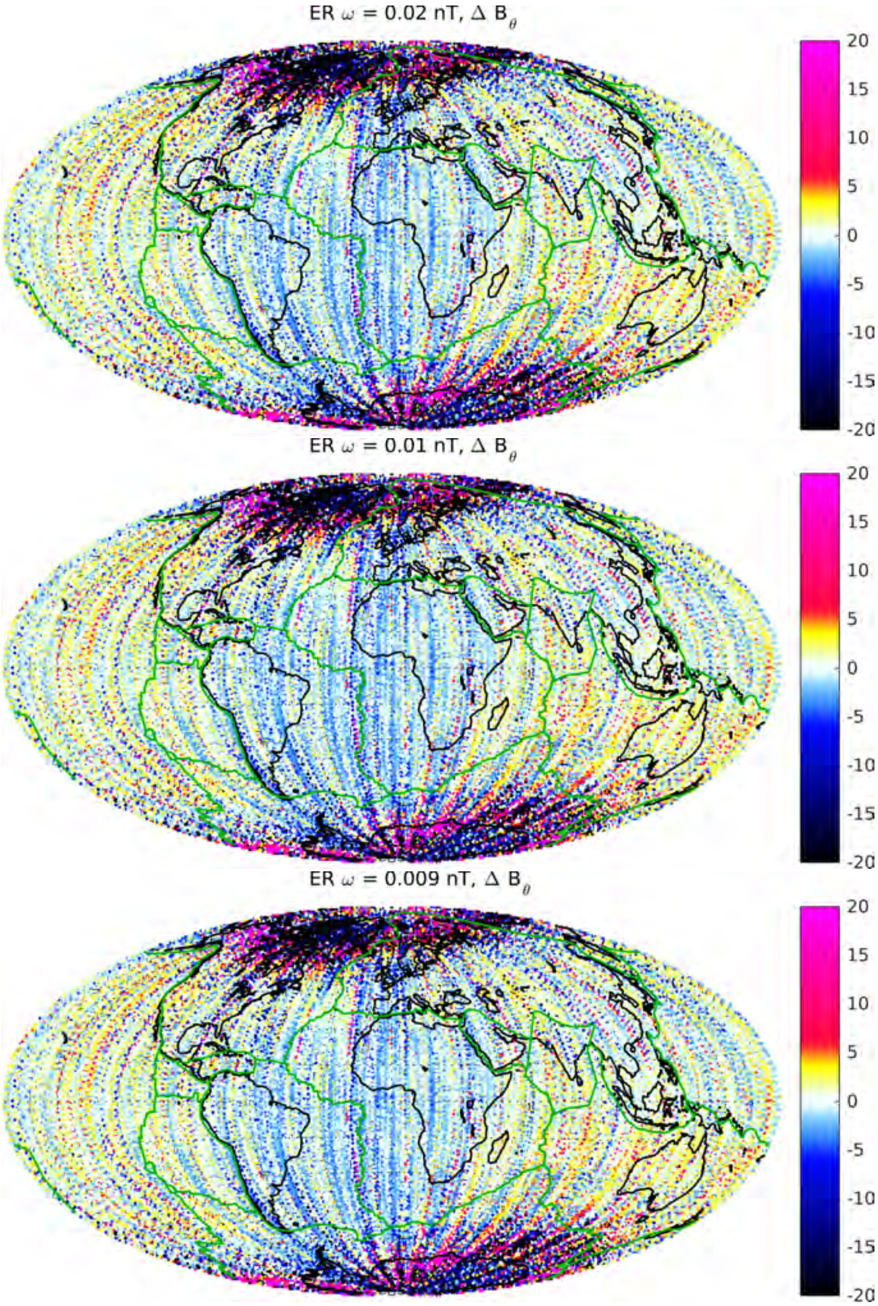

Figure 85 Latitudinal residuals at data altitude for the maximum entropy regularized models using $\alpha = 30\,\mathrm{nT}^{-2}$ and $\omega = 0.02\,\mathrm{nT}$ (top), $\alpha = 80\,\mathrm{nT}^{-2}$ and $\omega = 0.01\,\mathrm{nT}$ (middle) and $\alpha = 500\,\mathrm{nT}^{-2}$ and $\omega = 0.009\,\mathrm{nT}$ (bottom). The colorbar is given in nT.

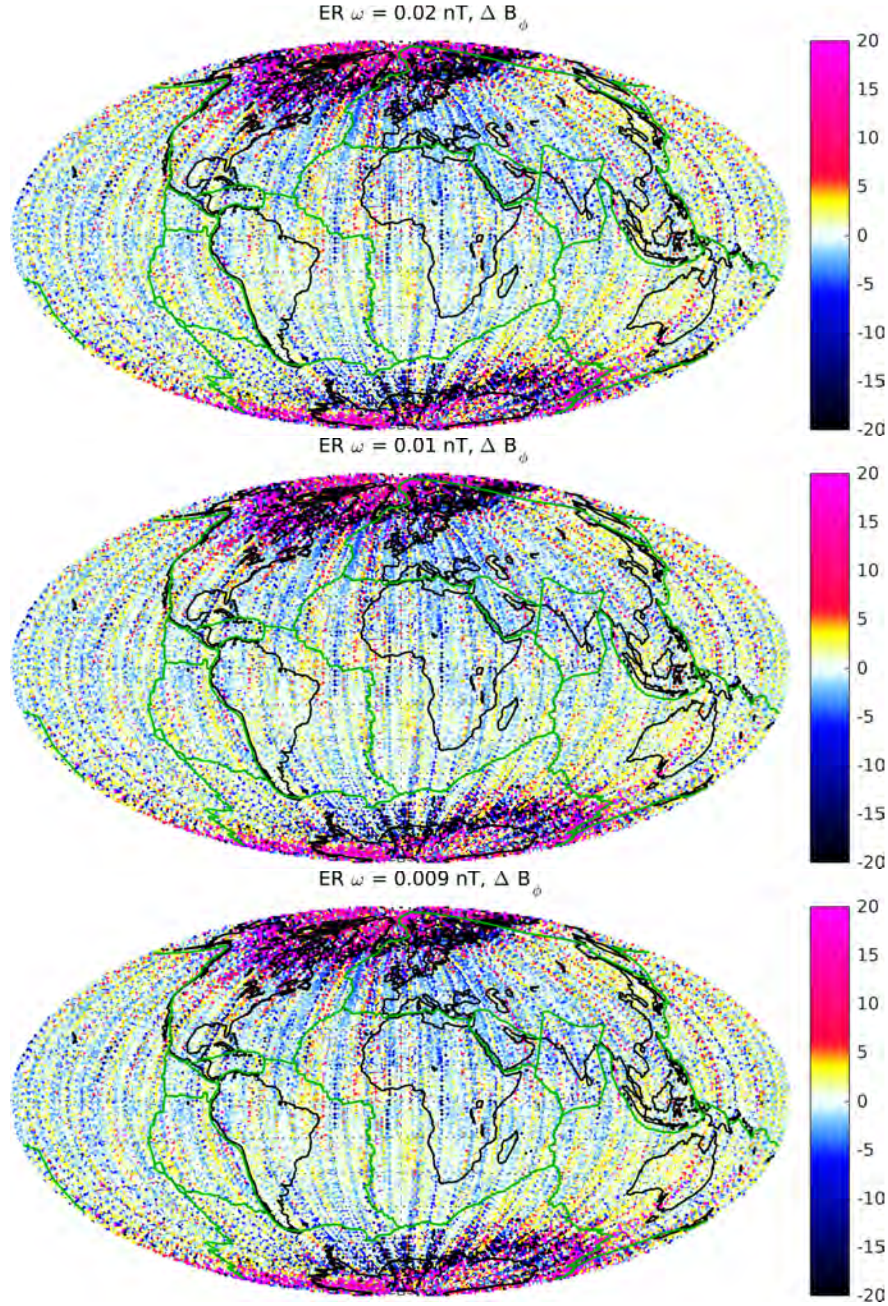

Figure 86 Longitudinal residuals at data altitude for the maximum entropy regularized models using $\alpha = 30\,\mathrm{nT}^{-2}$ and $\omega = 0.02\,\mathrm{nT}$ (top), $\alpha = 80\,\mathrm{nT}^{-2}$ and $\omega = 0.01\,\mathrm{nT}$ (middle) and $\alpha = 500\,\mathrm{nT}^{-2}$ and $\omega = 0.009\,\mathrm{nT}$ (bottom). The colorbar is given in nT.

D.3 L_1-norm regularized models

Maps of the radial field component at the Earth's surface

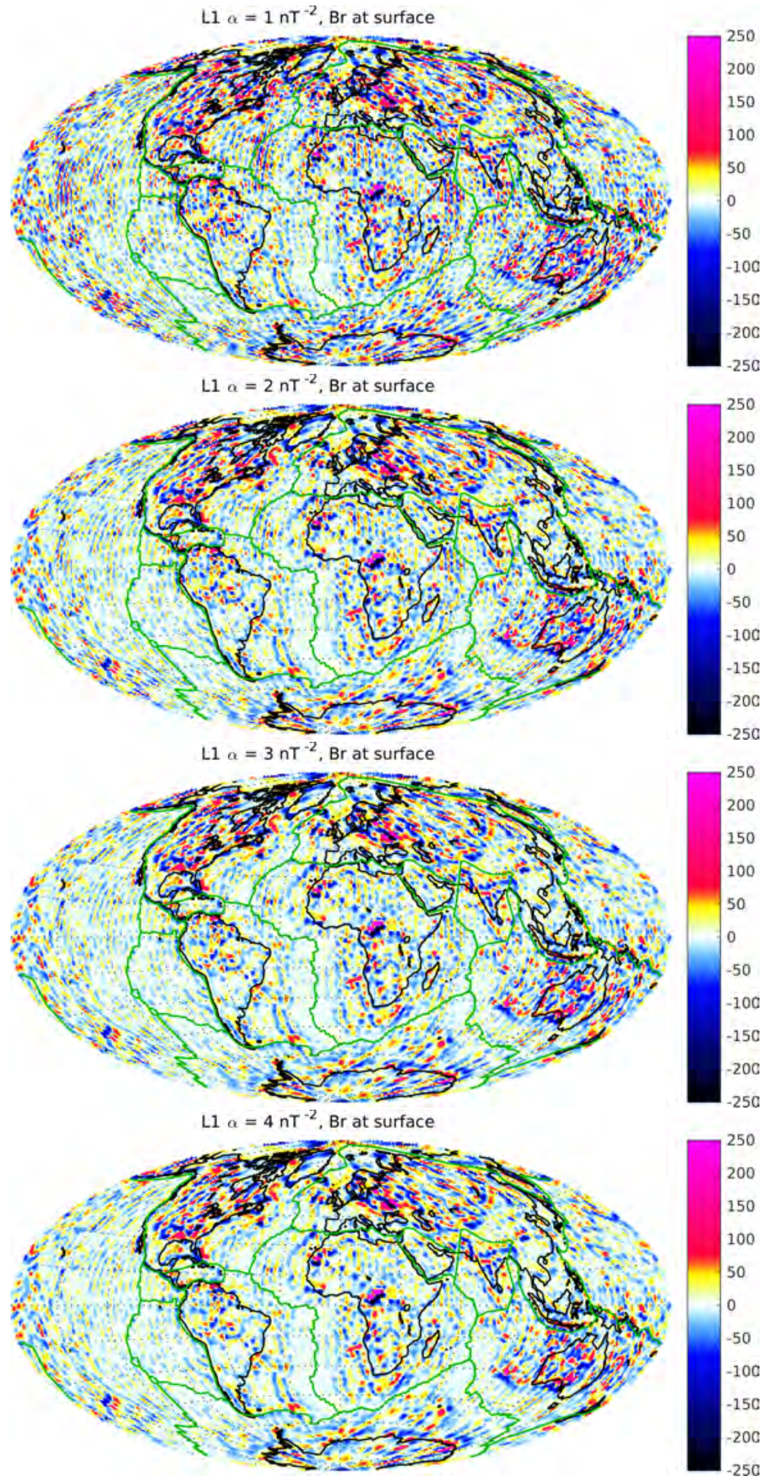

Figure 87 Radial lithospheric field component at the Earth's surface for the L1 regularized models using $\alpha = 1\,\mathrm{nT}^{-1}$, $\alpha = 2\,\mathrm{nT}^{-1}$, $\alpha = 3\,\mathrm{nT}^{-1}$ and $\alpha = 4\,\mathrm{nT}^{-1}$. The colorbar is given in nT.

Maps of the intensity field at the Earth's surface

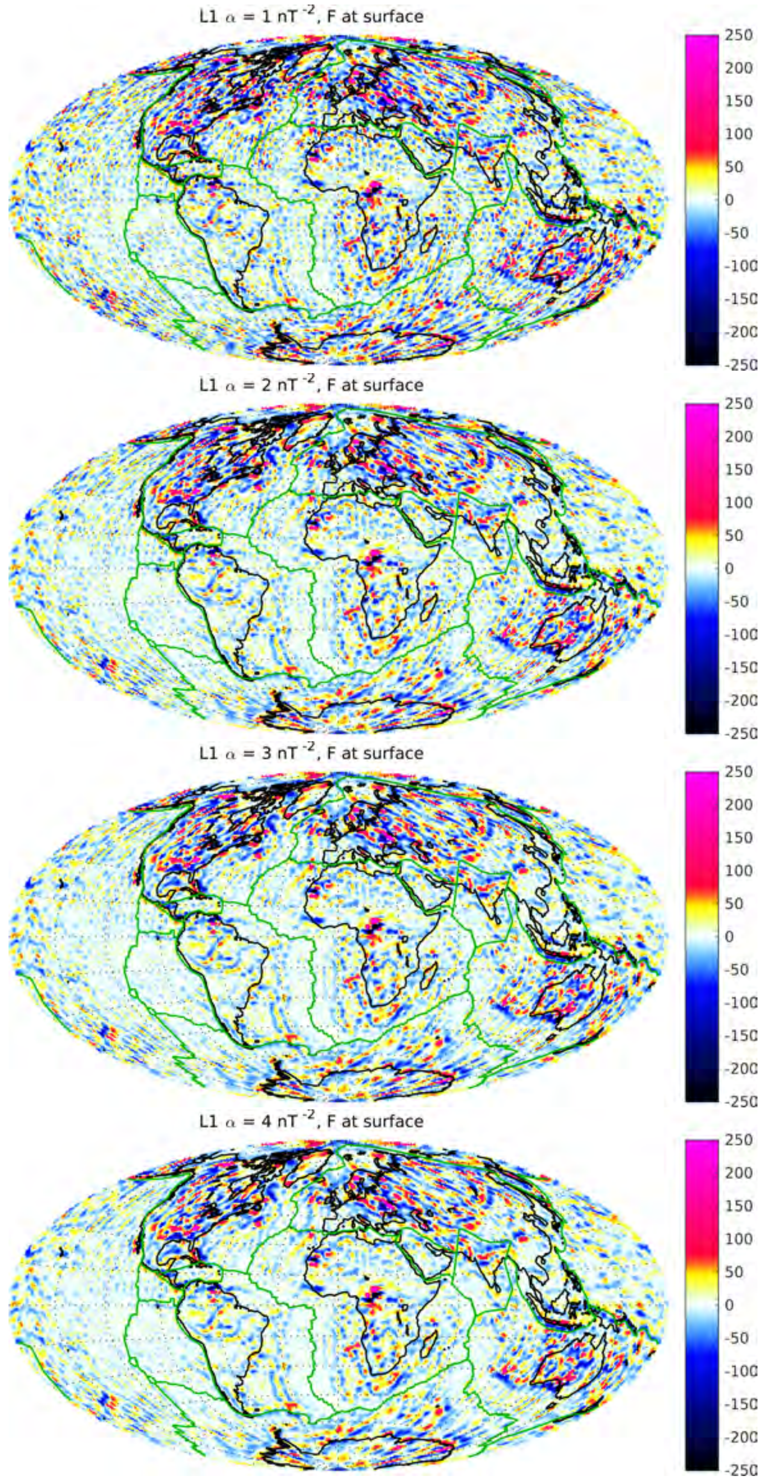

Figure 88 Lithospheric field intensity at the Earth's surface for the L1 regularized models using $\alpha = 1\,\mathrm{nT}^{-1}$, $\alpha = 2\,\mathrm{nT}^{-1}$, $\alpha = 3\,\mathrm{nT}^{-1}$ and $\alpha = 4\,\mathrm{nT}^{-1}$. The colorbar is given in nT.

Maps of the radial field component at 300 km altitude

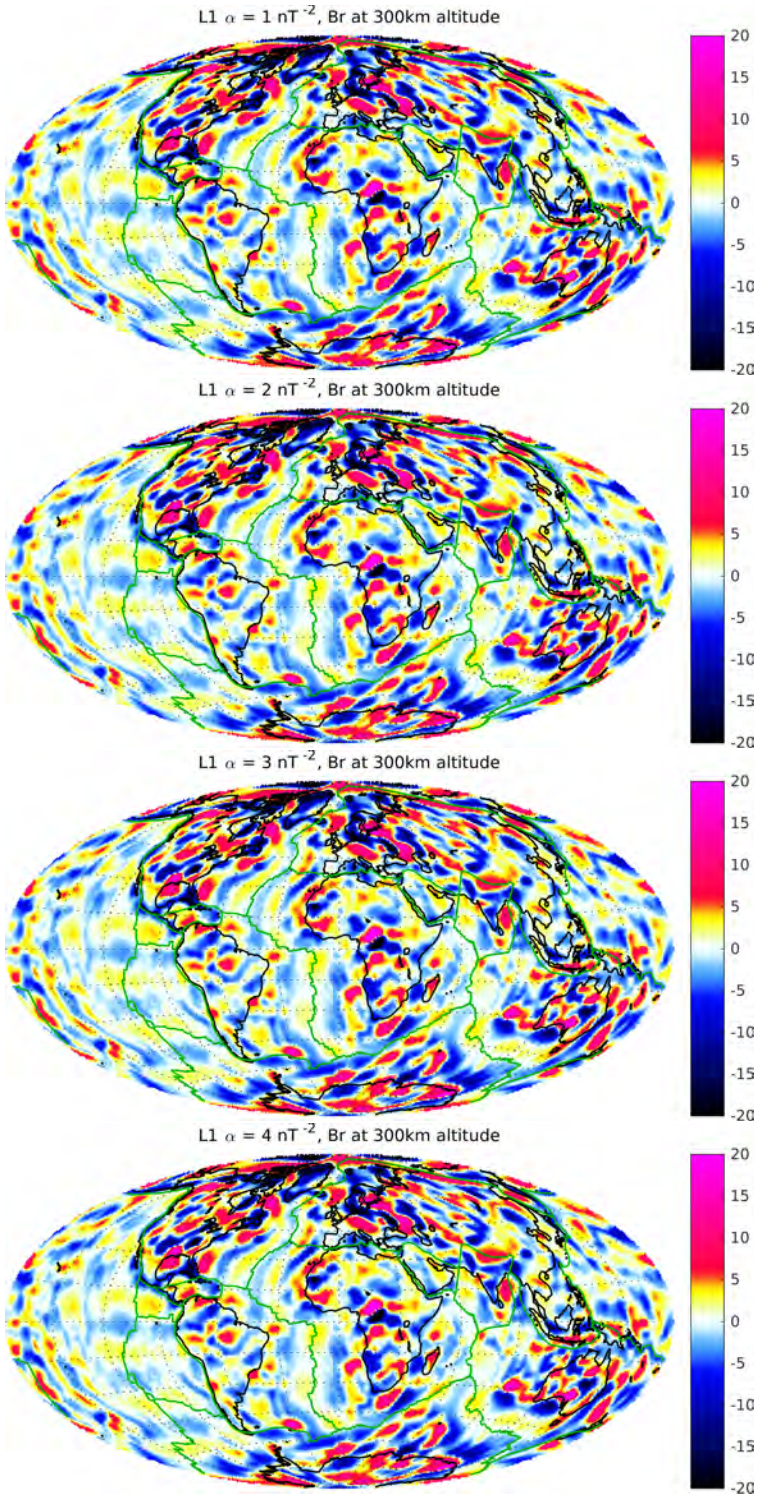

Figure 89 Radial lithospheric field component at 300 km altitude for the L1 regularized models using $\alpha = 1\,\mathrm{nT}^{-1}$, $\alpha = 2\,\mathrm{nT}^{-1}$, $\alpha = 3\,\mathrm{nT}^{-1}$ and $\alpha = 4\,\mathrm{nT}^{-1}$. The colorbar is given in nT.

Maps of the intensity field at 300 km altitude

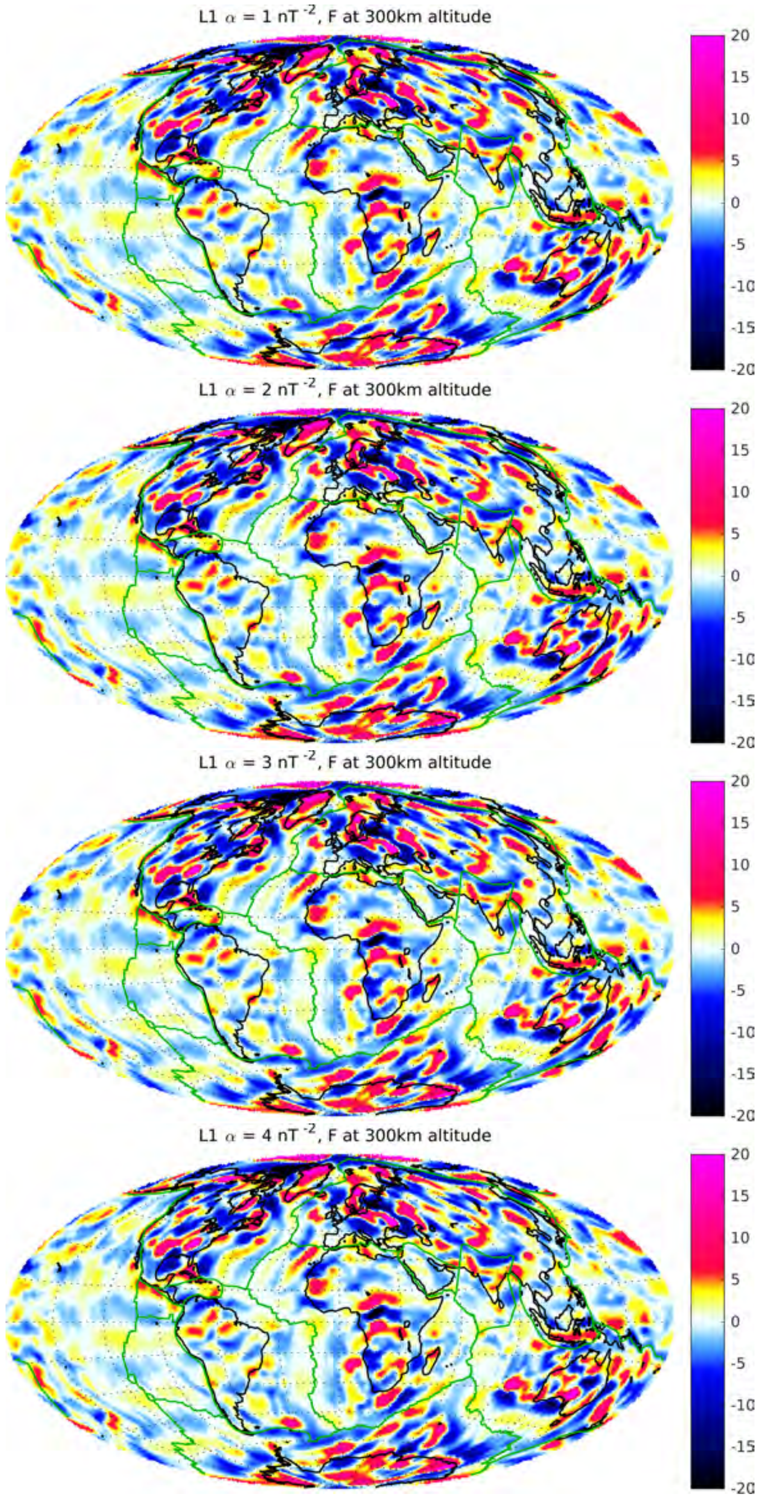

Figure 90 Lithospheric field intensity at 300 km altitude for the L1 regularized models using $\alpha = 1\,\mathrm{nT}^{-1}$, $\alpha = 2\,\mathrm{nT}^{-1}$, $\alpha = 3\,\mathrm{nT}^{-1}$ and $\alpha = 4\,\mathrm{nT}^{-1}$. The colorbar is given in nT.

Residual maps at data altitude

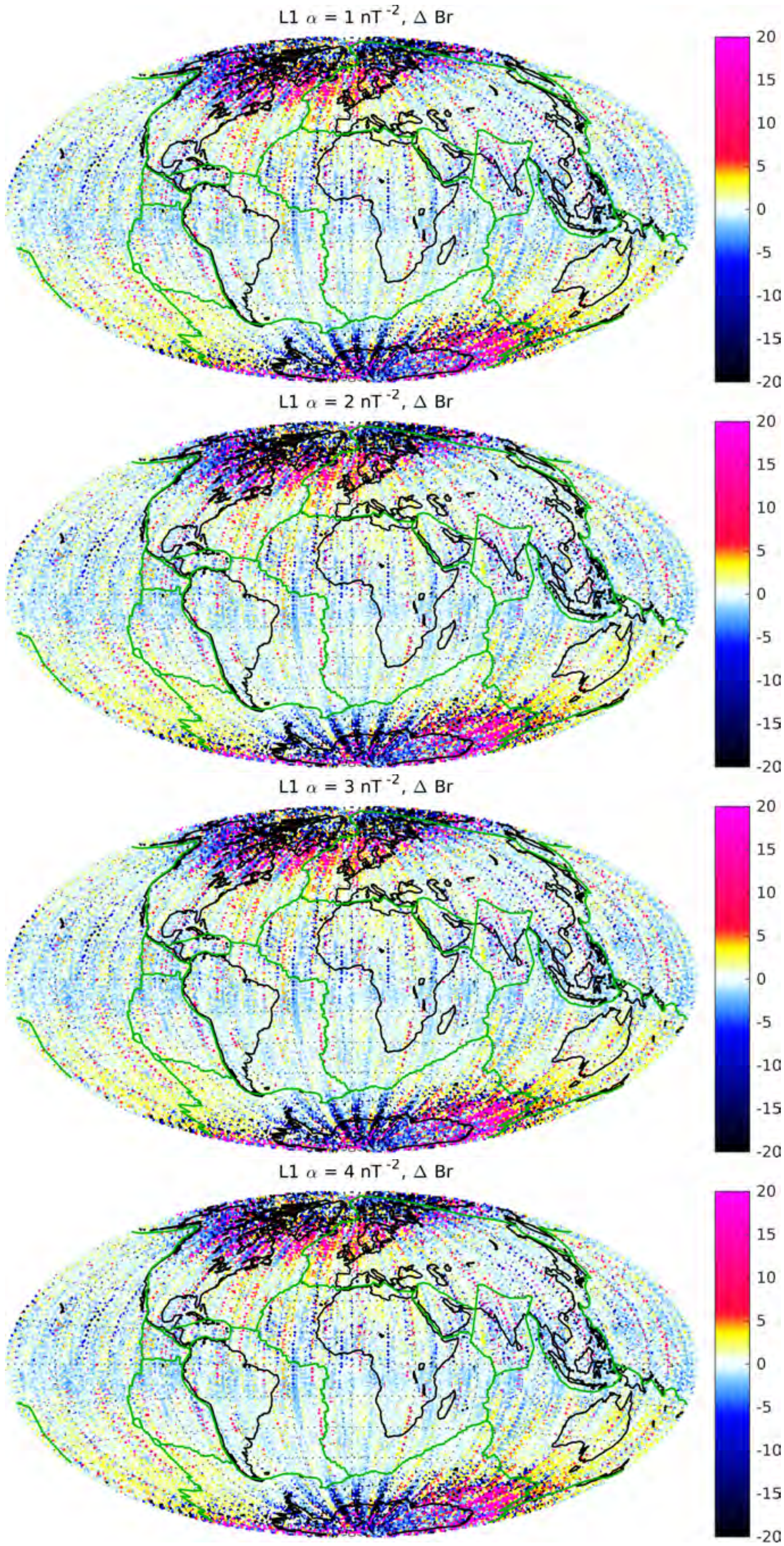

Figure 91 Radial residuals at data altitude for the L1 regularized models using $\alpha = 1\,\mathrm{nT}^{-1}$, $\alpha = 2\,\mathrm{nT}^{-1}$, $\alpha = 3\,\mathrm{nT}^{-1}$ and $\alpha = 4\,\mathrm{nT}^{-1}$. The colorbar is given in nT.

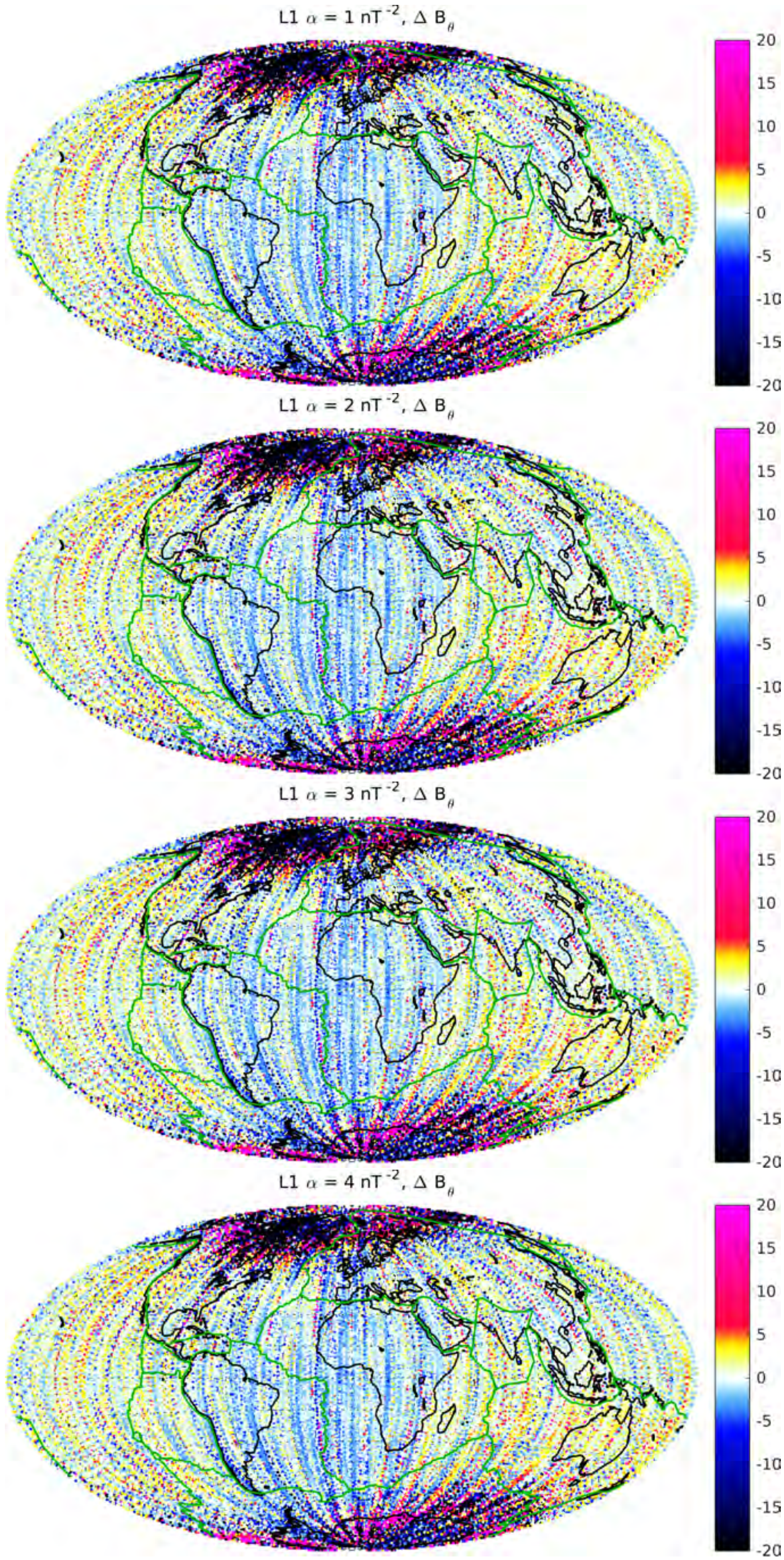

Figure 92 Latitudinal residuals at data altitude for the L1 regularized models using $\alpha = 1\,\mathrm{nT}^{-1}$, $\alpha = 2\,\mathrm{nT}^{-1}$, $\alpha = 3\,\mathrm{nT}^{-1}$ and $\alpha = 4\,\mathrm{nT}^{-1}$. The colorbar is given in nT.

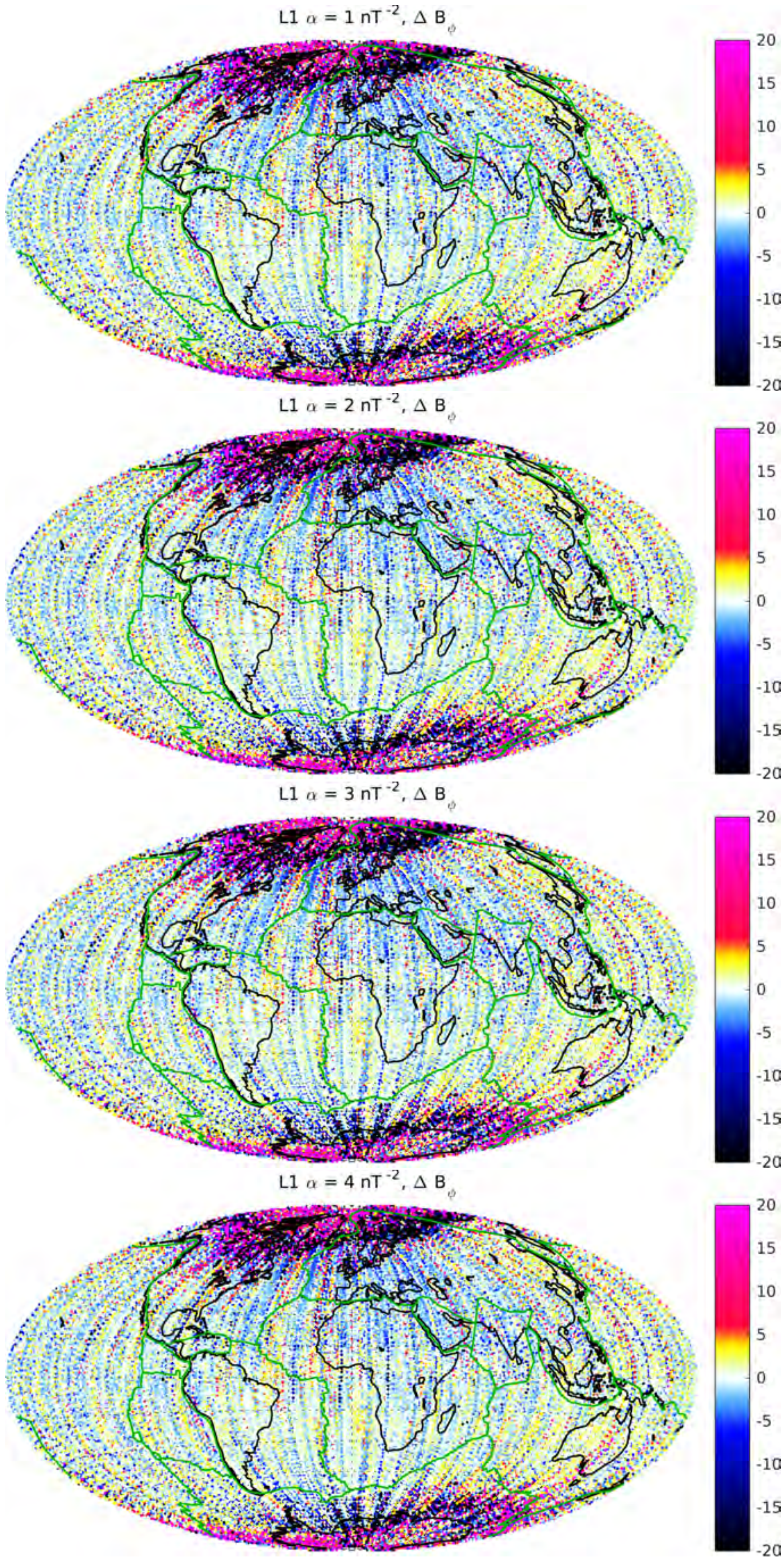

Figure 93 Longitudinal residuals at data altitude for the L1 regularized models using $\alpha = 1\,\mathrm{nT}^{-1}$, $\alpha = 2\,\mathrm{nT}^{-1}$, $\alpha = 3\,\mathrm{nT}^{-1}$ and $\alpha = 4\,\mathrm{nT}^{-1}$. The colorbar is given in nT.

D.4 Degree/order plots for model comparisons

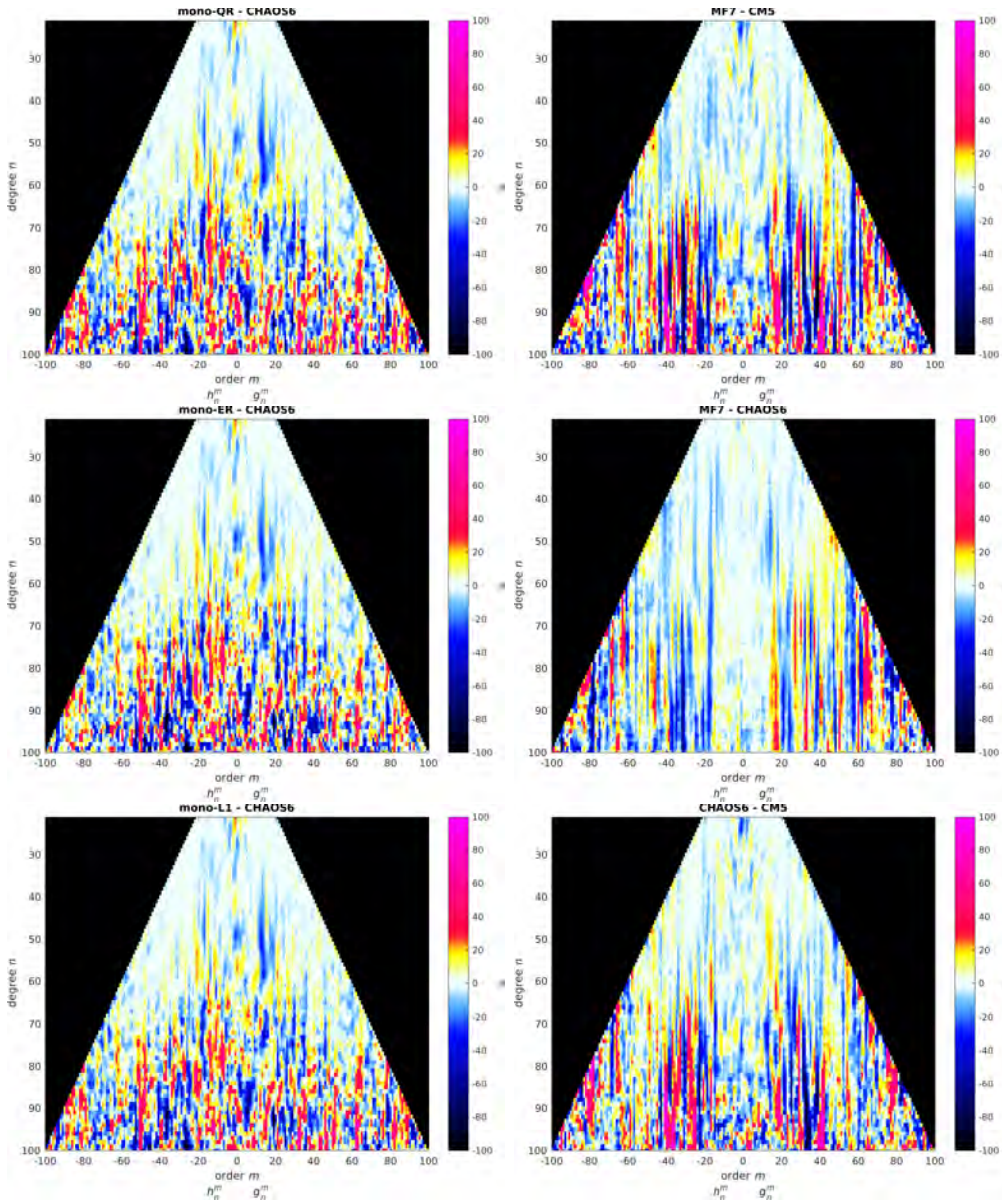

Figure 94 Normalized coefficient differences between mono-QR, mono-ER, mono-L1 and CHAOS-6 (left row) as well as between the models MF7, CM5, and CHAOS-6 (right row).

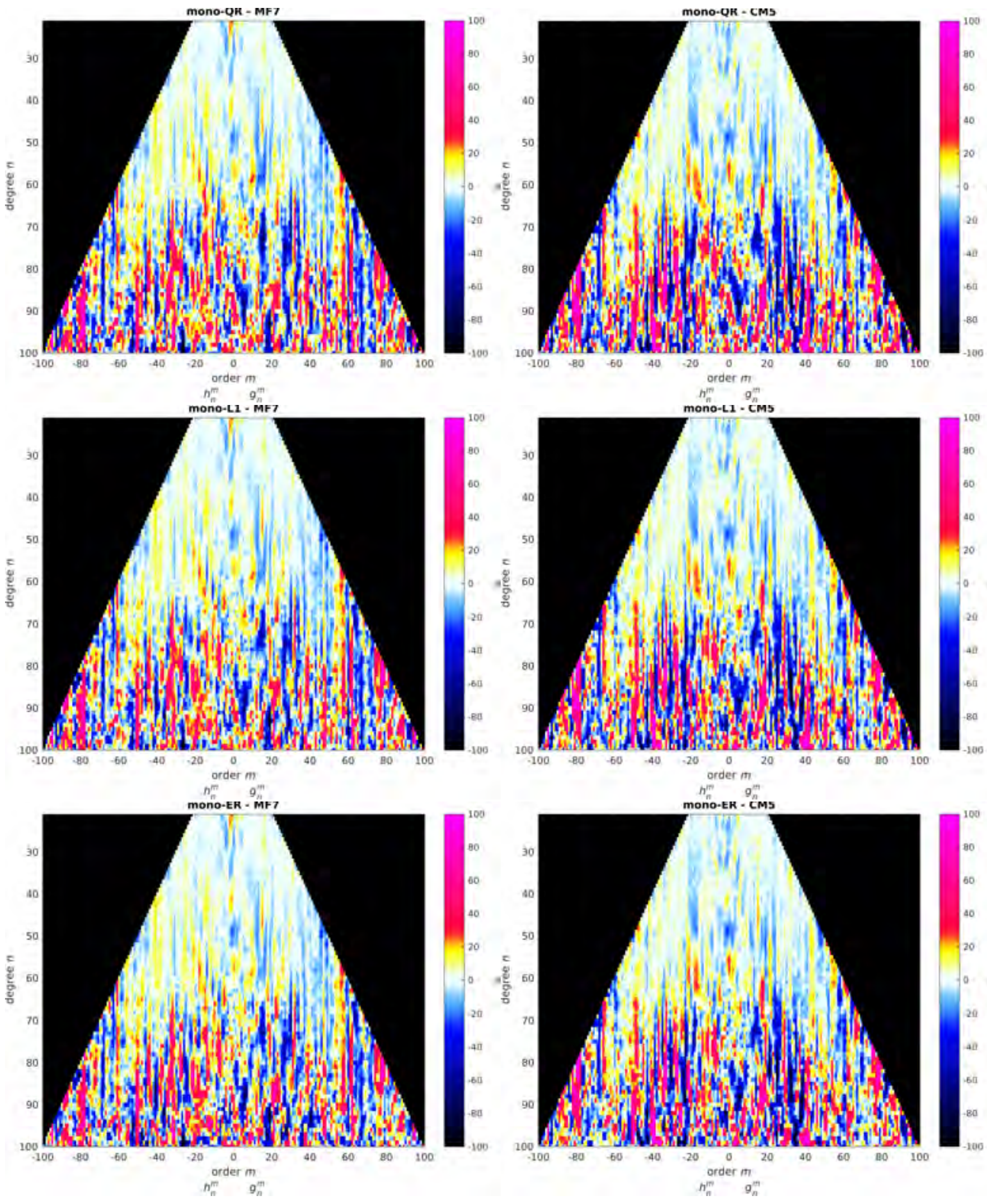

Figure 95 Normalized coefficient differences between mono-QR, mono-ER, mono-L1 and the models MF7 and CM5.

D.5 Regional plots for model comparisons

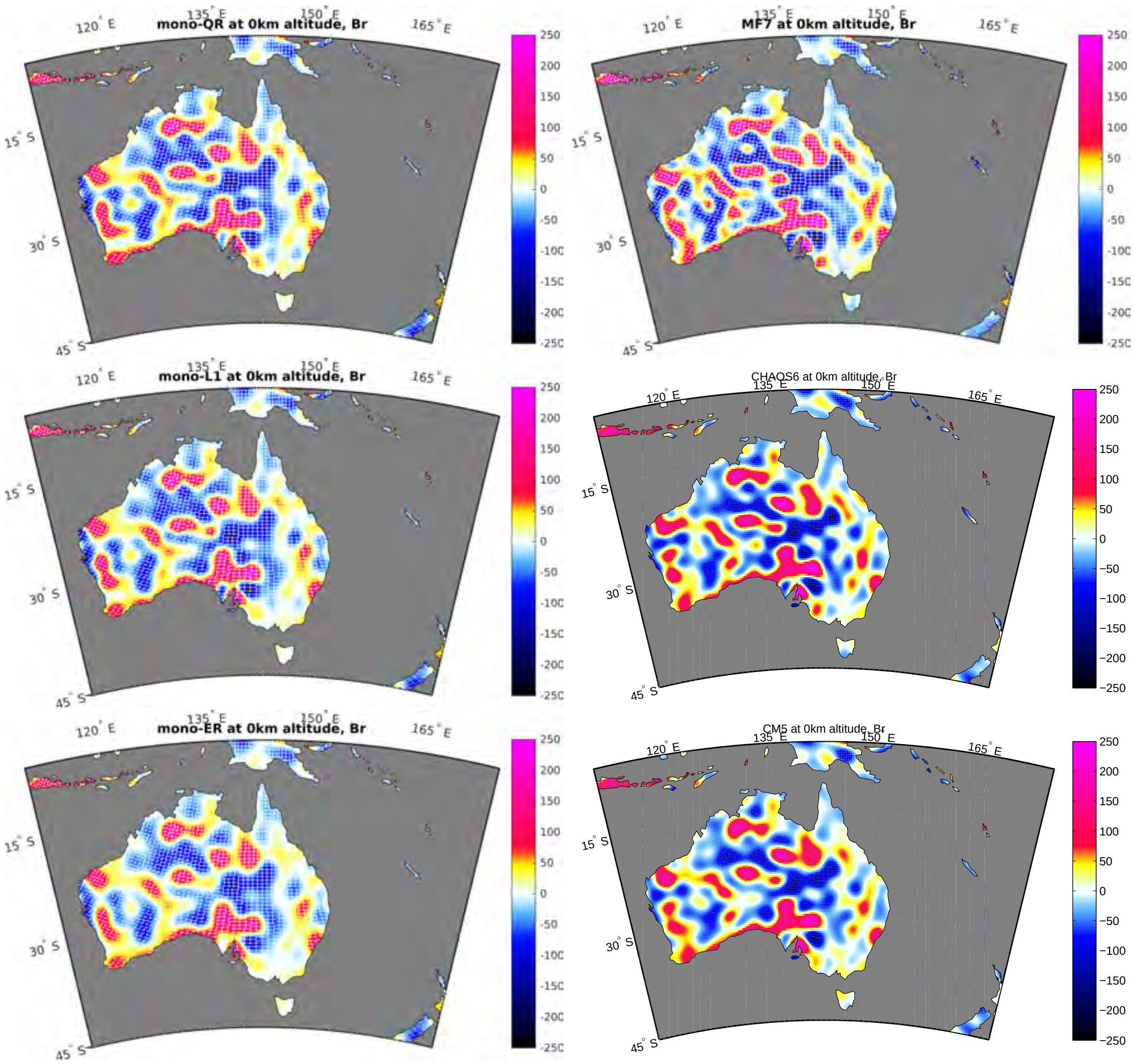

Figure 96 Radial lithospheric field at the Earth's surface over Australia for the three models mono-QR (top left), mono-L1 (middle left), mono-ER (bottom left), MF7 up to SH degree $n = 133$ (top right), CHAOS-6 up to SH degree $n = 120$ (middle right) and CM5 up to SH degree $n = 120$ (bottom right). The color scale is given in nT.

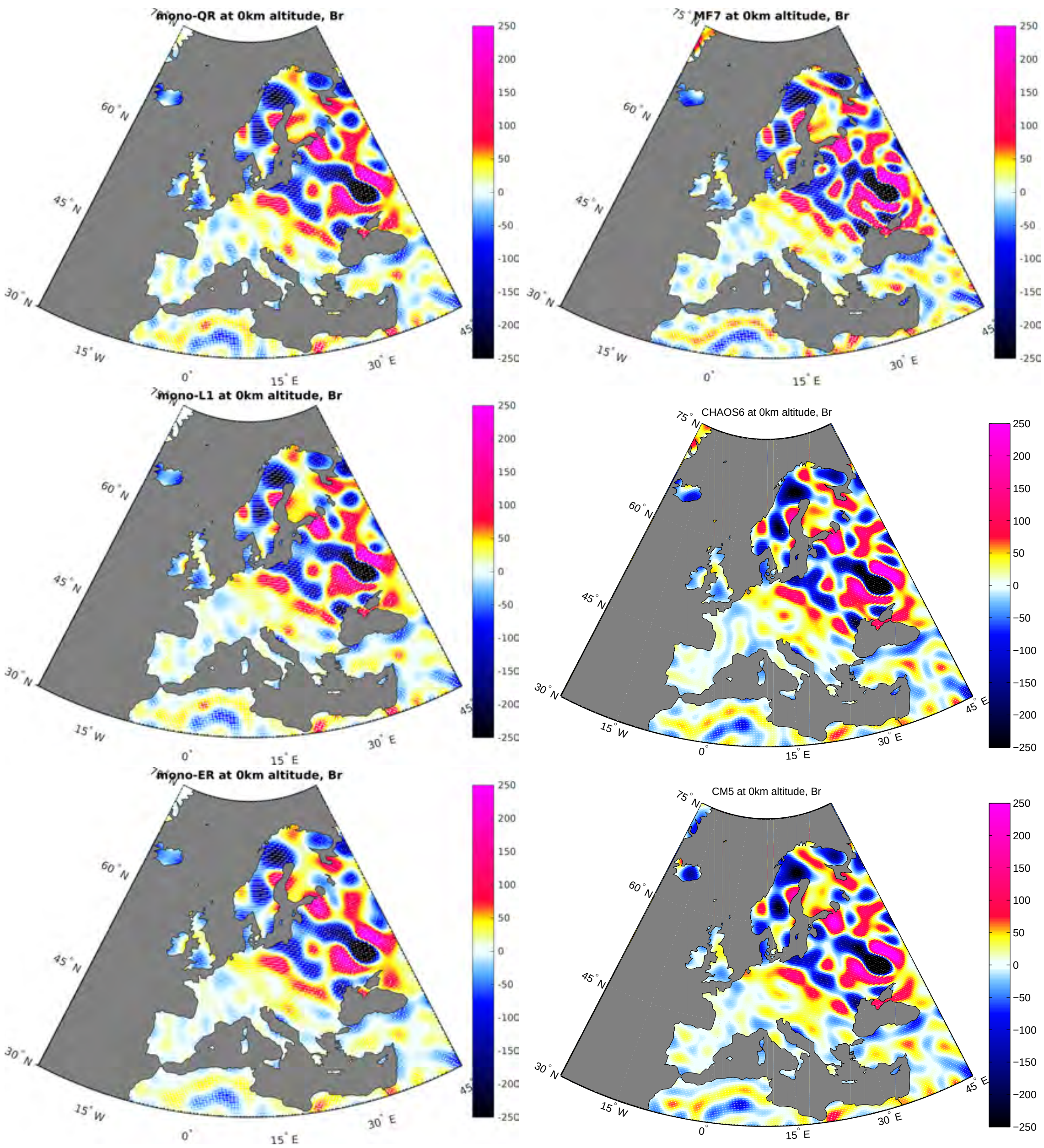

Figure 97 Radial lithospheric field at the Earth's surface over Europe for the three models mono-QR (top left), mono-L1 (middle left), mono-ER (bottom left), MF7 up to SH degree $n = 133$ (top right), CHAOS-6 up to SH degree $n = 120$ (middle right) and CM5 up to SH degree $n = 120$ (bottom right). The color scale is given in nT.

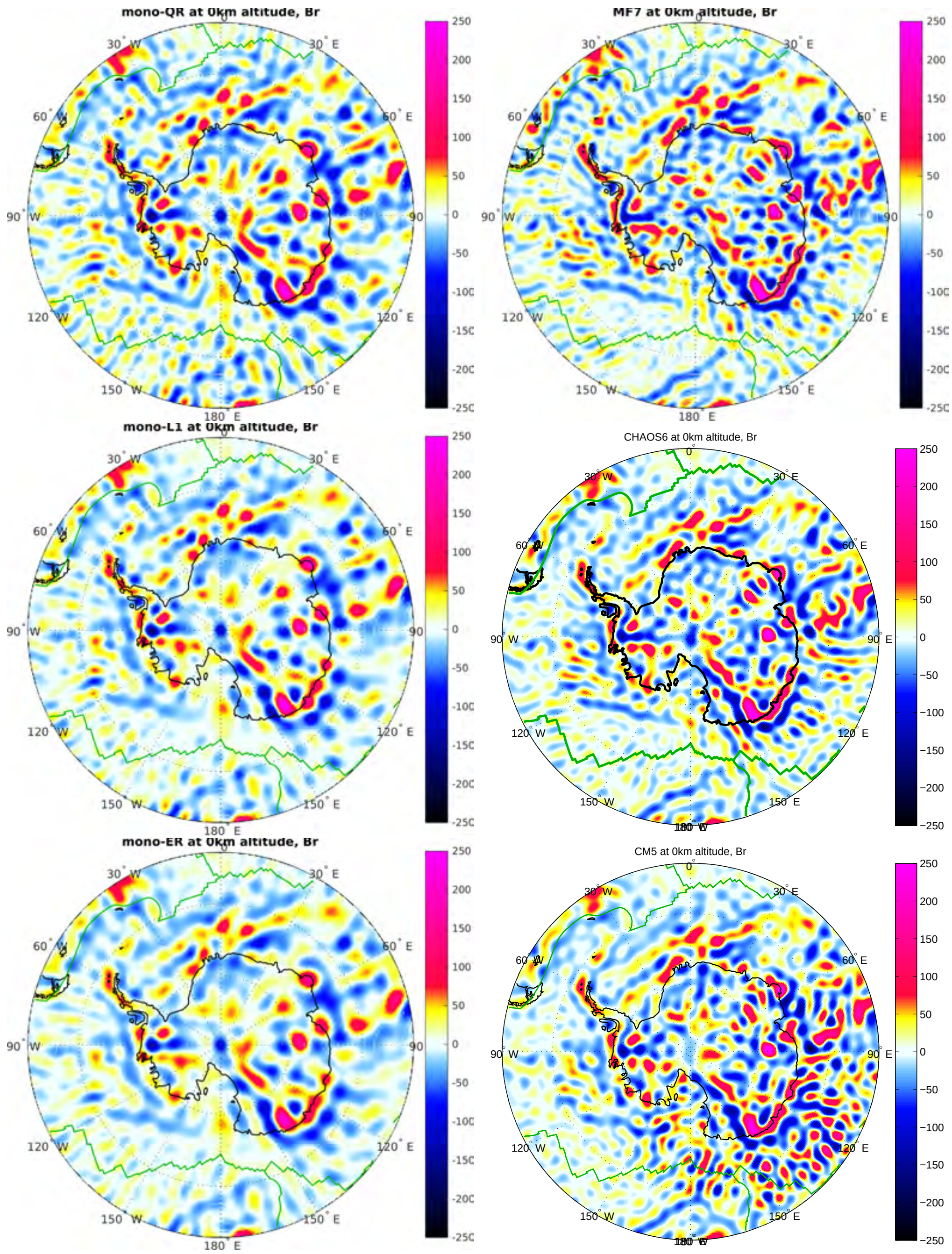

Figure 98 Radial lithospheric field at the Earth's surface over the South Pole for the three models mono-QR (top left), mono-L1 (middle left), mono-ER (bottom left), MF7 up to SH degree $n = 133$ (top right), CHAOS-6 up to SH degree $n = 120$ (middle right) and CM5 up to SH degree $n = 120$ (bottom right). The color scale is given in nT.

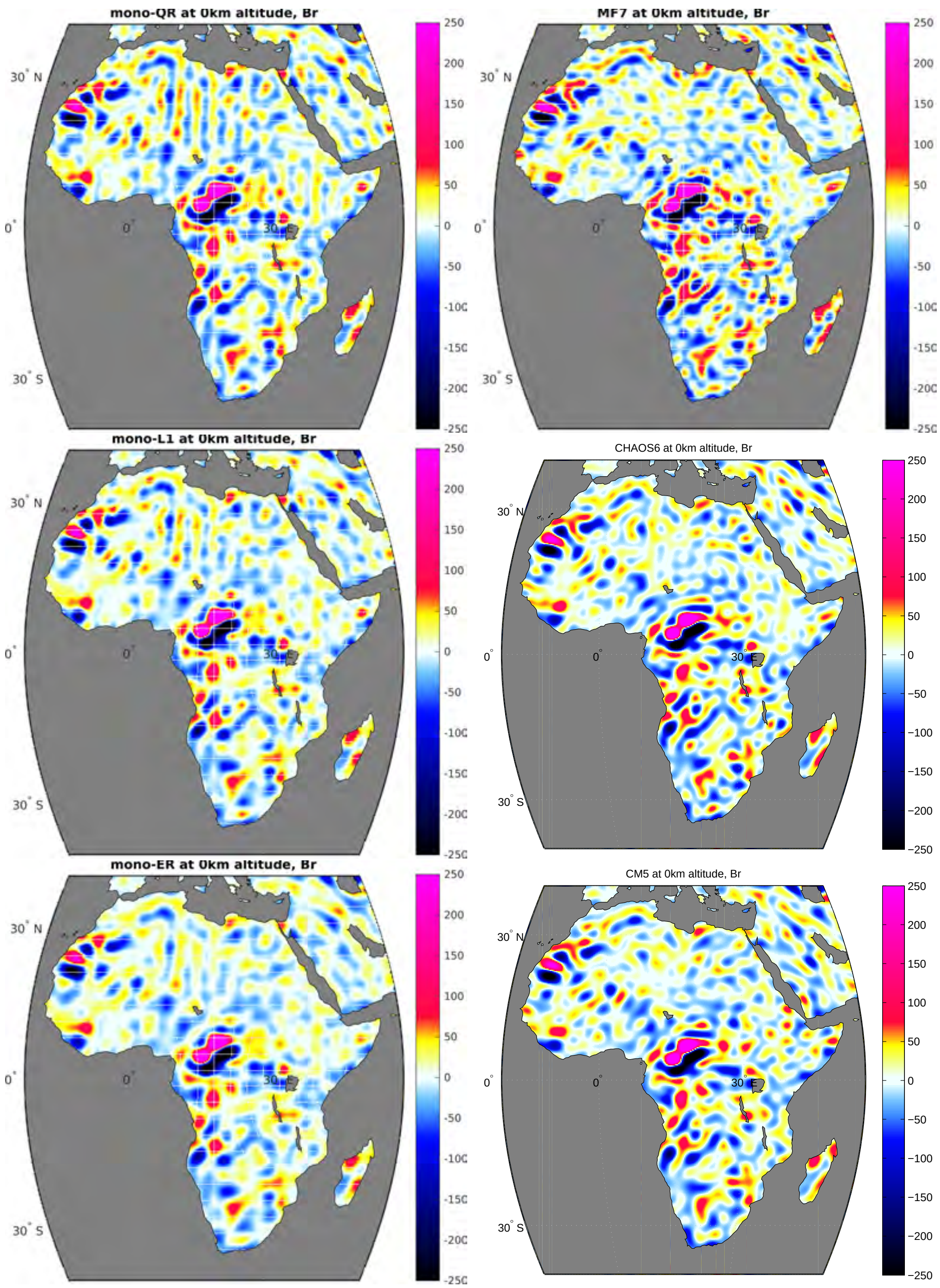

Figure 99 Radial lithospheric field at the Earth's surface over Africa for the three models mono-QR (top left), mono-L1 (middle left), mono-ER (bottom left), MF7 up to SH degree $n = 133$ (top right), CHAOS-6 up to SH degree $n = 120$ (middle right) and CM5 up to SH degree $n = 120$ (bottom right). The color scale is given in nT.

E Additional material for the analysis of regional lithospheric field models

E.1 Statistics for regional quadratic regularized models

	$\alpha = 0\,\mathrm{nT}^{-2}$	$\alpha = 50\,\mathrm{nT}^{-2}$	$\alpha = 100\,\mathrm{nT}^{-2}$	$\alpha = 200\,\mathrm{nT}^{-2}$	$\alpha = 400\,\mathrm{nT}^{-2}$	$\alpha = 600\,\mathrm{nT}^{-2}$	$\alpha = 800\,\mathrm{nT}^{-2}$	$\alpha = 1000\,\mathrm{nT}^{-2}$
mean ΔF (nT)	0.08	0.09	0.09	0.09	0.09	0.10	0.10	0.10
RMS ΔF (-)	2.31	2.27	2.28	2.28	2.29	2.30	2.30	2.30
min B_r (nT)	-197.26	-196.24	-194.86	-192.86	-190.89	-190.25	-189.79	-189.49
max B_r (nT)	266.39	244.25	243.31	241.94	241.97	251.99	251.70	251.51
mean B_r (nT)	-15.77	-9.01	0.52	15.05	28.51	36.00	39.69	42.11
min B_θ (nT)	-464.75	-426.40	-411.28	-388.53	-369.30	-372.33	-366.75	-363.09
max B_θ (nT)	989.15	875.79	743.23	541.17	356.49	261.32	210.08	176.51
mean B_θ (nT)	168.00	148.93	122.45	82.09	45.29	23.04	12.84	6.16
min B_ϕ (nT)	-714.76	-653.84	-572.81	-449.74	-359.49	-299.11	-290.99	-285.67
max B_ϕ (nT)	972.18	856.84	736.04	551.89	385.49	357.10	340.33	329.35
mean B_ϕ (nT)	154.21	124.74	101.44	65.84	33.32	25.62	16.52	10.55
min F (nT)	-146.15	-143.56	-143.04	-142.31	-141.87	-141.35	-141.21	-141.13
max F (nT)	161.25	160.92	163.10	166.41	169.52	172.99	173.83	174.38
mean F (nT)	-38.77	-38.66	-39.27	-40.20	-41.26	-41.71	-41.96	-42.13

Table 20 Fairey-71a quadratic regularized model statistics using a source depth of 23 km. The first two rows (gray) are direct model results at data locations, while the remaining values correspond to model predictions at the Earth's surface.

	$\alpha = 0\,\mathrm{nT}^{-2}$	$\alpha = 10\,\mathrm{nT}^{-2}$	$\alpha = 50\,\mathrm{nT}^{-2}$	$\alpha = 100\,\mathrm{nT}^{-2}$	$\alpha = 400\,\mathrm{nT}^{-2}$	$\alpha = 800\,\mathrm{nT}^{-2}$	$\alpha = 2500\,\mathrm{nT}^{-2}$	$\alpha = 3500\,\mathrm{nT}^{-2}$
mean ΔF (nT)	3.63	3.85	4.09	4.11	4.37	4.43	4.74	4.88
RMS ΔF (-)	8.84	9.13	9.22	9.29	9.31	9.46	9.59	9.65
min B_r (nT)	-24782.41	-7860.67	-5214.29	-3655.11	-1604.52	-1154.80	-514.54	-349.71
max B_r (nT)	12220.65	4204.97	1362.60	1395.86	1505.93	1107.65	701.73	601.78
mean B_r (nT)	-986.80	-807.25	-437.38	-265.33	-102.68	-70.85	-6.57	10.40
min B_θ (nT)	-37875.34	-6194.70	-1843.24	-1220.51	-886.21	-445.45	-542.32	-591.69
max B_θ (nT)	34879.46	16914.88	7063.07	4902.28	2131.27	1522.98	984.60	851.54
mean B_θ (nT)	4526.21	3112.23	1603.68	982.65	421.86	327.64	132.49	80.73
min B_ϕ (nT)	-54084.31	-20178.83	-6905.49	-3910.11	-2422.37	-1862.40	-1195.78	-939.14
max B_ϕ (nT)	17708.89	4059.23	2652.13	1857.90	918.72	723.03	938.99	930.07
mean B_ϕ (nT)	-6694.55	-3572.90	-1643.56	-935.19	-242.33	-134.14	-7.64	17.21
min F (nT)	-9924.98	-3589.31	-1497.44	-895.98	-1094.84	-877.26	-622.09	-545.37
max F (nT)	20074.44	4046.42	2728.35	1930.41	849.54	614.08	295.57	286.67
mean F (nT)	-265.13	-81.83	-27.45	-21.47	-24.74	-29.24	-33.97	-34.90

Table 21 NGU-74-75 quadratic regularized model statistics using a source depth of 37 km. The first two rows (gray) are direct model results at data locations, while the remaining values correspond to model predictions at the Earth's surface.

	$\alpha = 10\,\mathrm{nT}^{-2}$	$\alpha = 100\,\mathrm{nT}^{-2}$	$\alpha = 300\,\mathrm{nT}^{-2}$	$\alpha = 600\,\mathrm{nT}^{-2}$	$\alpha = 1000\,\mathrm{nT}^{-2}$	$\alpha = 2000\,\mathrm{nT}^{-2}$	$\alpha = 3000\,\mathrm{nT}^{-2}$	$\alpha = 4000\,\mathrm{nT}^{-2}$
mean ΔF (nT)	0.23	0.23	0.28	0.27	0.28	0.30	0.31	0.31
RMS ΔF (-)	2.11	2.15	2.18	2.20	2.25	2.28	2.31	2.33
min B_r (nT)	-5342.12	-2408.57	-1613.96	-1138.78	-1212.15	-1191.52	-1133.93	-1063.93
max B_r (nT)	1930.33	1384.14	594.25	489.60	344.57	265.95	225.31	187.29
mean B_r (nT)	19.47	-52.27	-96.08	-120.65	-108.03	-90.18	-74.34	-62.55
min B_θ (nT)	-2506.27	-1659.92	-417.23	-279.24	-254.93	-112.21	-45.44	-3.00
max B_θ (nT)	11908.51	3957.76	2384.60	1802.22	1921.78	1905.13	1826.11	1730.15
mean B_θ (nT)	357.17	417.36	437.65	466.28	409.38	337.41	281.68	241.50
min B_ϕ (nT)	-5416.54	-2828.15	-1835.84	-1303.19	-1082.45	-857.95	-982.19	-1029.08
max B_ϕ (nT)	6823.95	3893.93	1849.96	876.67	810.12	739.66	726.07	694.21
mean B_ϕ (nT)	-452.81	-403.32	-156.76	-72.62	17.10	58.91	58.58	49.05
min F (nT)	-1913.18	-1054.91	-767.27	-772.64	-560.01	-437.16	-363.04	-298.92
max F (nT)	1671.19	1091.90	826.77	562.46	600.26	588.62	557.16	518.60
mean F (nT)	-110.02	-58.00	-28.30	-15.12	-13.51	-11.29	-10.63	-10.26

Table 22 Viking-93 quadratic regularized model statistics using a source depth of 39 km. The first two rows (gray) are direct model results at data locations, while the remaining values correspond to model predictions at the Earth's surface.

E.2 Downward continuation of regional models

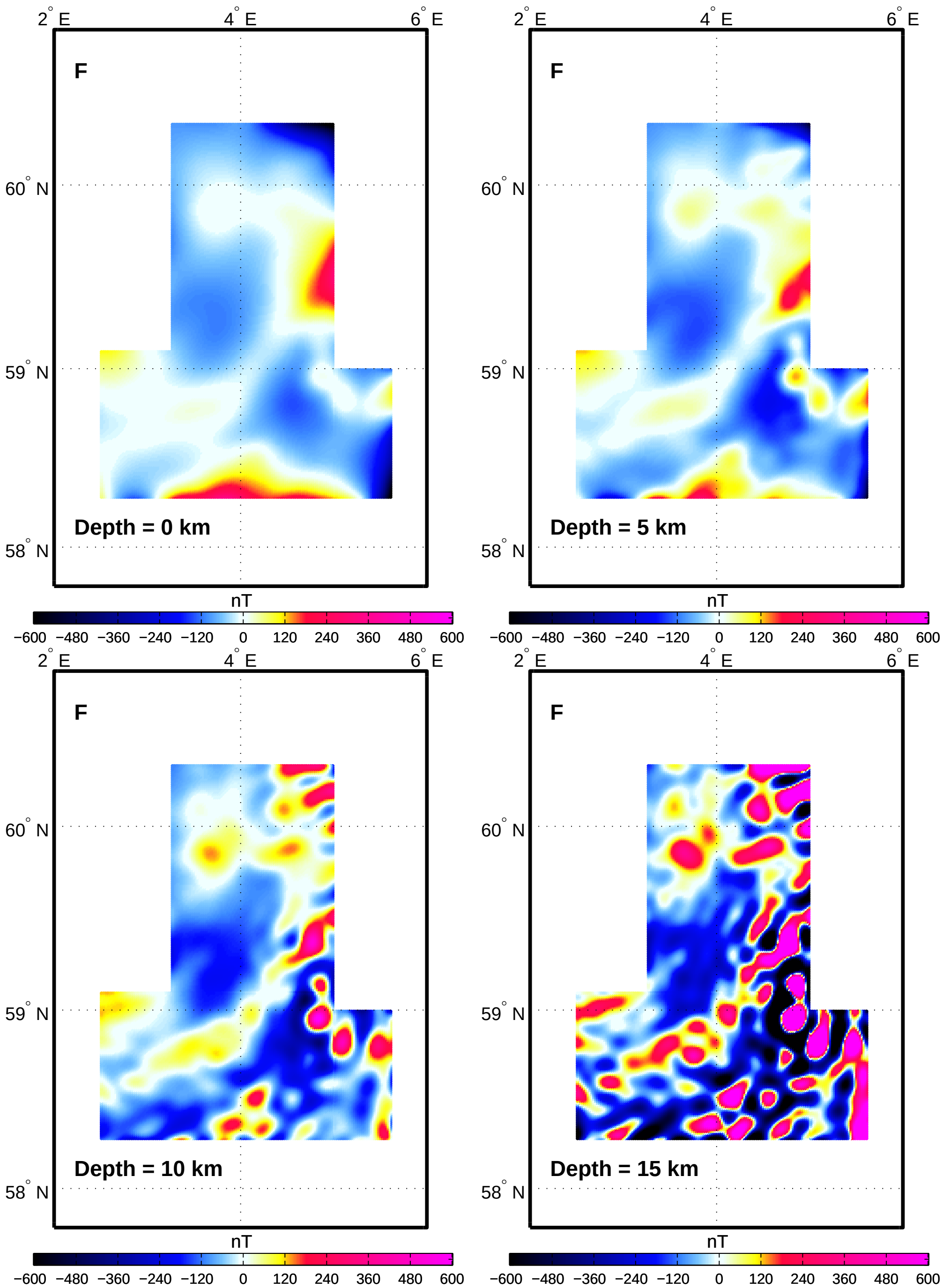

Figure 100 Model estimation of the lithospheric field intensity for different depth values below the Earth's surface $a = 6371.2\,\mathrm{km}$. The corresponding model values are based on the quadratic regularized ($\alpha = 2000\,\mathrm{nT}^{-2}$) NGU-74-75 model results with $L = 14$ and a source depth of $37\,\mathrm{km}$.

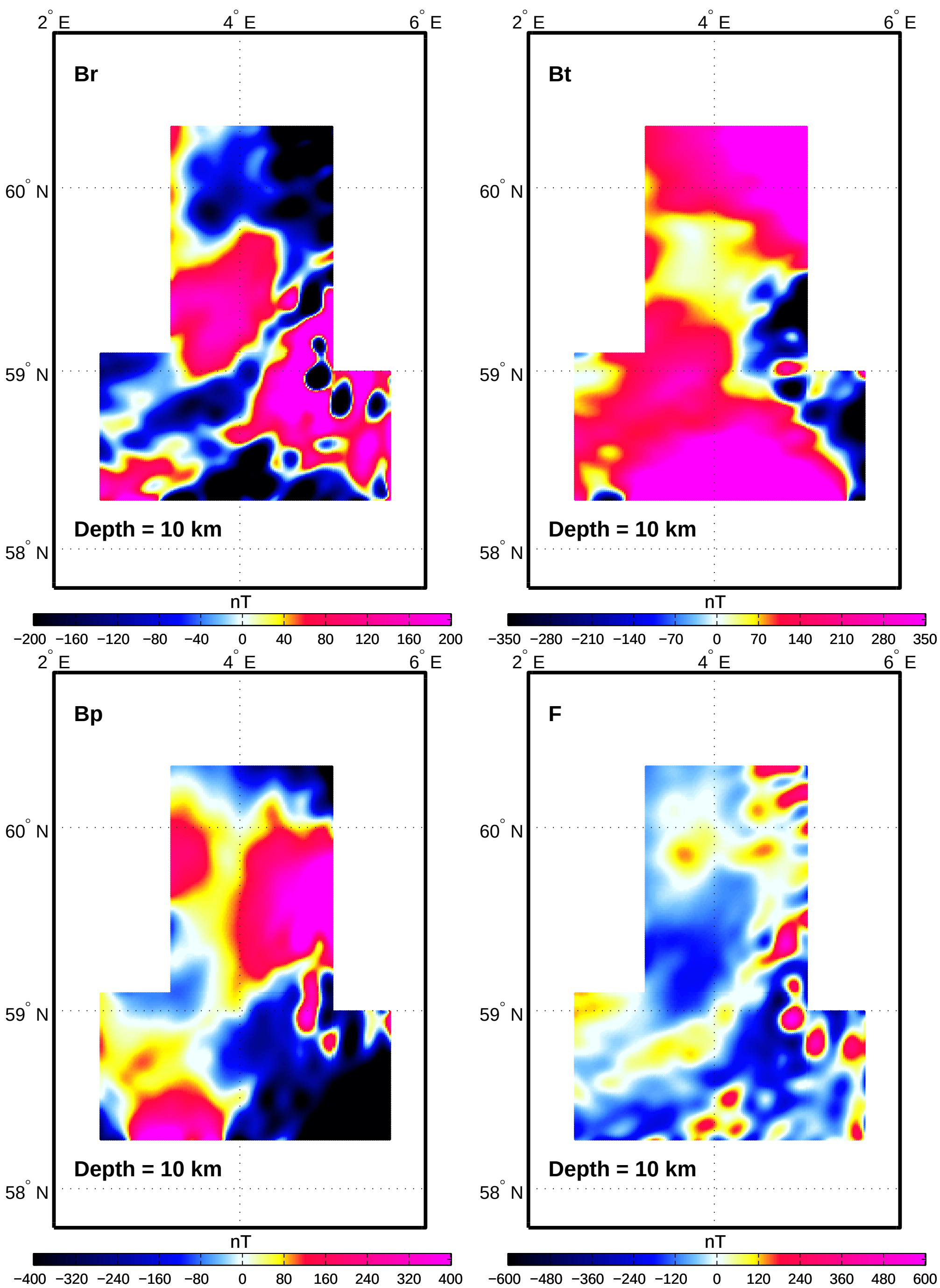

Figure 101 Model estimation of the three lithospheric field components and the field intensity at 10 km depth below the Earth's surface $a = 6371.2\,\text{km}$. The corresponding model values are based on the quadratic regularized ($\alpha = 2000\,\text{nT}^{-2}$) NGU-74-75 model results with $L = 14$ and a source depth of 37 km.

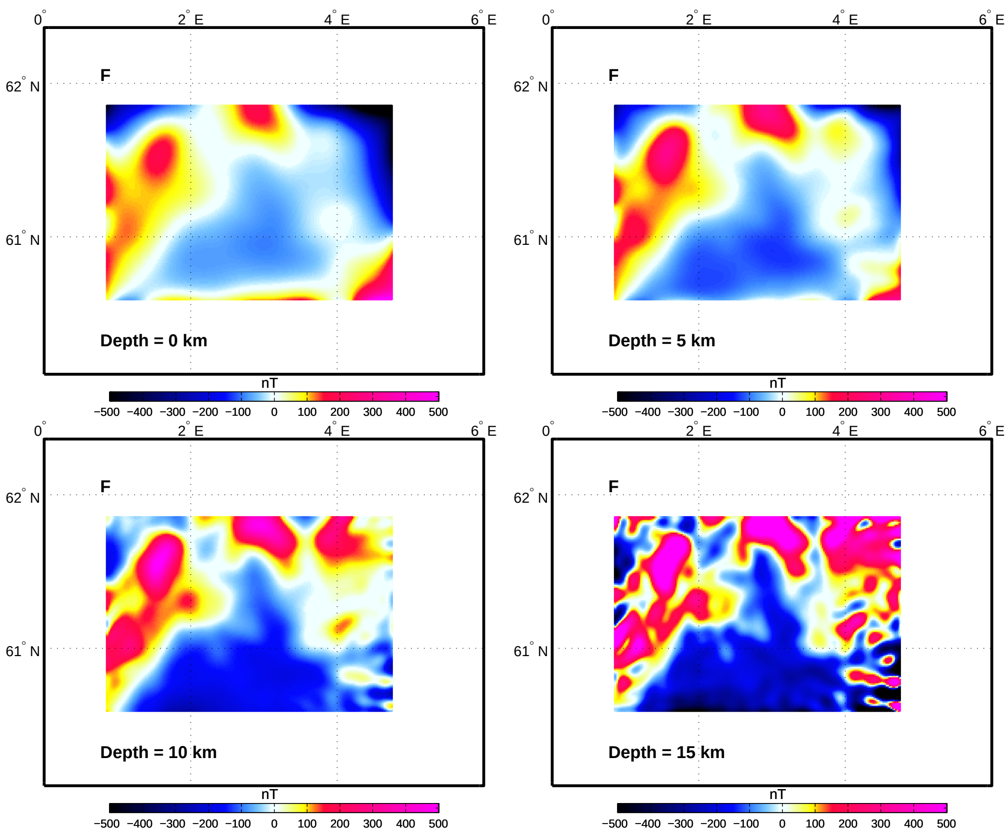

Figure 102 Model estimation of the lithospheric field intensity for different depth values below the Earth's surface $a = 6371.2\,\mathrm{km}$. The corresponding model values are based on the quadratic regularized ($\alpha = 600\,\mathrm{nT}^{-2}$) Viking-93 model results with $L = 16$ and a source depth of 39 km.

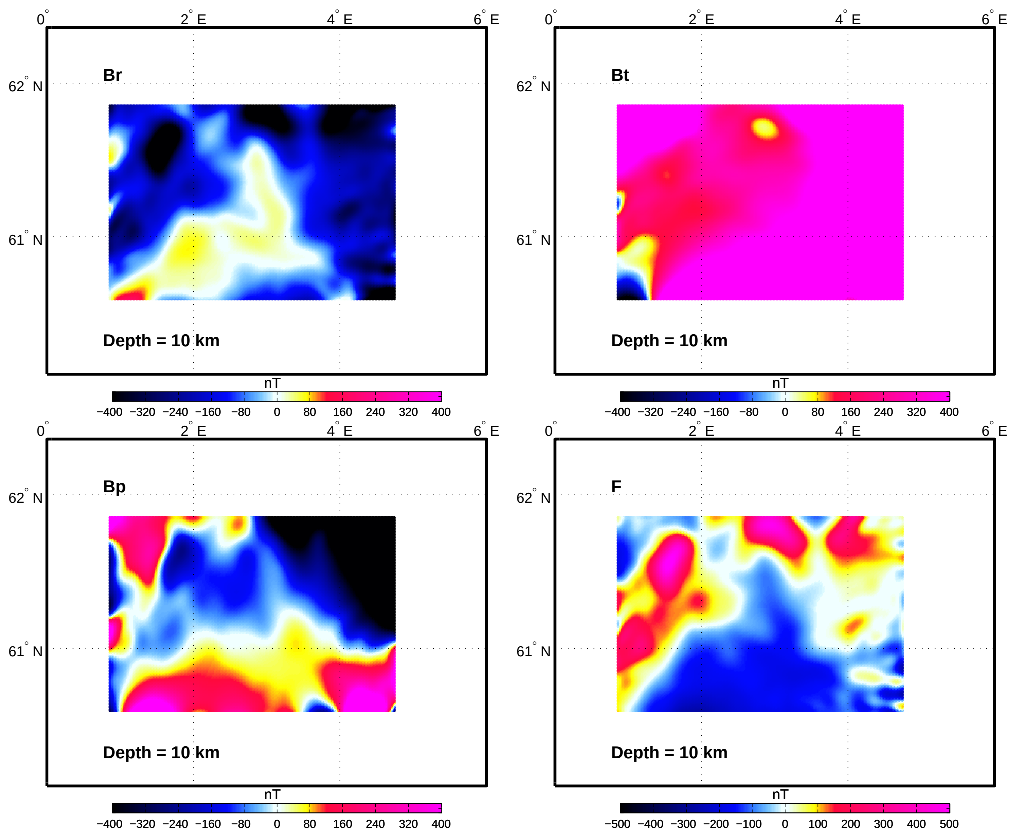

Figure 103 Model estimation of the three lithospheric field components and the field intensity at 10 km depth below the Earth's surface $a = 6371.2\,\mathrm{km}$. The corresponding model values are based on the quadratic regularized ($\alpha = 600\,\mathrm{nT}^{-2}$) Viking-93 model results with $L = 16$ and a source depth of 39 km.

F Additional material for Ekofisk case study

Definition of source grid size and depth

Un-regularized models were derived using source depth values between 0 and 100 km and grid refinements corresponding to a global source amount of $K_g = [500,000 : 500,000 : 4,500,000]$. Regarding the respective model statistics, no major model improvement can be achieved beyond $K_g = 3,500,000$, which henceforth is the used grid refinement level for equivalent source models of the MAGAN survey. This corresponds to 285 sources used for the model derivation, using only sources with minimal surface distances to the closest data point below 20 km.
In order to get a first impression of an appropriate source depth value for local field models of the MAGAN survey, 100 un-regularized inversions are performed with randomly picked depth values between 0 and 100 km. Fig.104 illustrates the corresponding Euclidean norm of the model residuals. No model convergence can be reached for depth values larger than 55 km. The preferred source depth is now determined using this maximum depth and the Metropolis Hastings algorithm of section 4.2.1. Figure 105 shows the proposed and accepted source depth values the MAGAN survey. The probability density functions for the corresponding normal distribution is given in the right part of the figure and reaches its maximum at 53 km source depth.

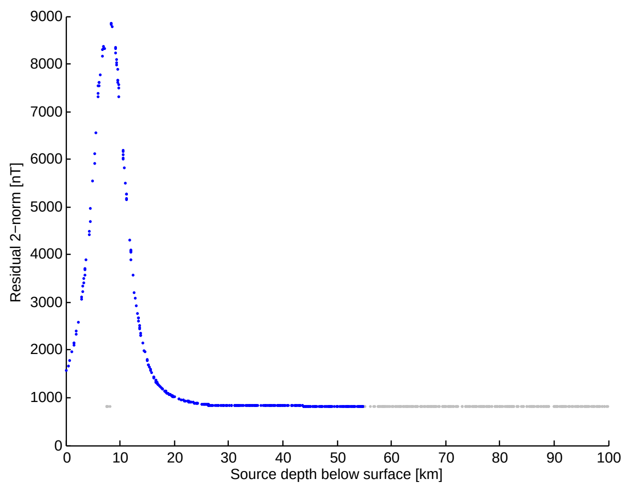

Figure 104 Residual 2-norm corresponding to 100 un-regularized models using the MAGAN data set and randomly picked source depth values between 0 and 100 km. No model convergence can be reached for depth values larger than 55 km. The curve peak corresponds to the original geocentric data altitude of approximately 8 km below the Earth's surface.

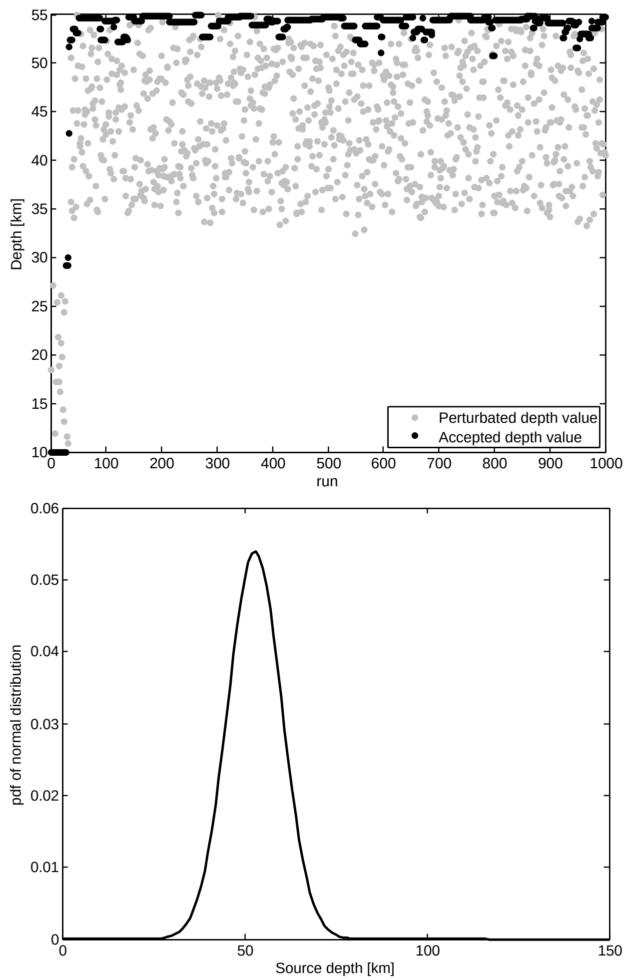

Figure 105 Perturbated (grey) and accepted (black) depth values due to the Metropolis Hastings algorithm for 1000 un-regularized model inversions of the MAGAN survey. The corresponding source grid sizes is $L = 6$. The initial depth is 10 km and maximum allowed perturbation in depth is $\Delta\delta = 20$ km. The right part of the figure gives the PDF for the normal distributions corresponding to the accepted source depth values. The corresponding peak is derived for 53 km.

	$\alpha = 10\,\mathrm{nT}^{-2}$	$\alpha = 100\,\mathrm{nT}^{-2}$	$\alpha = 300\,\mathrm{nT}^{-2}$	$\alpha = 600\,\mathrm{nT}^{-2}$	$\alpha = 1000\,\mathrm{nT}^{-2}$	$\alpha = 2000\,\mathrm{nT}^{-2}$
mean ΔF (nT)	0.03	0.02	0.03	0.04	0.04	0.05
RMS ΔF (-)	1.51	1.57	1.62	1.66	1.70	1.76
min B_r (nT)	-272.56	-143.85	-86.94	-58.14	-37.81	-25.38
max B_r (nT)	233.75	179.55	128.48	134.50	141.30	146.89
mean B_r (nT)	21.70	33.87	44.15	51.76	57.79	65.85
min B_θ (nT)	-252.59	-138.99	-119.77	-110.00	-106.66	-129.33
max B_θ (nT)	557.97	392.93	300.60	226.93	180.12	133.55
mean B_θ (nT)	121.36	86.53	56.88	34.63	17.05	-6.09
min B_ϕ (nT)	-378.64	-281.23	-247.08	-209.19	-169.36	-151.83
max B_ϕ (nT)	546.56	387.82	259.85	173.60	112.66	113.00
mean B_ϕ (nT)	115.39	86.51	45.31	23.03	12.44	4.48
min F (nT)	-189.52	-158.08	-158.90	-155.65	-149.47	-137.56
max F (nT)	138.20	82.48	58.26	44.42	34.99	23.74
mean F (nT)	-64.58	-63.51	-62.08	-61.18	-60.67	-60.31

Table 23 MAGAN quadratic regularized model statistics using 285 sources at 53 km depth. The first two rows (gray) are direct model results at data locations, while the remaining values correspond to model predictions at the Earth's surface.

MAGAN model regularization

Figure 106 illustrates the L-curve corresponding to quadratic regularized MAGAN models using 285 sources at 53 km depth. The final regularization parameter is chosen to be close to the knee-point of the L-curve, $\alpha = 300\,\mathrm{nT}^{-2}$ and will be used for generating models for upward and downward continuation.

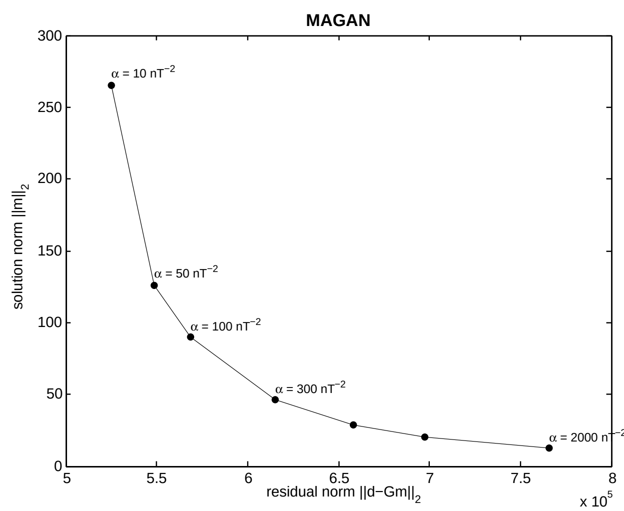

Figure 106 L-curve for quadratic regularized models using MAGAN data, 285 equivalent sources at 53 km depth. Corresponding model statistics are given in Table 23.

Downward continuation of MAGAN model

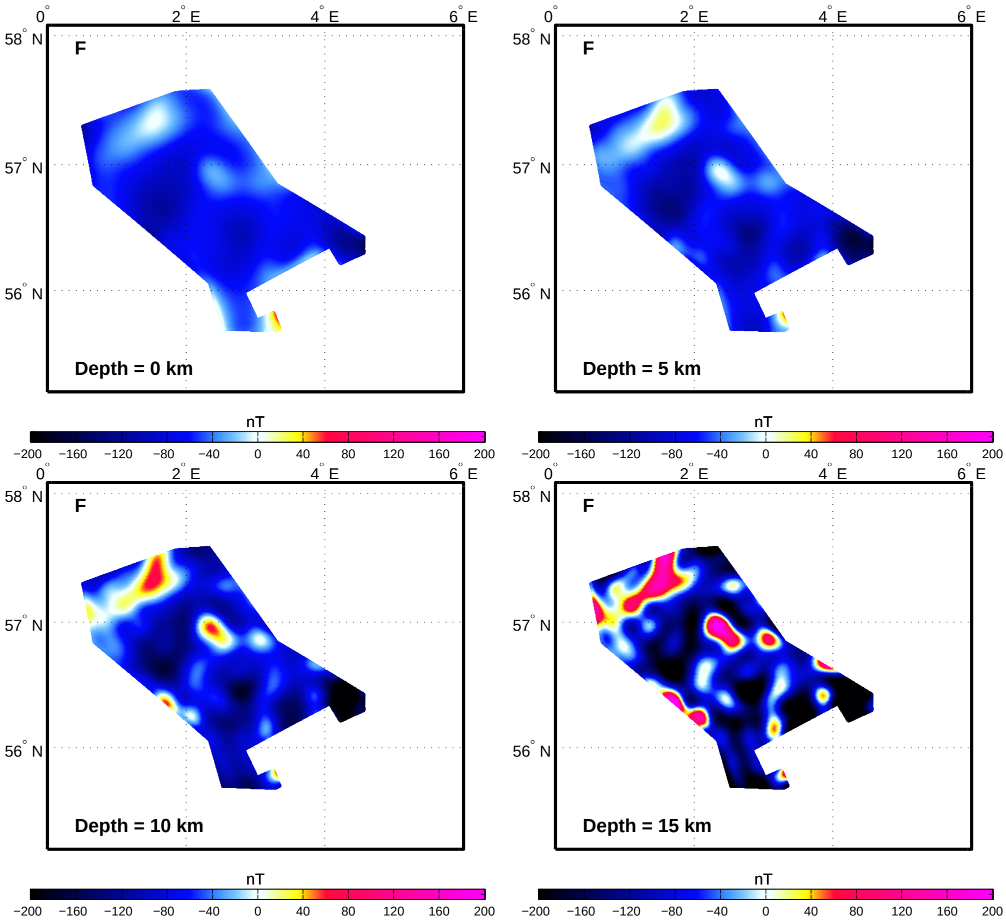

Figure 107 Model estimation of the MAGAN lithospheric field intensity for different depth values below the Earth's surface $a = 6371.2\,\mathrm{km}$. The corresponding model values are based on the quadratic regularized ($\alpha = 300\,\mathrm{nT}^{-2}$) model results with $L = 7$ and a source depth of $53\,\mathrm{km}$.

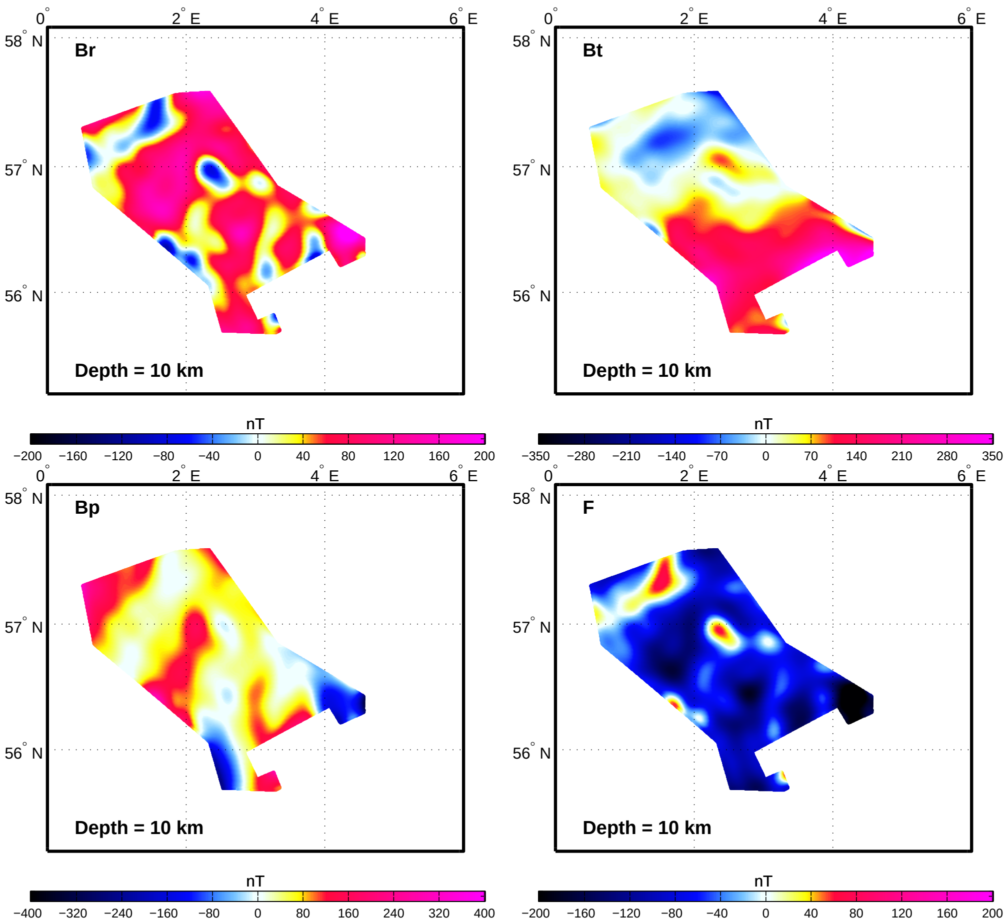

Figure 108 MAGAN model estimations of the three lithospheric field components and the field intensity at 10 km depth below the Earth's surface $a = 6371.2\,\mathrm{km}$. The corresponding model values are based on the quadratic regularized ($\alpha = 300\,\mathrm{nT}^{-2}$) results with $L = 7$ and a source depth of 53 km.

G Additional material for the combined satellite and near-surface measurement routine

G.1 Source grid of regional near-surface data

In order to determine the most appropriate source distribution for representing the near-surface measurements, un-regularized inversions are performed for seven different grid sizes (K_g = 450000:50000:750000) and for depth values between 10 km and 200 km. For calculation time efficiency, only NURE-NAMAM2008 data for the region 100-110 deg longitude and 35-40 deg latitude are used. By using every 30th data point, this corresponds to 9062 measurements in the chosen area. Similar to the regional equivalent source models of chapter 4, only sources in the vicinity of the survey area are taken into account for the model inversions. Figure 109 illustrates the residual 2-norm and correlation coefficient values for the derived models. No model convergence could be reached for source grids $K_g > 700000$. In order to represent the high resolution NURE-NAMAM2008 data set, the combined inversion scheme uses the highest possible source amount of $K_g = 700000$, which corresponds to approximately 27 km distance between to sources projected to the surface. Figure 109 shows that models using this source distribution converge up to a source depth value of 60 km. This value is also chosen for the combined inversion scheme, as it results in the most favorable values for both correlation coefficient and residual 2-norm.

Having a source grid of $K_g = 700000$ and only using sources within a 2° larger boundary margin than the near-surface data area, the combined data routine works with 29,846 sources corresponding to the NURE-NAMAM2008 data set.

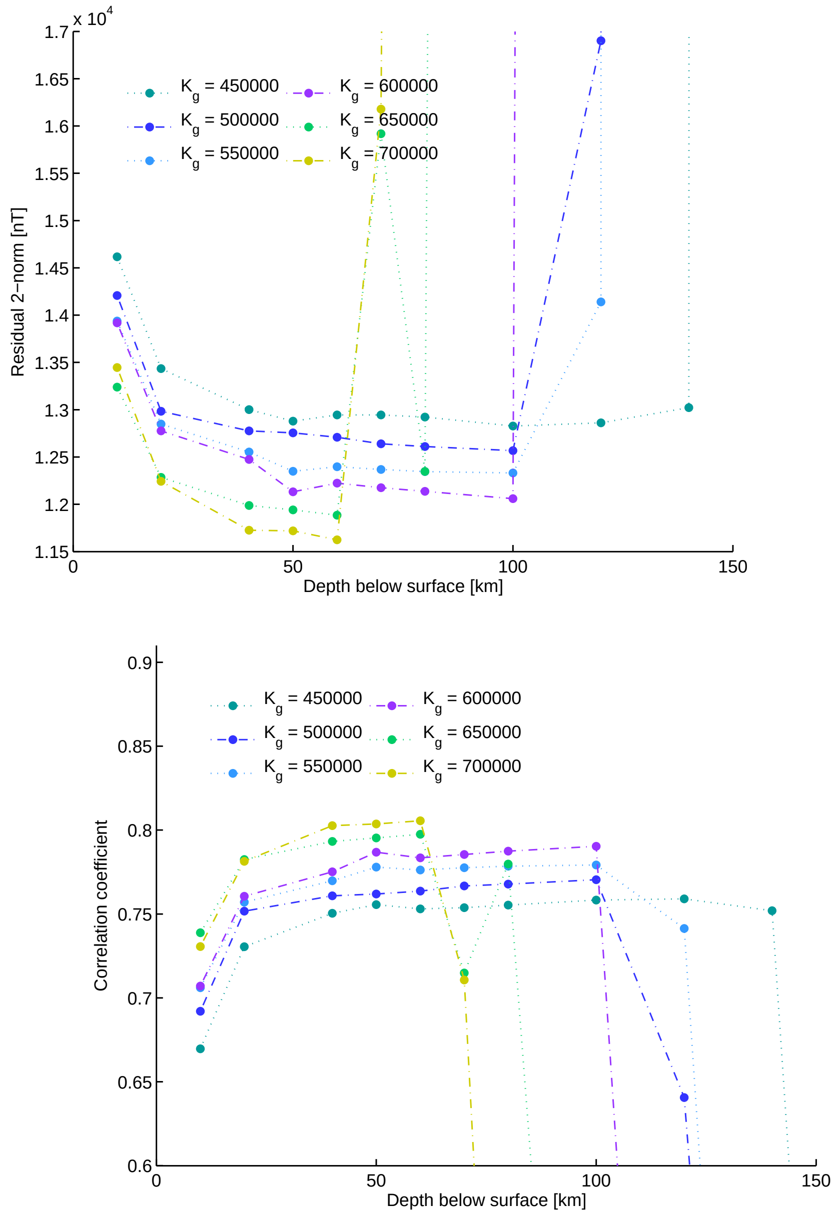

Figure 109 Residual 2-norm and correlation coefficient values for un-regularized equivalent source models using different source depth values and grid refinement levels. All models are based on every 30th magnetic intensity data point of NURE-NAMAM2008 for 110-100 deg longitude and 35-40 deg latitude.

G.2 Limited data amount for given source

For ideal inversion conditions, all data values are used to determine the amplitudes of the equivalent point sources. However, for the current combined inversion scheme, the used amount of measurements and sources exceeds the computational memory limit when generating $\underline{\underline{\mathbf{G}}}^T\underline{\underline{\mathbf{W}}}\underline{\underline{\mathbf{G}}}$ and $\underline{\underline{\mathbf{G}}}^T\underline{\underline{\mathbf{W}}}\mathbf{d}$. In order to solve this problem, only data in a certain area around a given source are used for the combined inversion scheme. The size of this area differs for the two data sets and is defined using an analytical test which investigates the decay of the Green's matrix components for increasing distances between a data-source pair. Using a random source location of 39.71°N and 94.03°W (which is within the NURE-NAMAM2008 data area) a source depth of 180 km and a data altitude of 360 km, the radial component of the Green's matrix $\underline{\underline{\mathbf{G}}}^r$ reaches 1% of its maximal value at a source-data distance of 31° (for constant longitude values) and 40° (for constant latitude values). The corresponding results for the near-surface data, using a source depth of 60 km and a data altitude of 1000 ft above mean sea level, are 3° and 4° ($\underline{\underline{\mathbf{G}}}^r$), 10° and 4° ($\underline{\underline{\mathbf{G}}}^\theta$) and and 14° ($\underline{\underline{\mathbf{G}}}^\phi$), respectively. Table 24 and Figs. 110 and 111 summarize the derived results. The amount of decay for $\underline{\underline{\mathbf{G}}}^{sca}$ is location dependent, but similar to $\underline{\underline{\mathbf{G}}}^r$ for latitudes like the NURE-NAMAM2008 data set.

Based on the above test, the combined inversion scheme uses satellite measurements which have a maximal distance (in both latitude and longitude) of 40°, and NURE-NAMAM2008 data up to 15° degrees latitudinal and longitudinal distance to a given source. This is probably not the most elegant method to circumvent the problem, but the resulting models are able to fulfill the objective of chapter 5: demonstrating that the equivalent point source routine can be used for combined global and regional data inversions.

	CHAMP		**NURE-NAMAM2008**	
	const. ϕ	const. θ	const. ϕ	const. θ
G_r	31	40	3	4
G_θ	74	171	10	4
G_ϕ	-	93	-	14

Table 24 Source distances [in degrees] corresponding to 1% of the absolute maximal value for G_r, G_θ and G_ϕ.

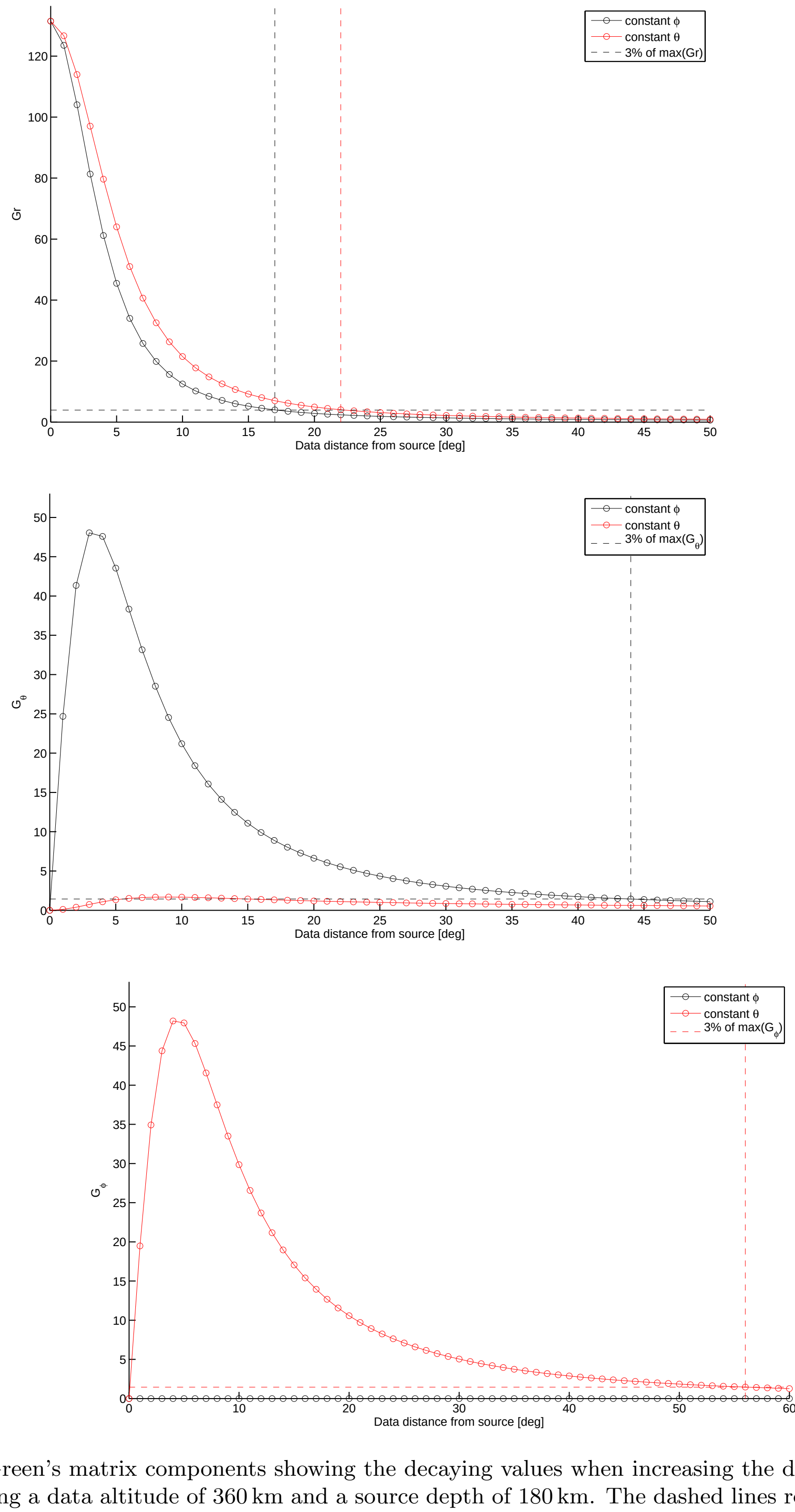

Figure 110 Green's matrix components showing the decaying values when increasing the distance between a data-source pair using a data altitude of 360 km and a source depth of 180 km. The dashed lines represent the 3% limit of the absolute maximum values.

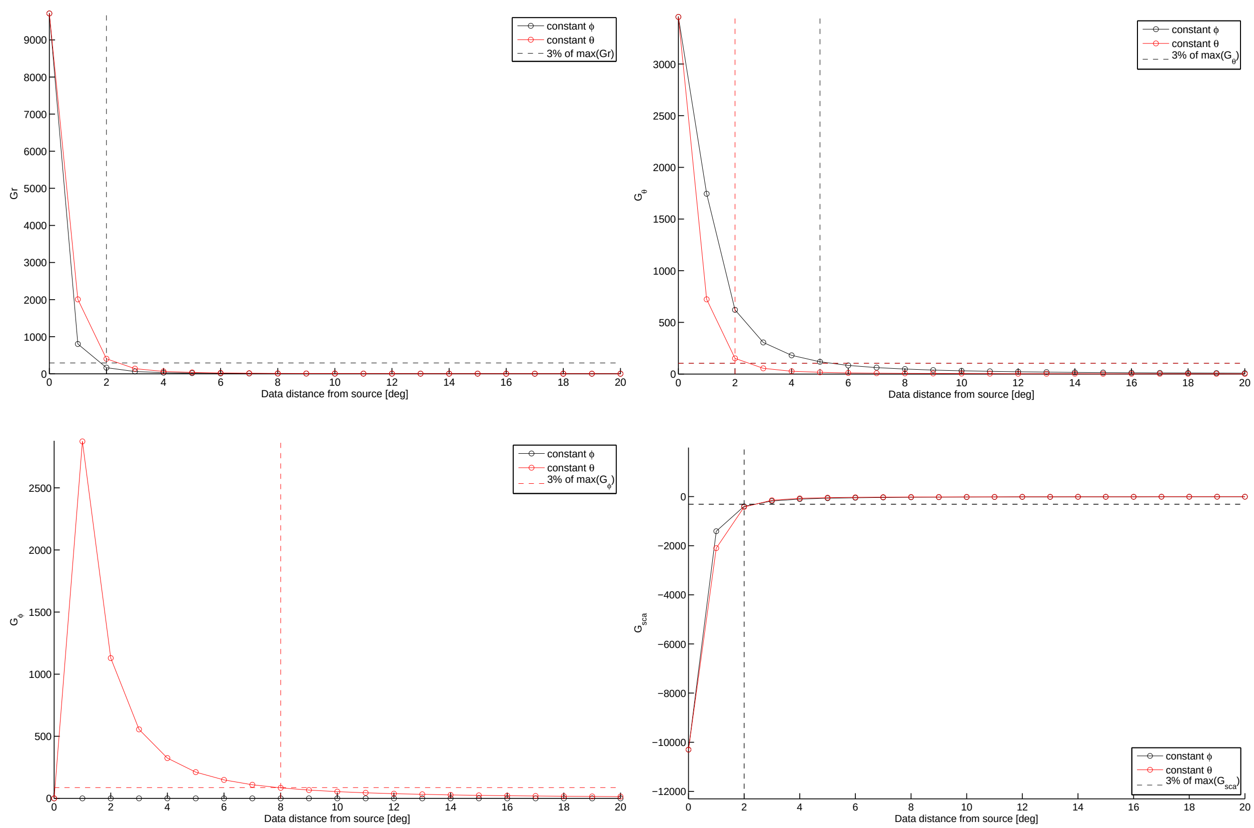

Figure 111 Green's matrix components showing the decaying values when increasing the distance between a data-source pair using a data altitude of 1000 ft a.m.s.l. and a source depth of 60 km. The dashed lines represent the 3% limit of the absolute maximum values.

H List of publications

- **Published:** An equivalent source method for modelling the global lithospheric magnetic field
- **In review process:** LCS-1: A high-resolution global model of the lithospheric magnetic field derived from CHAMP and Swarm satellite observations

Geophysical Journal International

Geophys. J. Int. (2015) **203,** 553–566 doi: 10.1093/gji/ggv317

GJI Geomagnetism, rock magnetism and palaeomagnetism

An equivalent source method for modelling the global lithospheric magnetic field

Livia Kother, Magnus D. Hammer, Christopher C. Finlay and Nils Olsen

Division of Geomagnetism, Technical University of Denmark - DTU Space, Kgs. Lyngby, Denmark. E-mail: livia@space.dtu.dk

Accepted 2015 July 27. Received 2015 July 23; in original form 2015 February 24

SUMMARY

We present a new technique for modelling the global lithospheric magnetic field at Earth's surface based on the estimation of equivalent potential field sources. As a demonstration we show an application to magnetic field measurements made by the CHAMP satellite during the period 2009–2010 when it was at its lowest altitude and solar activity was quiet. All three components of the vector field data are utilized at all available latitudes. Estimates of core and large-scale magnetospheric sources are removed from the measurements using the CHAOS-4 model. Quiet-time and night-side data selection criteria are also employed to minimize the influence of the ionospheric field. The model for the remaining lithospheric magnetic field consists of magnetic equivalent potential field sources (monopoles) arranged in an icosahedron grid at a depth of 100 km below the surface. The corresponding model parameters are estimated using an iteratively reweighted least-squares algorithm that includes model regularization (either quadratic or maximum entropy) and Huber weighting. Data error covariance matrices are implemented, accounting for the dependence of data variances on quasi-dipole latitude. The resulting equivalent source lithospheric field models show a degree correlation to MF7 greater than 0.7 out to spherical harmonic degree 100. Compared to the quadratic regularization approach, the entropy regularized model possesses notably lower power above degree 70 and a lower number of degrees of freedom despite fitting the observations to a very similar level. Advantages of our equivalent source method include its local nature, the possibility for regional grid refinement and the production of local power spectra, the ability to implement constraints and regularization depending on geographical position, and the ease of transforming the equivalent source values into spherical harmonics.

Key words: Inverse theory; Magnetic anomalies: modelling and interpretation; Magnetic field; Satellite magnetics.

1 INTRODUCTION

The magnetic investigation of the lithosphere, covering the Earth's crust and upper mantle, is of great importance for many aspects of Earth science, for example, plate tectonics (Molnar 1988), ocean ridge spreading, lithospheric thickness (Langel 1998) and historical meteorite impacts (Plado *et al.* 2000). Since the era of space missions, lithospheric magnetic field modelling techniques are also applicable to the investigation of other objects of our solar system, including Mars, Mercury and the Moon (Ness 1979; Connerney *et al.* 1999; Langlais *et al.* 2004; Whaler & Purucker 2005; Purucker & Nicholas 2010). Furthermore, lithospheric field maps play a significant role in the orientation of subsurface drilling devices (Inglis 1987).

In a source-free region, the geomagnetic field potential may be represented by harmonic functions, which are solutions of the Laplace equation. The most widely used functions for global geomagnetic field modelling are spherical harmonics (SH). However, several studies (e.g. O'Brien & Parker 1994; Chambodut *et al.* 2005) have concluded that local lithospheric features may not be well represented by an SH representation since the corresponding model parameters are global basis functions that depend on the entire data set and its associated noise. When modelling the lithospheric magnetic field, local basis functions may arguably be more suitable, for instance (depleted) harmonic splines (Langel & Whaler 1996), wavelet functions (Maisinger *et al.* 2004; Mayer & Maier 2006), spherical triangle tessellations (Stockmann *et al.* 2009) and equivalent dipole sources (e.g. Covington 1993; Langlais *et al.* 2004). Another possibility is to use spectral, but domain-limited basis functions, for example spherical caps (Haines 1985; Thébault 2006, 2008) or spherical Slepians (Beggan *et al.* 2013). The current study builds on the method introduced by O'Brien & Parker (1994), applying equivalent monopole sources to represent the lithospheric field. Advantages of this method include its ease of application to data from various altitudes, the possibility to carry out both global and local modelling, as well as the ease of transformation into a spherical harmonic form (see Section 2.2). The latter is extremely useful for comparisons to state-of-the-art spherical harmonic models of the global lithospheric field such as the MF7 serial model (Maus *et al.* 2008; Maus 2010), the CHAOS-4 model (Olsen *et al.* 2014) and CM5 (Sabaka *et al.* 2015), the latest version in the Comprehensive Model series. The use of local basis functions has the further advantage that when data noise is concentrated in specific regions (e.g. the polar regions), only model parameters in the vicinity are affected, while all model parameters are adversely affected if global basis functions such as spherical harmonics are used.

In Section 2, we present our formulation of the equivalent source method. The technique is then applied to a test case involving CHAMP data from January 2009 to September 2010. CHAMP data are currently the basis for the best available model of the lithospheric field (Maus *et al.* 2008; Maus 2010; Lesur *et al.* 2013; Sabaka *et al.* 2015). The CHAMP data and their processing are described in Section 3. Our model estimation procedure, involving iteratively reweighted least-squares (IRLS; Constable 1988; Olsen 2002) is described in Section 4. The approach involves over-parameterizing the number of monopoles and applying model regularization to control the model complexity. Following Stockmann *et al.* (2009), we test both conventional quadratic regularization (QR) and maximum entropy regularization (ER) techniques (Gull & Skilling 1999; Jackson *et al.* 2007). The former derives models of minimal source amplitudes, while the maximum entropy regularization models are characterized by minimal complexity for a given misfit to the observations. Results and their discussion are presented in Section 5 and we conclude in Section 6 with some perspectives regarding future applications of the method.

2 MODELLING TECHNIQUE

We describe the geomagnetic field in a geocentric reference frame by the spherical coordinates $\mathbf{r} = (r, \theta, \phi)$, where r denotes the radial distance from the centre of the Earth, θ denotes the geocentric co-latitude and ϕ denotes the eastern longitude. Currents in the ionosphere are neglected and the quasi-stationary approximation is adopted, such that the magnetic vector field $\mathbf{B}$ above the Earth's surface is described by a scalar potential $\mathbf{B} = -\nabla\Phi(r, \theta, \phi)$ where $\nabla^2\Phi(r, \theta, \phi) = 0$. The solution of Laplace's equation can then be written as a spherical harmonic expansion. The corresponding solution for internal geomagnetic sources is usually expressed as

$$\Phi(\mathbf{r}) = a \sum_{n=0}^{\infty} \left(\frac{a}{r}\right)^{n+1} \sum_{m=0}^{n} \left[g_n^m \cos(m\phi) + h_n^m \sin(m\phi)\right] P_n^m(\cos\theta), \tag{1}$$

where $a = 6371.2$ km is the reference radius given by the mean radius of the Earth, $P_n^m(\cos\theta)$ are the Schmidt semi-normalized associated Legendre functions and $[g_n^m, h_n^m]$ are the time-dependent Gauss coefficients of order m and degree n (Blakely 1996).

In this study, we have removed estimates of the core field and large-scale magnetospheric sources derived from the CHAOS-4 model from the magnetic field observations, hence we are only concerned with the static lithospheric field component.

2.1 Equivalent source formulation

Having N measurement locations $\mathbf{r}_i = [r_i, \theta_i, \phi_i]$ (for $i = 1, \ldots, N$), the magnetic scalar potential can be modelled as a linear combination of K globally distributed equivalent potential field sources (monopoles) located at $\mathbf{s}_k = [r_k, \theta_k, \phi_k]$ and with source strength q_k (for $k = 1, \ldots, K$) measured in nT. Following O'Brien & Parker (1994) and Blakely (1996), the corresponding potential can be expressed as

$$\begin{aligned}\hat{\Phi}(\mathbf{r}_i) &= \sum_{k=1}^{K} q_k \frac{r_k^2}{r_{ik}} \\ &= \sum_{k=1}^{K} r_k q_k \sum_{n=0}^{\infty} \left(\frac{r_k}{r_i}\right)^{n+1} P_n(\cos\mu_{ik}), \qquad \text{with } K < N\end{aligned} \tag{2}$$

where $r_{ik} = |\mathbf{r}_i - \mathbf{s}_k|$ and μ_{ik} are the distance and angle between the position vectors of measurement i and source k, respectively,

$$\begin{aligned} r_{ik} &= \sqrt{r_i^2 + r_k^2 - 2 r_i r_k \cos(\mu_{ik})} \\ \cos(\mu_{ik}) &= \cos(\theta_i)\cos(\theta_k) + \sin(\theta_i)\sin(\theta_k)\cos(\phi_i - \phi_k).\end{aligned} \tag{3}$$

Applying the decomposition formula for $P_n(\cos\mu_{ik})$ to eq. (2) (Torge 2001) and employing Schmidt-semi-normalization of the surface spherical harmonics (Blakely 1996), the potential due to monopole sources is

$$\begin{aligned}\Phi(\mathbf{r}_i) &= \sum_{k=1}^{K} r_k q_k \sum_{n=0}^{\infty} \left(\frac{r_k}{r_i}\right)^{n+1} \\ &\quad \times \sum_{m=0}^{n} P_n^m(\cos\theta_i) P_n^m(\cos\theta_k)\cos(m\phi_i - m\phi_k).\end{aligned} \tag{4}$$

Comparing the spherical harmonic and equivalent source potential expansion (eqs 1 and 4, respectively) enables the conventional spherical harmonic Gauss coefficients to be obtained directly from the equivalent source coefficients q_k,

$$g_n^m = \sum_{k=1}^{K} \left(\frac{r_k}{a}\right)^{n+2} q_k P_n^m(\cos\theta_k)\cos(m\phi_k) \tag{5}$$

$$h_n^m = \sum_{k=1}^{K} \left(\frac{r_k}{a}\right)^{n+2} q_k P_n^m(\cos\theta_k)\sin(m\phi_k). \tag{6}$$

Note that eqs (5) and (6) provide a means of estimating a local power spectrum by considering the monopoles only within a region of interest, implicitly assuming those elsewhere are zero and renormalizing the power spectra accounting only for the area considered.

The Mauersberger–Lowes spherical harmonic power spectrum $R(n)$ due to internal sources, which is the squared magnitude of the magnetic field averaged over a spherical surface of radius r, is given by (Lowes 1974)

$$R(n) = (n+1)\left(\frac{a}{r}\right)^{(2n+4)} \sum_{m=0}^{n} \left[\left(g_n^m\right)^2 + \left(h_n^m\right)^2\right]. \tag{7}$$

All power spectrum illustrations below are given for $r = a$.

The comparison of two different lithospheric field models, with different sets of Gauss coefficients, $[g_n^m, h_n^m]$ and $[g_n^{'m}, h_n^{'m}]$, respectively, can be visualized using the degree correlation (Langel (1998), eq. 4.23)

$$\rho(n) = \frac{\sum_{m=0}^{n}\left(g_n^m g_n^{'m} + h_n^m h_n^{'m}\right)}{\sqrt{\sum_{m=0}^{n}\left[(g_n^m)^2 + (h_n^m)^2\right] \sum_{m=0}^{n}\left[\left(g_n^{'m}\right)^2 + \left(h_n^{'m}\right)^2\right]}}. \tag{8}$$

Whenever $\rho \geq 0.7$, models are usually considered to be well correlated (Arkani-Hamed *et al.* 1994; Sabaka & Olsen 2006). Compared to the power spectra representation, degree correlations give no information on the magnetic field magnitudes but rather on the respective phase differences (Olsen *et al.* 2006).

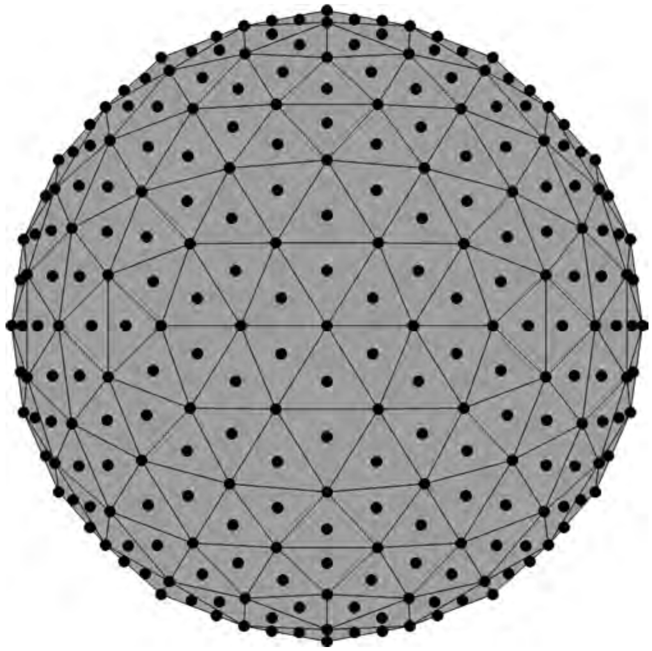

Figure 1. Icosahedron grid with refinement level $L = 2$. The corresponding sources are placed at the vertices and triangle midpoints. This study applies $L = 5$ corresponding to 30 722 source locations.

Another way of illustrating the model differences is by looking at the relative difference between each coefficient in a degree versus order matrix, $\underline{\underline{\mathbf{S}}}$. For the difference between g_n^m and $g_n^{\prime m}$ we have

$$S(n, m) = 100 \cdot \frac{g_n^m - g_n^{\prime m}}{\sqrt{\frac{1}{(2n+1)} \sum_{m=0}^{n} \left[\left(g_n^{\prime\prime m}\right)^2 + \left(h_n^{\prime\prime m}\right)^2 \right]}}, \quad (9)$$

and similarly for the corresponding h_n^m coefficients. The coefficient differences are normalized with respect to the mean spectral amplitude of a reference model, with $[g_n^{\prime\prime m}, h_n^{\prime\prime m}]$ being the corresponding Gauss coefficients (Olsen *et al.* 2005, eq. 5.3). Note that the factor 100 in eq. (9) indicates that the normalized coefficient differences are given in per cent.

We have chosen to use magnetic monopoles as equivalent sources due to their simplicity and mathematical convenience. Like dipoles, they are a solution to Laplace's equation and produce a potential field (e.g. Toyoshima *et al.* 2008). However, according to Maxwell's equations we have $\nabla \cdot \mathbf{B} = 0$, which means that individual monopoles do not exist. Here we use monopoles only as a mathematical tool for representing the lithospheric magnetic field models and impose an additional constraint (see Section 4.5) to ensure that the divergence-free constraint is satisfied.

2.2 Distribution of sources

In this study, we apply an icosahedral grid (Baumgardner & Frederickson 1985) with monopoles placed at both vertices and triangle midpoints. The corresponding grid size is defined by the source depth and grid refinement level L. A grid of refinement level $L = 0$ consists of 20 identical equilateral triangular faces and 12 vertices on a unit sphere. Each vertex is thereby surrounded by either five or six faces. Increasing the refinement level by 1, every face is further subdivided into four triangles, see Fig. 1. In this study, we use $L = 5$, consisting of $K = 30\,722$ locations at the vertices and midpoints, all projected on a sphere of radius $a - 100$ km so the distance between the satellite data and the monopoles is greater than the separation between the monopoles. We have chosen to include the centre points as a means of grid refinement without resorting to a higher refinement level, which would result in a large increase in the number of sources and hence the calculation time.

Table 1. Median angular distance and arc length between two adjacent sources for different icosahedron grid refinement levels L. The arc length is given at the Earth's surface. Both vertices and midpoints are taken into account in K.

L	K	Angular distance (deg)	Arc length (km)
3	1922	3.52	391
4	7683	1.75	195
5	30722	0.98	109
6	122882	0.49	54
7	491522	0.24	27

Table 1 lists the median angular separation between two adjacent sources for different grid refinement levels. The values are calculated from the average distance between sources and their five nearest neighbours. The applied grid refinement level corresponds to a median grid spacing of 0.98°, equivalent to an arc length of 109 km at the Earth's surface. Synthetic tests demonstrated that for the regularized models presented here, the surface field results were not affected by the equivalent source locations.

The chosen source depth of $a - 100$ km is based on a synthetic test where the magnetic field signatures at Earth's surface produced by monopoles with a horizontal spacing of 1° (very close to the applied angular distance of 0.98°) were found to be negligible.

3 DATA, PRE-PROCESSING AND ERROR BUDGET

CHAMP 30 s three-component vector field data between 2009 January 1 and 2010 September 2 are used in this study. During that period the satellite was at its lowest altitude (below 300 km) and solar activity was also rather quiet, making the data particularly suitable for lithospheric magnetic field studies. Estimates of core and large-scale magnetospheric sources are removed from the measurements using the geomagnetic field model CHAOS-4, and we use the same data selection as employed in CHAOS-4 (Olsen *et al.* 2006, 2014). Important to mention here are the quiet-time conditions (Kp-index $\leq 2^0$ for quasi-dipole (QD) latitudes equatorward of ±55° and the merging electric field at the magnetopause $E_m \leq 0.8$ mV m^{-1} for QD latitudes poleward of ±55°) and dark region data (sun at least 10° below the horizon) selection criteria, which aim to minimize the influence of the ionospheric field. Further, the contribution from disturbances of the magnetospheric ring current is minimized by only selecting data with hourly RC-index variations smaller than 2 nT hr^{-1} (Olsen *et al.* 2014).

Our implementation of IRLS assumes independent and Huber distributed (i.e. Gaussian distributed in the centre, Laplacian distributed in the tails) residuals. We additionally remove gross outliers with absolute residual values >100 nT from the data set in an effort to avoid mapping strongly correlated noise from badly disturbed tracks into the lithospheric magnetic field models.

Regarding the data error budget, we implement data uncertainties depending on the QD latitude (Richmond 1995; Emmert *et al.* 2010) independently for the three vector field components, B_r, B_θ and B_ϕ, as shown in Fig. 2. The uncertainties (standard deviations) $\boldsymbol{\sigma}_p$ (where $p = r$, θ or ϕ) are derived using the robust algorithm of Driessen & Rombouts (2007) applied to residuals (obtained by subtracting from the data predictions from the CHAOS-4 model,

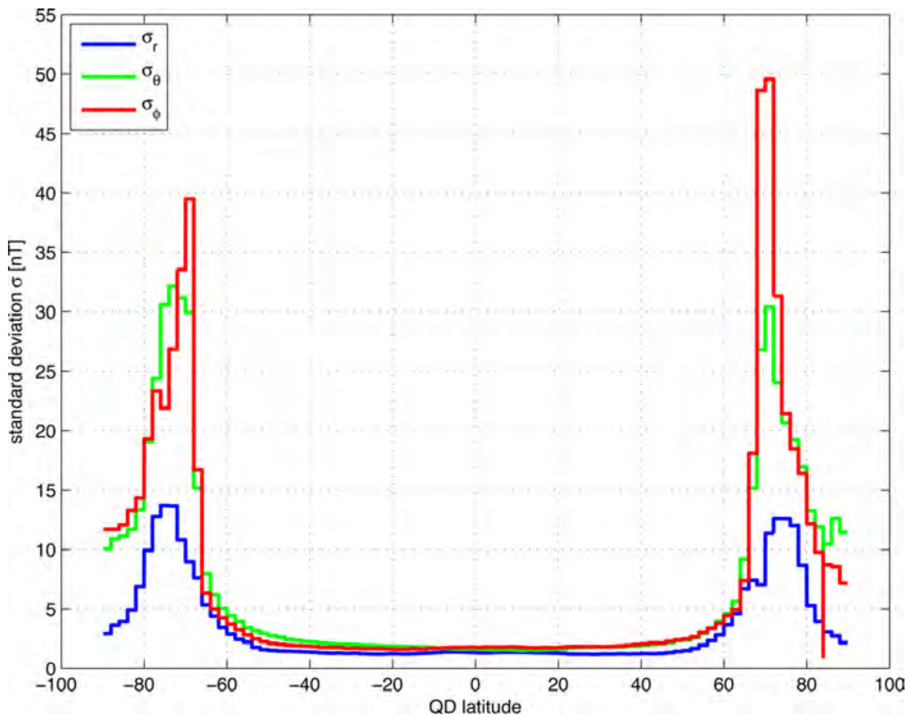

Figure 2. Latitude-dependent standard deviation values $\boldsymbol{\sigma}_p$ (where $p = r, \theta$ or ϕ). Values are derived for each QD latitude band of 2° (the Northern Hemisphere is indicated by positive QD latitude values) using the robust procedure of Driessen & Rombouts (2007).

including its core, crustal and external parts) in 2° latitudinal bands. The QD coordinate system is suitable for describing processes due to unmodelled ionospheric sources, which we assume dominate the residuals, especially at polar latitudes.

The CHAMP satellite tracks are defined by a near polar orbit with an inclination of 87.3°. Thus, there are no data within 2.7° of the poles, which introduces instabilities in the determination of high degree spherical harmonic zonal coefficients. In order to counteract this 'polar gap' effect, 12 257 synthetic (noise-free) values of the radial field component are added in the polar regions between ±0.5° and 4° at 300 km altitude derived from the CHAOS-4l model up to SH degree $n = 60$. The synthetic data represent 2.89 per cent of the total data set. Except for the polar gap regions, we use all three measurement components in the model derivation. We have also carried out tests without adding synthetic data in the polar gap and find very similar results at non-polar gap locations, see Section 5. This illustrates one advantage of the local nature of our equivalent source method.

4 MODEL ESTIMATION

In this section, we describe our scheme for estimating equivalent source models of the lithospheric field from satellite data. Based on a regularized IRLS approach, the scheme involves iteratively minimizing a penalty function measuring both the misfit to the observations and also the complexity of the model.

In Section 4.1, we present our mathematical formulation of the inverse problem. The IRLS numerical scheme used to obtain solutions is set out in Section 4.2. Section 4.3 gives the details in the case that model complexity is measured using a traditional quadratic norm, and Section 4.4 gives the corresponding details when an entropy-based measure of model complexity is instead employed. The method of enforcing the divergence-free condition, a necessary feature of any scheme based on monopoles, is described in Section 4.5. The diagnostic measures of model resolution we employ are given in Section 4.6, and finally a short summary of our lithospheric field model estimation scheme is given in Section 4.7.

4.1 Formulation of the inverse problem

The magnetic field **B** due to the equivalent monopole sources measured at a given location i is calculated using the negative gradient of eq. (2),

$$\mathbf{B}(\mathbf{r}_i) = -\nabla\hat{\Phi}(\mathbf{r}_i) = -\sum_{k=1}^{K} q_k \nabla \frac{r_k^2}{r_{ik}}. \tag{10}$$

The data for a particular field component p, where p can be r, θ, or ϕ, is the projection of **B** onto the direction given by the unit vector $\hat{\mathbf{e}}_p$,

$$B_{i,p} = -\sum_{k=1}^{K} q_k \left[\hat{\mathbf{e}}_{i,p} \cdot \nabla_p \frac{r_k^2}{r_{ik}}\right] = \sum_{k=1}^{K} q_k g_{ik,p}, \tag{11}$$

where $g_{ik,p}$ are the individual elements of the Green's matrix representing the directional derivatives of the kth source evaluated in the direction p and at the location $\mathbf{r}_i$.[1] The corresponding full expressions are given in the Appendix.

[1] The Green's matrix elements for equivalent sources are derived in O'Brien & Parker (1994). However, it appears that the corresponding eqs (C2) and (C3) contain a typographical error. In formula (C3) we have changed the signs in front of rs to be negative. In eq. (C2), the formulae for $B_\theta(\mathbf{r})$ and $B_\phi(\mathbf{r})$ have been multiplied by -2 and 2, respectively. In the formula of $B_r(\mathbf{r})$, the factor 2 was removed both in the numerator and denominator.

Applying the above scheme to all measurements, the forward problem described by eq. (11) may be written as

$$\mathbf{B} = \underline{\underline{\mathbf{G}}}\mathbf{q} \tag{12}$$

where $\mathbf{B} = [\mathbf{B}_r, \mathbf{B}_\theta, \mathbf{B}_\phi]$ is a column vector containing model predictions for all $3N$ vector components at the N locations of magnetic field measurements, $\underline{\underline{\mathbf{G}}} = [\underline{\underline{\mathbf{G}}}_r, \underline{\underline{\mathbf{G}}}_\theta, \underline{\underline{\mathbf{G}}}_\phi]$ represents the corresponding $3N \times K$ Green's matrix and $\mathbf{q}$ is the model vector of all K source strengths q_k.

The inverse problem then consists of finding a model $\mathbf{q}$ that minimizes the error vector $\mathbf{e}$ between the observed data $\mathbf{d}$ and the model predictions $\mathbf{B}$,

$$\begin{aligned}\mathbf{d} &= \mathbf{B} + \mathbf{e}\\ &= \underline{\underline{\mathbf{G}}}\mathbf{q} + \mathbf{e}\end{aligned} \tag{13}$$

4.2 Regularized IRLS solution

Determination of the lithospheric field at Earth's surface from noisy data collected at satellite altitude is an ill-posed and non-unique inverse problem. We find solutions to this problem using an IRLS algorithm (e.g. Walker & Jackson 2000) including model regularization. This involves minimizing both the differences between model predictions and measurements (a misfit norm) and also a measure of the model complexity $\mathbf{R}$ (regularization norm). The objective function Θ we minimize is of the form

$$\Theta(\mathbf{q}) = (\mathbf{d} - \underline{\underline{\mathbf{G}}}\mathbf{q})^T \underline{\underline{\mathbf{W}}}(\mathbf{d} - \underline{\underline{\mathbf{G}}}\mathbf{q}) + \lambda\mathbf{R}(\mathbf{q}) \tag{14}$$

where

$$\underline{\underline{\mathbf{W}}} = \underline{\underline{\mathbf{C}}}^{-1/2}\underline{\underline{\mathbf{H}}}\,\underline{\underline{\mathbf{C}}}^{-1/2}. \tag{15}$$

The data weight matrix $\underline{\underline{\mathbf{W}}}$ consists of two parts: (i) a diagonal inverse data error covariance matrix $\underline{\underline{\mathbf{C}}}^{-1} = \frac{\sin\theta}{\sigma^2}$ that accounts for the expected data error variances σ^2 (see Section 3) and provides equal area weighting; (ii) a Huber weighting matrix $\underline{\underline{\mathbf{H}}}$ that depends on the residuals between the model predictions and the observations (e.g. Constable 1988). The regularization parameter λ (nT^{-2}) quantifies the trade-off between the misfit and regularization norm (e.g. Menke 2012). Large λ values result in models of low complexity but with large residuals, while the opposite is the case for small λ values.

A Newton-type iterative scheme is used to minimize the objective function of eq. (14), such that the model prediction at the $j+1$ iteration is given by

$$\begin{aligned}\mathbf{q}_{j+1} = {}& (2\underline{\underline{\mathbf{G}}}^T\underline{\underline{\mathbf{W}}}_j\underline{\underline{\mathbf{G}}} + \lambda\nabla\nabla\mathbf{R}(\mathbf{q}_j))^{-1}\\ &\times (2\underline{\underline{\mathbf{G}}}^T\underline{\underline{\mathbf{W}}}_j\mathbf{d} + \lambda\nabla\nabla\mathbf{R}(\mathbf{q}_j)\mathbf{q}_j - \lambda\nabla\mathbf{R}(\mathbf{q}_j)).\end{aligned} \tag{16}$$

A new solution is thus derived from the model $\mathbf{q}_j$ and the Huber weights $\underline{\underline{\mathbf{H}}}_j$ (that appear in $\underline{\underline{\mathbf{W}}}_j$) from the previous iteration. We iterate eq. (16) until the convergence criterion $\|\mathbf{q}_j - \mathbf{q}_{j+1}\|/\|\mathbf{q}_{j+1}\| <$ 0.01 is met.

The Huber weights in the diagonal matrix $\underline{\underline{\mathbf{H}}}_j = [\mathbf{h}_{r,j}, \mathbf{h}_{\theta,j}, \mathbf{h}_{\phi,j}]$ (e.g. Huber 1964; Constable 1988) are obtained from the residuals $\mathbf{e}_{p,j}$ from the jth iteration, with $p = r$, θ or ϕ, normalized by the expected latitude-dependent standard deviation values σ_p from Fig. 2. Considering the ith vector field observation, the Huber weight for a given component p is

$$h_{p,j}(i) = \begin{cases} 1 & \text{if } \epsilon_{p,j}(i) \le 1.5,\\ 1.5/\epsilon_{p,j}(i) & \text{if } \epsilon_{p,j}(i) > 1.5\end{cases} \tag{17}$$

where

$$\boldsymbol{\epsilon}_{p,j} = |\mathbf{e}_{p,j}/\boldsymbol{\sigma}_p|. \tag{18}$$

This results in residuals much larger than expected being downweighted in the least-squares scheme. The changes in $\boldsymbol{\epsilon}_{p,j}$ with iteration j are due to changes in the model misfit $\mathbf{e}_{p,j}$, and not to changes in $\boldsymbol{\sigma}_p$.

4.3 Quadratic regularization

We consider a very simple form of quadratic regularization, defined by the Euclidean length of the model solution, $\mathbf{R}^{\mathrm{QR}}(\mathbf{q}) = \mathbf{q}^T\mathbf{q}$. Minimizing the objective function with respect to $\mathbf{q}$ then results in the following simplified version of eq. (16)

$$\mathbf{q}^{\mathrm{QR}}_{j+1} = (\underline{\underline{\mathbf{G}}}^T\underline{\underline{\mathbf{W}}}_j\underline{\underline{\mathbf{G}}} + \lambda\mathbf{I})^{-1}\underline{\underline{\mathbf{G}}}^T\underline{\underline{\mathbf{W}}}_j\mathbf{d}. \tag{19}$$

The corresponding solution has the smallest possible sum of squares of the monopole values, for a chosen level of misfit. This criterion, however, may not always be geologically useful, in particular because there are several very large amplitude local magnetic field anomalies, for example, the West African Craton anomaly and the Bangui anomaly. Allowing a model to possess high amplitude local anomalies, while at the same time retaining a simple morphology, is possible by regularizing the model entropy rather than its squared amplitude. This is the subject of the next section. The investigated quadratic regularization models, with their different λ values, share the same starting point, a well-converged, but unregularized ($\lambda = 0$), solution.

4.4 Maximum entropy regularization

In order to account for the large amplitudes of local lithospheric field anomalies, we investigate the effect of regularizing the model information complexity rather than its amplitude. The entropy regularization method applied here was previously described in detail by Jackson *et al.* (2007) and Stockmann *et al.* (2009). We note that maximum entropy regularization is naturally implemented in the physical domain, rather than in spectral model space; it can therefore be very easily implemented by considering the entropy of different arrangements of the equivalent sources.

Gull & Skilling (1999) define the entropy S of a model $\mathbf{q}$, which can consist of both negative and positive values, as

$$S(\mathbf{q}, \omega) = \sum_{k=1}^{K}\left[\psi_k - 2\omega - q_k \ln\left(\frac{\psi_k + q_k}{2\omega}\right)\right]. \tag{20}$$

We work with the related negative entropy (negentropy) regularization norm (Gillet *et al.* 2007)

$$\mathbf{R}^{\mathrm{ER}}(\mathbf{q}, \omega) = -4\omega S(\mathbf{q}, \omega) \tag{21}$$

with ω being a default parameter which defines the scale of the entropy function (Maisinger *et al.* 2004) and $\psi_k = \sqrt{q_k^2 + 4\omega^2}$. The negentropy $\mathbf{R}^{\mathrm{ER}}$ becomes identical to the quadratic norm for large values of ω, thus making comparisons between the two regularization methods possible. Using $\mathbf{R}^{\mathrm{ER}}(\mathbf{q}, \omega)$ as the regularization norm, eq. (16) becomes

$$\mathbf{q}^{\mathrm{ER}}_{j+1} = (2\underline{\underline{\mathbf{G}}}^T\underline{\underline{\mathbf{W}}}_j\underline{\underline{\mathbf{G}}} + \lambda\boldsymbol{\alpha}_j)^{-1}\left(2\underline{\underline{\mathbf{G}}}^T\underline{\underline{\mathbf{W}}}_j\mathbf{d} + \lambda\boldsymbol{\alpha}_j\mathbf{q}^{\mathrm{ER}}_j - 4\lambda\omega\boldsymbol{\beta}_j\right) \tag{22}$$

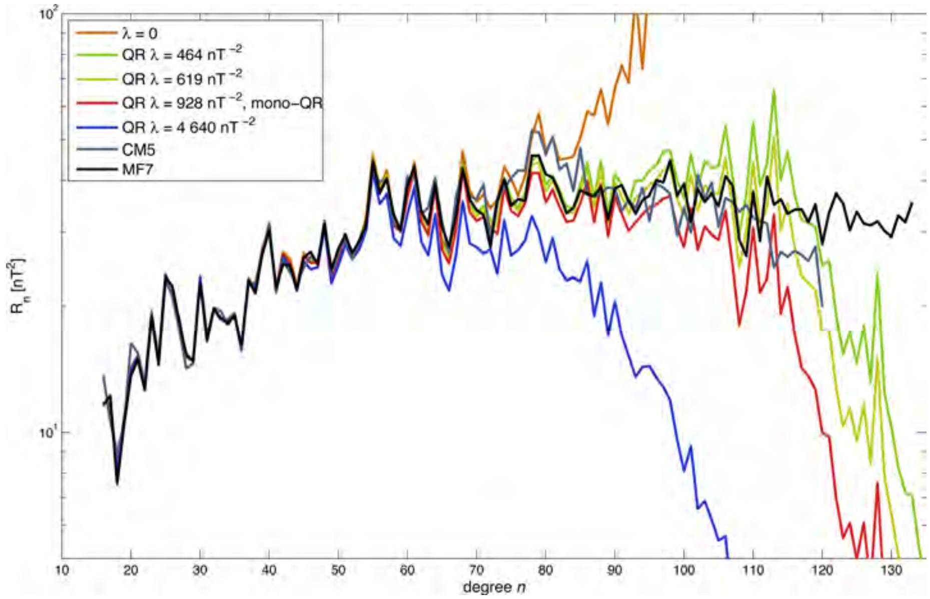

Figure 3. Power spectra for the investigated quadratically regularized (QR) models with different regularization parameters λ, compared to some recent lithospheric field models (CM5: Sabaka *et al.* (2015) and MF7: Maus *et al.* (2008); Maus (2010)). The model with $\lambda = 928\,\mathrm{nT}^{-2}$, represented by the red line, is chosen as our preferred model mono-QR. The corresponding lithospheric radial magnetic field at the Earth's surface is illustrated in the upper part of Fig. 4.

with

$$\boldsymbol{\alpha}_j = \mathrm{diag}\left(\frac{4\omega}{\psi_{1,j}}, \frac{4\omega}{\psi_{2,j}}, \ldots, \frac{4\omega}{\psi_{K,j}}\right)$$

$$\boldsymbol{\beta}_j = \left(ln\left(\frac{\psi_{1,j}+q_{1,j}}{2\omega}\right), ln\left(\frac{\psi_{2,j}+q_{2,j}}{2\omega}\right), \ldots, ln\left(\frac{\psi_{K,j}+q_{K,j}}{2\omega}\right)\right). \tag{23}$$

Converged quadratic regularization models with the same λ were used as the starting conditions for the investigated maximum entropy models.

4.5 Enforcing the divergence-free condition

Since isolated magnetic monopoles do not exist ($\nabla \cdot \mathbf{B} = 0$), we must also enforce an additional condition that ensures zero net magnetic flux (O'Brien & Parker 1994)

$$\sum_{k=1}^{K} q_k = 0. \tag{24}$$

This requirement can be implemented using a Lagrangian method by applying the following scheme (Sabaka, private communication, 2011):

$$\mathbf{q}^c_{j+1} = \mathbf{q}^* - \mathbf{AL}(\mathbf{L}^T\mathbf{q}^*)(\mathbf{L}^T\mathbf{AL})^{-1}$$
$$\mathbf{A} = (\underline{\underline{\mathbf{G}}}^T \underline{\underline{\mathbf{W}}}_j \underline{\underline{\mathbf{G}}} + \lambda\underline{\underline{\mathbf{I}}})^{-1}, \tag{25}$$

where $\mathbf{L}$ is a $1 \times K$ unity row vector and $\mathbf{q}^*$ now represents either a quadratic ($\mathbf{q}^{\mathrm{QR}}_{j+1}$) or maximum entropy ($\mathbf{q}^{\mathrm{ER}}_{j+1}$) unconstrained model solution from eqs (19) and (22).

4.6 Model resolution and number of degrees of freedom

An important method of quantitatively assessing inversion results is to compute the model resolution matrix $\underline{\underline{\mathcal{R}}}$. This represents the mapping between the estimated and true model parameters. For a quadratic regularization, $\underline{\underline{\mathcal{R}}}$ takes the form (e.g. Bloxham *et al.* 1989; Menke 2012)

$$\underline{\underline{\mathcal{R}}}^{\mathrm{QR}} = (\underline{\underline{\mathbf{G}}}^T \underline{\underline{\mathbf{WG}}} + \lambda\mathbf{I})^{-1} \underline{\underline{\mathbf{G}}}^T \underline{\underline{\mathbf{WG}}}. \tag{26}$$

The corresponding linearized approximation for the maximum entropy approach is

$$\underline{\underline{\mathcal{R}}}^{\mathrm{ER}} = (2\underline{\underline{\mathbf{G}}}^T \underline{\underline{\mathbf{WG}}} + \lambda\boldsymbol{\alpha})^{-1} 2\underline{\underline{\mathbf{G}}}^T \underline{\underline{\mathbf{WG}}}. \tag{27}$$

A comparison and assessment of the achieved resolution of two regularized models can thereby be performed. In particular, the effective number of degrees of freedom may be obtained from the trace of the respective resolution matrices.

4.7 Summary of model estimation scheme

For convenient reference, we summarize here our model estimation scheme:

(i) **Inputs:**
$\mathbf{d}$: the observed vector field magnetic data.
$\boldsymbol{\sigma}_p$: *a priori* standard deviations for the data errors (latitude-dependent for each field component).
λ: the regularization parameter, and ω the entropy default parameter for ER models.
$\underline{\underline{\mathbf{G}}}$: the Green's matrix connecting the data to the model parameters.

(ii) **Initial conditions**
Unregularized model ($\lambda = 0$): starts from unity Huber weights and model values $\mathbf{q}$ all set to zero.
QR models: start from converged $\lambda = 0$ model and corresponding Huber weights.
ER models: start from converged QR model with same λ and corresponding Huber weights.

(iii) **Iteration step: model $\mathbf{q}_{j+1}$ from model $\mathbf{q}_j$ and its associated Huber weights**
Unregularized model: iterate eq. (19) with $\lambda = 0$.
QR models: iterate eq. (19), with given and fixed λ.
ER models: iterate eq. (22), with given and fixed λ and ω.

Table 2. Normalized (by latitude-dependent standard deviation values) and un-normalized Huber-weighted RMS model residual values between the CHAMP observations and the models MF7 ($n_{\max} = 133$), CM5 ($n_{\max} = 120$), CHAOS-4 ($n_{\max} = 100$), and a selection of QR models and ER models at satellite altitude. The results for models mono-QR and mono-ER are highlighted in bold. Here we define $\Delta B = \sqrt{\Delta B_r^2 + \Delta B_\theta^2 + \Delta B_\phi^2}$. The suffixes 'polar' and 'non-polar' represent data of absolute QD latitudes $>55°$ and $<55°$, respectively.

	MF7	CM5	CHAOS-4	QR models				ER models	
$\lambda(nT^{-2}) =$	–	–	–	4640	928	619	464	928	4640
$\omega(nT) =$	–	–	–	–	–	–	–	55×10^{-4}	25×10^{-4}
Normalized									
RMS ΔB_r (–)	1.31	1.34	1.30	1.29	**1.29**	1.29	1.29	1.29	**1.29**
RMS ΔB_r polar (–)	1.43	1.45	1.43	1.43	**1.43**	1.43	1.43	1.43	**1.43**
RMS ΔB_r non-polar (–)	1.22	1.26	1.21	1.18	**1.18**	1.18	1.18	1.18	**1.18**
RMS ΔB_θ (–)	1.26	1.27	1.26	1.26	**1.26**	1.26	1.26	1.26	**1.26**
RMS ΔB_θ polar (–)	1.38	1.39	1.38	1.38	**1.38**	1.38	1.38	1.38	**1.38**
RMS ΔB_θ non-polar (–)	1.17	1.19	1.17	1.18	**1.17**	1.17	1.17	1.17	**1.18**
RMS ΔB_ϕ (–)	1.28	1.29	1.27	1.27	**1.27**	1.27	1.27	1.27	**1.27**
RMS ΔB_ϕ polar (–)	1.43	1.43	1.43	1.42	**1.42**	1.42	1.42	1.42	**1.42**
RMS ΔB_ϕ non-polar (–)	1.17	1.18	1.16	1.16	**1.16**	1.16	1.16	1.16	**1.16**
RMS ΔB (–)	1.28	1.30	1.28	1.27	**1.27**	1.27	1.27	1.27	**1.27**
RMS ΔB polar (–)	1.41	1.42	1.41	1.41	**1.41**	1.41	1.41	1.41	**1.41**
RMS ΔB non-polar (–)	1.19	1.21	1.18	1.17	**1.17**	1.17	1.17	1.17	**1.17**
Un-normalized									
RMS ΔB_r (nT)	7.41	7.44	7.39	7.41	**7.40**	7.40	7.40	7.40	**7.41**
RMS ΔB_r polar (nT)	11.43	11.44	11.41	11.45	**11.44**	11.44	11.44	11.44	**11.45**
RMS ΔB_r non-polar (nT)	1.66	1.71	1.64	1.61	**1.61**	1.60	1.60	1.60	**1.61**
RMS ΔB_θ (nT)	15.81	15.84	15.81	15.81	**15.81**	15.81	15.81	15.81	**15.81**
RMS ΔB_θ polar (nT)	24.52	24.56	24.52	24.51	**24.51**	24.51	24.51	24.51	**24.51**
RMS ΔB_θ non-polar (nT)	2.40	2.42	2.40	2.40	**2.40**	2.40	2.40	2.40	**2.40**
RMS ΔB_ϕ (nT)	17.29	17.29	17.28	17.26	**17.25**	17.25	17.25	17.25	**17.26**
RMS ΔB_ϕ polar (nT)	26.91	26.88	26.90	26.86	**26.86**	26.86	26.86	26.86	**26.86**
RMS ΔB_ϕ non-polar (nT)	2.25	2.27	2.23	2.23	**2.23**	2.23	2.23	2.23	**2.23**
RMS ΔB (nT)	14.19	14.21	14.18	14.17	**14.17**	14.17	14.17	14.17	**14.17**
RMS ΔB polar (nT)	22.05	22.06	22.04	22.02	**22.02**	22.02	22.02	22.02	**22.02**
RMS ΔB non-polar (nT)	2.13	2.16	2.12	2.11	**2.11**	2.11	2.11	2.11	**2.11**

Table 3. Similar to Table 2 but with statistics for only part of the African continent (area of the inserted plot in the left part of Fig. 10). The preferred models mono-QR and mono-ER are highlighted in bold. $\Delta B = \sqrt{\Delta B_r^2 + \Delta B_\theta^2 + \Delta B_\phi^2}$.

	MF7	CM5	CHAOS-4	QR models				ER models	
$\lambda(nT^{-2}) =$	–	–	–	4640	928	619	464	928	4640
$\omega(nT) =$	–	–	–	–	–	–	–	55×10^{-4}	25×10^{-4}
Normalized									
RMS ΔB_r (–)	4.05	4.29	4.07	1.20	**1.20**	1.20	1.20	1.20	**1.20**
RMS ΔB_θ (–)	2.10	2.21	2.11	1.11	**1.11**	1.11	1.11	1.11	**1.11**
RMS ΔB_ϕ (–)	2.52	2.57	2.47	1.15	**1.15**	1.15	1.15	1.15	**1.15**
RMS ΔB (–)	2.85	2.97	2.84	1.15	**1.15**	1.15	1.15	1.15	**1.15**
Un-normalized									
RMS ΔB_r (nT)	5.32	5.62	5.35	1.57	**1.57**	1.57	1.57	1.57	**1.57**
RMS ΔB_θ (nT)	3.76	3.95	3.79	2.01	**2.01**	2.01	2.01	2.01	**2.01**
RMS ΔB_ϕ (nT)	4.39	4.48	4.31	2.01	**2.01**	2.01	2.01	2.01	**2.01**
RMS ΔB (nT)	4.42	4.60	4.41	1.88	**1.87**	1.87	1.87	1.87	**1.88**

(iv) **Implement divergence free condition via eq. (25)**
(v) **Test convergence criterion**

$$\|\mathbf{q}_j - \mathbf{q}_{j+1}\| / \|\mathbf{q}_{j+1}\| \times \begin{cases} > 0.01 & \text{return to (iii) and start next iteration,} \\ < 0.01 & \mathbf{q}_{j+1} \text{ is the converged model solution. END.} \end{cases}$$

5 RESULTS AND DISCUSSION

We begin this section by describing the results obtained using the QR approach. A wide range of regularization parameters were investigated, and a selection of models from the vicinity of the knee of the L-curve (Hansen 1998), with regularization parameters $\lambda = 4640$,

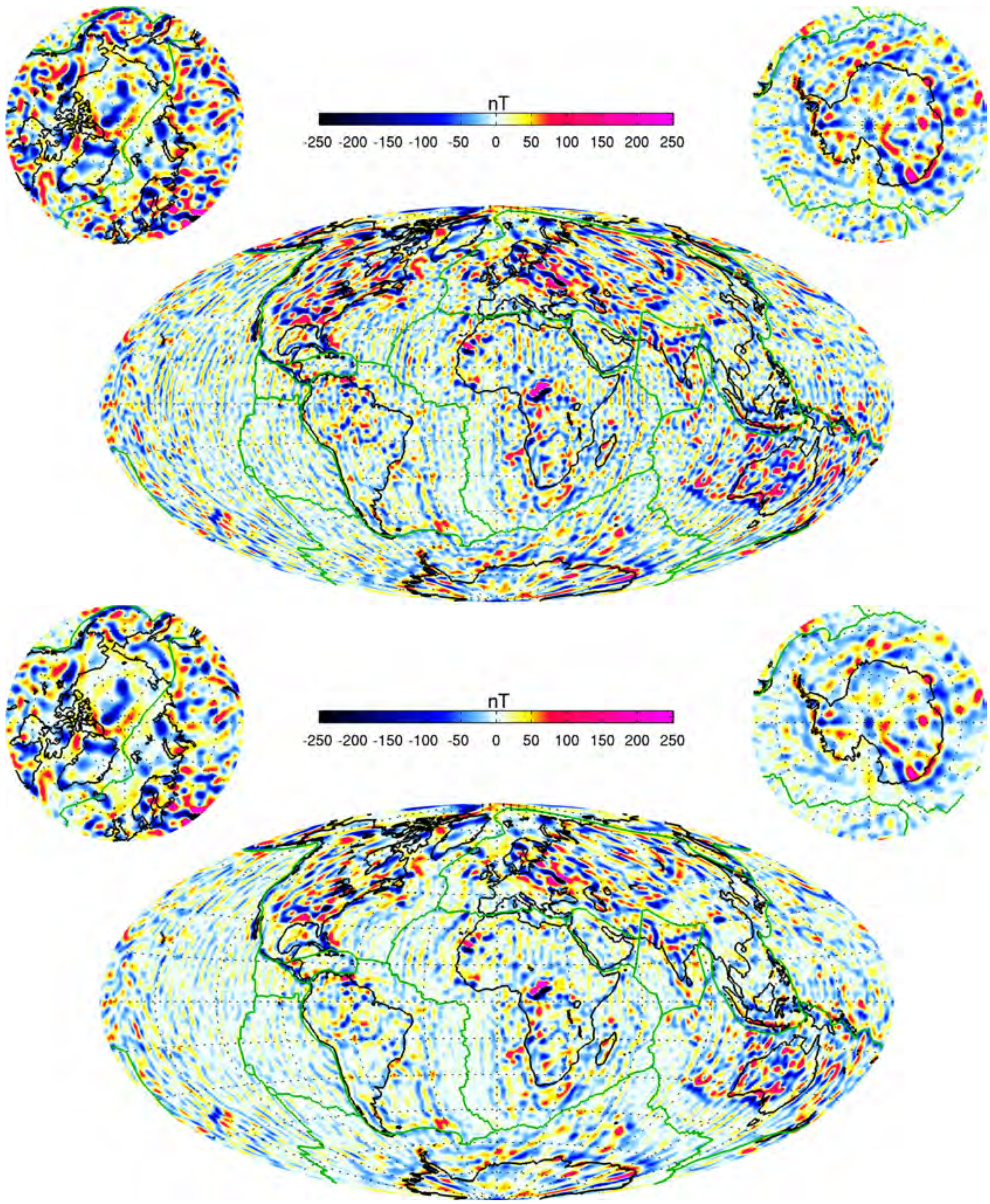

Figure 4. Top: lithospheric radial magnetic field corresponding to the preferred quadratic regularization model mono-QR with $\lambda = 928\,\mathrm{nT}^{-2}$ at the Earth's surface. Bottom: similar figure for the preferred maximum entropy regularization model mono-ER with $\lambda = 4640\,\mathrm{nT}^{-2}$ and $\omega = 25 \times 10^{-4}\,\mathrm{nT}$. The scale saturates at 250 nT. Note that both figures are the direct output of the corresponding monopole model rather than an approximation based on a truncated SH expansion. The corresponding model differences are illustrated in Fig. 8.

928 , 619 and $464\,\mathrm{nT}^{-2}$, were chosen for further analysis. All models were derived from the same unregularized ($\lambda = 0$) starting model, and they converged within five iterations. The model values $\mathbf{q}$ were then converted into the spherical harmonic Gauss coefficients g_n^m and h_n^m using eqs (5) and (6). Fig. 3 illustrates the corresponding Mauersberger–Lowes power spectra, eq. (7), compared to the state-of-the-art lithospheric field models CM5 (Sabaka *et al.* 2015) and MF7 (Maus *et al.* 2008; Maus 2010). We observe the expected decrease in power at high spherical harmonic degrees with increasing regularization parameter.

An interesting question is whether our monopole models are more or less sensitive to the lack of data within the polar gap regions, compared to SH field models which are known to be strongly affected by this problem above SH degree 60 (Olsen *et al.* 2014). We constructed models with and without synthetic data added in the polar gap regions. Both power spectra and global lithospheric field maps indicate that the monopole method is not dependent on having data in the polar gap regions. Differences in the field maps are only seen in the areas where synthetic data were added, while the power spectra are almost identical. The lack of sensitivity to the polar gap problem seems therefore to be an advantage of our models in comparison to models that are based on spherical harmonics.

Tables 2 and 3 present statistics comparing the fit of the models to selected CHAMP observations globally and locally (over

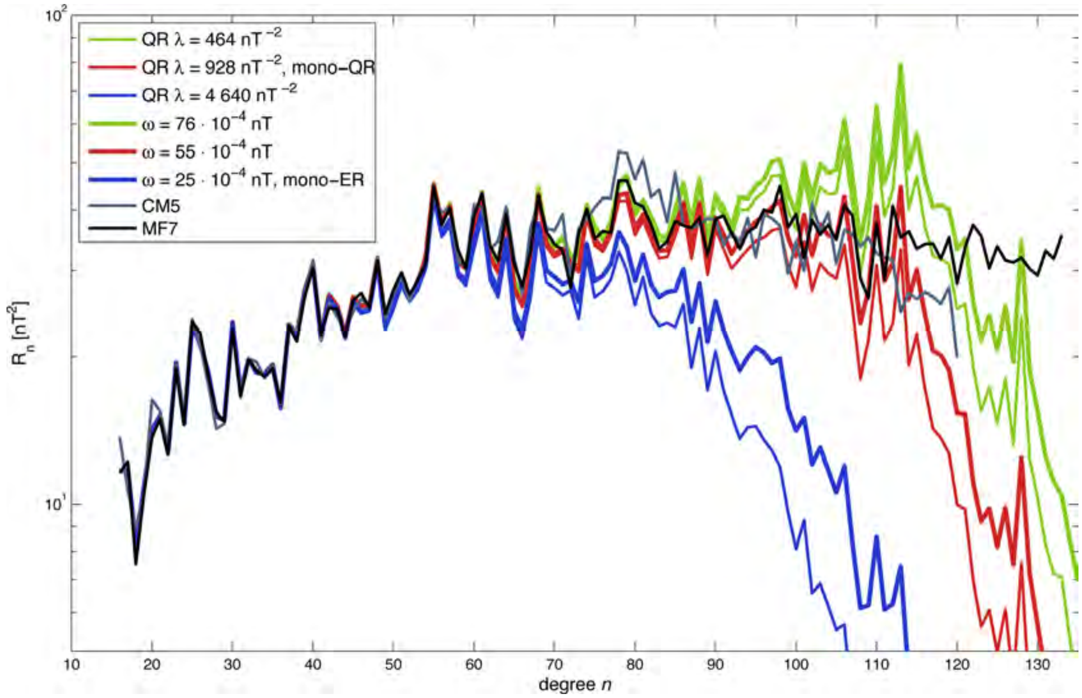

Figure 5. Power spectra for QR models (thin lines) and ER models (thick lines) compared to reference lithospheric field models. Models with the same regularization parameters are represented with the same colour.

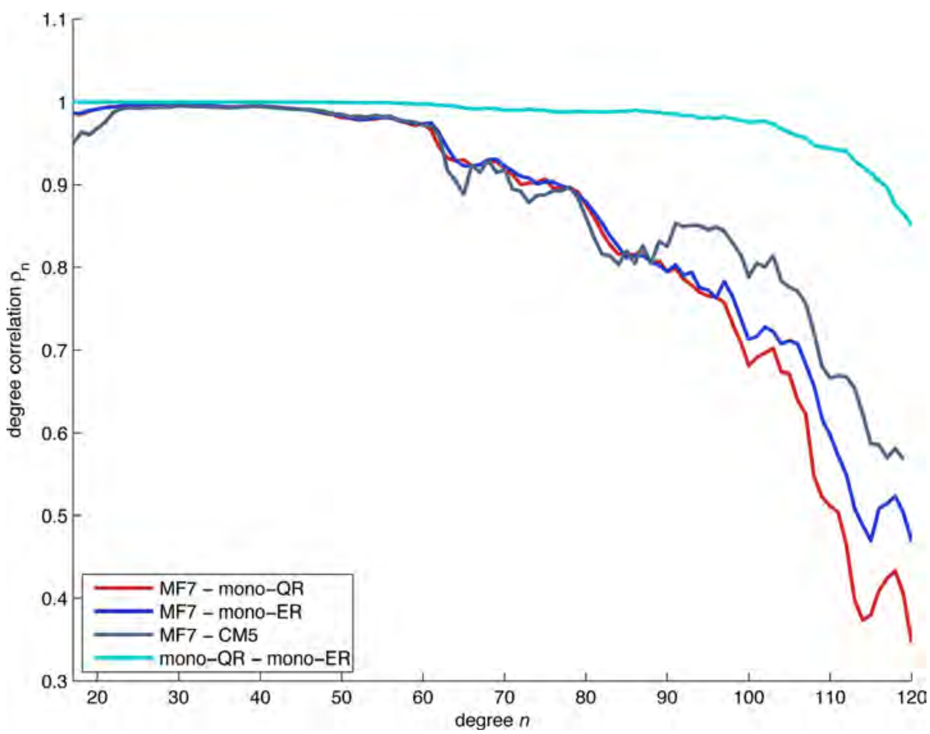

Figure 6. Degree correlation between MF7 and the spherical harmonic degrees of mono-QR, mono-ER and CM5. The monopole-based models reach a typical correlation limit of $\rho_n = 0.7$ (Arkani-Hamed *et al.* 1994; Sabaka & Olsen 2006) at SH degree $n = 100$. CM5 correlates well with MF7 up to SH degree $n = 108$. The light blue line shows the degree correlation between mono-QR and mono-ER.

part of the African continent), respectively. The corresponding model residual RMS values are given at satellite altitude and were derived using the weights implemented in the inversion. The upper half of the tables normalizes the values by dividing the residuals by the measurement error standard deviations of Fig. 2. As expected, the derived models in general fit the observations better than both MF7 and CM5 with the various QR models having very similar residual values. However, looking at their respective global lithospheric radial magnetic field maps (not given here), we observe larger residuals especially in oceanic regions for decreasing regularization parameters. For example, in the Pacific and the North Atlantic ocean, north–south striping features appear which we

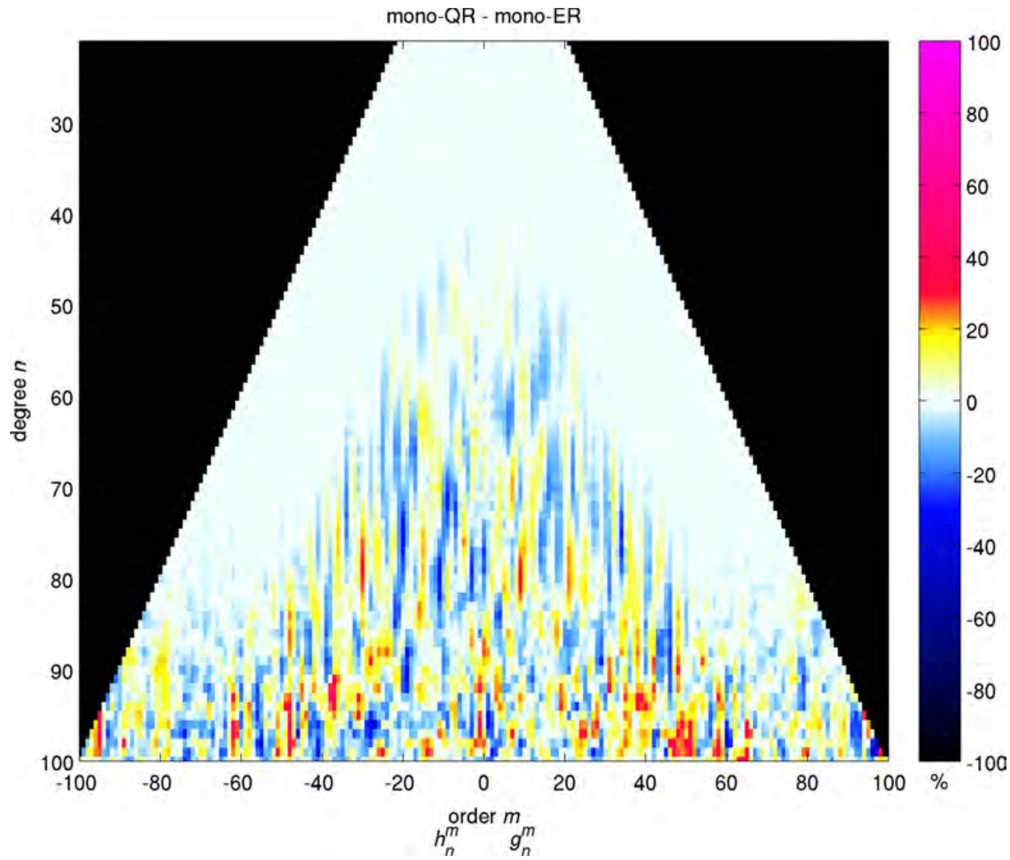

Figure 7. Normalized coefficient differences between mono-QR and mono-ER.

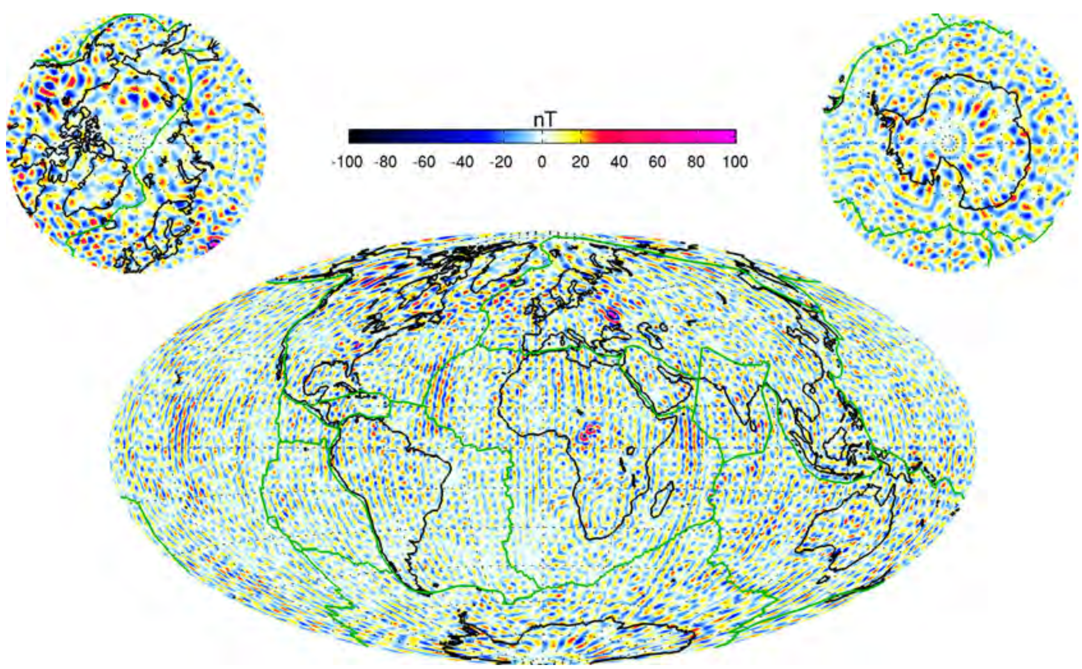

Figure 8. Lithospheric radial magnetic field difference between the quadratic regularization model mono-QR with $\lambda = 928\,\mathrm{nT}^{-2}$ (5 iterations) and the maximum entropy regularization model mono-ER with $\lambda = 4640\,\mathrm{nT}^{-2}$ and $\omega = 25 \times 10^{-4}$ nT (10 iterations) at the Earth's surface. Note that the scale saturates at only 100 nT.

associate with unmodelled magnetospheric field signals still present in the data set. Taking the power spectra, statistical comparisons and radial field maps into account, we select the model with $\lambda = 928\,\mathrm{nT}^{-2}$ to be the preferred QR model of this study. Henceforth, we refer to this as model 'mono-QR'. The corresponding lithospheric radial magnetic field at the Earth's surface is presented in the upper part of Fig. 4.

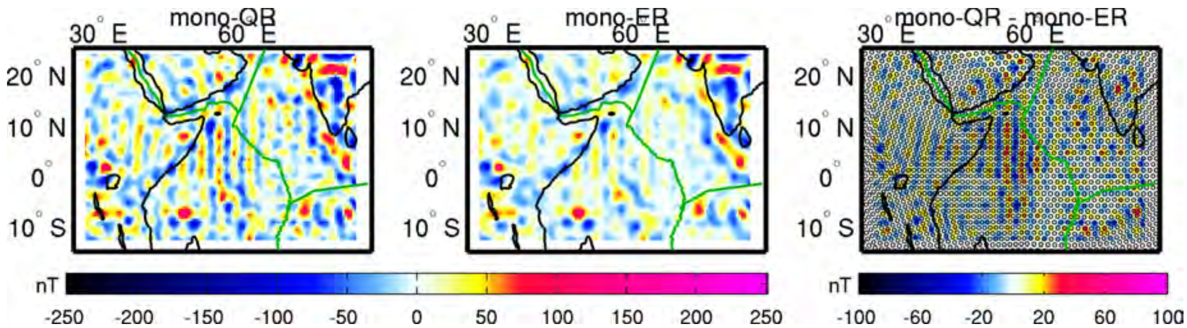

Figure 9. Lithospheric radial magnetic field at the Earth's surface for mono-QR with $\lambda = 928\,\mathrm{nT}^{-2}$, mono-ER with $\lambda = 4640\,\mathrm{nT}^{-2}$ and $\omega = 25 \times 10^{-4}$ nT and the corresponding differences. The illustrated region corresponds to the northwest area of the Indian ocean. Additionally, the individual source locations are indicated by the black circles in the right panel of the figure.

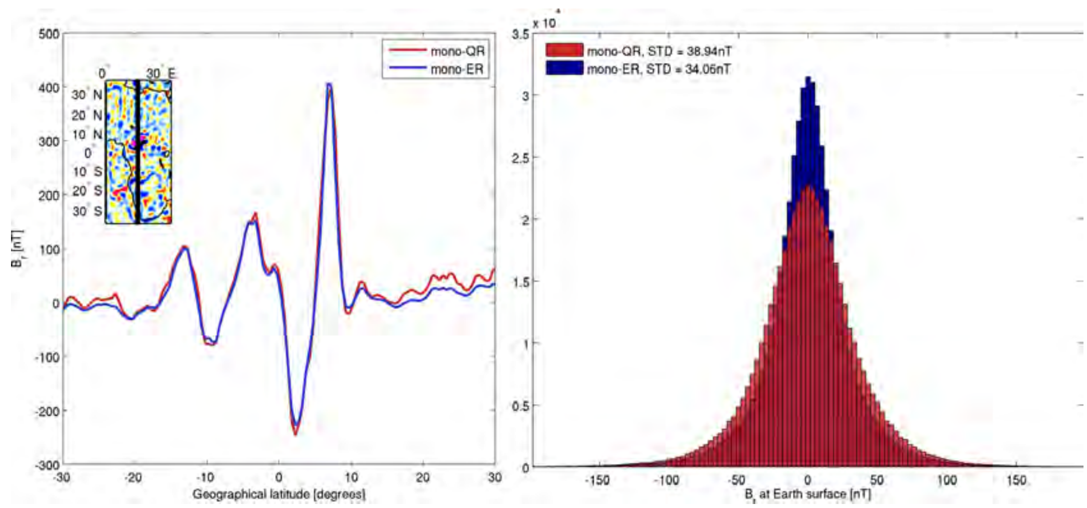

Figure 10. Left: model prediction for the radial lithospheric magnetic field at the Earth's surface (on a $0.5^\circ \times 0.5^\circ$ grid) along an orbital profile at longitude $\phi = 17.25^\circ$ crossing the Bangui magnetic anomaly (inserted figure). The result is given for mono-QR (red) and mono-ER (blue) models. Right: histogram comparing the global statistics of the modelled lithospheric radial magnetic field at the Earth's surface predicted by mono-QR (red) and mono-ER (blue). The corresponding surface locations are identical to monopole locations for a grid refinement level $L = 7$. Standard deviation values are given in the upper part of the figure.

Next we move on to consider the models derived using the maximum entropy regularization (ER) approach. ER models were derived applying the same regularization parameters as in Fig. 3 and using the respective QR solutions as the starting models. The entropy default parameter ω was initially set to a large value and then gradually decreased ensuring model convergence at each step. The presented values of ω are the minimum values for which we were able to obtain numerical convergence. Fig. 5 shows the power spectra for both the ER and QR models. As expected, the ER approach enhances local magnetic field amplitudes, resulting in slightly larger power at higher spherical harmonic degrees compared to QR models with the same λ. We found it advantageous to have a starting model with a minimum amount of noise mapped into the monopole sources. Our preferred ER model is therefore based on the largest investigated regularization parameter $\lambda = 4640\,\mathrm{nT}^{-2}$ and $\omega = 25 \times 10^{-4}$ nT. Henceforth, this model will be referred to as 'mono-ER'. The lower part of Fig. 4 illustrates the corresponding radial lithospheric field map at the Earth's surface. It is noteworthy that the oceanic regions are generally of lower amplitude in mono-ER compared to mono-QR (the mean value of the absolute radial field magnitude in the oceanic regions is 3.22 nT lower in mono-ER than in mono-QR), while over large continental anomalies the amplitude in mono-ER can be higher (left panel of Fig. 10 for $\sim 8^\circ$ north). The global and local differences between mono-QR and mono-ER are presented in Figs 8 and 9, respectively. The differences are globally distributed, with the largest values in the polar regions, around large local lithospheric field anomalies and in some specific oceanic regions (e.g. in the mid-Atlantic, north of Brazil and the Indian ocean). The right panel of Fig. 9 shows an example of the local differences between mono-QR and mono-ER models as well as monopole locations projected to the surface of the Earth. Model differences are generally of larger scale than the distance between individual sources.

Comparing the statistics for the mono-QR and mono-ER models (see Tables 2 and 3) we were able to arrive a very similar model misfit (difference < 0.1 per cent). This is surprising since mono-ER has much less power at high degree (Fig. 5) with which to fit observations to the same level as mono-QR.

Fig. 6 presents the degree correlation between MF7 and the models mono-QR, mono-ER and CM5. The mono-QR and mono-ER models are well correlated ($\rho > 0.7$) with MF7 up to SH degree $n = 100$, while this value is slightly larger for the correlation between MF7 and CM5 ($n = 108$). Fig. 6 also shows that the mono-QR and mono-ER models are themselves well correlated out to at least degree 120 (light blue curve).

Another illustration of the differences between models mono-QR and mono-ER is shown in Fig. 7. After transforming the model results to the SH domain, the Gauss coefficient differences are here

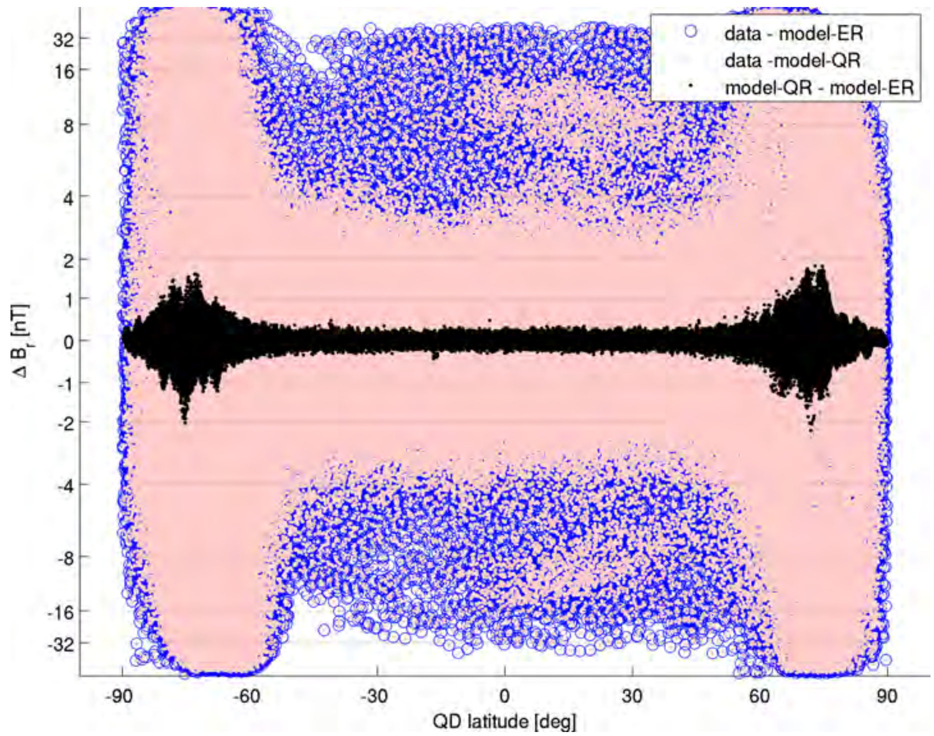

Figure 11. Radial field residuals between the CHAMP data and the mono-QR (red) and mono-ER (blue) models. Differences between the models are shown in black. The y-axis is nonlinear and proportional to $\frac{8}{\pi}$ arctan$(y/5)$ nT in order to emphasize near-zero values.

considered in a degree/order plot. The differences are normalized by the mean spectral amplitude of the MF7 coefficients according to eq. (9). The models start to differ notably above SH degree 60, partly because there is then much less power in the mono-ER compared with the mono-QR model. However, even at higher degree, the differences remain relatively small, in the range of 10 per cent. We attribute the differences between mono-QR and mono-ER shown here primarily to the applied regularization. Additionally, interesting vertical stripes are observed especially between degrees 60 and 95 in Fig. 7. These features are due to north–south directed structures which are especially seen in the oceanic regions of Fig. 4, being most prominent in model-QR (Fig. 9).

The right part of Fig. 10 presents the global surface radial magnetic field distribution of mono-QR and mono-ER by means of a histogram. The corresponding surface grid locations are identical to the monopole source locations for a grid refinement level $L = 7$. It illustrates that the mono-ER model predicts more field values closer to zero compared to the QR counterpart, while at the same time the ER model still allows larger field amplitudes where locally required by the data. The latter point is best appreciated by considering the maximum and minimum global radial field values, which are 577 nT and -893 nT for mono-QR and 727 nT and -1078 nT for mono-ER (note that the long tails of the mono-ER distribution are difficult to see in Fig. 10 due to the scale). In statistical terminology, the ER approach follows a more Laplacian distribution, as expected for crustal field anomalies (Walker & Jackson 2000).

The left part of Fig. 10 shows the surface radial magnetic field values along a constant longitude crossing the Bangui anomaly. Despite the similar morphology of the anomalies, the mono-ER model has smaller field amplitudes in regions with weak magnetic anomalies and sometimes has larger amplitudes than the mono-QR model over the large magnetic anomalies.

Fig. 11 illustrates the derived model residuals for mono-QR and mono-ER with respect to the corresponding QD latitudes. Differences between the individual model values are shown in black and emphasize the very similar model predictions as already seen in the previous figures as well as Tables 2 and 3.

We also derived the model resolution matrices for mono-QR and mono-ER. From the respective traces we found the number of degrees of freedom for models mono-QR and mono-ER to be 11635 and 9515, respectively, that is, mono-ER is able to obtain almost the same fit to the observations as mono-QR but with almost 20 per cent fewer effective degrees of freedom.

Overall we find that, compared to traditional SH models and the mono-QR model, the mono-ER model requires a smaller number of degrees of freedom to achieve the same level of fit to the observations and possesses Laplacian statistics with a small number of anomalies of high amplitude and many regions with very weak anomalies. The latter corresponds well with the lithospheric field expectations based on satellite, airborne and marine data (Thébault *et al.* 2010).

6 CONCLUSIONS AND OUTLOOK

We have presented a new method for modelling the global lithospheric magnetic field at the Earth's surface based on an icosahedral grid of equivalent monopole sources. We obtained model solutions by iterative least squares, with Huber weighting of misfit values and latitude-dependent data uncertainties implemented for all three vector field components at all latitudes. The approach was tested using CHAMP satellite data spanning the period 2009–2010.

Both QR and ER approaches based on monopole modelling were investigated. The former involves minimizing the Euclidean norm of the model parameters, while the maximum entropy approach minimizes an information-based measure of complexity.

The obtained model results have been compared statistically and by looking at the corresponding radial magnetic field values globally and locally at the Earth's surface. The preferred mono-QR and mono-ER models show very similar misfits, but the ER approach allows for larger lithospheric magnetic field values locally where there are strong anomalies, while at the same time favouring weaker values in oceanic regions in agreement with geological expectations. Furthermore, the mono-ER model has a much smaller number of degrees of freedom. The derived models correlate satisfactorily with MF7 up to SH degree $n = 100$.

The method does not involve spherical harmonics and is therefore also suitable for local geomagnetic field investigations with higher resolution. Nonetheless, whenever needed, the equivalent source model parameters can easily be transformed into spherical harmonics. Interestingly, eqs (5) to (6) can be used to produce spherical harmonic models and power spectra specifically for regions of interest, by retaining only the equivalent sources inside that region, and implicitly setting the amplitude of the remaining sources to zero. Note that the R-SCHA (Thébault & Vervelidou 2015) and spherical Slepian function (Beggan *et al.* 2013) approaches can also be used to derive local power spectra.

Future applications will make use of *Swarm* data in combination with high-resolution aeromagnetic measurements. For the latter, local refinement of the monopole grid will be implemented in the modelling approach.

Extending the method to also handle field differences, approximating gradients, along and across satellite tracks (Kotsiaros *et al.* 2015; Olsen *et al.* 2015) should lead to further improvements of the lithospheric field models, but this will require a more sophisticated treatment of the data covariance matrix $\underline{\underline{\mathbf{C}}}$.

ACKNOWLEDGEMENTS

The authors are grateful for the comments of the editor Prof Gary Egbert, the reviewer Dr Mike Purucker and an anonymous reviewer, who helped to improve the manuscript and clarify the mathematical presentation. Support by the Research Council of Norway through the Petromaks programme, by ConocoPhillips and Lundin Norway, and by the Technical University of Denmark is highly appreciated. The support of the CHAMP mission by the German Aerospace Center (DLR) and the Federal Ministry of Education and Research is gratefully acknowledged.

REFERENCES

Arkani-Hamed, J., Langel, R.A. & Purucker, M., 1994. Scalar magnetic anomaly maps of Earth derived from POGO and Magsat data, *J. geophys. Res.,* **99**(B12), 24 075–24 090.

Baumgardner, J.R. & Frederickson, P.O., 1985. Icosahedral discretization of the two-sphere, *SIAM J. Numer. Anal.,* **22**(6), 1107–1115.

Beggan, C.D., Saarimäki, J., Whaler, K.A. & Simons, F.J., 2013. Spectral and spatial decomposition of lithospheric magnetic field models using spherical slepian functions, *Geophys. J. Int.,* **193**(1), 136–148.

Blakely, R., 1996. *Potential Theory in Gravity and Magnetic Applications,* Cambridge Univ. Press.

Bloxham, J., Gubbins, D. & Jackson, A., 1989. Geomagnetic secular variation, *Phil. Trans. R. Soc. Lond., A,* **329,** 415–502.

Chambodut, A., Panet, I., Mandea, M., Diament, M., Holschneider, M. & Jamet, O., 2005. Wavelet frames: an alternative to spherical harmonic representation of potential fields, *Geophys. J. Int.,* **163**(3), 875–899.

Connerney, J. *et al.*, 1999. Magnetic lineations in the ancient crust of Mars, *Science,* **284**(5415), 794–798.

Constable, C., 1988. Parameter estimation in non-Gaussian noise, *Geophys. J. Int.,* **94**(1), 131–142.

Covington, J., 1993. Improvement of equivalent source inversion technique with a more symmetric dipole distribution model, *Phys. Earth planet. Inter.,* **76**(3), 199–208.

Driessen, K. & Rombouts, R., 2007. *Matlab Library for Robust Analysis,* Available at: http://wis.kuleuven.be/stat/robust.html.

Emmert, J., Richmond, A. & Drob, D., 2010. A computationally compact representation of Magnetic-Apex and Quasi-Dipole coordinates with smooth base vectors, *J. geophys. Res.,* **115**(A8), doi:10.1029/2010JA015326.

Gillet, N., Jackson, A. & Finlay, C.C., 2007. Maximum entropy regularization of time-dependent geomagnetic field models, *Geophys. J. Int.,* **171**(3), 1005–1016.

Gull, S. & Skilling, J., 1999. *Quantified Maximum Entropy - MemSys5 Users' Manual, Version 1.2,* Maximum Entropy Data Consultants Ltd.

Haines, G., 1985. Spherical cap harmonic analysis, *J. geophys. Res.,* **90**(B3), 2583–2591.

Hansen, P.C., 1998. *Rank-deficient and Discrete Ill-posed Problems: Numerical Aspects of Linear Inversion,* vol. 4, SIAM.

Huber, P.J., 1964. Robust estimation of a location parameter, *Annals of Mathematical Statistics,* **35**(1), 73–101.

Inglis, T., 1987. *Petroleum Engineering and Development Studies, Vol. 2: Directional Drilling,* Graham & Trotman.

Jackson, A., Constable, C. & Gillet, N., 2007. Maximum entropy regularization of the geomagnetic core field inverse problem, *Geophys. J. Int.,* **171**(3), 995–1004.

Kotsiaros, S., Finlay, C.C. & Olsen, N., 2015. Use of along-track magnetic field differences in lithospheric field modelling, *Geophys. J. Int.,* **200**(2), 878–887.

Langel, R. & Whaler, K., 1996. Maps of the magnetic anomaly field at Earth's surface from scalar satellite data, *Geophys. Res. Lett.,* **23**(1), 41–44.

Langel, R.A. & Hinze, W.J., 1998. *The Magnetic Field of the Earth's Lithosphere: The Satellite Perspective,* Cambridge Univ. Press.

Langlais, B., Purucker, M. & Mandea, M., 2004. Crustal magnetic field of Mars, *J. geophys. Res.,* **109**(E2), doi:10.1029/2003JE002048.

Lesur, V., Rother, M., Vervelidou, F., Hamoudi, M. & Thébault, E., 2013. Post-processing scheme for modelling the lithospheric magnetic field, *Solid Earth,* **4,** 105–118.

Lowes, F., 1974. Spatial power spectrum of the main geomagnetic field, and extrapolation to the core, *Geophys. J. R. astr. Soc.,* **36**(3), 717–730.

Maisinger, K., Hobson, M.P. & Lasenby, A., 2004. Maximum-entropy image reconstruction using wavelets, *Mon. Not. R. astr. Soc.,* **347**(1), 339–354.

Maus, S., 2010. *Magnetic Field Model MF7,* Available at: http://geomag.org/models/MF7.html.

Maus, S., Yin, F., Lühr, H., Manoj, C., Rother, M., Rauberg, J., Michaelis, I., Stolle, C. & Müller, R., 2008. Resolution of direction of oceanic magnetic lineations by the sixth-generation lithospheric magnetic field model from champ satellite magnetic measurements, *Geochem. Geophys. Geosyst.,* **9**(7), doi:10.1029/2008GC001949.

Mayer, C. & Maier, T., 2006. Separating inner and outer Earth's magnetic field from CHAMP satellite measurements by means of vector scaling functions and wavelets, *Geophys. J. Int.,* **167**(3), 1188–1203.

Menke, W., 2012. *Geophysical Data Analysis: Discrete Inverse Theory,* Academic press.

Molnar, P., 1988. Continental tectonics in the aftermath of plate tectonics, *Nature,* **335**(6186), 131–137.

Ness, N.F., 1979. The magnetic fields of Mercury, Mars, and Moon, *Annu. Rev. Earth Planet. Sci.,* **7,** 249–288.

O'Brien, M.S. & Parker, R.L., 1994. Regularized geomagnetic field modelling using monopoles, *Geophys. J. Int.,* **118**(3), 566–578.

Olsen, N., 2002. A model of the geomagnetic field and its secular variation for epoch 2000 estimated from Ørsted data, *Geophys. J. Int.,* **149**(2), 454–462.

Olsen, N. *et al.*, 2005. Swarm end-to-end mission performance simulator study, DSRI Report 1/2004, ISSN 1602-527X.

Olsen, N., Lühr, H., Sabaka, T., Mandea, M., Rother, M., Tøffner-Clausen, L. & Choi, S., 2006. CHAOS - a model of the Earth's magnetic field derived from CHAMP, Ørsted, and SAC-C magnetic satellite data, *Geophys. J. Int.,* **166**(1), 67–75.

Olsen, N., Lühr, H., Finlay, C.C., Sabaka, T.J., Michaelis, I., Rauberg, J. & Tøffner-Clausen, L., 2014. The CHAOS-4 geomagnetic field model, *Geophys. J. Int.,* **197**(2), 815–827.

Olsen, N. *et al.*, 2015. The swarm initial field model for the 2014 geomagnetic field, *Geophys. Res. Lett.*, **42**(4), 1092–1098.

Plado, J., Pesonen, L., Koeberl, C. & Elo, S., 2000. The Bosumtwi meteorite impact structure, Ghana: a magnetic model, *Meteorit. Planet. Sci.,* **35**(4), 723–732.

Purucker, M.E. & Nicholas, J.B., 2010. Global spherical harmonic models of the internal magnetic field of the Moon based on sequential and coestimation approaches, *J. geophys. Res.,* **115**(E12), doi:10.1029/2010JE003650.

Richmond, A., 1995. Ionospheric electrodynamics using magnetic apex coordinates, *J. Geomag. Geoelectr.,* **47**(2), 191–212.

Sabaka, T.J. & Olsen, N., 2006. Enhancing comprehensive inversions using the Swarm constellation, *Earth Planets Space,* **58**(4), 371–395.

Sabaka, T.J., Olsen, N., Tyler, R.H., Kuvshinov, A., Sabaka, T.J., Olsen, N., Tyler, R.H. & Kuvshinov, A., 2015. CM5, a pre-Swarm comprehensive geomagnetic field model derived from over 12 yr of CHAMP, Ørsted, SAC-C and observatory data, *Geophys. J. Int.,* **200**(3), 1596–1626.

Stockmann, R., Finlay, C.C. & Jackson, A., 2009. Imaging Earth's crustal magnetic field with satellite data: a regularized spherical triangle tessellation approach, *Geophys. J. Int.,* **179,** 929–944.

Thébault, E., 2006. Global lithospheric magnetic field modelling by successive regional analysis, *Earth Planets Space,* **58**(4), 485–495.

Thébault, E., 2008. A proposal for regional modelling at the Earth's surface, R-SCHA2D, *Geophys. J. Int.,* **174**(1), 118–134.

Thébault, E. & Vervelidou, F., 2015. A statistical power spectrum of the Earth's lithospheric magnetic field, *Geophys. J. Int.,* **201,** 605–620.

Thébault, E., Purucker, M., Whaler, K.A., Langlais, B. & Sabaka, T.J., 2010. The magnetic field of the Earth's lithosphere, *Space Sci. Rev.,* **155**(1–4), 95–127.

Torge, W., 2001. *Geodesy,* Walter de Gruyter.

Toyoshima, M., Shibuya, H., Matsushima, M., Shimizu, H. & Tsunakawa, H., 2008. Equivalent source mapping of the lunar crustal magnetic field using ABIC, *Earth Planets Space,* **60**(4), 365–373.

Walker, M. & Jackson, A., 2000. Robust modelling of the Earth's magnetic field, *Geophys. J. Int.,* **143,** 799–808.

Whaler, K. & Purucker, M., 2005. A spatially continuous magnetization model for Mars, *J. geophys. Res.,* **110**(E9), doi:10.1029/2004JE002393.

APPENDIX: GREEN'S MATRIX COMPONENTS

The Green's matrix $\underline{\underline{\mathbf{G}}}$ represents the linear relationship between the magnetic monopole sources $\mathbf{q}$ and the corresponding lithospheric magnetic field $\mathbf{B}$,

$$\begin{aligned} \mathbf{B} &= \underline{\underline{\mathbf{G}}}\mathbf{q} \\ Bi,\, p &= -\sum_{k=1}^{K} q_k \left[\hat{\mathbf{e}}_{i,p} \cdot \nabla_p \frac{r_k^2}{r_{ik}}\right] \\ &= \sum_{k=1}^{K} q_k g_{ik,p} \end{aligned} \tag{A1}$$

where i and k represent a given lithospheric magnetic field prediction and the equivalent source index, respectively.

The general formula for a given element p (for $p = r, \theta$ or ϕ) of the Green's matrix is

$$\underline{\underline{\mathbf{G}}}_p = g_{ik,p} = -\hat{\mathbf{e}}_{i,p} \cdot \nabla_p \frac{r_k^2}{r_{ik}}. \tag{A2}$$

Then

$$\begin{aligned} g_{ik,r} &= -\frac{\partial}{\partial r_i}\left(\frac{r_k^2}{r_{ik}}\right) \\ &= \frac{r_k^2}{r_{ik}^3}[r_i - r_k \cos(\mu_{ik})] \\ g_{ik,\theta} &= -\frac{1}{r_i}\frac{\partial}{\partial \theta_i}\left(\frac{r_k^2}{r_{ik}}\right) \\ &= \frac{r_k^3}{r_{ik}^3}[\sin(\theta_i)\cos(\theta_k) - \cos(\theta_i)\sin(\theta_k)\cos(\phi_i - \phi_k)] \\ g_{ik,\phi} &= -\frac{1}{r_i \sin(\theta_i)}\frac{\partial}{\partial \phi_i}\left(\frac{r_k^2}{r_{ik}}\right) \\ &= \frac{r_k^3}{r_{ik}^3}[\sin(\theta_k)\sin(\phi_i - \phi_k)]. \end{aligned} \tag{A3}$$

Geophys. J. Int. (2000) **142,** 000–000

LCS-1: A high-resolution global model of the lithospheric magnetic field derived from CHAMP and Swarm satellite observations

Nils Olsen[1] Dhananjay Ravat[2], Christopher C. Finlay[1], Livia K. Kother[1]
[1] *DTU Space, National Space Institute, Technical University of Denmark, Diplomvej 371, 2800 Kgs. Lyngby, Denmark.*
[2] *University of Kentucky, Department of Earth and Environmental Sciences, US America.*

Accepted xxxx. Received xxxx; in original form xxxx.

SUMMARY

We derive a new model, named LCS-1, of Earth's lithospheric field based on four years (Sept 2006 – Sept 2010) of magnetic observations taken by the CHAMP satellite at altitudes lower than 350 km, as well as almost three years (April 2014 to December 2016) of measurements taken by the two lower *Swarm* satellites Alpha and Charlie. The model is determined entirely from magnetic "gradient" data (approximated by finite differences): the North-South gradient is approximated by first differences of 15 second along-track data (for CHAMP and each of the two *Swarm* satellites), while the East-West gradient is approximated by the difference between observations taken by *Swarm* Alpha and Charlie. In total, we used 6.2 mio data points.

The model is parametrized by 35,000 equivalent point sources located on an almost equal-area grid at a depth of 100 km below the surface (WGS84 ellipsoid). The amplitudes of these point sources are determined by minimizing the misfit to the magnetic satellite "gradient" data together with the global average of $|B_r|$ at the ellipsoid surface (i.e. applying a L1 model regularisation of B_r). In a final step we transform the point-source representation to a spherical harmonic expansion.

The model shows very good agreement with previous satellite-derived lithospheric field models at low degree (degree correlation above 0.8 for degrees $n \leq 133$). Comparison with independent near-surface aeromagnetic data from Australia yields good agreement at horizontal wavelengths down to 250 km, corresponding to spherical harmonic degree $n \approx 160$.

The LCS-1 vertical component and field intensity anomaly maps at Earth's surface show similar features to those exhibited by the WDMAM2 and EMM2015 lithospheric field models truncated at degree 185 in regions where they include near-surface data and provide unprecedented detail where they do not. Example regions of improvement include the Bangui anomaly region in central Africa, the west African cratons, the East African Rift region in the continents and the Bay of Bengal, the southern 90° E ridge, the Cretaceous quiet zone south of the Walvis Ridge and the younger parts of the South Atlantic.

Key words: Geomagnetism, Earth's magnetic field, Satellite, CHAMP, Swarm, Spherical harmonics, Lithosphere

1 INTRODUCTION

Determination of global lithospheric field models requires accurate magnetic field observations with global coverage, which can only be obtained by satellites. Consequently, the construction of lithospheric magnetic field models is one of the main objectives of satellite missions such as CHAMP and *Swarm*. During the past decade a number of global lithospheric field models have been determined from data collected by these satellites (e.g., Thébault et al. 2016). In one class of models the lithospheric field is co-estimated together with other magnetic sources (e.g. from the core and magnetosphere) in a comprehensive approach; such models include the Comprehensive Model (CM) series (e.g., Sabaka et al. 2004, 2015), the GRIMM models (e.g. Lesur et al. 2008, 2015), the BGS model series (e.g. Thomson & Lesur 2007; Thomson et al. 2010), and the CHAOS model series (e.g. Olsen et al. 2014; Finlay et al. 2016). Models of the other class are derived in a sequential approach by first removing *a-priori* models of all known magnetic field contributions, except for the lithospheric field, from the magnetic field observations, followed by a careful data selection and application of empirical corrections. The MF model series (e.g.

Maus et al. 2002, 2008; Maus 2010) are examples of models determined using this approach; other examples are the models determined by Stockmann et al. (2009), Kother et al. (2015) and Thébault et al. (2016).

The MF7 model developed by Maus and co-workers is one of the most widely used global lithospheric field models. It formally describes the lithospheric field up to spherical harmonic degree $n = 133$ (corresponding to 300 km horizontal wavelength), and has been derived from along-track filtered CHAMP magnetic field observations after removal of *a-priori* models of the core and large-scale magnetospheric fields and of the ocean tidal magnetic signal, and line levelling between adjacent satellite tracks and nearby orbit cross-overs to minimise the variance between observations within a certain distance. Coefficients above $n > 80$ are damped (regularised) by minimizing the L2 norm of the radial magnetic field, which means minimising B_r^2 averaged over the Earth's surface.

As an alternative to the L2 norm of B_r, other regularisation schemes have also been used: Stockmann et al. (2009) and Kother et al. (2015) applied a maximum entropy regularisation (of B_r and equivalent source amplitudes respectively), while Morschhauser et al. (2014) used a L1 model regularisation (of B_r) for modelling the lithospheric field of Mars.

Lithospheric field models differ also in their model parametrisation. Whilst most models (including MF7) estimate the coefficients of a spherical harmonic expansion of the magnetic potential, alternatives have been explored. These include spherical triangle tessellations of B_r (Stockmann et al. 2009), (depleted) harmonic splines (Langel et al. 1996), equivalent dipole sources (e.g. Mayhew 1979; von Frese et al. 1981; Dyment & Arkani-Hamed 1998), spherical caps (e.g. Haines 1985; Thébault 2006, 2008) and an equivalent source method involving monopoles (O'Brien & Parker 1994; Kother et al. 2015).

In this article we present a new global model of the lithospheric field that has been derived using more satellite magnetic observations (utilizing four years of data from CHAMP and three years from *Swarm*) than in previous models, using an equivalent source model parametrisation consisting of 35,000 point sources (monopoles), and using a model regularisation that minimises the global average of $|B_r|$ at the ellipsoid.

Low altitude magnetic field measurements are crucial for constructing high quality lithospheric field models, due to the attenuation of the lithospheric signal with altitude. This is obvious from Figure 1 which shows the *Lowes-Mauersberger* spatial spectrum of the lithospheric field at various altitudes as given by the MF7 lithospheric model (Maus 2010).

At Earth's surface, the spectrum is essentially "flat" (i.e. independent of n) in the presented wavelength range ($\lambda = 300$ to 2500 km), whereas it strongly decreases with increasing harmonic degree n at satellite altitude. Focusing e.g. on lithospheric structures with horizontal wavelength $\lambda = 400$ km (corresponding to spherical harmonic degree $n = 100$), the mean lithospheric amplitude when averaging over Earth's surface is about 7 nT, whereas it is only 56 pT at 300 km altitude, which was the altitude of the CHAMP satellite during the last few months of the mission. At 450 km altitude, which is the present altitude of the lower *Swarm* satellite pair, the lithospheric signal is only 5.8 pT, 10 times weaker than at 300 km altitude. The attenuation with altitude is even stronger at higher spherical harmonic degrees.

Extracting the weak lithospheric signal from the satellite magnetic field observations is thus a major challenge which requires sophisticated statistical methods and data processing schemes. Spatial gradient information on the magnetic field, approximated by finite differences of measurements taken at nearby locations, help in removing the large-scale magnetic field contributions from the core and magnetosphere (and residuals of these effects in the data), and enhance the lithospheric signal. The lithospheric model that we present here relies entirely on such gradient information. We denote our new model as LCS-1 (**L**ithospheric model derived from **C**HAMP and ***S**warm* satellite data, version **1**).

Section 2 describes the data set that was used to derive and assess the lithospheric field model, and section 3 presents how the model is parametrized. Results are discussed in section 4, which also includes an investigation of the information content of the different data sets, thereby assessing the contribution of *Swarm* satellite data to the model. A discussion of the new lithospheric model is given in section 5. The paper concludes with a summary and outlook in section 6.

2 DATA

We use magnetic observations collected by the CHAMP and *Swarm* satellite missions. CHAMP (e.g. Maus 2007) was launched in July 2000 into a near polar (inclination 87.2°) orbit with an initial altitude of 454 km above a mean radius of $a = 6371.2$ km and had its atmospheric re-entry in September 2010. Altitude during the last four years of the mission was 350 km or lower, which makes this data set particularly interesting for lithospheric field modelling.

The satellite constellation mission *Swarm* (e.g. Friis-Christensen et al. 2006; Olsen et al. 2016b) was launched in November 2013. It consists of three identical spacecraft, two of which, *Swarm Alpha* and *Swarm Charlie*, fly closely together in near-polar orbits of inclination 87.4° at an altitude of about 450 km (as of March 2017). The East-West separation of their orbits is 1.4° in longitude, corresponding to 155 km at the equator. The third satellite, *Swarm Bravo*, flies at a slightly higher (about 520 km altitude in March 2017) orbit of inclination 88°. For our modelling effort we only use data from the two lower satellites *Swarm Alpha* and *Charlie*.

We selected CHAMP data from the four years September 2006 to September 2010 and from the lower *Swarm* satellite pair between April 2014 (since then the two lower satellites are flying in constellation) and December 2016. The top panel of Figure 2 shows mean altitude (red curve) and altitude range (red shaded) of the satellites together with solar flux $F_{10.7}$ (blue) w.r.t. time. The sudden increase in CHAMP altitude in 2009 is due to an orbit manoeuvre.

Unmodeled large-scale magnetospheric field contributions are one of the largest sources of noise for lithospheric field modelling, and

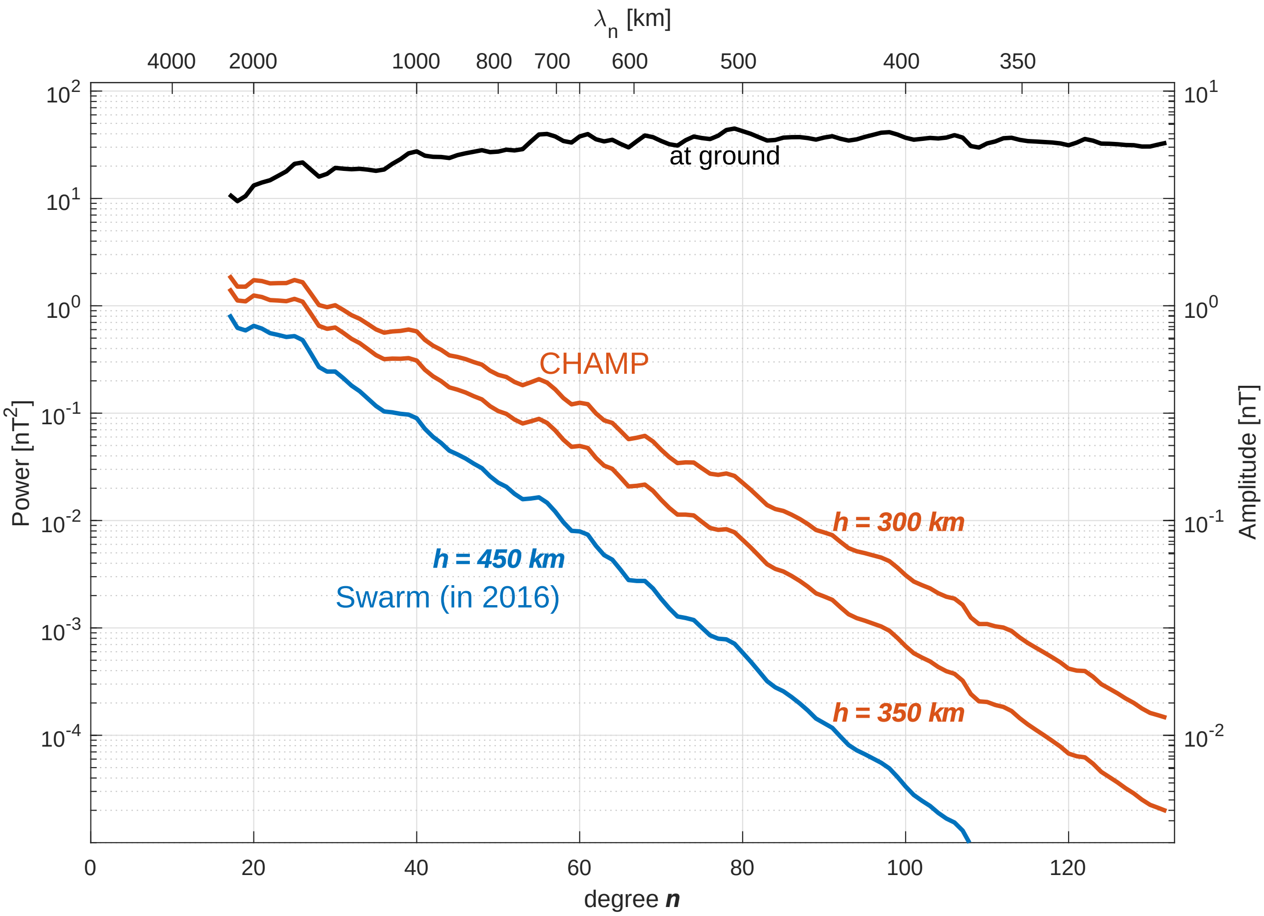

Figure 1. Spatial power spectrum of the lithospheric field at Earth's surface (black curve) and at various altitudes of CHAMP (red) and *Swarm* (blue), as given by the MF7 field model of Maus (2010). λ_n is the horizontal wavelength corresponding to degree n in a spherical harmonic expansion of the field.

various techniques have been used to eliminate these unwanted features from the data (see Thébault et al. (2016) for a recent overview). Often used techniques include high-pass filtering of the satellite magnetic field observations on an orbit-by-orbit basis and line levelling (e.g., Maus 2010). But such pre-processing of the data also removes part of the lithospheric signal, as demonstrated e.g. by Thébault et al. (2012).

However, large-scale magnetic field contributions such as those produced by magnetospheric currents are effectively reduced in gradient data compared to the magnetic field itself, which increases the lithospheric signal-to-noise ratio in gradient data. By relying entirely on gradient data, as done here, it is therefore possible to construct lithospheric field models without orbit-by-orbit high-pass filtering or line levelling.

Use of gradient data for lithospheric field modelling has several advantages: a) since gradient data are less affected by (large-scale) external field contributions it is possible to include data from times of higher geomagnetic activity, which increases the amount of times with data suitable for lithospheric modelling by up to 50%; b) gradient data are less correlated in time compared to field data, which enables a higher data sampling rate compared to field data. This further increases the amount of useful data for lithospheric field modelling.

For estimating our lithospheric model we entirely rely on horizontal difference data (which we in following denote as "gradient data"); we do not use magnetic field observations directly. Note, however, that magnetic field observations of course are used (differenced) when deriving the magnetic gradient data.

2.1 Selection of gradient data for model estimation

We select our data using similar selection criteria to those used for constructing the CHAOS-6 (Finlay et al. 2016) model; however, for the present model we sub-sampled the nominal 1 Hz data (Level-3 data for CHAMP, and Level-1b version 05 data for *Swarm*) at 30 s intervals (instead of the 60 sec sampling used for CHAOS-6).

Vector and scalar gradient data are selected for periods when (a) the strength of the magnetic signature of the magnetospheric ring current, described using the RC index (Olsen et al. 2014), changes by at most 3 nT/h; and (b) when the geomagnetic activity index $Kp \leq 3^0$ for quasi-dipole (QD) latitudes (Richmond 1995) equatorward of $\pm 55°$. Vector gradient data are only taken from non-polar (QD latitudes

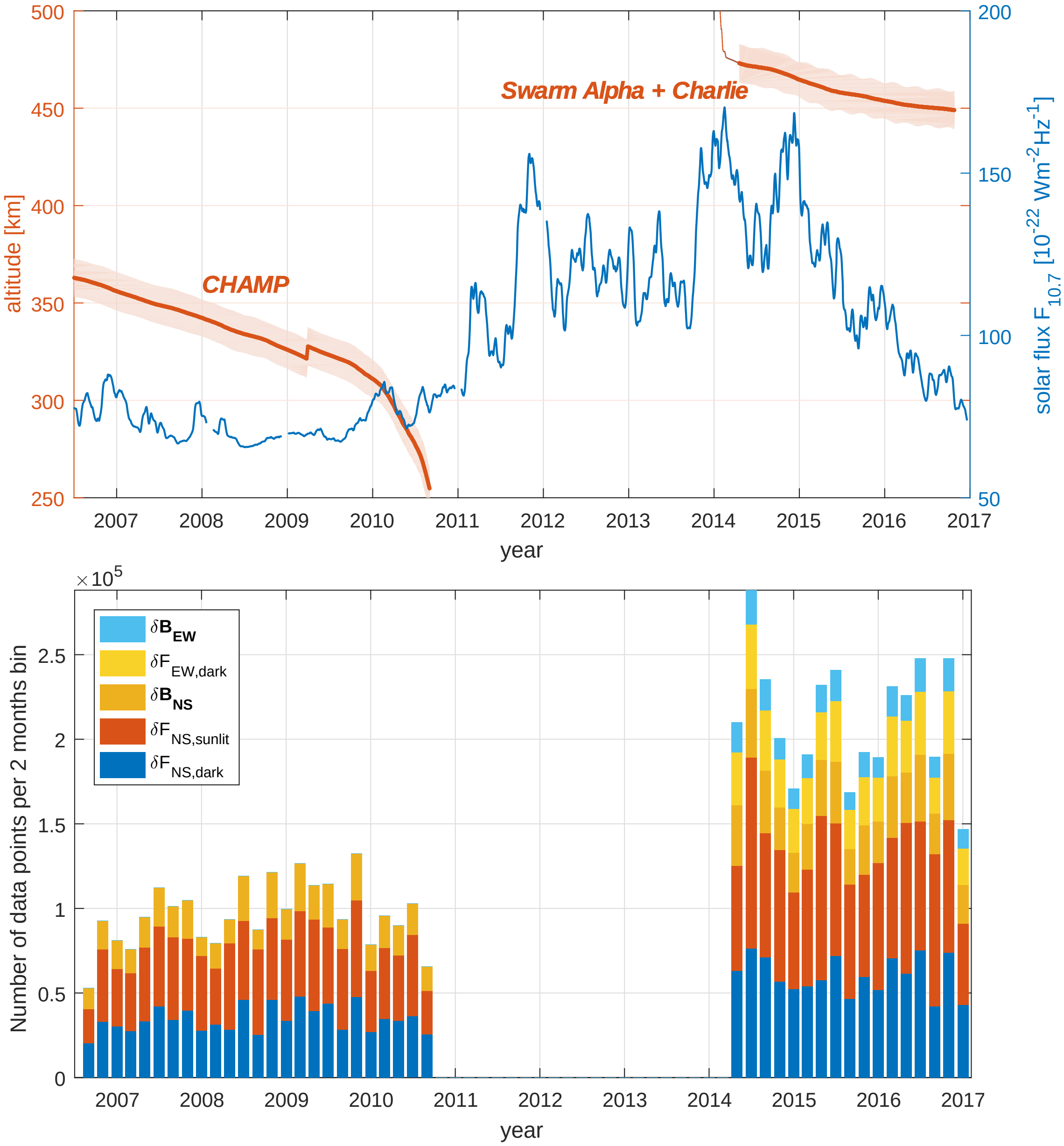

Figure 2. Top: Altitude of the CHAMP and *Swarm* satellites (red), and 27-day averages of solar flux index, $F_{10.7}$ (blue). The shaded red regions indicate the altitude range. Bottom: Total number of satellite data (stacked histogram) as a function of time, for bins of 2 months length.

equatorward of $\pm 55°$), while scalar gradient data are also taken from polar regions. Only data from dark regions (sun at least $10°$ below the horizon) are chosen with the exception of North-South scalar gradient data for which we also include data from sunlit (i.e. dayside) regions. However, we do not use any dayside data at QD-latitudes $< \pm 10°$ to avoid contamination by the Equatorial Electrojet, following the strategy described by Olsen et al. (2015, 2016a).

For each of the three satellites (j denotes CHAMP, *Swarm Alpha* or *Swarm Charlie*), the North-South (NS) gradient is approximated by the difference $\delta B_{\rm NS} = B(t_j, r_j, \theta_j, \phi_j) - B(t_j + 15{\rm secs}, r_j + \delta r, \theta_j + \delta\theta, \phi_j + \delta\phi)$ using subsequent data measured by the same satellite 15 secs later, corresponding to an along-track distance of ≈ 115 km ($\approx 1°$ in latitude). B may be either the scalar intensity F or one of the three magnetic vector components (B_r, B_θ, B_ϕ). Here $t_j, r_j, \theta_j, \phi_j$, are time, radius, geographic co-latitude and longitude of the observation, respectively.

The East-West (EW) gradient is approximated by the difference $\delta B_{\rm EW} = B_A(t_1, r_1, \theta_1, \phi_1) - B_C(t_2, r_2, \theta_2, \phi_2)$ of the magnetic observations taken by *Swarm Alpha* and *Charlie*. For each observation B_A (from *Swarm Alpha*) fulfilling the above selection criteria we

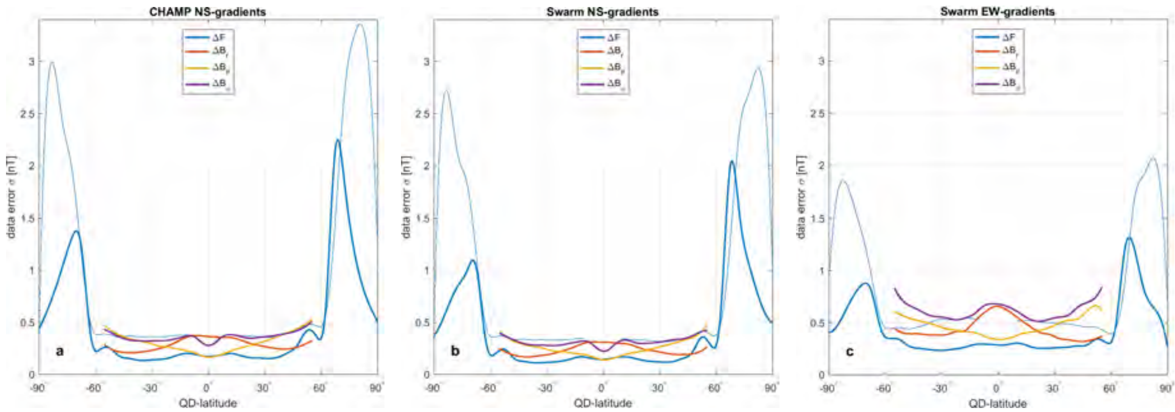

Figure 3. Assigned data uncertainties σ for the CHAMP (left) and *Swarm* (middle and right) satellite gradient data, in dependence on QD latitude. Left: CHAMP Along-track "gradient" (15 sec finite difference) data, approximating the North-South gradients $\delta F_{\text{NS}}, \delta \mathbf{B}_{\text{NS}}$. Middle: same, but for *Swarm*. Right: East-West "gradient" data (difference between simultaneous observations of *Swarm* Alpha and Charlie) $\delta F_{\text{EW}}, \delta \mathbf{B}_{\text{EW}}$. The thin blue curves represent estimated scalar gradient data uncertainties for sunlit conditions.

selected the corresponding value B_C (from *Swarm Charlie*) that was closest in co-latitude θ, with the additional requirement that the time difference $|\delta t| = |t_1 - t_2|$ between the two measurements should not exceed 50 secs.

The bottom panel of Figure 2 shows the number of data points in bins of 2-months length in time. The amount of *Swarm* data is twice that of the CHAMP data, owing to the availability of EW gradient data which is unique to the *Swarm* constellation mission. In total we use 5.2 mio NS gradient data $\delta F_{\text{NS}}, \delta \mathbf{B}_{\text{NS}}$ (2.4 mio from CHAMP and 2.8 mio from *Swarm*), and 0.95 mio EW gradient data $\delta F_{\text{EW}}, \delta \mathbf{B}_{\text{EW}}$ (*Swarm* only). This amounts to 6.2 mio data points in total.

We removed from all the magnetic observations predictions of the core field (up to spherical harmonic degree $n = 14$) and of the large-scale magnetospheric field as given by the CHAOS-6_x2 model (which is an extension of the model described in Finlay et al. (2016)). In the following, we will denote as "data" these differences between magnetic observations and model predictions.

We assign to each data point a data uncertainty that depends on QD latitude. These data uncertainties have been determined from the residuals of the data (observations minus core, crustal and magnetospheric field contributions) w.r.t. the CHAOS-6-x2 model by binning the residuals in QD latitudinal bins of 5° width and estimating standard deviation σ using a robust approach (Huber weighting). Figure 3 shows the assigned data uncertainties for the various data sources and for the CHAMP (left) and *Swarm* (middle and right) satellites.

2.2 Selection of magnetic field data for model assessment

For testing and evaluation purposes we selected a data set of magnetic field observations $\mathbf{B}$ and F, using data selection criteria similar to those used for constructing the CHAOS-6 model (Finlay et al. 2016). Since magnetic field data are more influenced by un-modelled external field contributions compared to gradient data it is necessary to restrict to periods of lower geomagnetic activity when selecting field data compared to selecting gradient data. Following Olsen et al. (2015) we take magnetic field data only during extremely quiet conditions when the RC index change by at most 2 nT/h (for gradient data we allow for changes up to 3 nT/hr) and when the geomagnetic activity index $Kp \leq 2^0$ (for gradient data we allow values for $Kp \leq 3^0$). As for gradient data we take vector magnetic field observations only from non-polar latitudes while scalar field data are used only in the polar regions.

In order to minimise temporal correlation of the data we down-sampled the field values to 2 minutes. This yields 72,000 polar scalar data (35,500 from CHAMP and 36,500 from *Swarm*) and 250,000 vector triplets (120,000 from CHAMP and 130,000 from *Swarm*). Note that this data set has not been used in the construction of the final LCS-1 lithospheric model.

3 MODEL PARAMETRISATION AND ESTIMATION

We describe the lithospheric magnetic field $\mathbf{B} = -\nabla V$ using a magnetic scalar potential V of internal origin. Following O'Brien & Parker (1994) and Kother et al. (2015), V is modelled as a linear combination of K equivalent potential field sources (monopoles) of amplitudes q_k, located at the positions $\mathbf{s}_k = [r_k, \theta_k, \phi_k], k = 1, \dots, K$ where r, θ, ϕ are spherical coordinates. The potential at the position of the N data positions $\mathbf{r}_i = [r_i, \theta_i, \phi_i], i = 1, \dots, N$ produced by the superposition of the K point sources is

$$V(\mathbf{r}_i) = \sum_{k=1}^{K} q_k \frac{r_k^2}{r_{ik}} \tag{1}$$

where $r_{ik} = |\mathbf{r}_i - \mathbf{s}_k|$ and μ_{ik} are the distance and angle between the position vectors of the observations, $\mathbf{r}_i$, and of the point sources $\mathbf{s}_k$, respectively;

$$r_{ik} = \sqrt{r_i^2 + r_k^2 - 2 r_i r_k \cos(\mu_{ik})} \tag{2a}$$

$$\cos(\mu_{ik}) = \cos(\theta_i)\cos(\theta_k) + \sin(\theta_i)\sin(\theta_k)\cos(\phi_i - \phi_k). \tag{2b}$$

We use $K = 35,000$ point sources placed horizontally on an approximately equal area grid defined by the "Recursive Zonal Equal Area (EQ) Sphere Partitioning" algorithm of Leopardi (2006). The angular distance d between each point and its nearest neighbours varies between 1.07° and 1.1°, with a median value of 1.088° corresponding to 120.7 km at the Earth's surface. Essentially the same value is found by dividing Earth's surface $4\pi a^2$ (approximated by a sphere of radius a) into K quadratic tesseroids of equal size d^2, which results in $d = a\sqrt{(4\pi/K)} =$ 120.7 km. The depth of the point sources is chosen as 100 km below the Earth's surface as given by the World Geodetic System 1984 (WGS84) ellipsoid.

Collecting the magnetic field observations $(B_{r,i}, B_{\theta,i}, B_{\phi,i}), i = 1, \ldots, N$ in the data vector $\mathbf{d_B}$, and the strength of the point sources, $q_k, k = 1, \ldots K$, in the model vector $\mathbf{m}$ results in the linear relationship

$$\mathbf{d_B} = \mathbf{G_B m}\,. \tag{3}$$

The elements of the data kernel matrix $\mathbf{G_B}$ are given in Appendix A of Kother et al. (2015).

Scalar data (i.e. magnetic field intensity) were treated by projecting the elements of the kernel matrices $\mathbf{G}_{\mathbf{B},r}, \mathbf{G}_{\mathbf{B},\theta}, \mathbf{G}_{\mathbf{B},\phi}$ describing the vector field components at data location $\mathbf{r}_i$ on the unit vector $\hat{\mathbf{B}} = \mathbf{B}_{mod}/|\mathbf{B}_{mod}|$ of the ambient core field (given by the CHAOS-6 core field model for spherical harmonic degrees $n = 1 - 14$) at that location.

Gradient data were handled in a manner similar to that described in Kotsiaros et al. (2015) by taking the difference of the kernel matrices $\mathbf{G_B}$ corresponding to the two positions (r_1, θ_1, ϕ_1) and (r_2, θ_2, ϕ_2).

Collecting the observations of vector gradient $\delta\mathbf{B}$ and scalar gradient δF in the data vector $\mathbf{d}$, we follow Farquharson & Oldenburg (1998) in estimating the model vector $\mathbf{m}$ by minimising the cost function $\Phi = \Phi_{data} + \alpha^2 \Phi_{model}$ consisting of the sum of the data misfit norm $\mathbf{e}^T \mathbf{W}_d \mathbf{e}$ and the model regularisation norm $\alpha^2 \mathbf{m}^T \mathbf{R m}$:

$$\Phi = \mathbf{e}^T \mathbf{W}_d \mathbf{e} + \alpha^2 \mathbf{m}^T \mathbf{R m} \tag{4}$$

where $\mathbf{e} = \mathbf{d} - \mathbf{G m}$ is the data misfit vector (difference between data $\mathbf{d}$ and model predictions $\mathbf{d}_{mod} = \mathbf{G m}$), $\mathbf{W}_d$ is the diagonal data weight matrix with elements w/σ^2 (where σ^2 are the data variances as shown in Figure 3 and w are the robust data weights), and $\mathbf{R}$ is a model regularisation matrix which results in the minimization of the global average of $|B_r|$ at Earth's surface ellipsoid. The parameter α^2 defines the relative weighting of data misfit vs. model regularisation and thus controls the amount of model regularisation.

For constructing the model regularisation matrix $\mathbf{R}$ we synthesize, for a given model $\mathbf{m}$, the radial magnetic field B_r at 50,000 equally distributed locations on the Earth's surface (ellipsoid, median spacing 100×100 km); collecting these values in the vector $\mathbf{b} = \{B_r\}$ allows us to write this transformation in matrix form as $\mathbf{b} = \mathbf{A m}$. The model regularisation matrix used in our scheme to implement the L1 norm is then iteratively found as $\mathbf{R} = \mathbf{A}^T \mathbf{W}_m \mathbf{A}$ where $\mathbf{W}_m$ is a diagonal matrix with elements $1/(B_r^2 + \epsilon^2)$, where $\epsilon = 10^{-6}$ nT is Ekblom's parameter (Farquharson & Oldenburg 1998).

We minimise the cost function eq. (4) by *Iteratively Reweighted Least Squares* using data weights w defined by Tukey's bi-weight function with tuning constant $c = 4.5$ (Farquharson & Oldenburg 1998). Both $\mathbf{W}_d$ and $\mathbf{R}$ are updated in each iteration until convergence. The iteration is terminated when the norm of the model change was less than 0.01% of the model norm. To ensure that the divergence of the magnetic field vector is zero, the sum over all monopole amplitudes has to vanish, $\sum_{k=1}^{K} q_k = 0$; this constraint is handled by the method described in section 4.5 of Kother et al. (2015).

In a final step we transform the point-source representation to a spherical harmonic expansion. Noting that the potential V of eq. (1) can also be described by a spherical harmonic expansion

$$V(r_i, \theta_i, \phi_i) = a \sum_{n=1}^{\infty} \sum_{m=0}^{n} \left(g_n^m \cos m\phi_i + h_n^m \sin m\phi\right) \left(\frac{a}{r_i}\right)^{n+1} P_n^m(\cos\theta_i), \tag{5}$$

the Gauss coefficients (g_n^m, h_n^m) are related to the point-source amplitudes q_k by means of (cf. eq. 5+6 of Kother et al. 2015)

$$g_n^m = \sum_{k=1}^{K} \left(\frac{r_k}{a}\right)^{n+2} q_k P_n^m(\cos\theta_k)\cos(m\phi_k) \tag{6a}$$

$$h_n^m = \sum_{k=1}^{K} \left(\frac{r_k}{a}\right)^{n+2} q_k P_n^m(\cos\theta_k)\sin(m\phi_k). \tag{6b}$$

Collecting the Gauss coefficients in the vector $\mathbf{g} = \{g_n^m, h_n^m\}$, this relationship can be written in matrix form as

$$\mathbf{g} = \mathbf{D m}. \tag{7}$$

We will use the transformation matrix $\mathbf{D}$ in section 4.2 in our discussion of the formal variances of the spherical harmonic expansion coefficients.

Table 1. Number N of data points, (Tukey-weighted) mean and rms misfit (in nT) of NS scalar ($\delta F_{\rm NS}$) and vector ($\delta B_{r,\rm NS}, \delta B_{\theta,\rm NS}, \delta B_{\phi,\rm NS}$) gradient data, and of EW scalar ($\delta F_{\rm EW}$) and vector ($\delta B_{r,\rm EW}, \delta B_{\theta,\rm EW}, \delta B_{\phi,\rm EW}$) gradient data, at polar ($> \pm 55°$) and non-polar ($< \pm 55°$) QD latitudes and for dark (sun at least 10° below horizon) and sunlit conditions.

	CHAMP			*Swarm* Alpha			*Swarm* Charlie			*Swarm* Alpha – Charlie		
	N	mean	rms	N	mean	rms	N	mean	rms	N	mean	rms
$\delta F_{\rm NS,polar}$	491767	-0.03	1.50	283355	-0.04	1.38	283430	-0.05	1.37			
$\delta F_{\rm NS,non-polar,dark}$	691933	-0.01	0.13	416965	-0.00	0.14	417455	-0.00	0.14			
$\delta B_{r,\rm NS,dark}$	469839	0.00	0.29	261843	-0.00	0.22	262195	-0.00	0.23			
$\delta B_{\theta,\rm NS,dark}$	469839	-0.00	0.31	261843	-0.00	0.24	262195	-0.00	0.25			
$\delta B_{\phi,\rm NS,dark}$	469839	-0.00	0.36	261843	-0.00	0.29	262195	-0.00	0.30			
$\delta F_{\rm NS,non-polar,sunlit}$	759368	0.01	0.34	456084	0.01	0.31	455305	0.01	0.31			
$\delta F_{\rm EW,polar}$										279628	-0.20	0.93
$\delta F_{\rm EW,non-polar,dark}$										414730	-0.07	0.27
$\delta B_{r,\rm EW,dark}$										259111	-0.00	0.42
$\delta B_{\theta,\rm EW,dark}$										259111	0.00	0.44
$\delta B_{\phi,\rm EW,dark}$										259111	0.01	0.57

4 RESULTS

4.1 Model statistics

We estimated models using different combination of data sets, including models that are only determined from low-altitude CHAMP data, models that are determined from field and gradient data (using a combination of the data sets described in sections 2.1 and 2.2), and models that do not make use of East-West gradient data. The models were assessed by visual inspection of maps of B_r and F at Earth's surface, by their spatial power spectra shown later, and by their formal model covariances (details are given below in subsection 4.2). From these investigations we conclude that a model determined entirely from magnetic gradient data (no direct use of magnetic field data) using a regularisation parameter $\alpha^2 = 3$ gave the most promising result. In the following we will concentrate on that model, which we refer to as LCS-1.

Table 1 lists the number of data points, together with means and root mean squared (rms) misfit values. Means and rms are the weighted values calculated from the model residuals $\mathbf{e} = \mathbf{d} - \mathbf{d}_{mod}$ using the robust Tukey weights w obtained in the final iteration. RMS misfits of the nightside non-polar scalar gradient data are impressive: 0.14 nT for the NS gradient of all three satellites, and 0.27 nT for the EW gradient data. The dayside rms misfits are slightly higher (0.31 to 0.34 nT for the NS gradient) due to enhanced ionospheric contributions. As expected, the rms misfit is also higher in the polar regions: 1.37 nT for *Swarm* and 1.50 nT for CHAMP for the along-track gradient $\delta F_{\rm NS}$, and 0.93 nT for the EW gradient $\delta F_{\rm EW}$. The rms misfit of the (non-polar) vector gradient data is slightly higher compared to scalar gradient data, varying between 0.23 nT and 0.36 nT for the NS gradient and between 0.42 nT and 0.57 nT for the EW gradient.

These numbers refer to the data that have been used to construct the final LCS-1 model. The difference between LCS-1 model predictions and magnetic field values (cf. section 2.2) that have *not* been used in model determination yields weighted rms values of about 4.5 nT for the scalar field in polar regions and of 1.4 nT to 2.8 nT for the vector components at non-polar latitudes.

All these numbers demonstrate the high quality and consistency of the satellite data, and thereby also of the lithospheric model derived from these data.

4.2 On the contribution of Swarm constellation data

The LCS-1 model includes, in addition to along-track (North-South) gradient data from the CHAMP satellite, North-South and East-West gradient data as provided by the *Swarm* satellite constellation. However, the *Swarm* spacecraft are presently at much higher altitude (450 km) than CHAMP during its final years ($<$ 350 km), and *Swarm* therefore measures a much weaker lithospheric signal than CHAMP. The question therefore arises how much do the *Swarm* satellite data contribute to the combined model, and whether or not they improve on a CHAMP-only model given the higher altitude of *Swarm*.

In order to investigate this we construct the model covariance matrix $\mathbf{C}_m$ for models determined using different data set combinations. The diagonal elements of $\mathbf{C}_m$ contain the variances σ_m^2 of the model parameters and enable an assessment of the relative contributions from the various data sets. A similar approach has been used by Olsen et al. (2010) to assess the relative performance of different satellite constellation concepts for geomagnetic field modelling.

The model covariance matrix, in the absence of regularisation ($\alpha^2 = 0$), is given by

$$\mathbf{C}_m = \left(\mathbf{G}^T \mathbf{W}_d \mathbf{G}\right)^{-1}. \tag{8}$$

To construct this matrix no actual data are used; the matrix is entirely calculated from the positions of the data points, the assigned data uncertainties, and the data type (field or gradient data). However, in our case $\mathbf{C}_m$ depends indirectly on the data through the robust data weights w which depend on the data residuals $\mathbf{e}$, i.e. on the differences between the observations and model predictions.

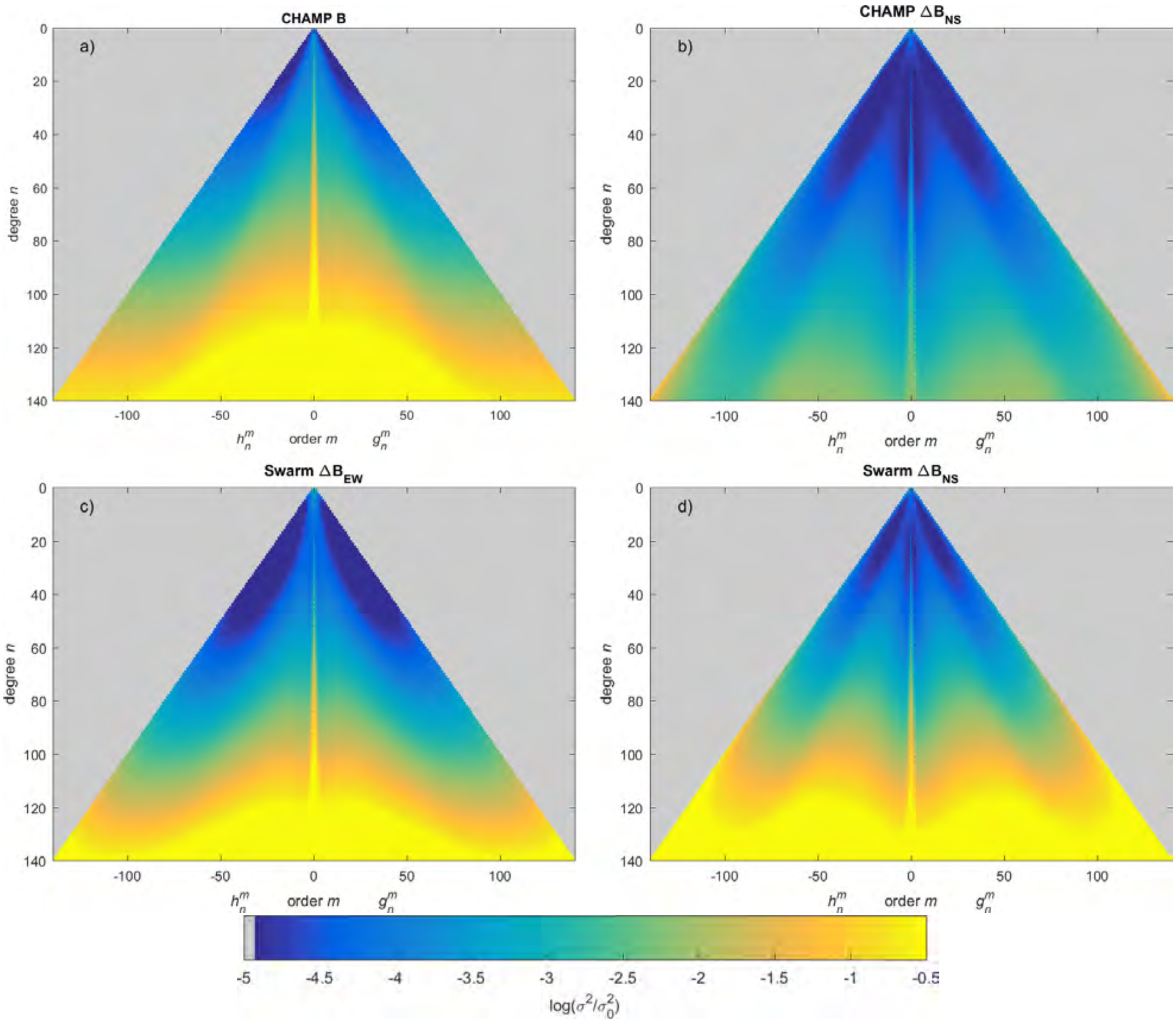

Figure 4. Variance of the spherical harmonic expansion coefficients g_n^m, h_n^m for various input data sets. Blue corresponds to well resolved coefficients (i.e. low variance) while yellow corresponds to poorly resolved coefficients (i.e. large variance).

Eq. (8) describes the covariances of the estimated point source amplitudes q_k. For comparing models determined from different data sets it is more convenient to look at the covariances of the spherical harmonic expansion coefficients $\mathbf{g} = \{g_n^m, h_n^m\}$. Using the inverse of $\mathbf{D}$ from eq. (7), the covariances of g_n^m, h_n^m are

$$\mathbf{C}_{g,h} = \left(\left(\mathbf{D^{-1}}\right)^T \mathbf{G}^T \mathbf{W}_d \mathbf{G}\, \mathbf{D^{-1}} \right)^{-1}, \tag{9}$$

and the diagonal elements of $\mathbf{C}_{g,h}$ are the variances $\sigma_{g,h}^2$ of the coefficients g_n^m, h_n^m.

Figure 4 shows the dependence of $\sigma_{g,h}^2$ on spherical harmonic degree n and order m (showing only up to $n = 140$), with $m \geq 0$ referring to the coefficients g_n^m and $m < 0$ referring to h_n^m. Since the *absolute* values of $\sigma_{g,h}^2$ rely on the assumption of uncorrelated data uncertainties – a condition that might not be fulfilled – we present here only the *relative* value of $\sigma_{g,h}^2$ on an arbitrary scale by dividing with a reference variance (arbitrarily chosen to be $\sigma_0^2 = 1$ nT^2) which, however, is the same for all the cases presented in the figure. Blue colours show low variances while yellow represent larger variances.

Figure 4a shows the variances $\sigma_{g,h}^2$ for a model that is based on CHAMP scalar and vector field (but no gradient) data, while Fig. 4b presents variances for a model that uses CHAMP scalar and vector NS gradient (but no field) data. NS gradient data improve the determination in particular of spherical harmonic terms of degree n larger than approximately 100 as can be seen from the reduced variance of those coefficients. NS gradient data are, however, not able to improve high-degree near-sectoral coefficients (i.e. coefficients with order $m \approx n$).

The variances shown in Fig. 4b are representative of what can be achieved with single satellite NS gradient data taken at altitudes of

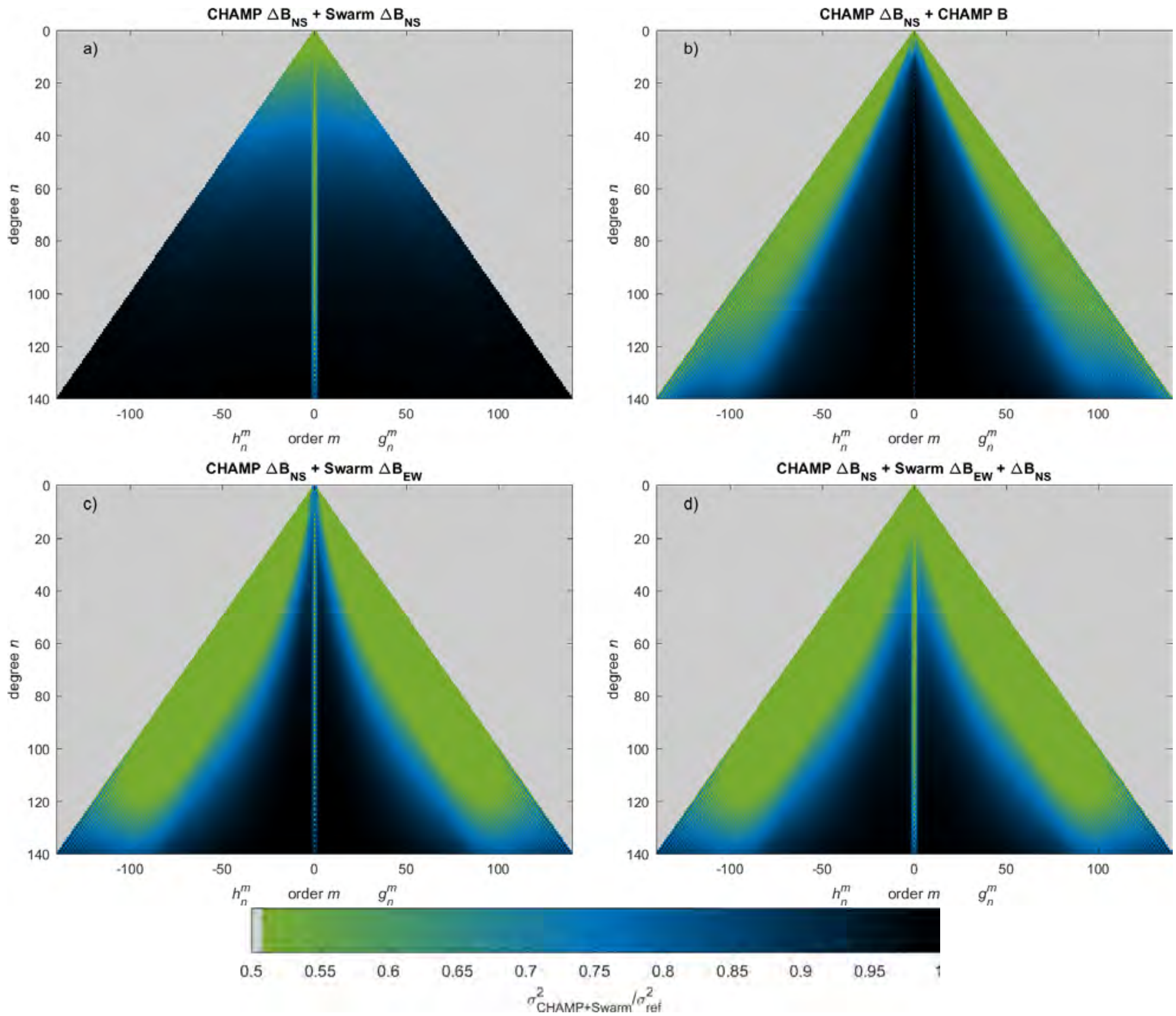

Figure 5. Left: Variance ratio for models estimated from combined CHAMP + *Swarm* data sets, compared to the CHAMP-only model of Figure 4b). Green corresponds to potential model improvement (i.e. reduction of variance), while black corresponds to no improvement.

350 km and below. The corresponding results for the *Swarm* satellite mission when both lower spacecraft are treated as single satellites (i.e. no use of EW gradient data) is shown in Fig. 4d; the variances are considerably larger, in particular for higher degrees n, due to the higher altitude of the *Swarm* satellites.

However, taking advantage of the unique constellation aspect of *Swarm*, we estimated coefficient variances from a data set that only consists of *Swarm* EW gradient data (i.e. no use of NS gradient data). The results, presented in Fig. 4c, are similar as those obtained with *Swarm* NS gradient data (Fig. 4d) and CHAMP field data (Fig. 4a).

From these results it is obvious that the low-altitude CHAMP NS gradient data set is the single data set which provides most information on the lithospheric field. We therefore will use the CHAMP gradient-only model of Figure 4b as reference in an investigation of the *incremental* value of adding other data sets in addition to the CHAMP NS gradient data.

Figure 5 shows the ratio of the coefficient variances of different data set combinations, divided by the variances of the CHAMP gradient-only solution (which is now taken as the reference model). A value of that ratio close to 1 (presented by black) indicates no improvement, whereas values below 1 (green and blue) represent a potential model improvement.

Results for a model that is based on CHAMP and *Swarm* NS gradient data (but neither field nor *Swarm* EW gradient data) are shown in Figure 5a: the variance ratio is close to 1 for most of the coefficients, indicating only marginal improvement of the combined model compared to the CHAMP-only reference solution (panel 4b). Exceptions are low-degree coefficients ($n <\approx 40$) and the near-zonal terms (i.e. terms with order $m \approx 0$); they are obviously improved for all degrees n. The reason for this could be the slightly higher orbital inclination of the lower *Swarm* pair (87.4°) compared to CHAMP (87.2°), thereby reducing the "polar gap" (which is the region around the geographic poles that is left unsampled).

Inclusion of CHAMP field data (the additional data set described in section 2.2 with data uncertainties assigned similar to the approach used for the gradient data) together with the CHAMP NS gradient data results in an improvement of the near-sectoral terms ($m \approx n$), as can be seen from Figure 5b.

However, a similar variance reduction can also be achieved when including *Swarm* EW gradient data instead of the CHAMP field data, as demonstrated in Fig. 5c. (Note that the actual model improvement might be even larger than the variance reduction shown in this figure since gradient data are less affected by remaining external field contamination.)

We finally determined the model improvement when using *Swarm* NS and EW gradient data together with the CHAMP NS gradient data. As expected, this combines the model improvements of Figures 5a and c, resulting in variance ratios shown in Fig. 5d.

We conclude that combining CHAMP NS and *Swarm* NS and EW gradient data leads to a significant reduction of variances by up to 50% (corresponding to a reduction of the variance ratio from 1 to 0.5) compared to a CHAMP-only model, clearly demonstrating that *Swarm* data can improve lithospheric field models, despite their higher altitude, and without the need to include magnetic field data.

5 DISCUSSION

Maps of the vertical component Z and of the scalar anomaly F at Earth's surface from the LCS-1 model are shown in Figure 6, synthesized for spherical harmonic degrees $n = 16 - 185$. The maps show the expected anomaly features throughout the world: the cratonic regions of the continents (Archeans and Proterozoic domains) have stronger anomalies than the accreted Paleozoic and younger crusts and the long wavelength features associated with and sub-parallel to the oceanic magnetic reversal stripes are seen consistently on or near widely separated isochrones, especially near the edges of the Cretaceous quiet zones where the width of the magnetic contrast zones is large. For the first time we can observe from maps prepared from the satellite data alone the EW oceanic features associated with the reversal stripes formed in the last 50 Ma of separation history of Australia from Antarctica. In previous field models, these features have been overwhelmed presumably by along-track noise lending them more NS trending appearance which is not expected from the alignment of stripes and their offsets across transform faults in this region.

A number of other features on the ocean crust are seen for the first time. For example, there are NS trending lows in the vertical component map that appear to be associated with the NS trending 85° E ridge in the Bay of Bengal. Near the magnetic equator, NS features do not have distinct anomaly signatures in the intensity anomaly and this characteristic of the 85° E ridge has not previously been recognized as the near surface magnetic anomaly data are intensity field and the Z-component in MF7 does not show a distinct correlation with the ridge. A second new feature is a linear doublet of NS trending anomalies along the southern segment of the 90° E ridge (between 15° S and 30° S latitudes where it lies just west of the 90° E longitude). Only the anomaly features associated with the Broken Ridge in the southernmost part of this NS feature were known prior to this study as there are only a few marine profiles in the southern segment of the 90° E ridge.

Another interesting feature is the NS trending anomaly south of the Walvis Ridge within the Cretaceous quiet zone (between 30° S and 45° S latitudes and along approx. 5° E longitude) and not parallel to the nearby edge of the Cretaceous quiet zone. Available marine magnetic grids (e.g., EMAG3 and EMAG2_V3 models) show data in the region but in the tracks available to us in the region there are many gaps as well. Since the LCS-1 model has more uniform data coverage in the region, we believe this feature is real and could be associated with coalescence of magnetic anomalies (Taylor & Ravat 1995) leading to linear trends (Ravat 2011) from processes such as later magmatic intrusions, variable magma supply, variable Fe content, variable magnetic thickness, geomagnetic excursions and variability of the paleomagnetic field (Granot et al. 2012). The EMM2015 lithospheric field model developed by Maus and co-workers (www.ngdc.noaa.gov/geomag/EMM/) and the WDMAM2 model (Lesur et al. 2016), truncated to degree 185, also have features cross-cutting the central South Atlantic isochrones. This region also has very few marine magnetic tracks similar to the southern oceans regions away from continental margins. In LCS-1 these cross-cutting features are significantly subdued.

On the continents, where there are aeromagnetic data in EMM2015 and WDMAM2, the features in LCS-1 (in both Z and F, Figure 6) are similar to those models truncated at degree 185. The importance of LCS-1 is apparent where the aeromagnetic or near-surface data do not exist or are sparse. The detail for the Bangui anomaly region and several regions in Africa has improved substantially in comparison to the truncated EMM2015 or WDMAM2 models. The boundaries of features of Bangui are better defined in LCS-1 Z-component anomalies. Similarly, the Kenya and Ethiopian domes are places where NS features are expected because of the geology of the East African Rift but could not be observed in previous maps. In the LCS-1 Z-component map (Figure 6 top), we now observe a distinct alignment of positive features skirting east of Lake Victoria and also an alignment of negative features on the western flank of the Ethiopian dome. Not all sources of the lows can be related to the rift or the flood basalts and these need to be investigated further in detail.

The lithospheric power is higher in continental regions compared to oceanic regions, as expected due to the generally thicker continental/cratonic crust. The global average of B_r^2 at Earth's surface is 48.5 nT^2 (for spherical harmonic degrees $n = 16 - 185$), the power in continental regions is 66.1 nT^2 while that of the oceanic regions is only 39.4 nT^2. Use of L1 model regularisation (i.e. minimizing the global average of $|B_r|$ at the surface) helps in achieving this difference between continents and oceans; a L2-regularised model (i.e. constructed to minimise the global average of B_r^2) that has the same *global* power (48.5 nT^2) as the L1 model has a smaller continental power (63.6 nT^2) and higher oceanic power (40.1 nT^2) than the L1-regularised model. As a result, the L2-regularised model shows more spurious features

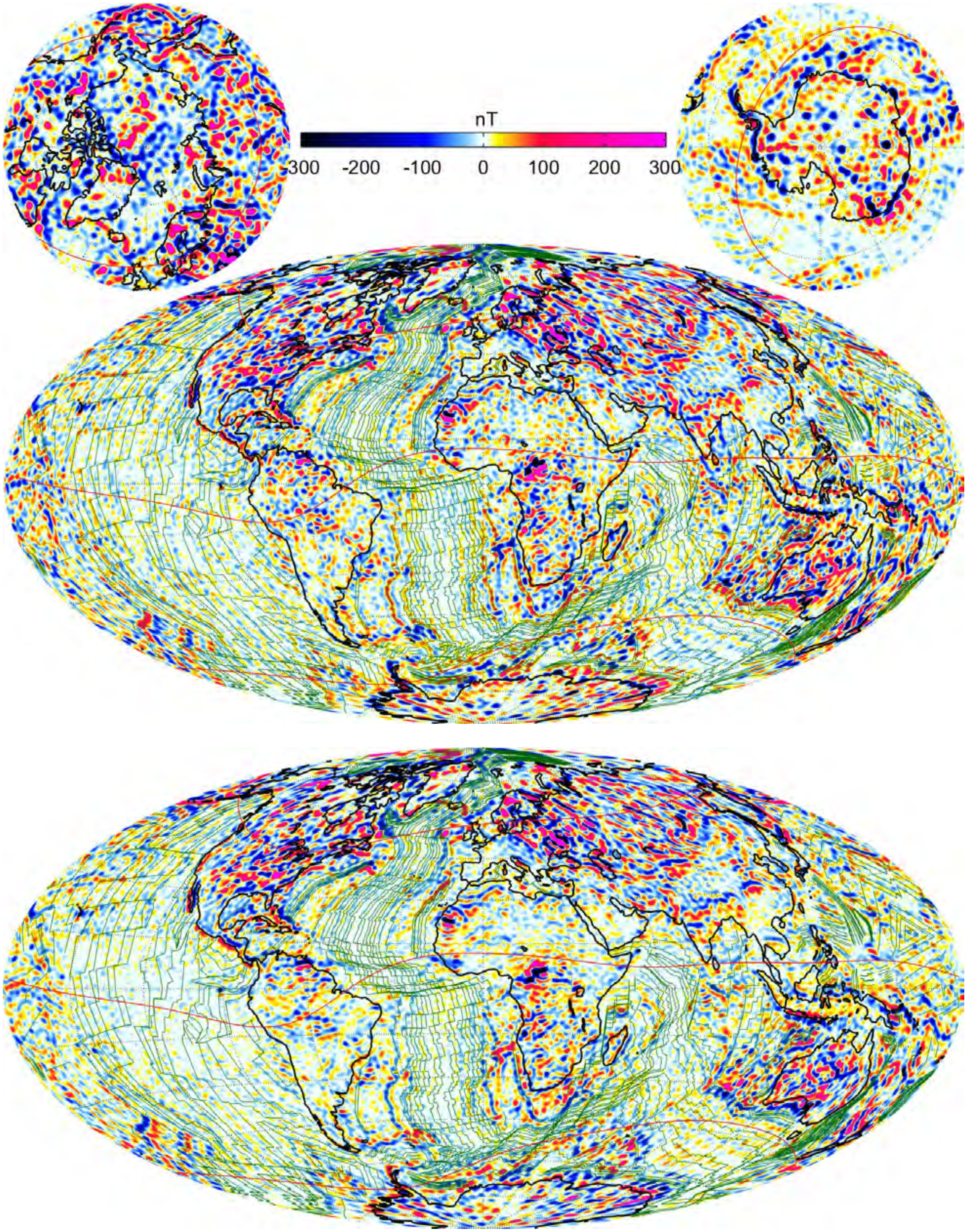

Figure 6. Maps of the lithospheric field vertical component Z (top) and of scalar anomaly F (bottom) at Earth's surface (ellipsoid) from the LCS-1 model, for spherical harmonic degrees $n = 16 - 185$. Red curves represent QD-latitudes of $\pm 55^{\circ}$, resp. 0°, while green curves show isochrones

in oceanic regions than the L1-regularised model with the same global power; avoiding spurious oceanic features using L2-regularization requires heavier damping which results in reduced global power. This clearly illustrates an advantage of L1-regularisation for deriving global models that include both high-amplitude (e.g. continental) and low-amplitude (e.g. oceanic) regions.

Global *Lowes-Mauersberger* spatial spectra for various lithospheric field models are compared in the top panel of Figure 7. There is excellent agreement between the various models for spherical harmonic degrees up to, say, $n = 90$ (the power, a quadratic measure, of our L1-regularised model LCS-1 is slightly less than that of the L2-regularised models MF7, CHAOS-6 and EMM2015). For degrees $n = 90$ to 130 the power of LCS-1 and MF7 is at a similar level while that of CHAOS-6 is slightly higher (probably indicating limitations of CHAOS-6 at higher degrees). The decrease of power for $n > 130$ is influenced by the regularisation. The EMM2015 model is a combination of MF7 (for $n \leq 133$) and the EMAG2_V3 marine/aeromagnetic data sets ($n \geq 133$), formally going up to spherical harmonic degree and order 720. The EMAG2_V3 data set is, however, not of uniform global coverage, and therefore the EMM2015 model, although formally a *global* model, only contains accurate short-wavelength lithospheric field features (corresponding to degrees $n > 133$) in regions with sufficient near-surface data coverage. Although EMM2015 shows the highest power of all models at $n > 133$ it is therefore likely that EMM2015 also underestimates the global lithospheric power above degree 133.

The lower panel of Figure 7 shows the degree correlation ρ_n (see eq. 4.23 of Langel & Hinze (1998) for a definition) between LCS-1 and various other field models. The degree correlation is above 0.9 for all degrees $n \leq 100$ and above 0.8 for all degrees $n \leq 130$. No other satellite-derived global lithospheric models exist for degrees above $n = 133$ and therefore an assessment of the high-degree part of our model is not straightforward. Despite the limitations of EMM2015 in providing a global representation of the lithospheric field for degrees $n > 133$, the degree correlation between LCS-1 and EMM205 for $n = 134$ to 140 (where EMM2015 is entirely based on near-surface data where available) is above 0.7, which is encouraging.

Next we assess our lithospheric field model using independent near-surface magnetic data. Australia is the only continent with a near perfect regional aeromagnetic coverage. This coverage was possible due to the backbone of baseline Australia-wide Airborne Geophysical Surveys (AWAGS and AWAGS2 flight lines supplemented with a network of magnetic base stations, Milligan et al. (2010)); thus, this region has the best long wavelength control for assessing different global models. We compare the wavelength content of LCS-1, MF7, and EMM2015 models with respect to this Australian data set. Figure 8 shows a spatial comparison of magnetic field intensity anomalies in the Australian aeromagnetic anomaly grid (filtered with a lowpass wavelength cutoff of 225 km) and the LCS-1 and MF7 models. It is clear that most of the anomaly features in the 225 km filtered data are observable in the LCS-1 field intensity anomalies with nearly the same resolution (except in south-central Australia). MF7 is limited by its highest spherical harmonic degree and order of 133.

The visual comparison in Figure 8 is corroborated with the estimates of coherency (which is comparable to global degree correlations shown in the bottom panel of Figure 7) in the central third of Australia (Figure 9). For estimating coherency (normalized cross-spectrum, see eq. 9.1.36 of Priestley 1981) between two maps we use two identical data windows and 2D multitapering (Hanssen 1997) to improve statistical properties of the low wavenumbers of the spectra of the signals (because there are only a few estimates of Fourier amplitudes available in the low wavenumbers), and compute annular averages over a band of wavenumbers.

If certain wavelengths are not present in the data sets being compared or the signal at those wavelengths is corrupted or phase-shifted, coherency is reduced. Since the Australian magnetic data are of very high fidelity and full spectrum, based on the degree/order of the spherical harmonic expansion of EMM2015, LCS-1, and MF7 models, we expect their coherency with the Australian aeromagnetic data to degrade around wavelengths of 55 km, 215 km, and 300 km, respectively. This is seen to occur at the coherency value of 0.5 in each case and is reasonable. EMM2015 reflects the fact that the model uses the Australian aeromagnetic database for wavelengths less than 300 km. LCS-1 has clearly benefited in terms of resolution by using gradients of the fields from CHAMP and *Swarm* satellites. LCS-1 also has better coherence at the longest wavelengths ($900 - 1500$ km) in the central Australian spectral window. Similar analysis has been performed over other Australian regions with similar results.

The coherency analysis has also been performed over the U.S. where the U.S. NURE aeromagnetic data have been processed using the CM4 continuous core field model (Sabaka et al. 2004) instead of IGRF/DGRF and merged with the North American magnetic anomaly database. The continental U.S. part of the NURE-NAMAM2008 database is full spectrum to the extent possible (Ravat et al. 2009) without flying new back-bone aeromagnetic surveys as done in Australia. This analysis suggests that the wavelength content of the LCS-1 model is limited to 250 km while MF7 performs similarly to the central Australian case. EMM2015 on the other hand degrades much more rapidly in North America compared to Australia, reaching coherency of about 0.5 at 85 km wavelength. This is because EMM2015 used Decade of North American Geology (DNAG) magnetic database in the U.S. and not the intermediate and long-wavelength corrected NURE-NAMAM2008 database (Ravat et al. 2009). Since no other regional compilations in the world has proven high quality intermediate- and long-wavelength coverage, based on the Australian and the U.S. comparisons, we conclude that the LCS-1 model will be able to improve satellite based magnetic anomaly definition globally at wavelengths > 250 km (i.e. for degrees $n < 160$).

Where can LCS-1 help immediately in magnetic interpretations? Clearly, that would be in regions of the world not covered presently with near-surface magnetic data. This covers large parts of the African continent, regions in South America where data are not publicly available and parts of the southern oceans without adequate magnetic ship-tracks. In Figure 10, we show 3-D surface plots of the field intensity magnetic anomaly over one of the highest amplitude magnetic features on the Earth, the Bangui anomaly in central Africa. The associated high-low-high pattern of anomalies has been interpreted by different researchers since the days of the POGO and Magsat satellites: as magnetic contrast between a large crustal-scale intrusive body situated under the Congo basin and the surrounding central African shields (Regan et al. 1975); as strongly magnetized thick iron-formation as well as differences in magnetic contrasts between the basins and surrounding shields (Ravat

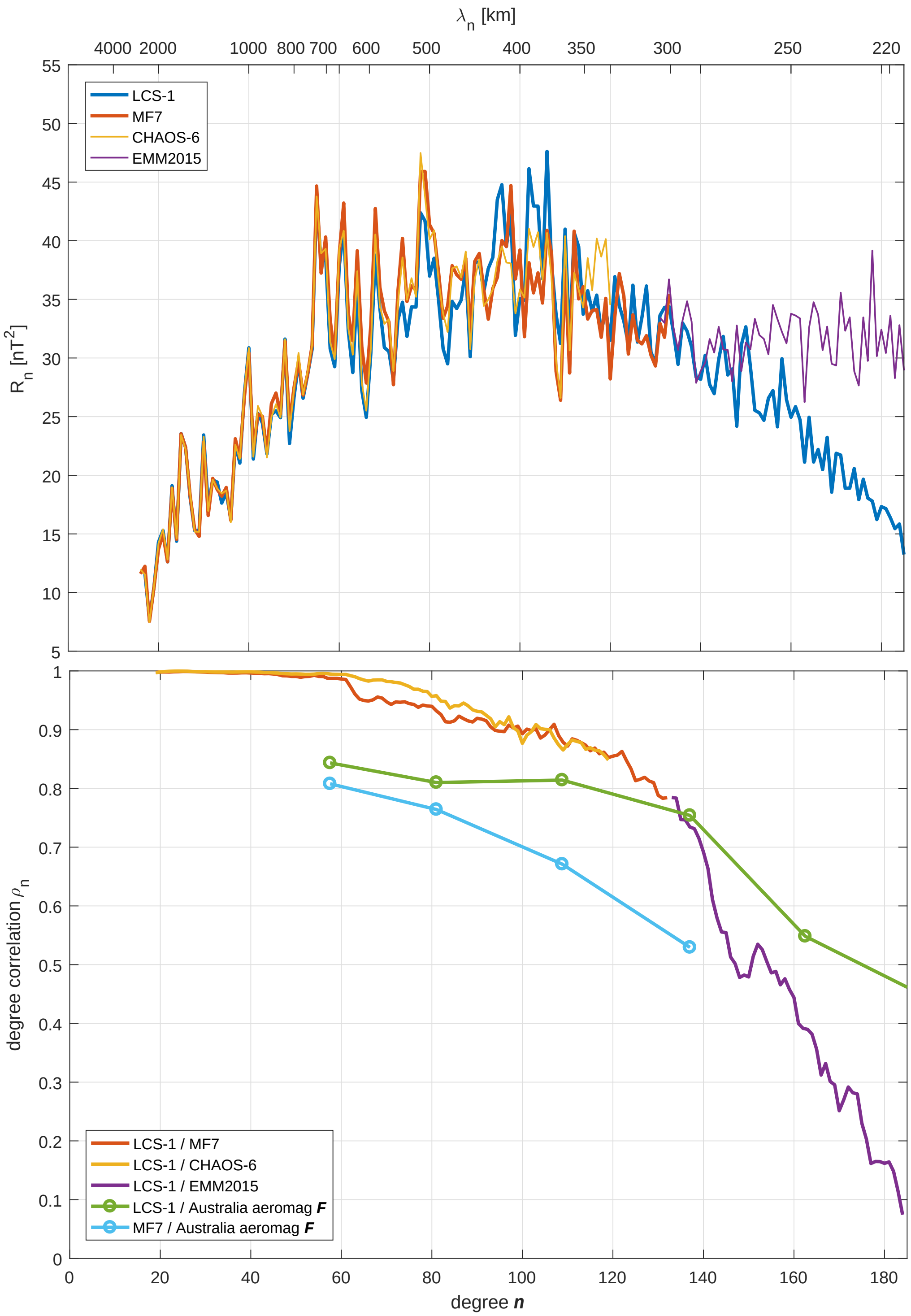

Figure 7. Top panel: Spatial power spectrum at Earth's surface for various lithospheric field models in dependence on spherical harmonic degree ρ_n (bottom $x-$axis), resp. equivalent wavelength λ_n (top axis). Bottom panel: spherical harmonic degree correlation (solid curve). For comparison the regional coherency (dashed curves) for Australia are also shown (cf. Fig. 9).

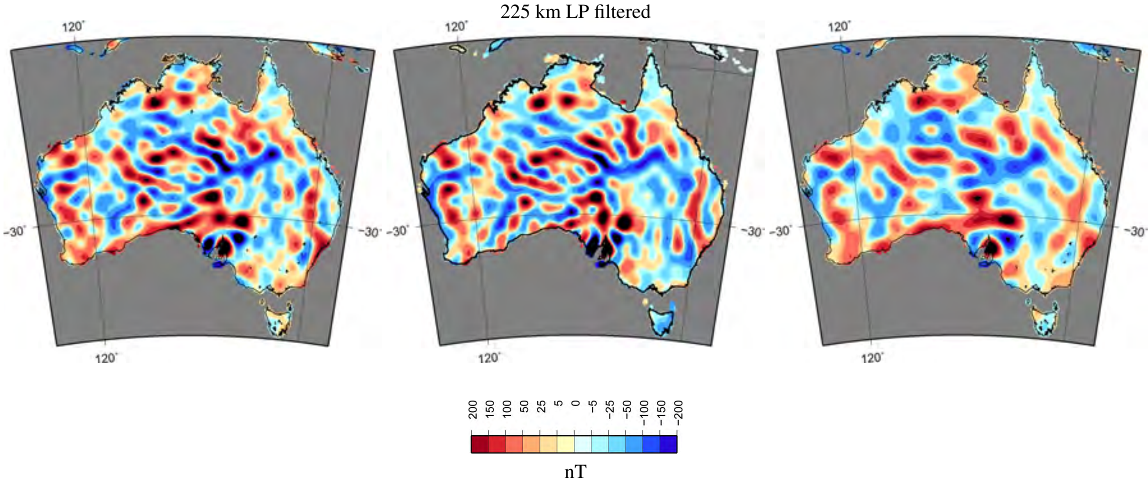

Figure 8. Comparison of intensity magnetic anomalies from LCS-1 and MF7 models with the lowpass filtered Australian data set. In places the LCS-1 model has spatial resolution approaching 225 km.

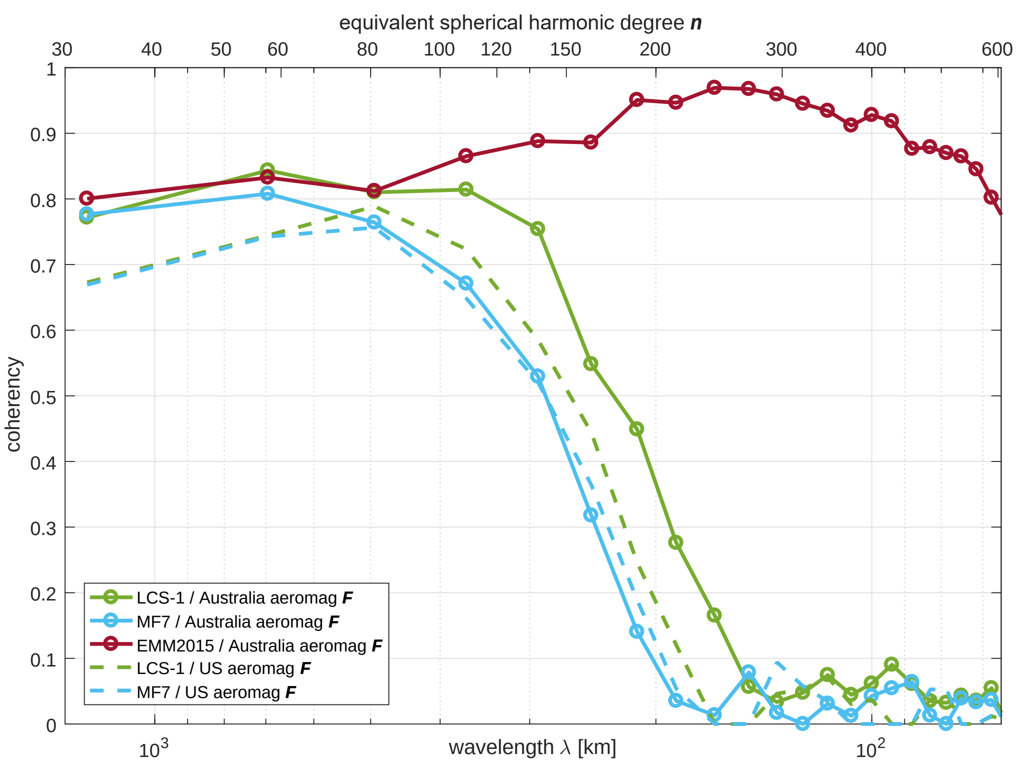

Figure 9. Solid lines: Spectral comparison (coherency) between the Australian full spectrum data in the central third of Australia and LCS-1, MF7, and EMM2015 models. The region of comparison is limited by the maximum Cartesian dimension of a study region and hence is limited to 1500 km. All data were projected to Lambert Conical projection and gridded in Cartesian coordinates using identical projection and gridding parameters. Dashed lines: A similar spectral comparison of the models with NURE-NAMAM2008 database in the central U.S. Bottom axis shows horizontal wavelength; top axis shows the equivalent spherical harmonic degree.

1989; Ravat et al. 1992); and as a large circular region magnetized by asteroid impact (Girdler et al. 1989, 1992; Ravat et al. 2002). The only known near-surface magnetic data in the region are sparse ground data which show central lobes of -1000 to -1400 nT of $0.5° - 1°$ half wavelength and northern and southern side lobes of $+400$ to $>$ 600 nT of $0.25° - 1°$ half wavelength (J. Vassal, unpublished data, 1978, in Regan et al. 1975) and hence the high resolution satellite anomaly models are extremely valuable in the assessment of the origin of geologic sources and economic resources of the region. The LCS-1 field intensity anomaly (three narrow and 300 to 400 nT positive peaks and a couple of narrow 300 to 500 nT negative troughs, Figure 10b) shows significant improvement in spatial resolution over the MF7 field (a couple of broader and lower amplitude positive and negative peaks each, Figure 10a). A similar improvement is also seen in the features of west African cratons and the intervening Taoudeni basin in the NW section of the surface plots (for geology and preliminary magnetic crustal models, see Ravat (1989), and references therein).

6 SUMMARY AND CONCLUSIONS

We have used four years of CHAMP satellite and three years of *Swarm* satellite constellation magnetic "gradients" observations (approximated by finite differences of magnetic field observations) to derive a global model of Earth's lithospheric field. The model is regularised by minimizing the L1-norm of the radial magnetic field, $|B_r|$, averaged over Earth's surface.

The resulting model shows very good agreement with other satellite-derived lithospheric field models (degree correlation above 0.8 for all degrees $n \leq 133$). Comparison with independent near-surface aeromagnetic data from Australia yields good agreement at horizontal wavelengths down to 250 km (corresponding to spherical harmonic degree $n = 160$). Crucial for achieving this result is the East-West "gradient" information that is provided by the unique *Swarm* constellation, despite of the presently rather high altitude of the Swarm lower satellites (of about 450 km) compared to the altitude of CHAMP (below 350 km) during the last four years of the mission. This is very encouraging for future lithospheric field modelling: including forthcoming *Swarm* data taken at lower altitude will certainly further increase the spatial resolution of satellite-derived lithospheric field models.

REFERENCES

Dyment, J. & Arkani-Hamed, J., 1998. Equivalent source magnetic dipoles revisited, *Geophys. Res. Lett.*, **25**(11), 2003–2006.

Farquharson, C. G. & Oldenburg, D. W., 1998. Non-linear inversion using general measures of data misfit and model structure, *Geophys. J. Int.*, **134**, 213–227.

Finlay, C. C., Olsen, N., Kotsiaros, S., Gillet, N., & Tøffner-Clausen, L., 2016. Recent geomagnetic secular variation from Swarm and ground observatories as estimated in the CHAOS-6 geomagnetic field model, *Earth Planets Space*, **68**(1).

Friis-Christensen, E., Lühr, H., & Hulot, G., 2006. *Swarm*: A constellation to study the Earth's magnetic field, *Earth Planets Space*, **58**, 351–358.

Girdler, R., Taylor, P., & Frawley, J., 1989. Some new thoughts on Bangui, *EOS – Transactions of the AGU*, **70**, 314.

Girdler, R., Taylor, P., & Frawley, J., 1992. A possible impact origin for the Bangui magnetic anomaly (Central Africa), *Tectonophysics*, **212**(1), 45 – 58.

Granot, R., Dyment, J., & Gallet, Y., 2012. Geomagnetic field variability during the cretaceous normal superchron, *Nature Geoscience*, **5**(3), 220–223.

Haines, G. V., 1985. Spherical cap analysis, *J. Geophys. Res.*, **90**, 2583–2591.

Hanssen, A., 1997. Multidimensional multitaper spectral estimation, *Signal Processing*, **58**(3), 327–332.

Kother, L., Hammer, M. D., Finlay, C. C., & Olsen, N., 2015. An equivalent source method for modelling the global lithospheric magnetic field, *Geophys. J. Int.*, **203**(1), 553–566.

Kotsiaros, S., Finlay, C. C., & Olsen, N., 2015. Use of along-track magnetic field differences in lithospheric field modelling, *Geophys. J. Int.*, **200**(2), 878–887.

Langel, R. A. & Hinze, W. J., 1998. *The magnetic field of the Earth's lithosphere: The satellite perspective*, Cambridge University Press, Cambridge.

Langel, R. A., Sabaka, T. J., Baldwin, R. T., & Conrad, J. A., 1996. The near-earth magnetic field from magnetospheric and quiet-day ionospheric sources and how it is modeled, *Phys. Earth Planet. Int.*, **98**, 235–267.

Leopardi, P., 2006. A partition of the unit sphere into regions of equal area and small diameter, *Electronic Transactions on Numerical Analysis*, **25**(12), 309–327.

Lesur, V., Wardinski, I., Rother, M., & Mandea, M., 2008. GRIMM: the GFZ Reference Internal Magnetic Model based on vector satellite and observatory data, *Geophys. J. Int.*, **173**, 382–294.

Lesur, V., Rother, M., Wardinski, I., Schachtschneider, R., Hamoudi, M., & Chambodut, A., 2015. Parent magnetic field models for the IGRF-12 GFZ-candidates, *Earth Planets Space*, **67:87**.

Lesur, V., Hamoudi, M., Choi, Y., Dyment, J., & Thébault, E., 2016. Building the second version of the World Digital Magnetic Anomaly Map (WDMAM), *Earth Planets Space*, **68**(1), 1.

Maus, S., 2007. CHAMP magnetic mission, in *Encyclopedia of Geomagnetism and Paleomagnetism*, pp. 59–60, eds Gubbins, D. & Herrero-Bervera, E., Springer, Heidelberg.

Maus, S., 2010. Magnetic field model MF7, www.geomag.us/models/MF7.html.

Maus, S., Rother, M., Holme, R., Lühr, H., Olsen, N., & Haak, V., 2002. First scalar magnetic anomaly map from CHAMP satellite indicates weak lithospheric field, *Geophys. Res. Lett.*, **29**(10), 47–1.

Maus, S., Yin, F., Lühr, H., Manoj, C., Rother, M., Rauberg, J., Michaelis, I., Stolle, C., & Müller, R., 2008. Resolution of direction of oceanic magnetic lineations by the sixth-generation lithospheric magnetic field model from CHAMP satellite magnetic measurements, *Geochem. Geophys. Geosyst.*, **9**(7), Q07021.

Mayhew, M., 1979. Inversion of satellite magnetic anomaly data, *J. Geophys.*, **45**, 119–128.

Milligan, P., Franklin, R., Minty, B., Richardson, L., & Percival, P., 2010. Magnetic anomaly map of australia (5th edition), 1: 5 000 000 scale (digital data set at geophysical archive data delivery system), Tech. rep., Geoscience Australia, Canberra.

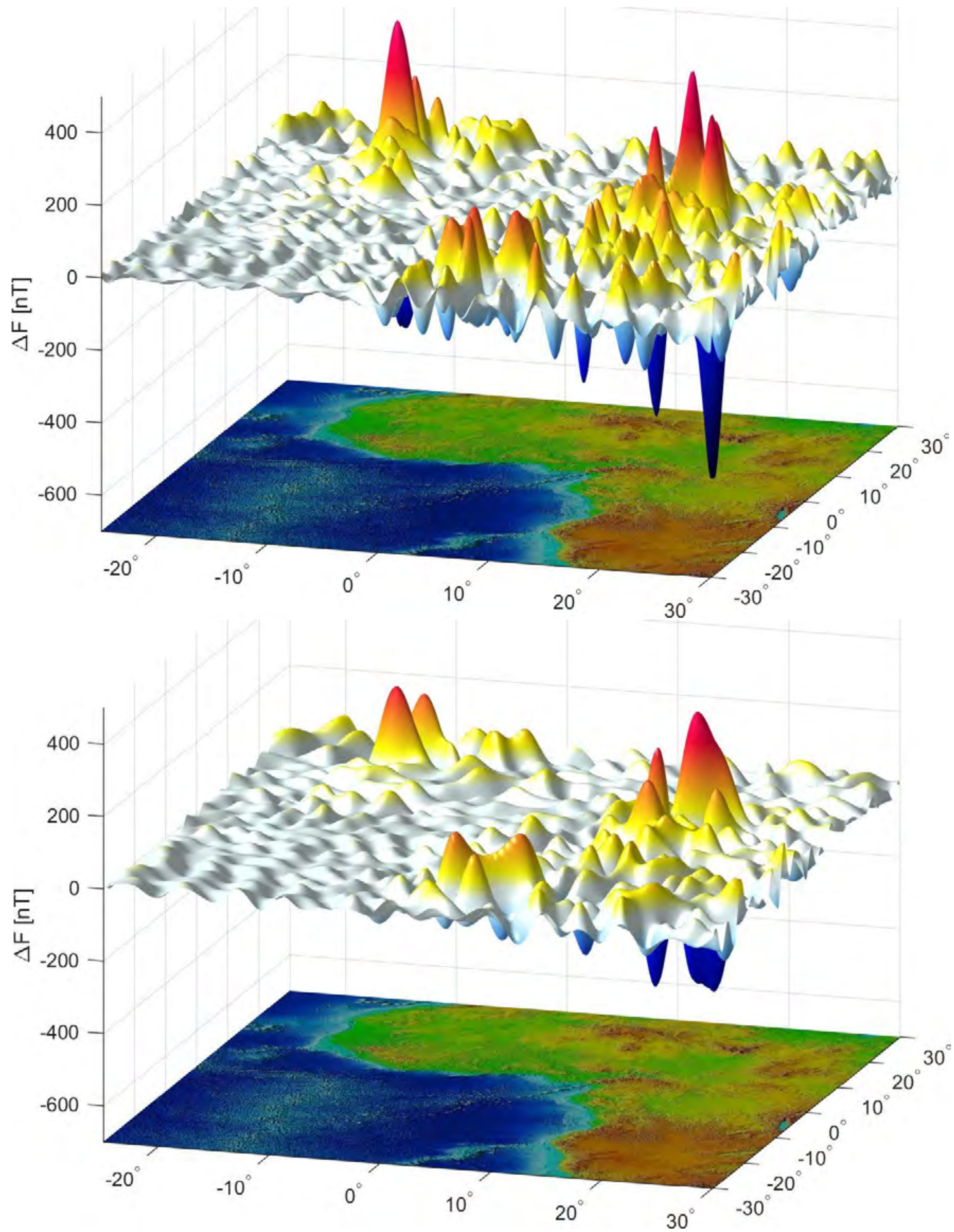

Figure 10. Scalar field anomaly close to Bangui in West-Africa as given by the LCS-1 model (top) and the MF7 model (bottom).

Morschhauser, A., Lesur, V., & Grott, M., 2014. A spherical harmonic model of the lithospheric magnetic field of Mars, *J. Geophys. Res.*, **119**(6), 1162–1188.

O'Brien, M. S. & Parker, R. L., 1994. Regularized geomagnetic field modelling using monopoles, *Geophys. J. Int.*, **118**, 566–578.

Olsen, N., Hulot, G., & Sabaka, T. J., 2010. Measuring the Earth's Magnetic Field from Space: Concepts of Past, Present and Future Missions, *Space Sci. Rev.*, **155**, 65–93.

Olsen, N., Lühr, H., Finlay, C. C., Sabaka, T. J., Michaelis, I., Rauberg, J., & Tøffner-Clausen, L., 2014. The CHAOS-4 Geomagnetic Field Model, *Geophys. J. Int.*, **197**, 815 – 827.

Olsen, N., Hulot, G., Lesur, V., Finlay, C. C., Beggan, C., Chulliat, A., Sabaka, T. J., Floberghagen, R., Friis-Christensen, E., Haagmans, R., Kotsiaros, S., Luehr, H., Tøffner-Clausen, L., & Vigneron, P., 2015. The Swarm Initial Field Model for the 2014 geomagnetic field, *Geophys. Res. Lett.*, **42**(4), 1092–1098.

Olsen, N., Finlay, C. C., Kotsiaros, S., & Tøffner-Clausen, L., 2016a. A model of Earth's magnetic field derived from two years of Swarm satellite constellation data, *Earth Planets Space*, **68**, 124.

Olsen, N., Stolle, C., Floberghagen, R., Hulot, G., & Kuvshinov, A., 2016b. Special issue "Swarm science results after 2 years in space", *Earth Planets Space*, **68**(1), 172.

Priestley, M. B., 1981. *Spectral analysis and time series*, Academic press.

Ravat, D., 1989. *Magsat investigations over the greater African region*, Ph.D. thesis, Ph. D. thesis, Purdue Univ., West Lafayette, Ind.

Ravat, D., 2011. Interpretation of Mars southern highlands high amplitude magnetic field with total gradient and fractal source modeling: New insights into the magnetic mystery of Mars, *Icarus*, **214**(2), 400–412.

Ravat, D., Hinze, W., & von Frese, R., 1992. Analysis of Magsat magnetic contrasts across Africa and South America, *Tectonophysics*, **212**(1-2), 59–76.

Ravat, D., Wang, B., Wildermuth, E., & Taylor, P. T., 2002. Gradients in the interpretation of satellite-altitude magnetic data: an example from central Africa, *J. Geodyn.*, **33**(1-2), 131–142.

Ravat, D., Finn, C., Hill, P., Kucks, R., Phillips, J., Blakely, R., Bouligand, C., Sabaka, T., Elshayet, A., Aref, A., & Elawadi, E., 2009. A preliminary full spectrum magnetic anomaly database of the united states with improved long wavelengths for studying continental dynamics, in *U.S. Geological Survey Open-File Report*, vol. 1, pp. 2009–1258.

Regan, R. D., Cain, J. C., & Davis, W. M., 1975. A global magnetic anomaly map, *J. Geophys. Res.*, **80**, 794–802.

Richmond, A. D., 1995. Ionospheric electrodynamics using magnetic Apex coordinates, *J. Geomagn. Geoelectr.*, **47**, 191–212.

Sabaka, T. J., Olsen, N., & Purucker, M. E., 2004. Extending comprehensive models of the Earth's magnetic field with Ørsted and CHAMP data, *Geophys. J. Int.*, **159**, 521–547.

Sabaka, T. J., Olsen, N., Tyler, R. H., & Kuvshinov, A., 2015. CM5, a pre-*Swarm* comprehensive magnetic field model derived from over 12 years of CHAMP, Ørsted, SAC-C and observatory data, *Geophys. J. Int.*, **200**, 1596–1626.

Stockmann, R., Finlay, C., & Jackson, A., 2009. Imaging Earth's crustal magnetic field with satellite data: a regularized spherical triangle tessellation approach, *Geophys. J. Int.*, **179**(2), 929–944.

Taylor, P. & Ravat, D., 1995. An interpretation of the Magsat anomalies of central Europe, *Journal of applied geophysics*, **34**(2), 83–91.

Thébault, E., 2006. Global lithospheric magnetic field modelling by successive regional analysis, *Earth Planets Space*, **58**, 485–495.

Thébault, E., 2008. A proposal for regional modelling at the Earth's surface, R-SCHA2D, *Geophys. J. Int.*, **174**(1), 118–134.

Thébault, E., Vervelidou, F., Lesur, V., & Hamoudi, M., 2012. The satellite along-track analysis in planetary magnetism, *Geophys. J. Int.*, **188**, 891–907.

Thébault, E., Lesur, V., Kauristie, K., & Shore, R., 2016. Magnetic field data correction in space for modelling the lithospheric magnetic field, *Space Sci. Rev.*, pp. 1–33.

Thébault, E., Vigneron, P., Langlais, B., & Hulot, G., 2016. A Swarm lithospheric magnetic field model to SH degree 80, *Earth Planets Space*, **68**(1).

Thomson, A., Hamilton, B., Macmillan, S., & Reay, S., 2010. A novel weighting method for satellite magnetic data and a new global magnetic field model, *Geophys. J. Int.*, **181**, 250–260.

Thomson, A. W. P. & Lesur, V., 2007. An improved geomagnetic data selection algorithm for global geomagnetic field modelling, *Geophys. J. Int.*, **169**(3), 951–963.

von Frese, R. R., Hinze, W. J., & Braile, L. W., 1981. Spherical earth gravity and magnetic anomaly analysis by equivalent point source inversion, *Earth Planet. Sci. Lett.*, **53**(1), 69–83.